1-1-1984

The modeling of shear and axisymmetric extensional polymer flows/

Paul R. Soskey
University of Massachusetts Amherst

THE MODELING OF SHEAR AND AXISYMMETRIC EXTENSIONAL POLYMER FLOWS

A Dissertation Presented

By

PAUL RAYMOND SOSKEY

Submitted to the Graduate School of the
University of Massachusetts in partial fulfillment
of the requirements for the degree of

DOCTOR OF PHILOSOPHY

September 1984

Polymer Science and Engineering

THE MODELING OF SHEAR AND AXISYMMETRIC

EXTENSIONAL POLYMER FLOWS

A Dissertation Presented

By

PAUL RAYMOND SOSKEY

Approved as to style and content by:

H. Henning Winter

Professor H. Henning Winter
Chairperson of Committee

Richard S. Stein

Professor Richard S. Stein, Member

Edwin L. Thomas

Professor Edwin L. Thomas, Member

William J. MacKnight

Professor William J. MacKnight
Department Head
Polymer Science and Engineering

In memory of my mother, Louise
who began this journey with me.

For my father, Benjamin
who guided my way.

And for Amy
who now travels by my side.

ACKNOWLEDGEMENT

I wish to thank my advisor, Professor Henning Winter, for his constant support and encouragement. I hope that some of his enthusiasm has been instilled in me. Working with him has greatly enriched me both as a person and a scientist. I also wish to thank Professor Stein for his help with the flow birefringence experiments and Professor Thomas for his advice in upgrading the quality of this dissertation.

Grants from General Electric Co., Shell Development Co., Exxon Chemical Co. and the Office of Naval Research (N00014-82-K-0083), which made this research possible, are gratefully acknowledged.

I thank all the students in the Polymer Science & Engineering and Chemical Engineering departments who made my stay here a rewarding one. I also want to thank my research group, especially Tom, Kung Hwa, Francois, Laurel, Steve and George for their helpful discussions and interactions during the course of this dissertation. A special thanks to Paul, Don and Dick whose technical support kept the experiments functioning.

Finally, I wish to express my gratitude and love for Amy whose love has filled my life with joy and whose constant encouragement, especially during the past year, was instrumental in the completion of this dissertation.

ABSTRACT

The Modeling of Shear and Axisymmetric

Extensional Polymer Flows

(September 1984)

Paul Raymond Soskey

B.S.Ch.E., University of Dayton

M.S., Ph.D., University of Massachusetts

Directed by: Professor H. Henning Winter

The objective of this dissertation was the modeling of complex axisymmetric flow of polymer melts in annular extrusion dies having both shear and extensional deformations superimposed, with the use of a suitable memory integral constitutive equation. The constitutive equation utilized was developed from the network theory of polymer melts and is a strain dependent form of the Lodge rubberlike liquid equation.

Three polymers, both low and high density polyethylene and an atactic polystyrene were rheologically characterized in shear and equibiaxial extension. The small strain properties were determined in oscillatory shear experiments.

The large shear strain properties were determined in step strain and capillary flow experiments. The shear step strain experiments were performed in a parallel disk rheometer. A correction method for the non-homogeneous strain in the parallel disks was proposed and experimentally verified. The shear relaxation modulus was separable into functions of time and strain. A sigmoidal form of the shear strain function was proposed.

Large extensional strain properties were measured in step strain experiments using a lubricated squeezing technique. The extensional relaxation modulus was also separable into functions of time and strain. The direct determination of the extensional strain function suggests that, for equibiaxial extension, the parameter in the generalized strain invariant proposed by Wagner is $\alpha=1$.

Flow experiments were performed in constant annular, converging and diverging extrusion dies. The different stress levels in the flowing polymer, due to the extension in the converging and diverging sections, was measured using a flow birefringence technique.

The process model gave a good prediction of the pressure drops in all three dies. The modeling calculations accurately predicted the extensional behavior and together with the measured flow birefringence indicate that material elements were subjected to an uniaxial extensional type deformation in the converging section and a biaxial extensional type deformation in the diverging section of the dies.

The modeling procedure was found to be very sensitive to the rheological properties of a polyethylene melt. The accurate characterization of the properties associated with the long relaxation times is very important in annular die flow.

TABLE OF CONTENTS

LIST OF TABLES

LIST OF FIGURES

C H A P T E R I

INTRODUCTION

The ability to model shaping processes of polymeric materials in the melt state is of utmost importance in the design of a particular process and in relating the resultant properties to the molecular orientation induced by the deformation. Accurate description and simulation of polymer melt processing depends on the selection of a suitable constitutive equation which can describe the viscoelastic behavior of the melt as it is processed. A constitutive equation, a relationship between stress and strain history, is often tested by comparing its prediction to the behavior of melts in rheologically simple flows. There are few instances where accurate viscoelastic constitutive equations have been used to model complex processing flows.

Some processing flows of considerable interest include melt extrusion, calendering, roll coating, fiber spinning, film blowing, injection molding and blow molding. Established models of these processes and others have been described in several polymer processing textbooks (McKelvey, 1962; Middleman, 1977; Tadmor and Gogos, 1979; Throne, 1979). All of these models treat the polymer melts as viscous liquids having no elastic properties. As a first approximation, these processes have been modeled assuming that the polymer behaves like a Newtonian liquid. This assumption may be adequate at very low shear rates but at moderate shear rates, which occur in most processing flows, polymers exhibit a decrease in shear viscosity known as "shear

thinning." As an improvement, this non-Newtonian shear viscosity behavior is described by a strain rate dependent viscosity relation such as the power law (Ostwald-deWaele model). Reasonable predictions of pressure drops and flow rates have been obtained for processes involving mostly steady shear flow using these inelastic models. For more complex flows having extensional deformations, these models are inadequate due to their inability to describe extensional rheological behavior.

Important phenomena such as stress relaxation, molecular orientation in flow and extrudate swell, which are associated with the elasticity of the polymer, are also not described by such simple relations for the steady state shear viscosity. These phenomena are influenced by the entire processing history of the deforming polymer. Due to the long chain nature of the molecule, polymeric materials have the ability to "remember" the prior deformation history to which they have been subjected. Therefore, in order to model flows that are influenced by the entire processing history, a rheological constitutive equation which includes "memory effects" must be employed.

Many constitutive equations which exhibit memory have been proposed. Both integral equations and rate equations are able to describe observed phenomena in time dependent shear and time dependent extensional deformations (Bird et al., 1977). Constitutive equations which exhibit memory have been used by several authors in the modeling of polymer processes. Integral equations are useful in modeling studies when the kinematics of the flow are well known.

A well tested memory integral constitutive equation is the "rubberlike liquid" equation (Lodge, 1964) which will be described below in more detail. The equation contains a memory function which describes the fading memory of a polymer solution or melt by means of a spectrum of relaxation time constants. The most simple form of the rubberlike liquid contains only one time constant and is called the Maxwell fluid.

Both solution procedures (Crochet and Bezy, 1979; Viriyayuthakorn and Caswell, 1980; Bernstein and Malkus, 1981; Malkus, 1981) and experimental correlations for film blowing (Petrie, 1973 and 1975), fiber spinning (Fisher and Denn, 1972), die swell (Huang and White, 1979 and 1980) and injection molding (Dietz and White, 1978) have been reported for the Maxwell fluid. Although the Maxwell fluid exhibits memory and is useful in observing the effects of elasticity on the solutions for the process modeling, it only qualitatively describes the true behavior of polymeric materials. For instance, the Maxwell fluid does not predict the transient stress relaxation of polymers in the linear viscoelastic region. The rubberlike liquid with a spectrum of relaxation times is able to describe transient stress growth and stress relaxation in the linear viscoelastic region of small strains or strain rates, however, it is inadequate at large strains or strain rates.

Various non-linear forms of integral equations have been considered which describe rheological behavior at large strains or high strain rates (Bernstein et al., 1963 and 1964; Bird and Carreau, 1968; Bogue and White, 1970; Chen and Bogue, 1972; Leonov, 1976). A melt spinning process, both isothermal (Chen et al., 1972; Spearot and

Metzner, 1972) and non-isothermal (Matsui and Bogue, 1976) has been modeled using non-linear forms of an integral equation. The memory integral constitutive equation gave a good description of the steady uniaxial extensional flow in the spinning process. The injection molding process has also been successfully modeled by such non-linear equations (Tadmor, 1974; Isayev and Hieber, 1980).

The modeling of axisymmetric annular extrusion is of great interest because it is an essential starting point of other processes such as film blowing, blow molding and wire coating. The modeling must handle complex mixed flows where shear and extensional deformations are superimposed due to the constraining walls and tapering sections in the extrusion die. In fact many different molecular orientation distributions can be generated by these complex flows just by changing the channel geometries and flow rates in the extrusion die. Different orientations, on a macroscopic scale, of short, treated cellulose fibers were obtained in rubber hose extruded from dies of differing upstream channel geometries (Goettler et al., 1979). The orientation of the fibers in the final part was dependent on the die geometry as seen in Figure 1.1.

The modeling of the stress distributions in annular extrusion dies using a memory integral constitutive equation has been developed by Winter and Fischer (1981). An integral constitutive equation which was shown to describe both shear and uniaxial extensional data of a LDPE melt was used in the analysis. The effect of different upstream die geometries on the calculated stress distributions at the die exit was investigated. This modeling has been extended to capillary die swell

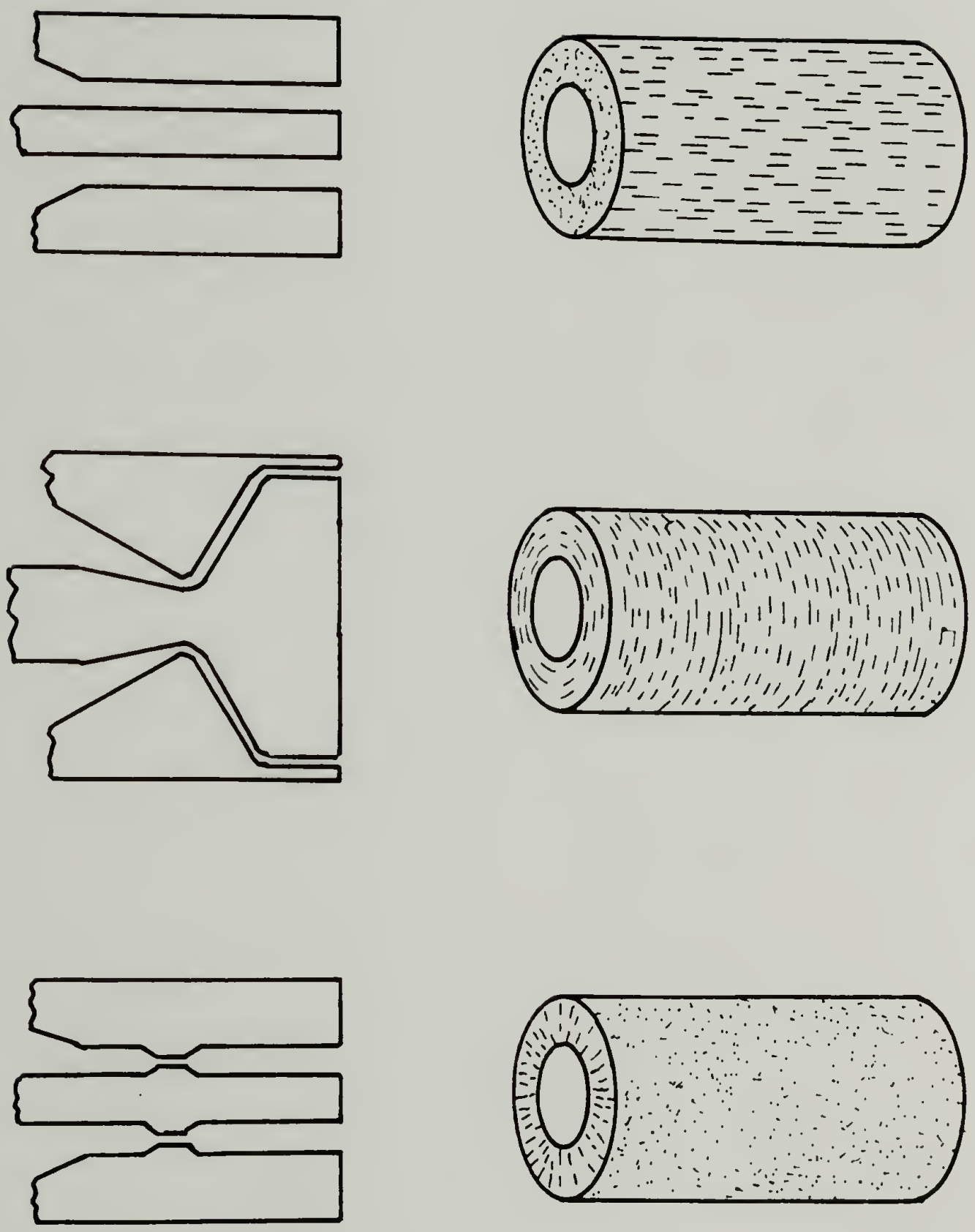

Figure 1.1. Fiber orientation patterns obtained from dies of differing geometries (Goettler et al., 1979).

(Fischer, 1981a), blow molding (Winter and Soskey, 1981), and film blowing (Fischer, 1981b; Soskey and Winter, 1982).

The objective of this dissertation is to model the complex axisymmetric flow in annular extrusion dies, having both shear and extensional deformations superimposed, using a memory integral constitutive equation. For the modeling to be successful, two areas must be investigated. First, a suitable constitutive equation must be obtained to describe the rheological behavior of polymer melts and associated rheological experiments performed in order to obtain the required material parameters for the constitutive equation. Secondly, the deformation history must be determined for each material element in the processing flow. This is accomplished by means of a continuum tracking technique. An integration scheme is then used to calculate stress distributions at various positions in a die and comparisons are made with experimental measurements.

In chapter two, a suitable constitutive equation for polymer melts is formulated from a molecular network theory. An equation capable of describing the non-linear behavior of polymer melts is presented and the rheological material parameters for such an equation are then determined.

The rheological characterization of two different polyethylene melts and a polystyrene melt is presented in chapter three. Both the linear viscoelastic (small strain) and the non-linear (large strain) rheological properties of the melts are determined in both shear and equibiaxial extension. Two novel rheological experimental techniques

are developed during the course of this work. First, stress relaxation after a step in shear strain is performed in a parallel disk shear rheometer. A correction method for the nonhomogeneous strain in the parallel disk geometry is proposed and experimentally verified. Secondly, stress relaxation after a step in equibiaxial extensional strain and stress growth at constant extension rate are experimentally measured using a lubricated squeezing technique to obtain novel equibiaxial extensional rheological data. The appropriate material parameters for the constitutive equation are then determined from these experiments and the rheological behavior of the polymer melts is completely described.

The process modeling procedure is then be discussed in chapter four. The deformation history of a material element is determined from the geometry and kinematics of the process by tracking the material elements along the pathlines of the flow. From the rheological parameters of the particular polymer and the deformation history of the process, the constitutive equation is numerically integrated to calculate the stress distributions at some point in the process.

In chapter five, flow experiments through annular extrusion dies of differing channel geometries are presented. The stress at a particular point inside the extrusion dies is measured using a flow birefringence technique. The comparison to the predictions of the modeling calculations is then discussed.

The sensitivity of the modeling technique to variations in the polymer rheology is investigated in chapter six. The effect that slight

changes in the rheological parameters have on the calculated stress distributions in dies of differing geometries are discussed.

Finally, suggestions for future research in the field of extensional rheometry and process modeling is presented in chapter seven.

C H A P T E R I I

DEVELOPMENT OF A MEMORY INTEGRAL CONSTITUTIVE EQUATION FOR POLYMER MELTS

A constitutive equation relates the stress to the deformation of a material. A constitutive equation capable of describing the transient non-linear behavior of polymer melts in both shear and extensional flow is needed to model complex axisymmetric flows. The development of a suitable strain dependent memory integral equation which is derived from the network theory of polymer melts is given in this chapter.

2.1 Description of Strain

In the development of a constitutive equation for the relationship between the stress and deformation of a material, a description of a strain measure is an essential starting point. The material is assumed to be a continuous distribution of point-particles filling a three dimensional region of space in each state. Each state is associated with a time, where the time at the present state is t and the time at some prior state is t'. A deformation is continuous if no two particles in space occupy the same place and neighboring particles in one state are neighboring particles in any other state, which implies that no breaks occur in the material.

To describe the strain of a particle P, a set of three independent material vectors $\underline{e}_i$, which are orthonormal (unit length, right angles) at time t, are chosen as shown in Figure 2.1. The relative strain is

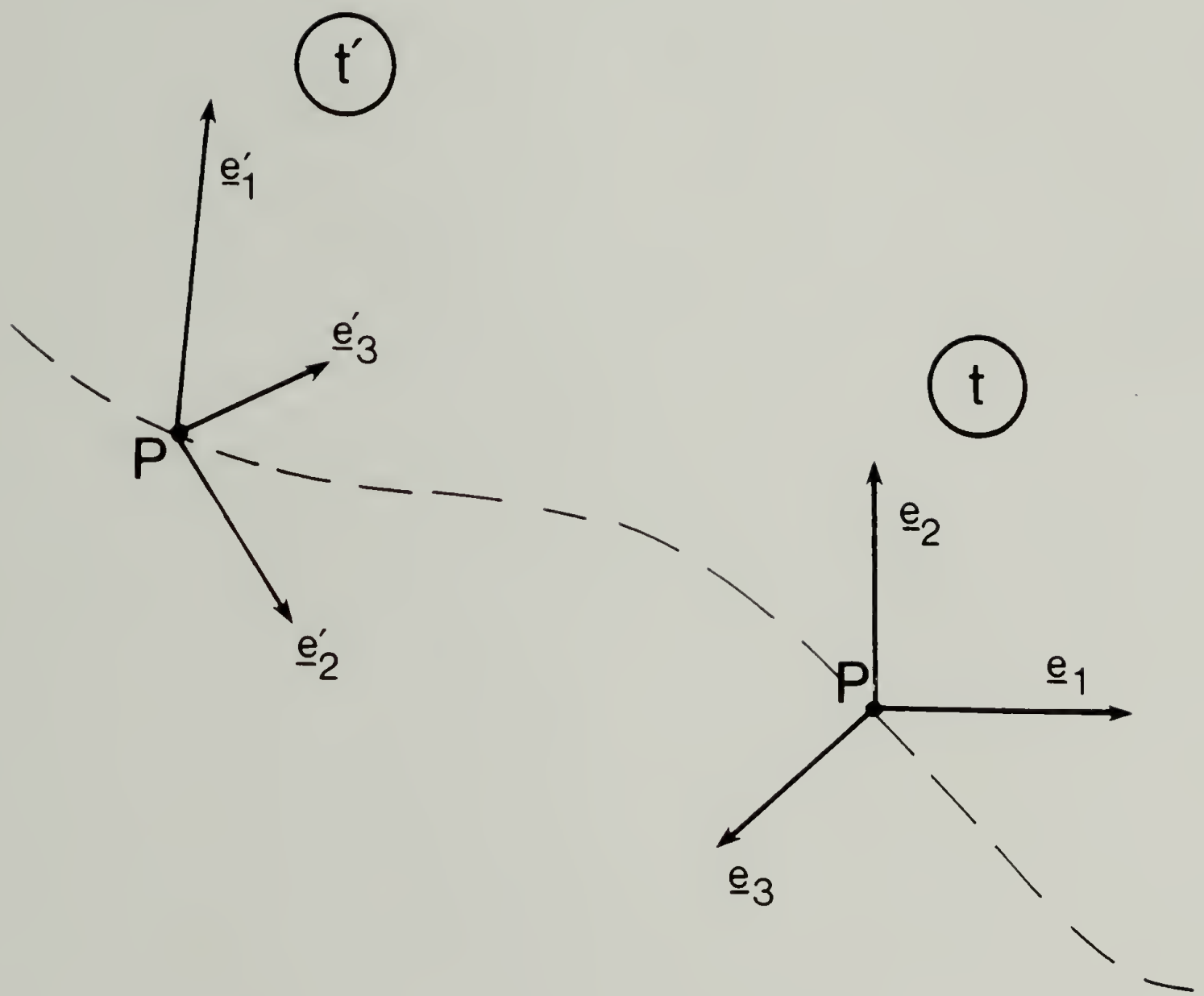

Figure 2.1. Three independent material vectors which define the strain between times t' and t.

completely defined by the change in these material vectors between times t' and t where the material vectors deform affinely with the material. At prior times, t', the three material vectors, $\underline{e}'_i$, were stretched and tilted due to the strain of the material in the particular deformation and are related by

$$\underline{e}'_i = \underline{e}_i(t') = \underline{\underline{F}} \cdot \underline{e}_i(t) \tag{2.1}$$

where $\underline{\underline{F}}$ is the deformation gradient tensor. The change in length and change in angle of these material vectors are given by the relative Cauchy-Green strain tensor

$$[\underline{\underline{C}}(t',t)]_{ij} = \underline{e}'_i \cdot \underline{e}'_j = [\underline{\underline{F}}^T \cdot \underline{\underline{F}}]_{ij} \tag{2.2}$$

which describes the strain as a function of time from state, t', to state, t. The material element marked by the material vectors is assumed to be small enough to make the influence of strain gradients on the components of $\underline{\underline{C}}$ negligible.

The inverse of the Cauchy-Green strain tensor is the Finger strain tensor, $\underline{\underline{C}}^{-1}(t',t)$, and is obtained by means of the Cayley-Hamilton theorem as

$$\underline{\underline{C}}^{-1} = (\underline{\underline{C}}^2 - I_C \underline{\underline{C}} + II_C \underline{\underline{1}})/III_C \tag{2.3}$$

where the invariants are defined, in this case for the Cauchy-Green tensor

$$I_C = \text{trace}(\underline{\underline{C}}) \tag{2.4}$$

$$II_C = (I_C^2 - \underline{\underline{C}} : \underline{\underline{C}})/2 \tag{2.5}$$

$$III_C = \det(\underline{\underline{C}}) \tag{2.6}$$

and the unit tensor is

$$\underline{\underline{1}} = \begin{pmatrix} 1 & 0 & 0 \\ 0 & 1 & 0 \\ 0 & 0 & 1 \end{pmatrix} \qquad (2.7).$$

For constant volume deformations $III_C=1$. Whereas, the Cauchy-Green strain tensor describes changes in material lines, the Finger strain tensor describes changes in material planes. The Finger strain tensors for various types of flow will be discussed further.

2.1.1 Shear

A shear deformation between t' and t is shown in Figure 2.2 where 1 is the direction of shear, 2 is the normal to the shear plane and 3 is the neutral direction. The angle of shear, θ, is the inclination of the vector $\underline{e}_2'$ to the shearing plane normal. The magnitude of shear is

$$\gamma(t',t) = \tan\theta = \int_{t'}^{t} \dot{\gamma}(t'')dt'' \qquad (2.8)$$

where $\dot{\gamma}$ is the shear rate normal to the shearing plane. The resultant material vectors are

$$\underline{e}_1' = (1,0,0) \qquad (2.9)$$

$$\underline{e}_2' = (-\gamma,1,0) \qquad (2.10)$$

$$\underline{e}_3' = (0,0,1) \qquad (2.11).$$

The Finger strain tensor for <u>shear</u> is then from Eqs. (2.2) and (2.3)

$$\underline{\underline{C}}^{-1}(t',t) = \begin{pmatrix} 1+\gamma^2 & \gamma & 0 \\ \gamma & 1 & 0 \\ 0 & 0 & 1 \end{pmatrix} \qquad (2.12)$$

with the invariants of the Finger strain tensor being

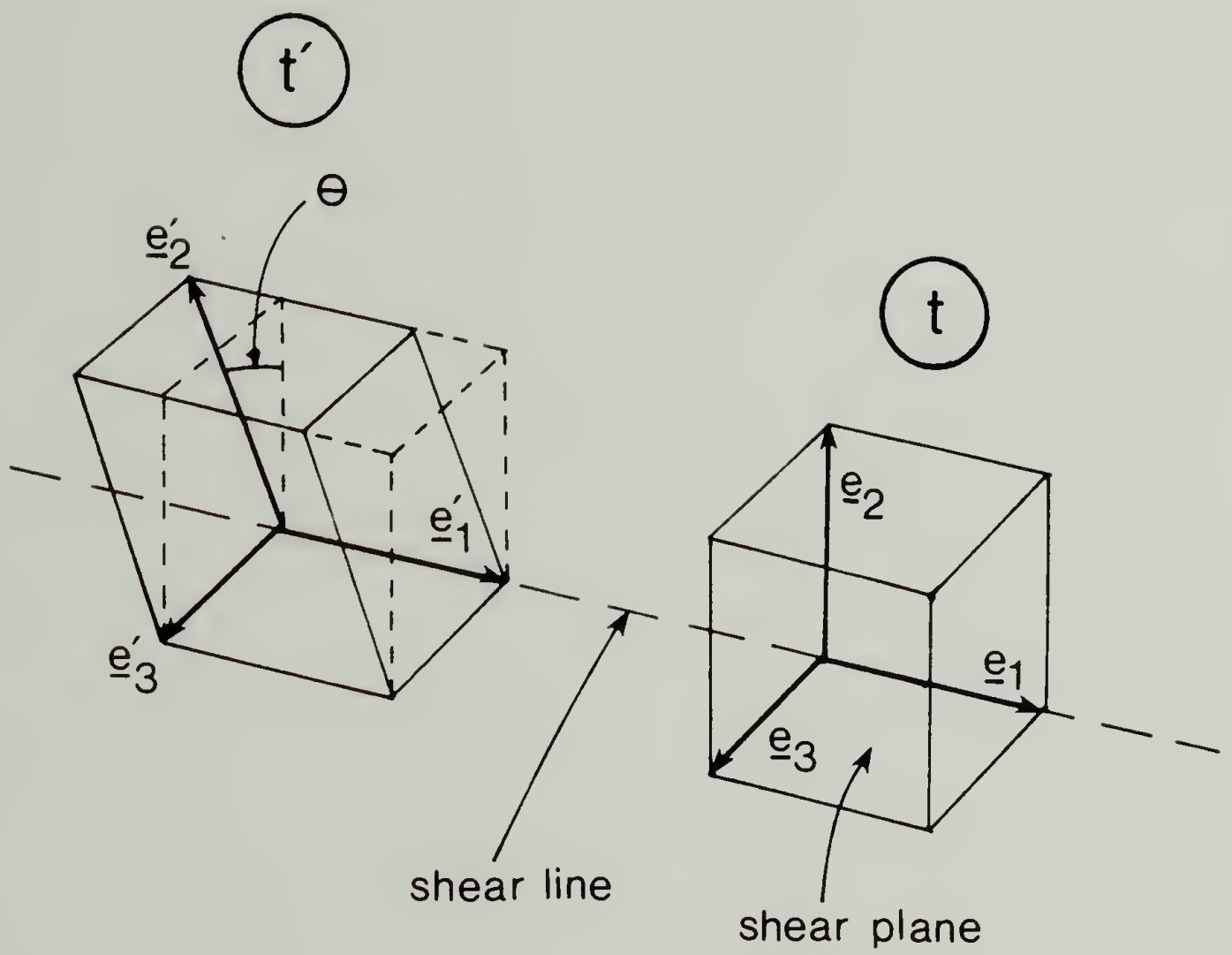

Figure 2.2. Material vectors for shear flow.

$$I_{C^{-1}} = I_1(\gamma) = \gamma^2+3 \tag{2.13}$$

$$II_{C^{-1}} = I_2(\gamma) = \gamma^2+3 \tag{2.14}$$

$$III_{C^{-1}} = 1 \tag{2.15}.$$

2.1.2. Axisymmetric Extension

An axisymmetric extension between t' and t is shown in Figure 2.3 where 1 is the symmetry axis of the deformation and 2 and 3 are orthogonal to 1. The change in length, L, associated with the direction of the symmetry axis, is related to the axisymmetric extension rate, $\dot{\varepsilon}_a$, by

$$\dot{\varepsilon}_a = \dot{\varepsilon}_1(t) = dL(t)/(L(t)dt) \tag{2.16}.$$

The axisymmetric strain is then

$$\varepsilon_a(t',t) = \varepsilon_1(t',t) = \int_{t'}^{t} \dot{\varepsilon}_1(t'')dt'' \tag{2.17}.$$

The resultant material vectors are

$$\underline{e}'_1 = (\exp(-\varepsilon_a),0,0) \tag{2.18}$$

$$\underline{e}'_2 = (0,\exp(\varepsilon_a/2),0) \tag{2.19}$$

$$\underline{e}'_3 = (0,0,\exp(\varepsilon_a/2)) \tag{2.20}.$$

The Finger strain tensor for axisymmetric extension is then from Eqs. (2.2) and (2.3)

$$\underline{\underline{C}}^{-1}(t',t) = \begin{pmatrix} \exp(2\varepsilon_a) & 0 & 0 \\ 0 & \exp(-\varepsilon_a) & 0 \\ 0 & 0 & \exp(-\varepsilon_a) \end{pmatrix} \tag{2.21}$$

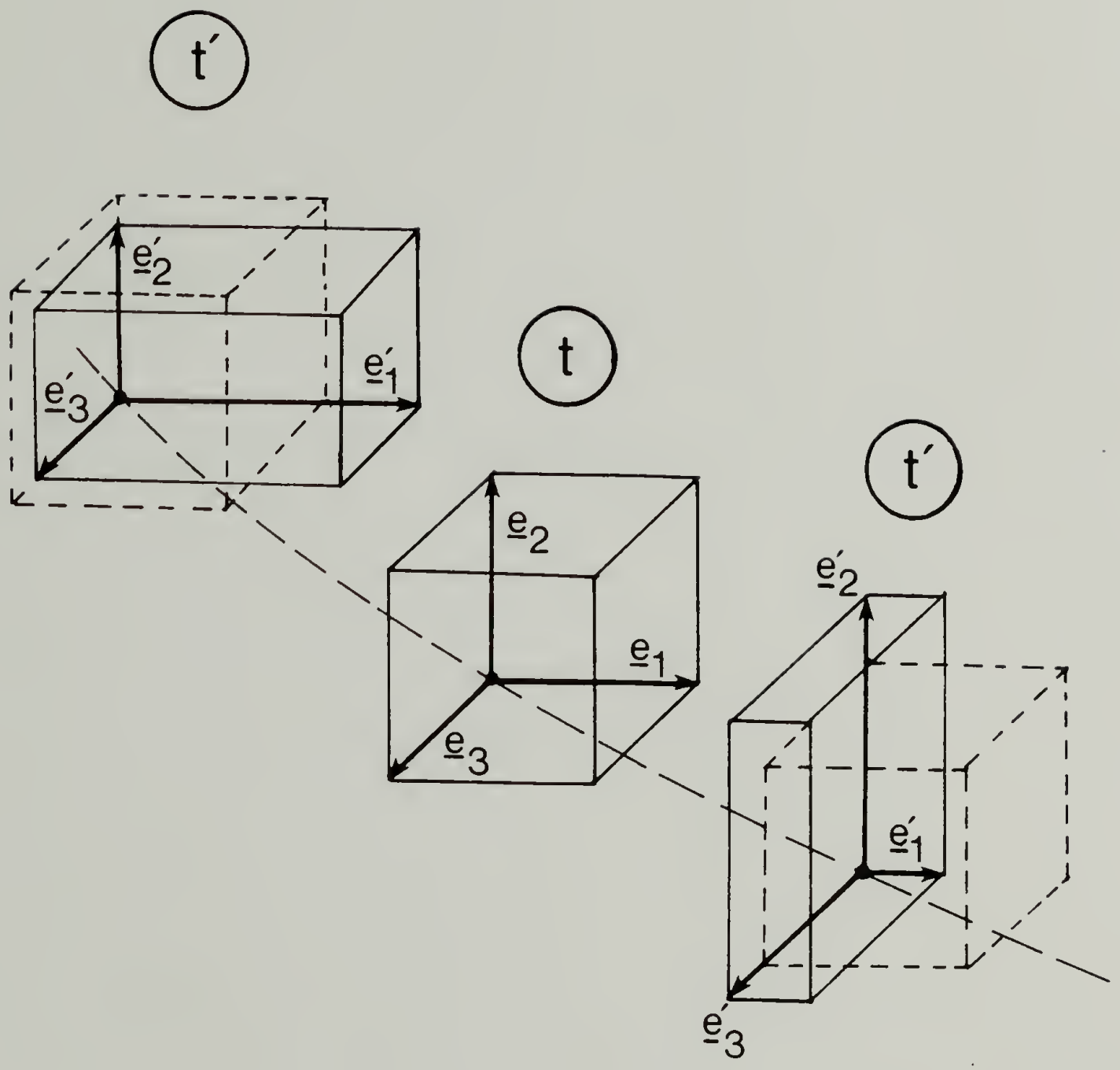

Figure 2.3. Material vectors for axisymmetric extension. For uniaxial extension, the extension rate $\dot{\varepsilon}_1$ is positive and for equibiaxial extension $\dot{\varepsilon}_1$ is negative with $\dot{\varepsilon}_2 = \dot{\varepsilon}_3 = -\dot{\varepsilon}_1/2$.

with the invariants of the Finger strain tensor being

$$I_{C^{-1}} = I_1(\varepsilon_a) = \exp(2\varepsilon_a) + 2\exp(-\varepsilon_a) \tag{2.22}$$

$$II_{C^{-1}} = I_2(\varepsilon_a) = \exp(-2\varepsilon_a) + 2\exp(\varepsilon_a) \tag{2.23}$$

$$III_{C^{-1}} = 1 \tag{2.24}.$$

The axisymmetric strain, ε_a, is positive for uniaxial extension and negative for equibiaxial extension. An equibiaxial strain, ε_b, is then

$$\varepsilon_b = \varepsilon_2(t',t) = -\varepsilon_a/2 \tag{2.25}$$

and the Finger strain tensor for equibiaxial extension is then from Eqs. (2.21) and (2.25)

$$\underline{\underline{C}}^{-1}(t',t) = \begin{pmatrix} \exp(-4\varepsilon_b) & 0 & 0 \\ 0 & \exp(2\varepsilon_b) & 0 \\ 0 & 0 & \exp(2\varepsilon_b) \end{pmatrix} \tag{2.26}$$

with the invariants of the Finger strain tensor being

$$I_{C^{-1}} = I_1(\varepsilon_b) = \exp(-4\varepsilon_b) + 2\exp(2\varepsilon_b) \tag{2.27}$$

$$II_{C^{-1}} = I_2(\varepsilon_b) = \exp(4\varepsilon_b) + 2\exp(-2\varepsilon_b) \tag{2.28}$$

$$III_{C^{-1}} = 1 \tag{2.29}.$$

2.2 Network Theory of Rubber Elasticity

A molecular theory, known as the kinetic, statistical or network theory of rubber elasticity, has been developed to describe the elastic properties of rubber and other polymers that behave similarly (Treloar, 1975). The theory describes an isotropic incompressible perfectly

elastic solid and will be the basis for the development of a network theory for polymer melts.

The structure of rubber on which the kinetic theory is based appears in Figure 2.4. A sample of rubber consists of many long chain molecules linked together at a few points forming a three-dimensional network throughout the sample. A given molecule in the network may be linked at two or more points. The segments between these junctions consist of many links or repeat units and the length of these segments will depend on the number of links between the junctions. The points of cross-linkage between chain molecules are considered to be permanent junctions consisting of chemical bonds. In any given chain molecule, there are a large number of bonds along the main chain about which free rotation is possible. Therefore, a great many configurations of equal potential energy are possible. The change of shape at constant volume involves a change in the number of configurations of equal potential energy and hence involves a change in configurational entropy without a change of internal energy. The stress at thermodynamic equilibrium at any time, t, can be calculated from the change of configurational entropy which the network undergoes when the material is deformed from the stress free state at time, t_o.

The network theory, which is described in detail by Treloar (1975), makes use of the following assumptions.

(a) The network contains N_o segments per unit volume.

(b) The mean-square end-to-end distance for the whole assembly of segments in the unstrained state is the same as for a corresponding set

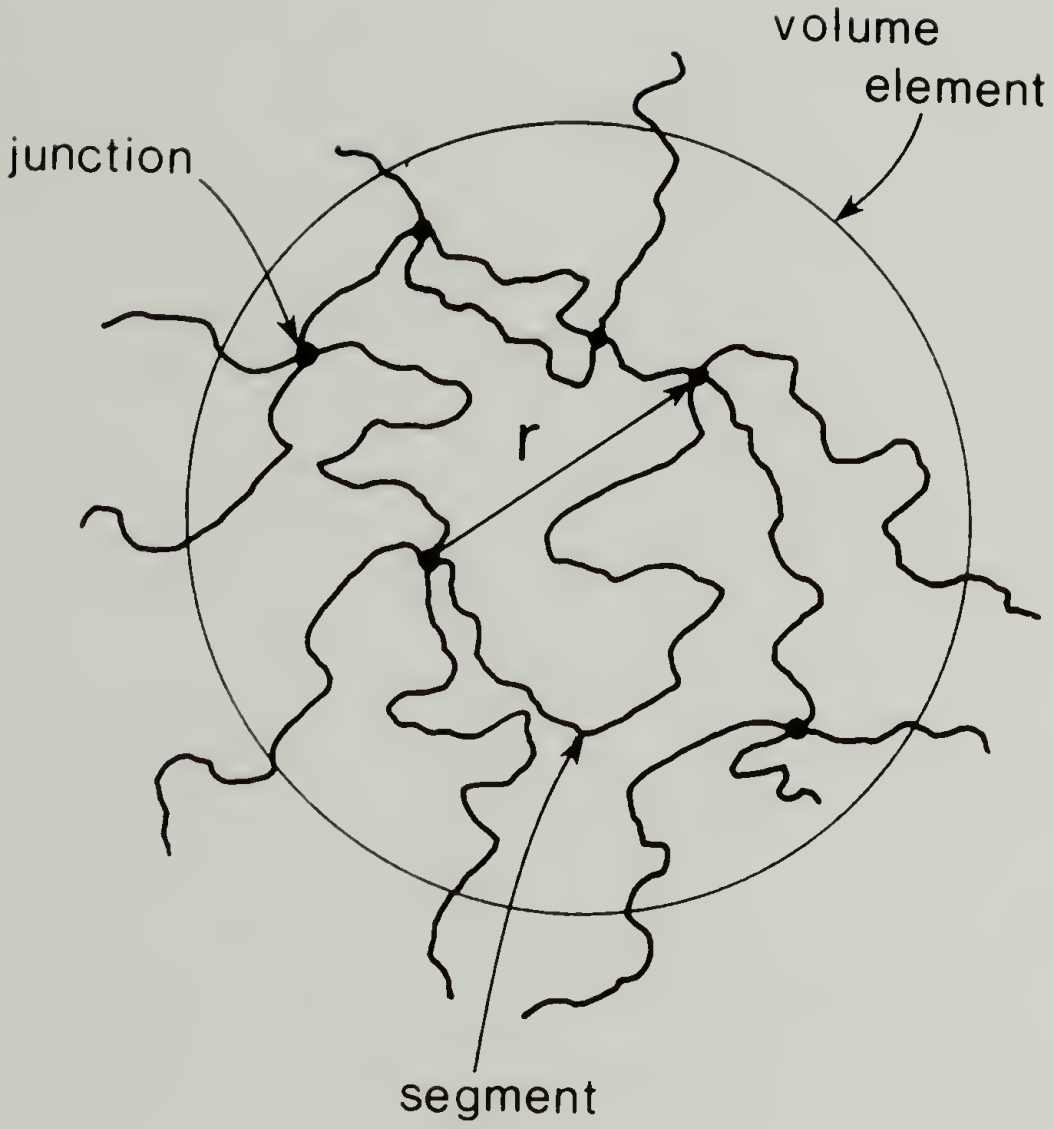

Figure 2.4. The macromolecular network structure.

of free segments

$$\overline{r^2} = n\ell^2 \tag{2.30}$$

where r is the distance between junctions, ℓ is the length of the freely-jointed rigid links and n is the number of links.

(c) There is no change of volume on deformation.

(d) The deformation is affine.

(e) The network is assumed to be a "Gaussian" network. This says that the probability of finding the ends of a randomly jointed segment a distance r apart and within a small volume element can be expressed as a probability density, P, which has the Gaussian form (Kuhn, 1934 and 1936):

$$P(r) = (3/2\pi n\ell^2)^{3/2}\exp(-3r^2/n\ell^2) \tag{2.31}$$

(f) The entropy of the network is the sum of the entropies of the individual segments. The entropy of the individual segments, S, is given by:

$$S(r) = c - (3kr^2/2n\ell^2) \tag{2.32}$$

where c is a constant and k is Boltzman's constant.

Now for a homogeneous strain, the work of deformation can be obtained from the total change in entropy of the deformation, assuming that there is no change of the internal energy on deformation. The stress can then be calculated from the work done by the applied forces which are responsible for the deformation. In doing so, the well known equation of rubber elasticity, also known as the equation of state for a neo-Hookean solid, is obtained

$$\underline{\underline{g}}(t) = -p\underline{\underline{I}} + N_o kT\underline{\underline{C}}^{-1}(t_o,t) \qquad (2.33)$$

where $\underline{\underline{g}}$ is the stress tensor, p is the isotropic pressure contribution and T is the absolute temperature.

2.3 Network Theory of Polymer Melts

A constitutive equation for polymer melts must describe not only elastic behavior, but also the viscous nature. Therefore, the network theory of rubber elasticity must be "liquified." Theories have been developed to describe this liquid nature by Green and Tobolsky (1946) and modified by Yamamoto (1956, 1957 and 1958) and Lodge (1956, 1964 and 1968).

The network junctions are no longer considered to be permanent chemical crosslinks as was assumed for the rubberlike solid, but are assumed to be temporary junctions or entanglements. Although the theory has been developed for concentrated solutions, it is applicable to polymer melts as well.

The network theory of polymer melts is based on certain assumptions which are expressed as (Lodge, 1956 and 1968).

(a) The polymer melt is an incompressible homogeneous continuum at a constant temperature.

(b) At any instant in time, long chain molecules are linked at a few points along their length by temporary physical entanglements. These entanglements extend throughout the network and create segments which are parts of a chain that are terminated either by two

entanglement junctions or by one junction and a boundary point of a very small volume element as shown in Figure 2.4.

(c) Due to the effects of thermal motion, segments are continually being lost and new ones formed. At any instant, t, the concentration of segments which were formed in a previous time interval (t', t'+dt'), and still exist at time, t, is

$$N(t-t')dt' \tag{2.34}$$

where N is the creation rate of segments per unit volume. This creation rate of segments depends on the time interval, (t-t') and not on t or t' separately. Now assuming that all segments of the same type i have (1) the same constant relaxation time, λ_i, which is the reciprocal of the probability per unit time of the segment leaving the network, and (2) the same constant creation rate per unit volume, N_i, then the overall creation rate can be expressed as (Lodge, 1968):

$$N(t-t') = \sum_i N_i \exp[-(t-t')/\lambda_i] \tag{2.35}.$$

(d) The creation rate of segments per unit volume is assumed to be independent of the flow history. This says that the process of formation and loss of the entanglement junctions is not affected by the deformation of the network. It is this assumption that causes the rubberlike liquid theory to predict a constant steady state shear viscosity even at high rates of shear. The modification of the resultant constitutive equation to predict a shear viscosity which

depends on shear rate will require that the concentration of segments somehow depends on the flow history.

(e) The network is at time, t, in thermodynamic equilibrium with regard to changes of the network configuration. This implies that the attainment of thermodynamic equilibrium in each state that the network passes through is infinitely rapid compared to the times involved in the flow.

(f) In a flowing polymer melt, the network will deform and the associated change of configurational entropy will cause a non-isotropic contribution to the stress. It is also assumed that any unattached chain molecules or very low molecular weight units cause negligible non-isotropic contributions to the stress.

(g) To calculate the stress at time t, for any arbitrary flow history, the contributions to the extra stress must be summed up from all previous times t'. The contribution to the extra stress from t' arises from segments which joined the network in the time interval (t', t'+dt') and are still part of the network at the current time t. The contribution from these segments is given by the kinetic theory of rubber elasticity, as described above, for a network having a stress free state at t', and a stressed state at t, with the concentration of segments per unit volume being $N(t-t')dt'$.

From these assumptions, the stress at time t, is given by the time integral (Lodge, 1968)

$$\underline{\underline{g}}(t) = -p\underline{\underline{I}} + kT\int_{-\infty}^{t} N(t-t')\underline{\underline{C}}^{-1}(t',t)dt' \qquad (2.36)$$

which becomes the famous Lodge rubberlike liquid equation (Lodge, 1964)

$$\underline{\underline{g}}(t) = -p\underline{\underline{I}} + \int_{-\infty}^{t} \mu(t',t)\underline{\underline{C}}^{-1}(t',t)dt' \qquad (2.37)$$

when the memory function, $\mu(t',t)$ is, from Eq. (2.35)

$$\mu(t',t) = kT\sum_i N_i \exp[-(t-t')/\lambda_i] \qquad (2.38).$$

The rubberlike liquid theory only assumes that there exists a memory function, but a specific form of the memory function is not predicted for a polymer fluid. In view of the molecular relaxation processes which occur in polymers, it is reasonable to suppose that the prior states will have less importance than the more recent states and hence that the memory function is a decreasing function of the time interval.

From linear viscoelastic experiments, the memory function is found to be related to the relaxation spectrum, $H(\lambda)$, by:

$$\mu(t',t) = \int_{-\infty}^{+\infty} \frac{H(\lambda)}{\lambda} \exp[-(t-t')/\lambda]\ d\ \ln\lambda \qquad (2.39)$$

and

$$\mu(t',t) = d\overset{\circ}{G}(t-t')/dt \qquad (2.40)$$

where $\overset{\circ}{G}$ is the linear viscoelastic relaxation modulus (Ferry, 1980).

For a discrete relaxation spectrum of M relaxation times, the memory function becomes

$$\mu(t',t) = \sum_{i=1}^{M} \frac{g_i}{\lambda_i} \exp[-(t-t')/\lambda_i] \tag{2.41}$$

and the linear viscoelastic relaxation modulus becomes

$$\mathring{G}(t) = \sum_{i=1}^{M} g_i \exp[-t/\lambda_i] \tag{2.42}$$

where g_i are relaxation moduli associated with each relaxation time, λ_i.

The rubberlike liquid theory was an important step in developing a constitutive equation for polymer melts. It describes a viscoelastic liquid having the properties of high shear viscosity, a positive primary normal stress difference, frequency dependence of the dynamic viscosity, a large elastic recoil, slow stress relaxation, an increase of extensional viscosity with extension rate and the phenomena of die swell. The theory does have its limitations, however. It predicts no secondary normal stress difference which experimentally has been measured to be small but finite and does not predict large strain behavior.

The rubberlike liquid theory gives a very good description of the rheological behavior of polymer melts for both shear (Wagner, 1976) and extension (Chang and Lodge, 1972) in the linear viscoelastic limit (small strains and low strain rates); however, outside the linear viscoelastic limit (high strains) the predictions are inadequate. For the transient shear viscosity and primary normal stress coefficient, only the very low strain rate data are described by Eq. (2.37). No shear stress or normal stress overshoot is predicted for start-up experiments and the shear viscosity and primary normal stress coefficient are predicted to be independent of shear rate for steady state experiments;

whereas, the experimental data show otherwise. An infinite viscosity is predicted for uniaxial extension at long times but the experimental data fall below the prediction and later experiments indicate that the extensional viscosity actually levels off then decreases (Raible et al., 1979; Wagner et al., 1979).

By the deviations of the transient shear and uniaxial extensional viscosities and the primary normal stress coefficient at large strains, a change of the structure of the temporary entanglement network is indicated, possibly by the disentanglement of the temporary junctions due to the deformation. This suggests that the memory function may not only be time dependent but strain dependent as well.

2.4 Strain Dependent Network Theory

Several authors have made modifications to the existing theory to better describe the large strain behavior of polymer melts. Kaye (1966) has extended the network theory to give a constitutive equation which admits a non-constant viscosity as a function of shear rate. This was accomplished by assuming the rate of breakage of entanglement junctions is stress dependent. The resulting constitutive equation is no longer explicit for the stress and is therefore difficult to solve. A more promising approach to the development of a non-linear constitutive equation has been taken by Kaye (1962) and Bernstein, Kearsley and Zapas (1963 and 1964), who developed a constitutive equation, the K-BKZ equation, for finite deformations from non-equilibrium thermodynamic considerations which describes fading memory in terms of a quantity

dependent on the strain or past deformational history of the material. Their theory suggests that the fading memory can be described by a function which depends on both the time difference and the first and second invariants of the deformation tensor. This function is not required to be a product of a strictly time-dependent function and a strictly strain-dependent function; however, experimental evidence (Laun, 1978) has led to the assumption that indeed the time and strain dependence can be separated into two distinct functions and leads to what is known as the separability assumption.

2.4.1 Separability Assumption

The non-linear behavior of polymer melts can be attributed to the disentanglement of the temporary entanglement junctions with increasing deformation. To account for this change in the network structure with increasing deformation, a modification of the network theory was proposed by Wagner (1979).

In contrast to Lodge's assumption that the deformation has no effect on the formation and loss of the entanglement junctions, and hence the concentration of segments, Wagner assumed that there are two independent decay mechanisms for segments of type i: (1) a time dependent linear viscoelastic relaxation where the probability of a network segment i to survive a time difference (t-t') is $\exp[-(t-t')/\lambda_i]$, and (2) a strain dependent disentanglement by deformation. The probability of a network segment to survive a relative deformation between the instant of formation, t', and the instant of observation, t, is

independent of the index i and equal to $h(I_1(t',t),I_2(t',t))$, where I_1 and I_2 are the first and second invariants of the relative Finger strain tensor respectively. The total probability of a network segment of type i to survive a given time difference (t-t') and a deformation given by the invariants, I_1 and I_2, is then the product of $\exp[-(t-t')/\lambda_i] \cdot h(I_1,I_2)$.

This hypothesis leads to the following constitutive equation

$$\underline{\underline{\sigma}}(t) = -p\underline{\underline{1}} + \int_{-\infty}^{t} m(t',t)\underline{\underline{C}}^{-1}(t',t)dt' \qquad (2.43)$$

where the memory function, m(t',t) is now separable into time and strain dependent functions

$$m(t',t) = \mu(t',t)\cdot h(I_1,I_2) \qquad (2.44)$$

where $\mu(t',t)$ is the linear viscoelastic memory function of Eq. (2.41) and $h(I_1,I_2)$ is called the "damping" or strain function. The strain function tends to one for small strains and decreases to zero at higher strains

$$1 \geq h(I_1,I_2) \geq 0 \qquad (2.45).$$

The form of Eq. (2.44) requires that all the segments of the network, irrespective of their "structure" which is characterized by their index i, show the same strain dependence. This is referred to as the separability assumption and experimental evidence supports this idea (Laun, 1978).

Since the linear viscoelastic memory function cannot be calculated from first principles, but is a material function which must be

determined from experiments, it is reasonable to consider the non-linear part of the memory function, the strain function, as a material function itself, which also has to be determined from appropriate experiments. Due to the dependence on the invariants of the Finger strain tensor, the experimental determination of the strain function must be done separately for the different kinds of flows. For example, shear flow experiments will only yield, $h_s(\gamma)$, while the extensional strain function, $h_e(\varepsilon_a)$, must be obtained from axisymmetric extension experiments.

In an attempt to obtain a strain function that is applicable to both shear and extensional flows, the separate strain functions were combined by expressing them in terms of a generalized strain invariant I (Wagner, 1979; Wagner and Stephenson, 1979b),

$$I = \alpha I_1 + (1-\alpha)I_2;\ 0 \leq \alpha \leq 1 \tag{2.46}$$

where α is a material parameter.

For shear flow, I is independent of the value of α since $I_1(\gamma)$ and $I_2(\gamma)$ are identical

$$I(\gamma) = I_1(\gamma) = I_2(\gamma) = \gamma^2 + 3 \tag{2.47}.$$

For axisymmetric extension (positive ε_a), the generalized strain invariant becomes

$$I(\varepsilon_a) = \alpha I_1(\varepsilon_a) + (1-\alpha)I_2(\varepsilon_a) \tag{2.48}$$

where $I_1(\varepsilon_a)$ and $I_2(\varepsilon_a)$ are given by Eqs. (2.22) and (2.23).

For equibiaxial extension (negative ε_a), the generalized strain invariant can be written in terms of ε_b

$$I(\varepsilon_b) = \alpha I_1(\varepsilon_b) + (1-\alpha) I_2(\varepsilon_b) \tag{2.49}$$

where $I_1(\varepsilon_b)$ and $I_2(\varepsilon_b)$ are given by Eqs. (2.27) and (2.28).

A generalized strain function can then be written in terms of the invariant I with a suitable function having the form of the sum of two exponential functions (Osaki, 1976)

$$h(I) = f \exp(-n_1\sqrt{I-3}) + (1-f) \exp(-n_2\sqrt{I-3}) \tag{2.50}.$$

The material parameters f, n_1 and n_2 can be determined from shear step strain experiments and the material parameter α can be determined from extensional step strain experiments. Other forms of Eq. (2.50) are possible and will be discussed in more detail in the chapter on rheological characterization.

The strain-dependent integral constitutive equation, Eq. (2.43), has been extensively tested in several different rheological experiments. The time dependency of the non-linear stress-growth of a low density polyethylene (LDPE) in shear (Wagner, 1976) and uniaxial extension (Wagner et al., 1979) has been described well by this equation. Laun (1978) applied this theory to predict the steady state shear viscosity and primary normal stress coefficient as functions of shear rate and temperature together with the stress-growth at the inception and stress relaxation after the cessation of steady shear flow for a LDPE melt. The creep and recoverable strain from constrained elastic recovery experiments in shear (Wagner and Laun, 1978), the creep behavior in uniaxial extension (Laun and Munstedt, 1976; Wagner, 1978) have both been described well by Eq. (2.43). The time dependence of the shear

stress, primary normal stress difference and also, by using the stress-optical law, the extinction angle and flow birefringence of a polystyrene melt in intermittent shear flows (Laun et al., 1979) have also been described well by the strain-dependent constitutive equation. As of now no application of this equation to biaxial extensional deformations has been undertaken.

The description of rheological behavior of polymer melts with Eq. (2.43) is excellent as long as the strain is always increasing. However, unconstrained elastic recovery experiments in uniaxial extension have shown that an additional assumption concerning the irreversibility of the deformation dependent entanglement network is necessary (Wagner, 1978).

2.4.2 Irreversibility Assumption

Since the strain function represents the probability of a network segment to survive a given relative deformation, the process of the loss of disentanglement junctions is expected to be irreversible (i.e., the reduction of the strain after the event of network rupture will not lead to a reentanglement of the disentangled network segments in the stressed state) (Wagner and Stephenson, 1979a and 1979b). Equation (2.43) is valid as long as the relative deformation of all parts of the network is "nondecreasing." For "decreasing" deformations, the irreversibility assumption is imposed.

Segments lost during a "nondecreasing" deformation are not reformed during a "decreasing" deformation. The strain function, $h(I_1,I_2)$,

is therefore replaced by a functional of the strain

$$H^*(I_1,I_2) = \underset{t''=t'}{\overset{t''=t}{\text{Min}}} [h(I_1(t',t''),I_2(t',t''))] \qquad (2.51)$$

where Min is a functional operator, which gives the minimum value attained by h in the time interval (t,t') for a fixed creation time, t'. The idea of "nondecreasing" and "decreasing" deformations is shown in Figure 2.5. A "nondecreasing" deformation is defined as a deformation in which the function h is decreasing, while for a "decreasing" deformation, h is increasing.

This irreversibility assumption is essential in describing flows having first a "nondecreasing" deformation with a subsequent "decreasing" deformation. One such flow is the unconstrained elastic recovery of a polymer melt in uniaxial extension, where during the recovery process, parts of the network are subjected to the "decreasing" deformation of uniaxial compression (or biaxial extension). By use of the irreversibility assumption, elastic recoil measurements have successfully been predicted (Wagner and Stephenson, 1979b). Similar flows can occur in extrusion dies having first a converging tapered section where the shear and extensional deformations are "nondecreasing," then having a diverging tapered section where the relative shear and extensional deformations are "decreasing."

Instead of using the invariants of the strain tensor to describe the strain dependency of the memory function, other authors (Carreau, 1972; Bird et al., 1977b) have proposed to introduce the invariants of

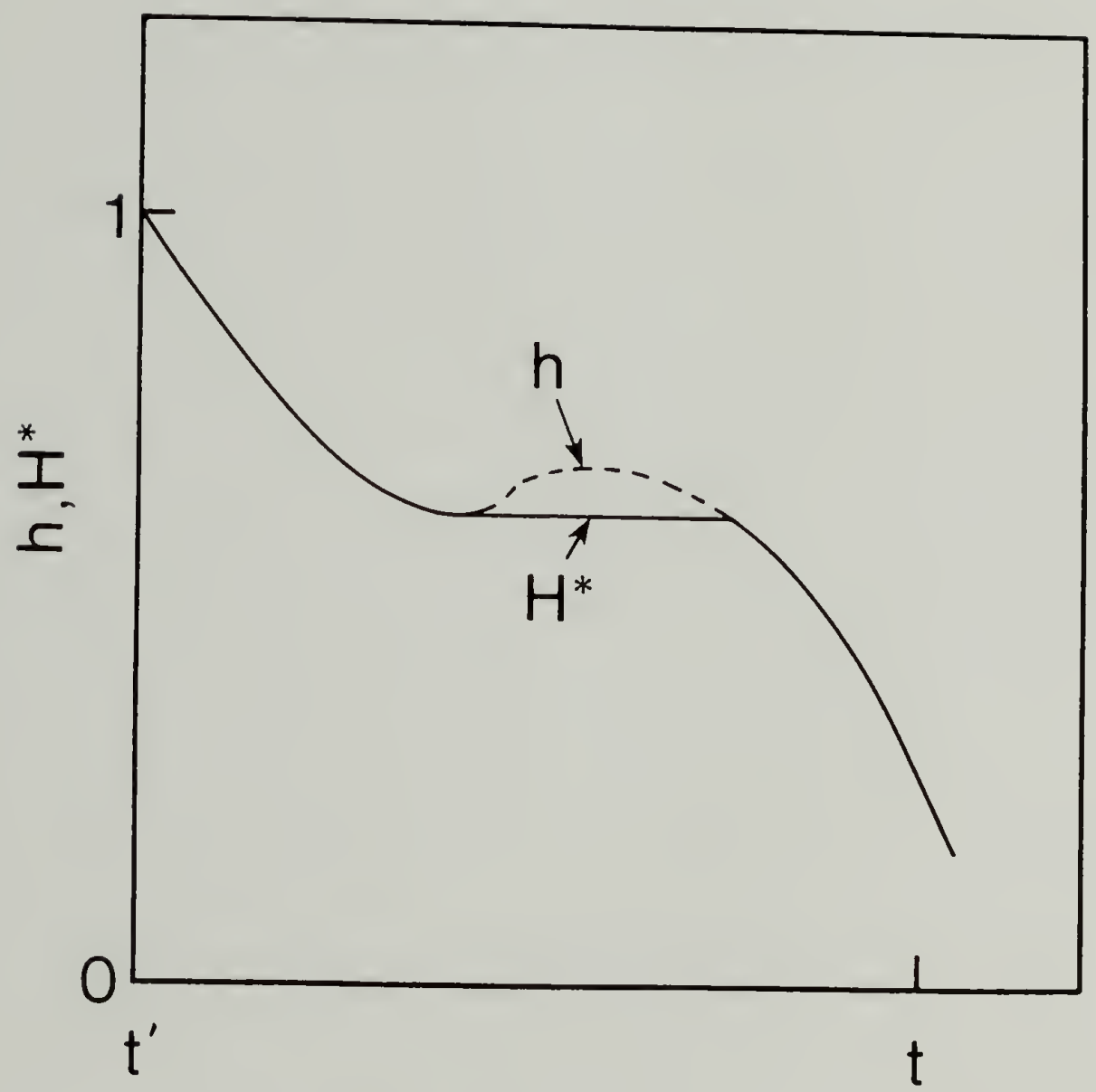

Figure 2.5. The strain function, $h(I_1,I_2)$, and the strain functional, $H^*(I_1,I_2)$, between the time interval (t',t).

the rate of strain tensor into the memory function. Whereas the introduction of the invariants of the strain measure is unambiguous since the strain is accumulated over the entire time span from the previous time, t', to the present time, t, the question arises whether the invariants of the rate of strain tensor have to be introduced for the previous time, t', for the present time, t, or whether averages of the invariants over the whole time interval between t' and t must be used. Experimental data suggest that the rate of strain should not be introduced into the strain function. The stress-growth at constant strain rate for both uniaxial extension (Chang and Lodge, 1972) and shear (Wagner, 1976) agree well with the Lodge rubberlike liquid theory up to total strains of about unity, independent of the applied strain rate. Also a step strain experiment (Laun, 1978) would influence the memory function drastically if there was an influence of the strain rate, since the strain rate would temporarily be extremely high at the start of the experiment. None of these influences of strain rate are seen in experiments, so the invariants of the strain tensor are used exclusively in this dissertation.

2.5 Temperature Dependent Network Theory

Although only isothermal cases have been considered in this dissertation, the memory integral constitutive equation can be easily extended to incorporate temperature changes which may occur during the flow history. Temperature changes are incorporated by means of the time-temperature superposition concept (Ferry, 1980) which allows one to

normalize linear viscoelastic experiments done at different times (rates) and temperatures.

In light of the network theory, it is assumed that all the segments, irrespective of their relaxation time, λ_i, have the same temperature dependence. Since the linear viscoelastic memory function of the integral constitutive equation contains the time dependency of the network segments, it will also contain the temperature dependency. These assumptions lead to the following relations (Ferry, 1950) for the discrete relaxation time constants:

$$\lambda_i(T) = a_T(T)\lambda_i^o \tag{2.52}$$

and

$$g_i(T) = [\rho(T)T/\rho_o T_o]g_i^o \tag{2.53}$$

where "o" denotes a reference state, T is the absolute temperature, ρ is the density and a_T is the shift factor. The shift factor is commonly described with the well known WLF equation (Williams et al., 1955)

$$\log a_T(T) = -C_1(T-T_o)/(C_2+T-T_o) \tag{2.54}$$

where C_1 and C_2 are material constants. This WLF equation is valid for $T_g \leq T_o \leq T_g+100°K$ where T_g is the glass transition temperature of the polymer. For polymer melts where $T_o > T_g+100°K$, another equation for the shift factor is appropriate (Laun, 1978)

$$\ln a_T(T) = \frac{E_o}{R}\left(\frac{1}{T} - \frac{1}{T_o}\right) \tag{2.55}$$

where E_o is an activation energy and R is the gas constant.

An equation describing density changes as a function of temperature is required and an appropriate equation has the form

$$\rho(T) = \beta\rho_o(T_o - T) + \rho_o \tag{2.56}$$

where β is the volume expansion coefficient.

Now, if the temperature becomes time dependent, $T=T(t)$, then the relaxation times and moduli become time dependent and Eq. (2.41) becomes

$$\mu(t',t) = \sum_{i=1}^{M} \frac{g_i(T(t'))}{\lambda_i(T(t'))} \exp\left[- \int_{t'}^{t} \frac{dt''}{\lambda_i(T(t''))} \right] \tag{2.57}.$$

Upon substitution of Eqs. (2.52) and (2.53), one obtains the temperature dependent linear viscoelastic memory function

$$\mu(t',t) = \sum_{i=1}^{M} \frac{g_i^o}{\lambda_i \rho_o T_o} \frac{\rho(T(t'))T(t')}{a_T(T(t'))} \exp\left[\frac{1}{\lambda_i} \int_{t}^{t'} \frac{dt''}{a_T(T(t''))}\right] \tag{2.58}.$$

Since the strain function depends only on the deformation and therefore describes purely geometrical effects, it is independent of temperature. This can be concluded from the fact that temperature independent master curves can be constructed even for non-linear experiments of shear creep and constrained elastic recovery by use of the linear viscoelastic time-temperature shift factor (Wagner and Laun, 1978).

One can then obtain a non-isothermal memory integral constitutive equation by combining Eqs. (2.58) and (2.50) with (2.43). A similar non-isothermal integral constitutive equation has been developed for a strain rate dependent memory function (Matsui and Bogue, 1977).

2.6 Flow Birefringence

Polymers exhibit birefringence (the difference in magnitude of the principal values of the refractive index tensor) due to the difference in electron mobility along the backbone and the side chains of the molecule. A detailed discussion of the optical theory is given by Kuhn and Grün (1942) and Stein (1976). An amorphous polymer in its isotropic state does not exhibit birefringence; however, if the polymer sample is made anisotropic (i.e., during stretching or shearing flow) birefringence occurs and can be used as a measure of the average orientation of the polymer molecules. Birefringence also occurs in polymers that have crystalline phases and at the crystal-amorphous interface. The birefringence due to the interface between the amorphous and crystalline regions is known as form birefringence. Birefringence has been utilized to study the molecular orientation in injection molded parts (Wales et al., 1972; Wales, 1976; Dietz et al., 1978; White and Dietz, 1979), melt spun fibers (Oda et al., 1978), extruded and drawn sheet (Jones, 1976) and blown film (Stein, 1958; Holmes and Palmer, 1958; Choi et al., 1980 and 1982). The birefringence in the final part, fiber or film has been related to the flow patterns in the mold or to the upstream processing history.

Another, and more important aspect of birefringence in this dissertation, is its use to study the stress in polymer melts during flow. This has been termed flow birefringence. Flow birefringence has been used extensively in the field of polymer melt rheology. Rheological data obtained by optical techniques complement data obtained by the

conventional mechanical techniques. An excellent discussion of this area of research is supplied by Janeschitz-Kriegl (1983).

2.6.1 The Stress-Optical Law

During flow, polymer molecules tend to orient preferentially in a certain direction depending on the type of flow. As a result, the polymer becomes highly birefringent. A relation between the stress and birefringence has been formulated from the network theory and is called the stress-optical law (Lodge, 1956 and 1960; Treloar, 1975). This relation states that the refractive index and stress ellipsoids are coaxial and that the birefringence, which is the difference in magnitude of the principal axes of the refractive index ellipsoid, is simply proportional to the corresponding difference in principal stresses. This statement is expressed by:

$$\Delta n = C\,\Delta\sigma \tag{2.59}$$

where Δn is the difference between two principal refractive indices, which can be measured as a birefringence in a suitable experimental arrangement, C is the stress-optical coefficient, which depends on the polymer material and $\Delta\sigma$ is the difference between the respective principal stresses. In tensor notation Eq. (2.59) is expressed as

$$(\underline{\underline{n}}-n_o\underline{\underline{1}}) = C(\underline{\underline{\sigma}}+p\underline{\underline{1}}) \tag{2.60}$$

where n_o is the average refractive index of the birefringent medium.

The validity of Eq. (2.60) for polymer melts in shearing flows has been extensively verified using two different rheologically simple flows. A cone-and-plate apparatus was used to verify the validity of

Eq. (2.60) for different polymer melts (Wales and Janeschitz-Kriegl, 1967; Gortemaker et al., 1976a; Wales, 1976) up to high shear rates near the point of melt fracture (van Aken et al., 1980). For very low shear rates, a Couette system was also used to check the validity (Gortemaker et al., 1976b). A slight deviation from the linear stress-optical law was observed at very high tensile stresses during the uniaxial extension of a polystyrene melt at low extension rates (Matsumoto and Bogue, 1977). It should be mentioned, however, that the temperatures at which these high stresses were measured, were close to the T_g and may not be representative for the state of a rubberlike liquid. Biaxial extension experiments also indicate that the stress-optical law is valid up to fairly high strains (van Aken and Janeschitz-Kriegl, 1980).

Flow birefringence data of a sheared polymer melt have been described well by the Lodge rubberlike liquid theory, Eq. (2.37), at low shear rates and for any shear rate when the total shear applied does not exceed unity (Gortemaker et al., 1976b). Both steady and time-dependent birefringence data in shear flow have also been described well by the strain dependent memory integral equation, Eq. (2.43), even at high strains (Laun et al., 1979). The stress-optical law was shown to hold not only in steady flows, but also in time-dependent flows. This implies that the principal axes of the refractive index tensor and the stress tensor do indeed coincide at all relevant times and shear rates.

This relation has been used by many authors to measure stress levels in non-rheometric polymer flows which occur in processing operations. Stress levels of polymeric materials have been measured at the

entrance of slit dies (Han and Drexler, 1973a; Brizitsky et al., 1978; Racano et al., 1979), converging dies (Han and Drexler, 1973b; Han, 1975; Yoo and Han, 1981) and diverging dies (Adams et al., 1965) while spinline stresses have been correlated for fiber spinning processes (Oda et al., 1978; Talbott and Goddard, 1979).

CHAPTER III

MATERIALS AND THEIR RHEOLOGICAL CHARACTERIZATION

3.1 Polymers Investigated

The rheological properties of three polymer melts were determined. The polymer melts used were a low density polyethylene (high pressure), LDPE, a high density polyethylene, HDPE, and an atactic polystyrene, PS. Their molecular weight characterization appears in Table 3.1.

The LDPE is a typical resin used in film blowing, the HDPE is a bottle blow molding resin and the PS is a commercial injection molding resin. The HDPE was kindly supplied by Dr. J.M. Dealy of McGill University where further characterization has been reported for this polymer (Orbey, 1983).

These polymers were chosen for two reasons. First, the large strain rheological behavior of polymers having low chain branching (PS), high long chain branching (LDPE) and intermediate short chain branching (HDPE) was of interest especially for a check on the correction method for shear step strain in the parallel-disk rheometer and the equibiaxial step strain experiments. Secondly, the polymers are transparent in the melt state thus making flow birefringence measurements in the annular flow experiments possible.

Samples for the rheological experiments were melt pressed into disks of 25.4 mm diameter and approximately 2.5 mm thick at 190°C for four minutes then quenched in water. The polystyrene was melt pressed

Table 3.1. Molecular weights of polymers studied

Polymer	Manufacturer and Trade Name	$\bar{M}_n$	$\bar{M}_w$	$\bar{M}_w/\bar{M}_n$
LDPE	duPont Alathon 20	25,000	200,000	8.0
HDPE	duPont of Canada Sclair 59A	12,000	120,000	10.0
PS	Dow Styron 666	90,000	220,000	2.4

under vacuum and slowly cooled to below 100°C before removal from the press to eliminate bubble formation in the sample upon reheating. Smaller diameter samples were cut from these pressed disks for the equibiaxial extensional experiments.

3.2 Shear Rheometry

Two regions of rheological behavior were investigated by shear rheometry. The small strain properties in the region of linear viscoelasticity were obtained from oscillatory shear experiments and compared to the properties obtained in small step strain experiments. The linear viscoelastic properties could just as well have been determined in an extensional experiment, but the shear geometry is easier to use for polymer melts. The large strain rheological properties in the nonlinear region were obtained from large step strain experiments and compared to the properties obtained from capillary flow experiments with the use of the constitutive equation developed in the previous chapter.

3.2.1 Oscillatory Shear

For oscillatory shear experiments, a polymer sample is subjected to a sinusoidally varying strain

$$\gamma_{21} = \gamma_{21}^{o} \sin \omega t \qquad (3.1)$$

where γ_{21}^{o} is the strain amplitude and ω is the angular frequency. For small strain amplitudes, the resulting stress is given by

$$\sigma_{21} = \sigma_{21}^{o} \sin(\omega t+\delta) \qquad (3.2)$$

where σ_{21}^{o} is the amplitude of the stress and δ is the phase angle between the stress and strain. From a fundamental trigonometric identity the previous equation becomes

$$\sigma_{21} = (\sigma_{21}^{o} \cos \delta)\sin \omega t + (\sigma_{21}^{o} \sin \delta)\cos \omega t \qquad (3.3).$$

Eq. (3.3) is then conveniently written as

$$\sigma_{21} = \gamma_{21}^{o}(G' \sin \omega t + G'' \cos \omega t) \qquad (3.4)$$

where the first term on the right side of the equation is the in-phase component of the modulus to the strain and the second term is the out-of-phase component. The storage modulus

$$G' = (\sigma_{21}^{o}/\gamma_{21}^{o})\cos \delta \qquad (3.5)$$

gives an indication of the "elastic" nature of a material while the loss modulus

$$G'' = (\sigma_{21}^{o}/\gamma_{21}^{o})\sin \delta \qquad (3.6)$$

gives an indication of the "viscous" nature. A complex viscosity is defined as

$$|\eta^*(\omega)| = [(G'/\omega)^2 + (G''/\omega)^2]^{1/2} \qquad (3.7).$$

The relaxation spectrum of linear viscoelasticity, $H(\lambda)$, is related to the storage and loss moduli by (Ferry, 1980)

$$G'(\omega) = \int_{-\infty}^{+\infty} H(\lambda) \frac{\lambda^2\omega^2}{1+\lambda^2\omega^2} \, d \ln \lambda \qquad (3.8)$$

and

$$G''(\omega) = \int_{-\infty}^{+\infty} H(\lambda) \frac{\lambda\omega}{1+\lambda^2\omega^2} \, d \ln \lambda \qquad (3.9).$$

The choice of a discrete relaxation spectrum then gives

$$G'(\omega) = \sum_{i=1}^{M} g_i \frac{\lambda_i^2\omega^2}{1+\lambda_i^2\omega^2} \qquad (3.10)$$

and

$$G''(\omega) = \sum_{i=1}^{M} g_i \frac{\lambda_i\omega}{1+\lambda_i^2\omega^2} \qquad (3.11).$$

A more detailed discussion of linear viscoelasticity can be found in the textbook by Ferry (1980).

The complex modulus can be measured in rotational rheometers. For a cone-and-plate geometry, Figure 3.1, the strain is independent of the radius

$$\gamma_{21} = \Theta/\Phi \qquad (3.12)$$

where Θ is the angular displacement and Φ is the cone angle. The total torque, τ, on the plate during an experiment is

$$\tau = 2\pi \int_0^R \sigma_{21} r^2 dr \qquad (3.13)$$

where R is the radius of the plate. Since γ_{21} is independent of r, σ_{21} is also and Eq. (3.13) can be integrated to yield

$$\sigma_{21} = 3\tau/2\pi R^3 \qquad (3.14).$$

CONE AND PLATE

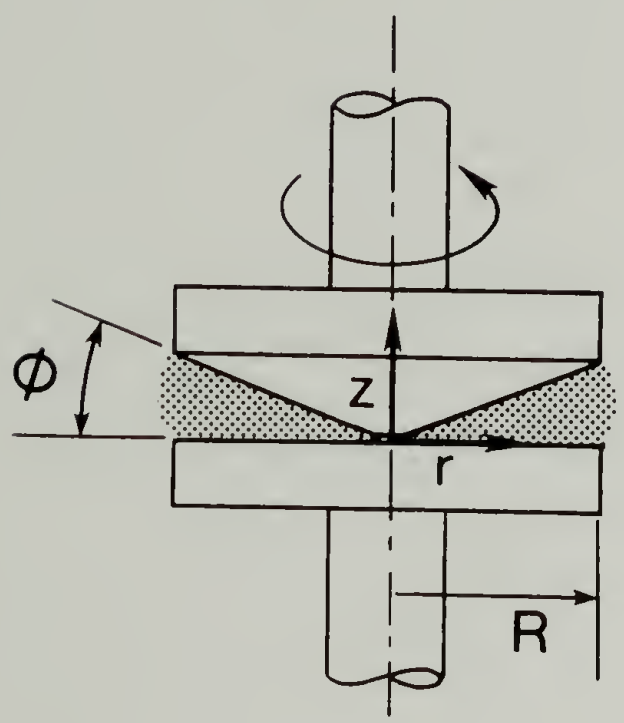

$$\gamma = \frac{\theta}{\Phi}$$

PARALLEL DISK

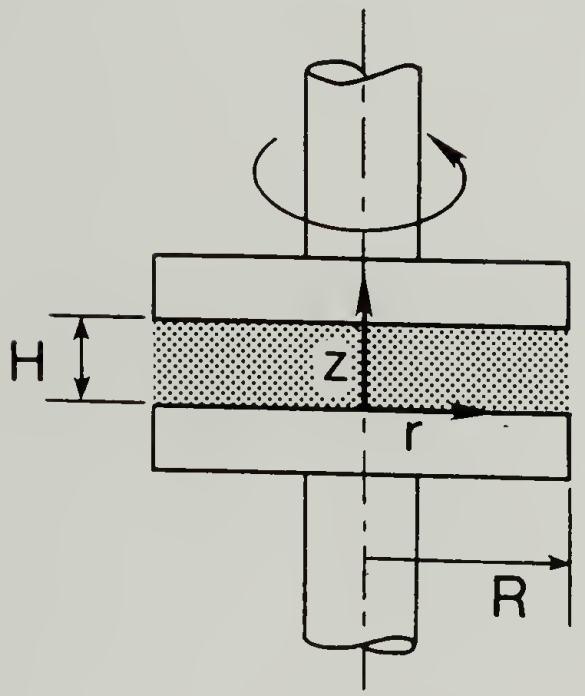

$$\gamma_R = \frac{\theta R}{H}$$

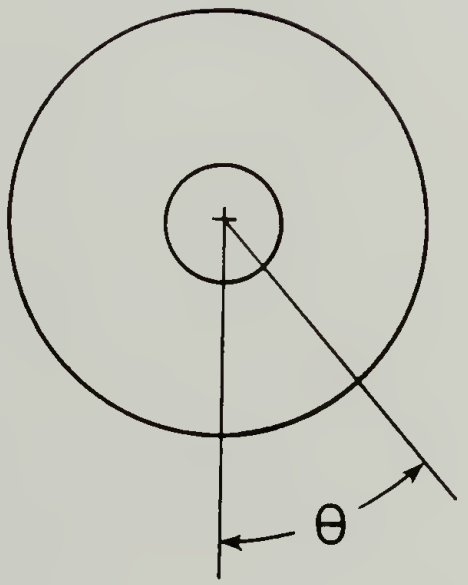

Figure 3.1. Sketch of cone-and-plate and parallel disk geometries for shear rheometry.

Therefore for a cone-and-plate rheometer the storage and loss moduli become

$$G' = (3\Phi\tau_o/2\pi R^3\Theta_o)\cos\delta \tag{3.15}$$

and

$$G'' = (3\Phi\tau_o/2\pi R^3\Theta_o)\sin\delta \tag{3.16}.$$

where Θ_o is the applied angular displacement amplitude and τ_o is the measured torque amplitude.

3.2.2 Step Strain in Shear

The step shear strain experiment is a direct means of measuring the strain dependent rheology of polymeric liquids (Zapas and Phillips, 1971; Einaga et al., 1973). In the experiment, a test sample is placed into a shear rheometer and the system is kept at rest until the sample is completely relaxed to the stress free state. At time t=0, a finite shear strain is "instantaneously" applied and held constant thereafter. The resulting shear stress is measured as it relaxes with time. The analysis of step strain data is especially easy since only two states of strain are involved, assuming that the finite rise time of the strain has negligible influence. The result of the measurement is the time and strain dependent shear relaxation modulus

$$G_s(t,\gamma) = \frac{\sigma_{21}(t,\gamma)}{C_{21}^{-1}} = \frac{\sigma_{21}}{\gamma} \tag{3.17}$$

where σ_{21} is the shear stress and γ is the shear strain.

The corresponding transient first normal stress difference has been discussed by Lodge and Meissner (1972) who predict that the ratio of the transient first normal stress difference to the transient shear stress equals the shear strain and is independent of time. This relation has been experimentally verified for several polymeric liquids (Laun, 1978; Osaki et al., 1979b; Kimura et al., 1981; Osaki et al., 1981). In this dissertation, the discussion is limited to the relaxation of the shear stress.

The step strain experiment is also a direct method of measuring the linear viscoelastic relaxation modulus of polymeric liquids. In the limit of small strain the linear viscoelastic relaxation modulus is given by Eq. (2.42) where a discrete relaxation spectrum is chosen. The choice of a discrete spectrum will not affect the arguments below. In the following discussion, a step strain is termed "large" if the corresponding relaxation modulus is a function of time and strain.

Previously, the large step strain test has been performed in rheometers in which the test sample is subjected to a homogeneous strain. Such rheometers are the cone-and-plate rotational rheometer (Zapas and Phillips, 1971; Einaga et al., 1973; Fukuda et al., 1975; Laun, 1978; Osaki, 1980; Lin, 1984), the sandwich device (Kimura et al., 1981; Osaki et al., 1981) and, to a good approximation, the Couette system (Osaki et al., 1979a and 1979b). An alternative method is proposed here for rotational rheometers which are limited in their angular displacement. The main reason for developing this new method is the need for a large strain.

The rotational rheometer in our laboratory has a drive system with a maximum angular displacement, Θ_{max}=0.5 rad. For the cone-and-plate geometry, Figure 3.1, with a cone angle Φ=0.1 rad, the maximum strain obtainable is

$$\gamma_{max} = \frac{\Theta_{max}}{\Phi} = 5 \qquad (3.18).$$

This strain, although outside the linear viscoelastic region, is relatively small. It can be increased by choosing smaller cone angles. Lin (1984) obtained large step strain data with a cone angle Φ=0.018 rad. Small cone angles (below 0.1 rad for a modified Weissenberg Rheometer) were, however, found to cause errors in transient stress measurements (Meissner, 1972). The errors were attributed to the lack of stiffness of the rheometer against axial forces which originate from the normal stress in the sheared liquid. These errors were severe for the normal stress measurement, but they seem to be tolerable for the shear stress.

Another way to increase the magnitude of the strain for an instrument with limited angular displacement is to use the parallel-disk geometry, as shown in Figure 3.1 and to decrease the gap thickness. This second method is preferred, since (1) it does not require many cones having different angles, (2) the sample preparation is simpler for the parallel-disk system, (3) the rise time in step strain is more easily controlled, and (4) the sensitivity to errors in gap setting is reduced. The problem of the parallel-disk experiment, however, is the non-homogeneous strain of the sample.

3.2.2.1. Correction for non-homogeneous strain. The transient torque response has to be corrected for the non-homogeneous strain. The correction method is similar to the one of Rabinowitsch (1929) for evaluating steady shear flow in capillary rheometers. It also applies to steady shear flow in a parallel-disk rheometer (Bird et al., 1977a). These corrections apply to steady state shear flow; whereas the correction discussed here has to accommodate the transient response of the step strain.

The analysis is based on the assumptions that inertial effects and viscous heating in the sample are negligible and also, more importantly, that for the parallel-disk geometry, Figure 3.1, the planes in the z-direction are shear planes (i.e., the material planes parallel to the boundary disks move rigidly). Thus, the shear strain increases linearly in the radial direction

$$\gamma_{z\Theta}(r,t) = \Theta(t)r/H, \quad 0<r<R \tag{3.19}$$

and is the same in each of the shear planes, ($\gamma_{z\Theta}$ independent of z). Edge effects at r=R are also neglected. H is the gap (and sample) thickness and $\Theta(t)$ is the relative angular displacement of the disks. In the step strain experiment, the angular displacement is a constant, Θ_o, at t>0. The shear strain is independent of time during the stress relaxation

$$\gamma_{z\Theta}(r) = r\Theta_o/H = \gamma_R r/R, \quad 0<t \tag{3.20}$$

where γ_R is the strain at the outer edge of the disks.

The total transient torque is

$$\tau(t,\gamma_R) = 2\pi \int_0^R \sigma_{z\Theta}(r,t) r^2 dr \qquad (3.21).$$

By substitution of the shear stress with the shear relaxation modulus, Eq. (3.17), and a change of variables according to Eq. (3.20) the following relation is obtained

$$\tau(t,\gamma_R) = \frac{2\pi R^3}{\gamma_R^3} \int_0^{\gamma_R} G_s(t,\gamma)\gamma^3 d\gamma \qquad (3.22).$$

After differentiation with respect to γ_R, Eq. (3.22) becomes

$$G_s(t,\gamma_R) = \frac{2\tau(t,\gamma_R)}{\pi R^3 \gamma_R} \left[\frac{3}{4} + \frac{1}{4} \frac{\partial \ln(2\tau(t,\gamma_R)/\pi R^3)}{\partial \ln \gamma_R}\right] \qquad (3.23).$$

In the linear viscoelastic limit, the torque is proportional to the strain γ_R and the magnitude of the term in brackets reduces to unity. In the limit of small strain, the linear viscoelastic modulus measured by parallel-disks is

$$\mathring{G}(t) = \lim_{\gamma_R \to 0} G_s(t,\gamma_R) = 2\tau(t,\gamma_R)/(\pi R^3 \gamma_R) \qquad (3.24).$$

Therefore, an apparent relaxation modulus for step strain in the parallel-disk geometry can be defined as:

$$G_a(t,\gamma_R) = 2\tau(t,\gamma_R)/(\pi R^3 \gamma_R) \qquad (3.25)$$

which is obtained directly from each relaxation experiment. The term in brackets in Eq. (3.23) becomes, after substitution with the apparent relaxation modulus,

$$\chi(t,\gamma_R) = 1 + \frac{1}{4}\frac{\partial \ln G_a(t,\gamma_R)}{\partial \ln \gamma_R} \qquad (3.26).$$

This correction factor is determined from a set of relaxation experiments at different magnitudes of γ_R. The resulting equation for the correction due to non-homogeneous strain is

$$G_s(t,\gamma_R) = G_a(t,\gamma_R)\left[1 + \frac{1}{4}\frac{\partial \ln G_a(t,\gamma_R)}{\partial \ln \gamma_R}\right] \qquad (3.27).$$

It should be noted that the derivation of Eq. (3.27) follows directly from a balance of forces. No specific type of constitutive equation is assumed.

3.2.3. Capillary Rheometry

Capillary flow is an easily generated shear flow from which the shear viscosity of fluids can be measured at high shear rates. The molten polymer is forced from a reservoir by means of a piston and through a capillary of known diameter at a constant volumetric flow rate. The pressure required to sustain the flow is constant during steady state operation. A steady shear flow is developed after a certain entrance length in which the streamlines are parallel to the capillary axis. The velocity profile in the steady shear flow region, however, depends on the rheological behavior of the fluid. Since the

velocity profile of non-Newtonian fluids is not known unless a specific constitutive equation is applied, special techniques and correction methods must be utilized in order to calculate the shear viscosity from capillary flow experiments.

Assuming the steady, isothermal and symmetrical flow of an incompressible fluid in a capillary of diameter D and length L the shear viscosity is defined as

$$\eta_s(\dot{\gamma}) = \tau_w/\dot{\gamma}_w \qquad (3.28).$$

where the shear stress at the wall is

$$\tau_w = -\Delta P_w D/(4L) \qquad (3.29)$$

and the shear rate at the wall is

$$\dot{\gamma}_w = \dot{\gamma}_a\left[3/4 + (1/4)\frac{d \log \dot{\gamma}_a}{d \log \tau_w}\right] \qquad (3.30)$$

where the apparent shear rate is

$$\dot{\gamma}_a = 32Q/(\pi D^3) \qquad (3.31).$$

ΔP_w is the axial pressure gradient at the wall and Q is the volumetric flow rate. The term in brackets in Eq. (3.30) is commonly called the "Rabinowitsch correction" (Rabinowitsch, 1929). It is obvious from Eq. (3.31) that several experiments at different flow rates must be performed in order to determine the shear viscosity as a function of $\dot{\gamma}_w$.

In order to calculate the correct τ_w, the pressure gradient measured must be corrected for entrance and exit effects. The axial pressure gradient is equal to the difference between the pressure at the

capillary entrance, P_e, and the ambient pressure at the capillary exit, P_o. Since for polymer melts $P_e >> P_o$, $(-\Delta P_w)$ is set equal to P_e. As the fluid in the reservoir approaches the capillary entrance the velocity field begins to change and a fully developed profile occurs at some "entrance length" down the capillary. Because the wall shear stress is larger near the entrance of the capillary than for the case of fully developed flow, the wall pressure gradient is larger than for fully developed flow and it must be corrected. As the fluid approaches the capillary exit, the velocity field profile may rearrange to plug flow outside the capillary. The wall pressure gradient in this region would then be larger than for fully developed flow. The correction of these end effects can be accomplished by using capillaries of different length and measuring the pressure, P_e, at the same volume flow rates.

A method of correction proposed by Bagley (1957) involves the use of an end correction, e, where the shear stress at the wall becomes

$$\tau_w = P_e/[4(L/D + e)] \qquad (3.32).$$

The product, eD, is the length of fully developed capillary flow having a pressure drop equal to the excess pressure drop resulting from end effects. A graphical method of determining the correction factor is illustrated in Figure 3.2 and is referred to as a "Bagley plot." The correction factor is found by extrapolating P_e vs. L/D data at constant $\dot{\gamma}_a$ and is a function of shear rate.

The capillary flow experiments require measuring P_e and $\dot{\gamma}_a$ for capillaries of different L/D and determining the correction factors from

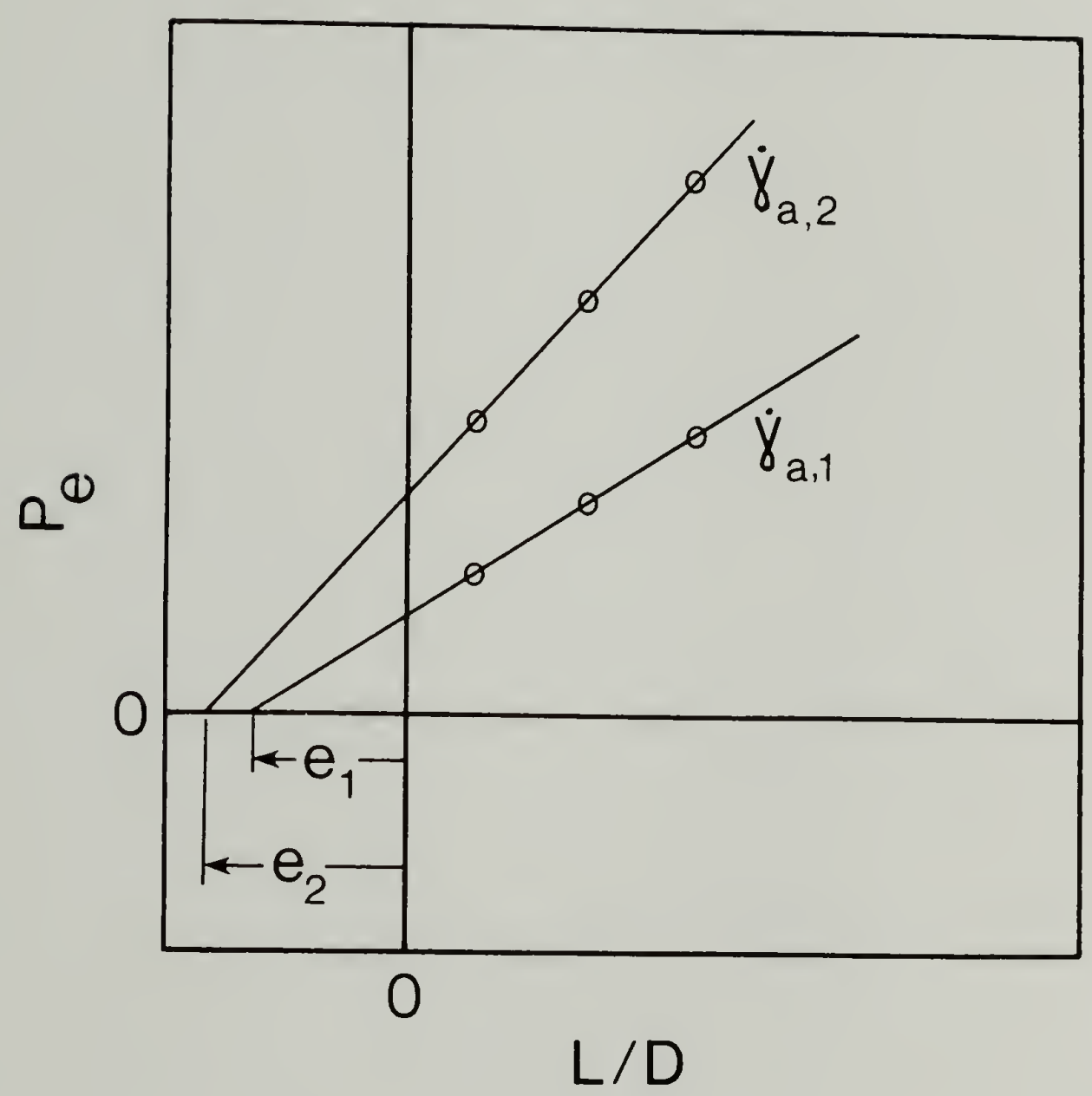

Figure 3.2. Bagley Plot for determining the pressure correction factor in capillary rheometry.

Bagley plots. The true shear stress at the wall is then calculated from Eq. (3.32) and the true shear rate at the wall is obtained by using the Rabinowitsch correction. The shear viscosity is then calculated from Eq. (3.28).

Viscous heating and pressure effects may affect the measured shear viscosity at very high shear rates and a detailed discussion of these effects is given by Dealy (1982).

3.2.4. Experimental Procedure and Results

A rotational rheometer (Rheometrics Dynamic Spectrometer, RDS) was used for both the oscillatory shear and step shear strain experiments. The geometries of the test fixtures were cone-and-plate (D=25 mm, Φ=0.1 rad) and parallel-disks (D=25 mm). Having been designed primarily for oscillatory experiments requiring small strains ($\gamma<0.5$), the rheometer produces a maximum angular displacement of only 0.5 rad. The transducer measures a maximum torque of 0.2 Nm.

3.2.4.1 Oscillatory shear. Oscillatory shear experiments at small strains ($0.10<\gamma<0.25$) using the cone-and-plate geometry were performed to determine the storage modulus, $G'(\omega)$, and the loss modulus, $G''(\omega)$, as a function of angular frequency in the range $0.1<\omega<100$ rad/s. The experiments were performed at several temperatures and the shift factors, a_T, were determined by shifting the data to produce a master curve at some reference temperature, T_o. The reference temperatures for LDPE, HDPE and PS were 150°C, 170°C and 180°C respectively. The temperature dependent shift factors appear in Figures 3.3 and 3.4. The

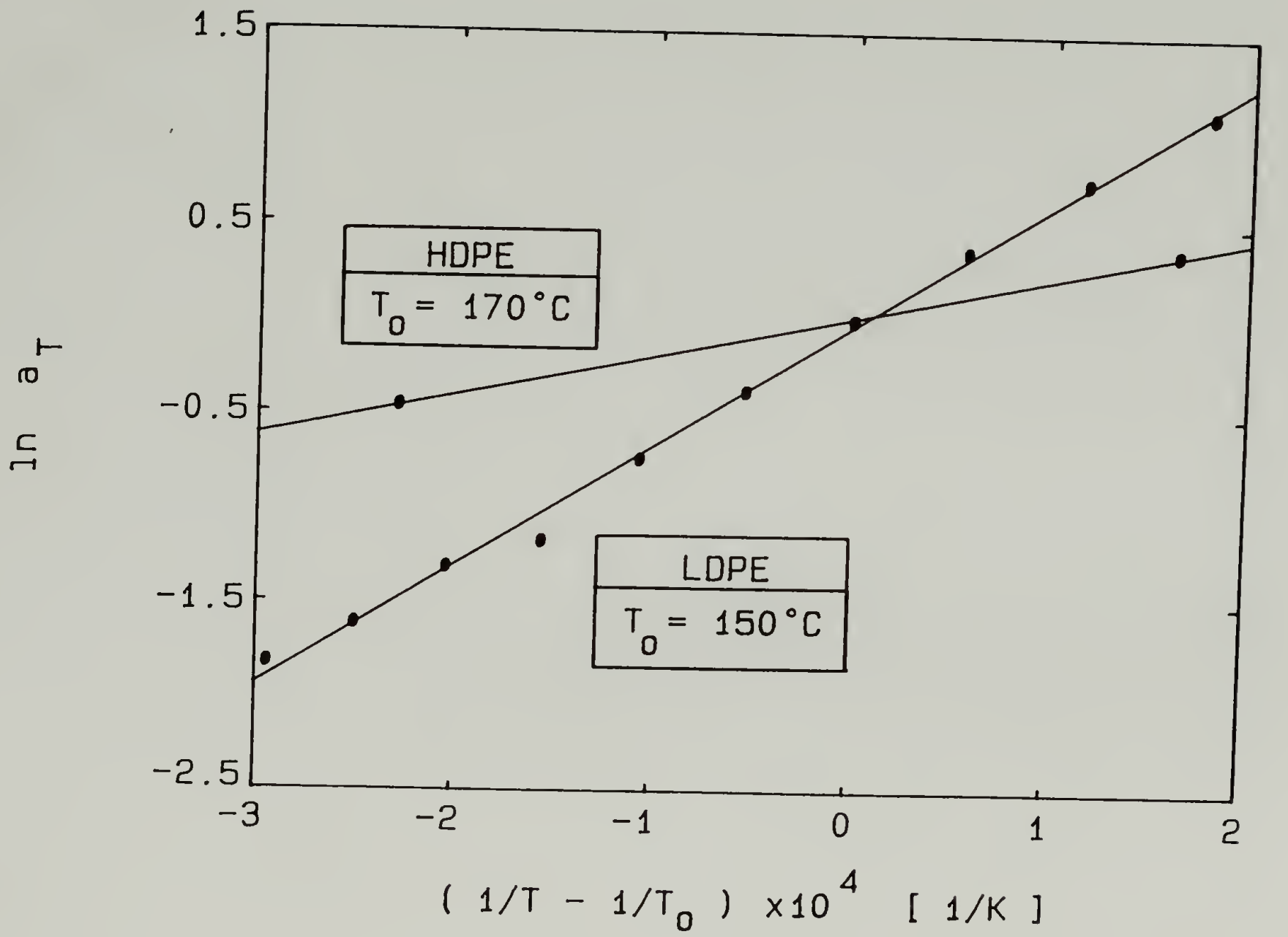

Figure 3.3. Temperature dependent shift factors for LDPE and HDPE obtained from oscillatory shear measurements.

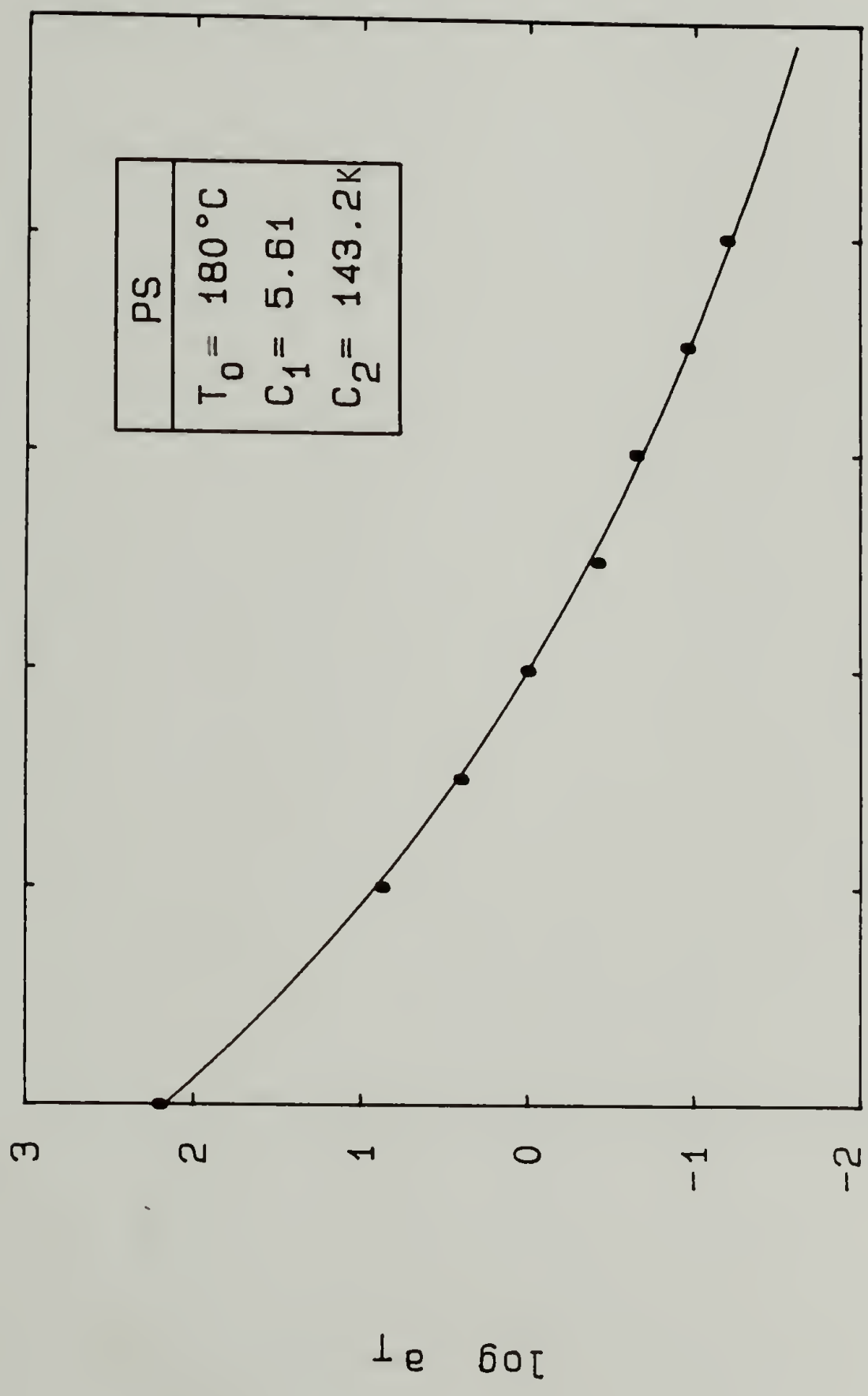

Figure 3.4. Temperature dependent shift factors for PS obtained from oscillatory shear measurements.

polyethylene data were fit to Eq. (2.55) while the polystyrene data were fit to Eq. (2.54) since for PS, $T_g \sim 100°C$. The shift factor parameters appear in Table 3.2.

The master curves appear in Figures 3.5, 3.6 and 3.7. The parameters of a discrete relaxation spectrum were obtained by fitting both Eq. (3.10) and Eq. (3.11) to the storage and loss moduli data. Discrete values of λ_i and g_i were determined by means of a finite difference Levenberg-Marquardt routine (Marquardt, 1963) and are listed in Table 3.3. The full lines in Figures 3.5, 3.6 and 3.7 were then calculated according to Eqs. (3.10) and (3.11), using the values in Table 3.3.

3.2.4.2 Shear step strain. Large step shear strain experiments were performed at varying finite strains. The strains obtained for the various geometries appear in Table 3.4. Values of γ_R with the parallel-disk geometry were chosen to overlap the range of strain obtained with the cone-and-plate geometry.

A finite rise time, Δt, is required for the motor to rotate the upper disk to the prescribed angle Θ_0. Figure 3.8 shows the transient angular displacement. The rise time should be as small as possible in order to avoid corrections to the relaxation modulus at intermediate times (Laun, 1978). An important observation is that the rise time was proportional to the angular displacement and independent of the torque which changed with gap setting and sample. The rise time never exceeded 55 ms, even at the largest strain, $\gamma=25$.

Table 3.2. Parameters for temperature dependent shift factors obtained from oscillatory shear experiments.

Polymer	Reference Temperature T_o[°C]	Parameters C_1	C_2[K]	Activation Energy E_o[kcal/mole]
LDPE	150	-	-	12,600
HDPE	170	-	-	4,160
PS	180	5.61	143.2	-

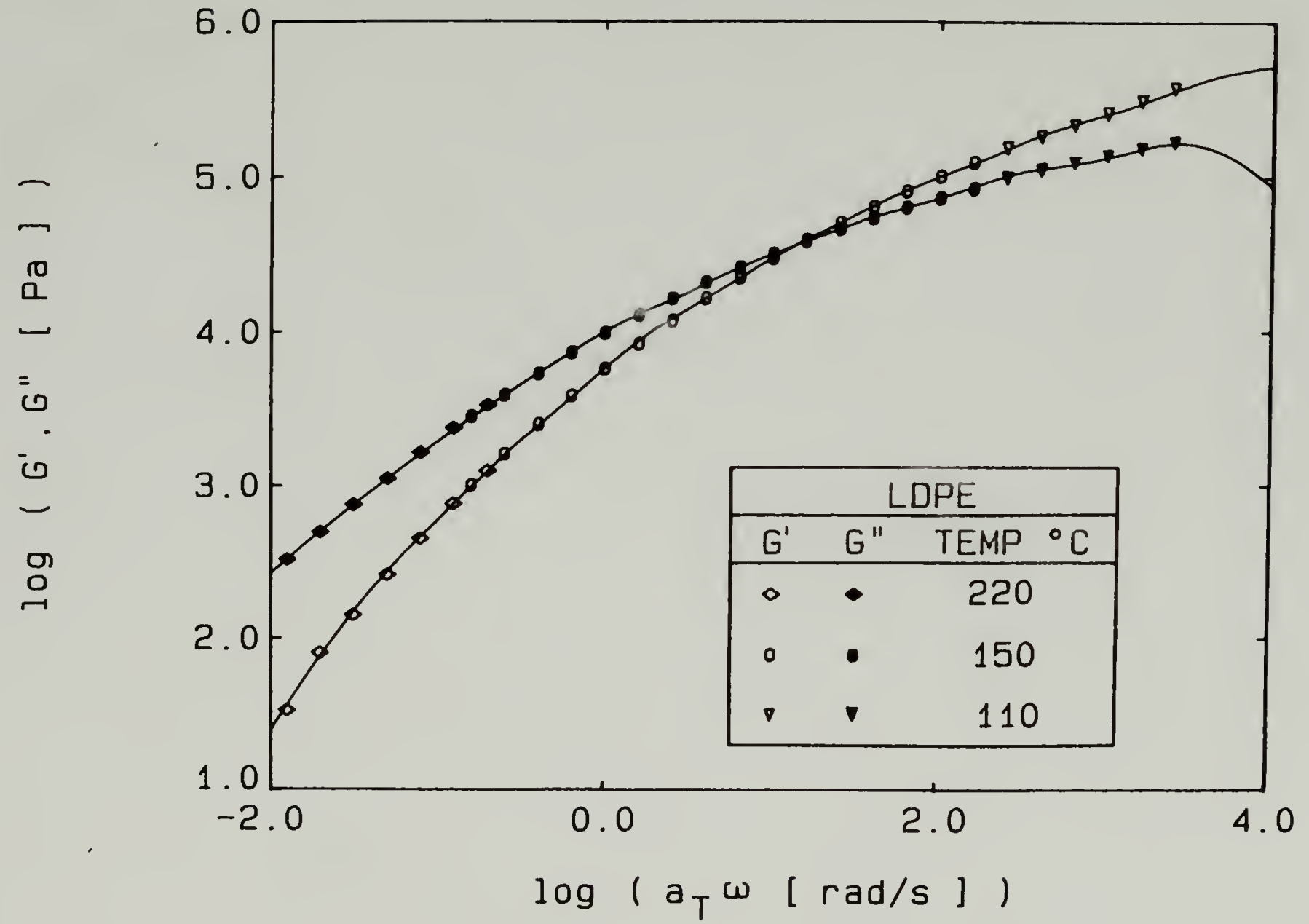

Figure 3.5. Storage and loss moduli as functions of reduced angular frequency for LDPE, T_o=150°C. The solid lines were calculated from Eqs. (3.10) and (3.11) using the values in Table 3.3.

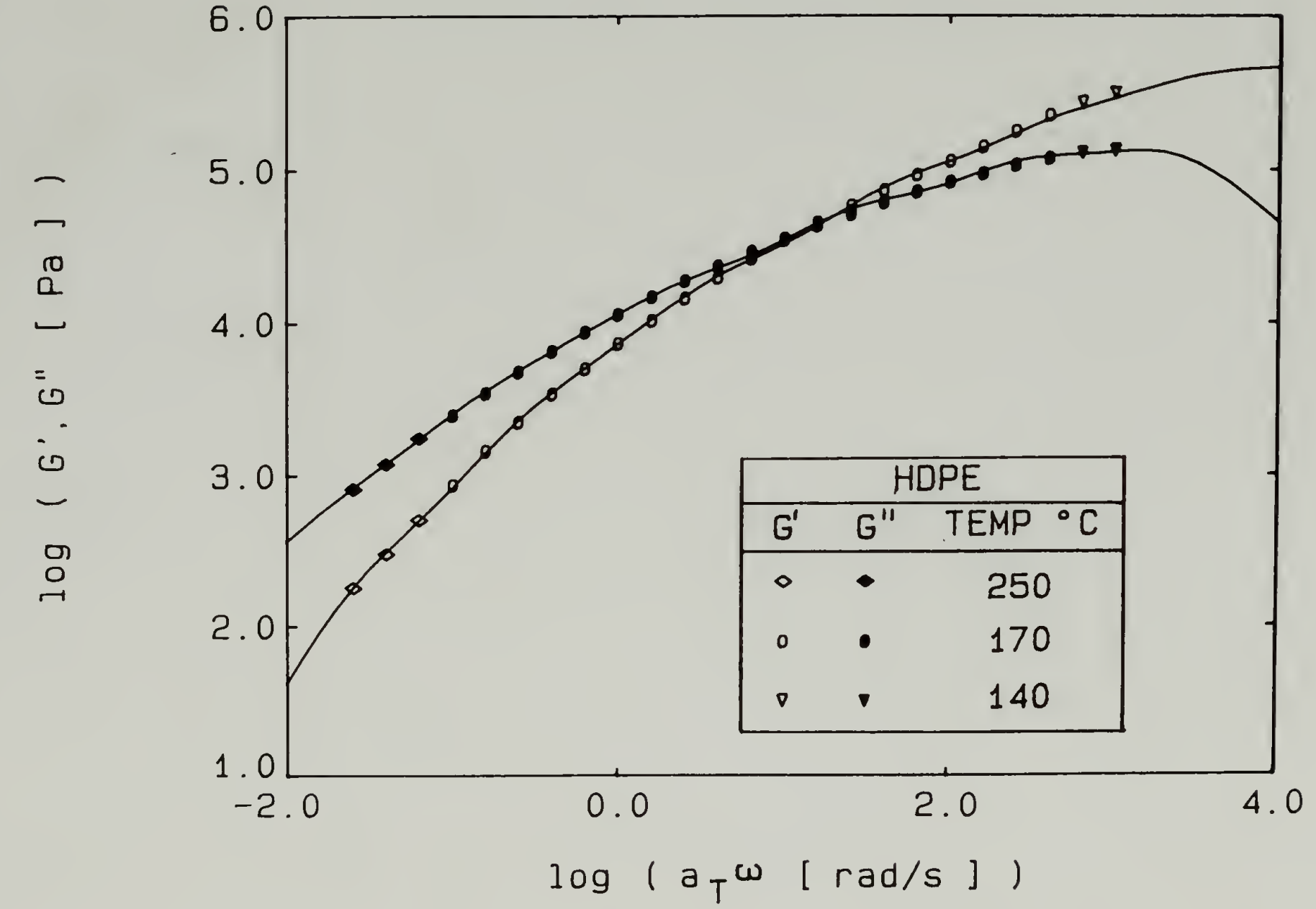

Figure 3.6. Storage and loss moduli as functions of reduced angular frequency for HDPE, T_o=170°C. The solid lines were calculated from Eqs. (3.10) and (3.11) using the values in Table 3.3.

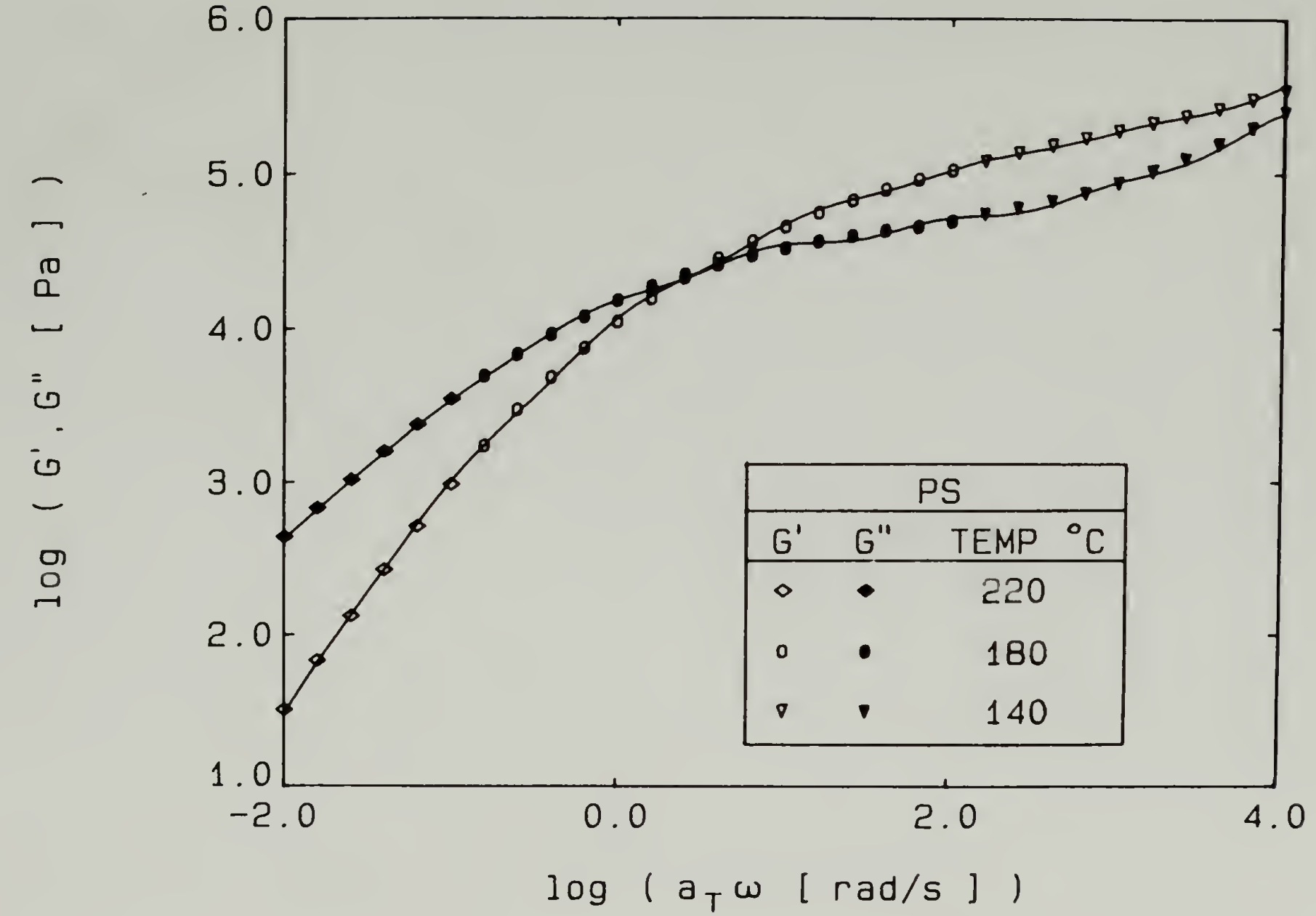

Figure 3.7. Storage and loss moduli as functions of reduced angular frequency for PS, T_0=180°C. The solid lines were calculated from Eqs. (3.10) and (3.11) using the values in Table 3.3.

Table 3.3. Discrete relaxation spectra obtained from oscillatory shear experiments.

Polymer	Discrete Relaxation Spectrum λ_i [s]	g_i [Pa]
LDPE T_o=150°C	5.913×10^{1} 1.817×10^{1} 3.680×10^{0} 6.606×10^{-1} 1.073×10^{-1} 2.060×10^{-2} 3.026×10^{-3} 3.381×10^{-4}	3.776×10^{1} 3.710×10^{2} 1.952×10^{3} 1.085×10^{4} 2.806×10^{4} 6.040×10^{4} 1.371×10^{5} 3.027×10^{5}
HDPE T_o=170°C	3.435×10^{1} 4.282×10^{0} 1.035×10^{0} 3.082×10^{-1} 4.120×10^{-2} 2.302×10^{-2} 3.378×10^{-3} 5.155×10^{-4}	3.434×10^{2} 2.925×10^{3} 5.048×10^{3} 1.864×10^{4} 4.180×10^{4} 3.840×10^{4} 1.565×10^{5} 2.115×10^{5}
PS T_o=180°C	5.152×10^{1} 8.669×10^{0} 5.135×10^{0} 1.018×10^{0} 1.107×10^{-1} 1.065×10^{-2} 9.927×10^{-4} 5.821×10^{-5}	7.763×10^{1} 1.338×10^{3} 9.275×10^{2} 1.762×10^{4} 5.004×10^{4} 6.978×10^{4} 1.009×10^{5} 5.558×10^{5}

Table 3.4. Range of strains experimentally obtained in RDS for step strain.

Geometry	Gap[mm]	Strain
Cone-and-plate	-	$0.1 < \gamma < 5$
Parallel-disk	1.00	$0.4 < \gamma_R < 4.5$
	0.50	$1 < \gamma_R < 12$
	0.25	$5 < \gamma_R < 25$

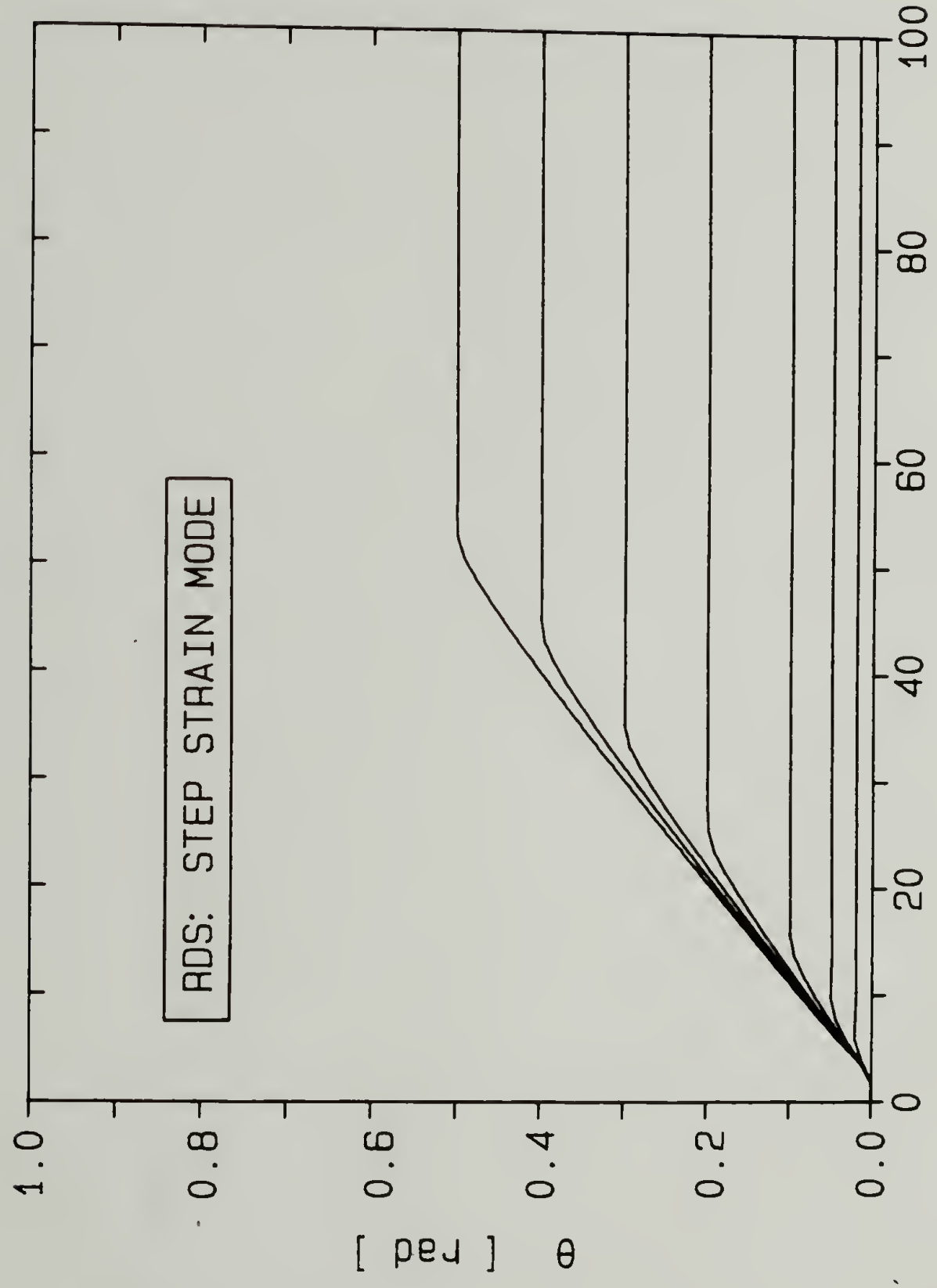

Figure 3.8. Measured angular displacement as a function of time for shear step strain experiment on RDS.

The stress response to the step strain is shown in Figures 3.9, 3.10 and 3.11 in the form of transient moduli. For the cone-and-plate geometry, the true relaxation modulus is plotted, while for the parallel-disk geometry the apparent relaxation modulus, Eq. (3.25), is plotted. The flat regions at short times occur because the transducer was overloaded at the beginning of the experiment. This overload also resulted in an offset at long times (about 0.5% of the transducer range) which is evident in the gradual leveling off of the relaxation modulus. Even though the data were corrected for this offset, results beyond 10 s have substantial scatter due to the inaccuracy of the transducer at torque levels less than 5×10^{-4} Nm. Therefore, reliable data were obtained over two time decades, $0.1<t<10$ s.

To obtain the true transient shear relaxation modulus at large strains from the parallel-disk geometry, the apparent modulus was corrected according to Eq. (3.27). The correction method was used for all three melts but only the intermediate results of the LDPE and PS data are presented for brevity. First, the apparent modulus was plotted against the shear strain, γ_R, with time as a parameter, see Figures 3.12 and 3.13. The solid curves were determined by fitting the experimental points to a third order polynomial (Bevington, 1969). The slope of these curves was used in Eq. (3.26) to determine the correction factor $\chi(t,\gamma_R)$. At small strains, the slope of the curves is zero and the correction factor approaches unity, $\chi=1$. At larger strains, the slope becomes increasingly negative. No limiting slope was observed for the range of the shear strains studied. The corrected shear relaxation

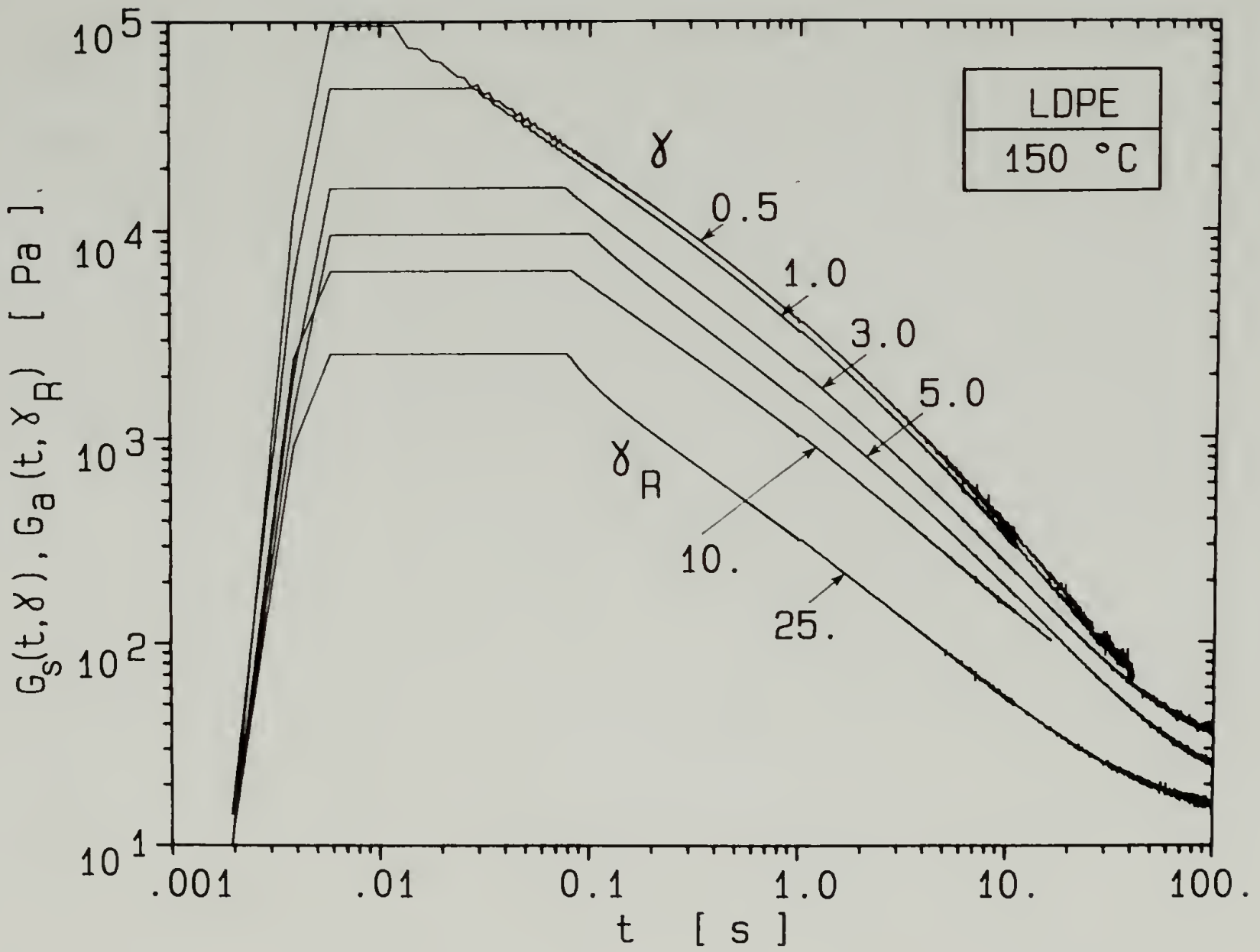

Figure 3.9. Transient shear relaxation modulus plotted directly by rheometer for LDPE. $G_S(t,\gamma)$ is plotted for cone-and-plate geometry ($0.5 \leq \gamma \leq 5.0$) and $G_a(t,\gamma_R)$ is plotted for parallel disk geometry (γ_R=10 and 25).

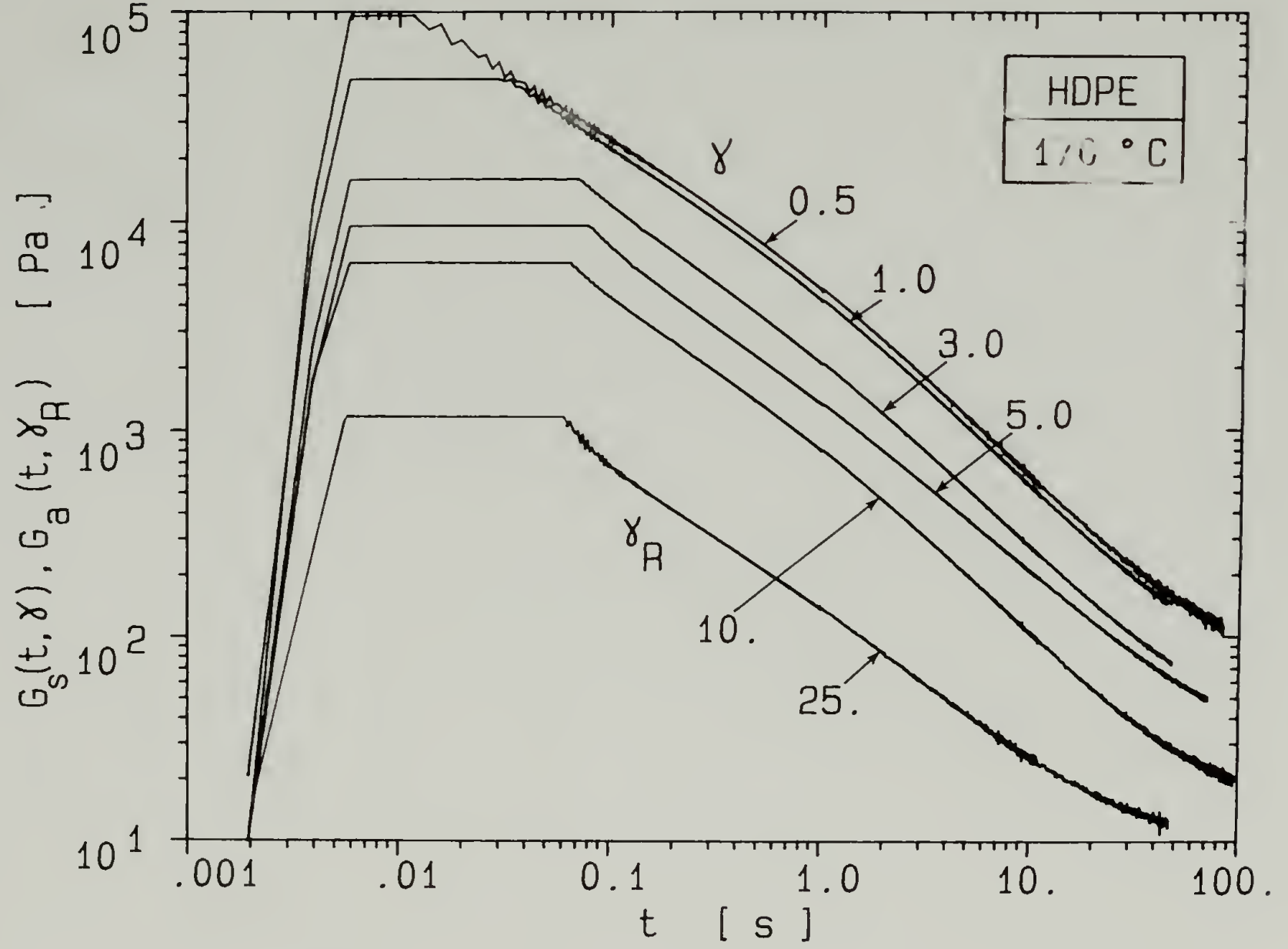

Figure 3.10. Transient shear relaxation modulus plotted directly by rheometer for HDPE. $G_s(t,\gamma)$ is plotted for cone-and-plate geoemtry ($0.5 \leq \gamma \leq 5.0$) and $G_a(t,\gamma_R)$ is plotted for parallel disk geometry (γ_R=10 and 25).

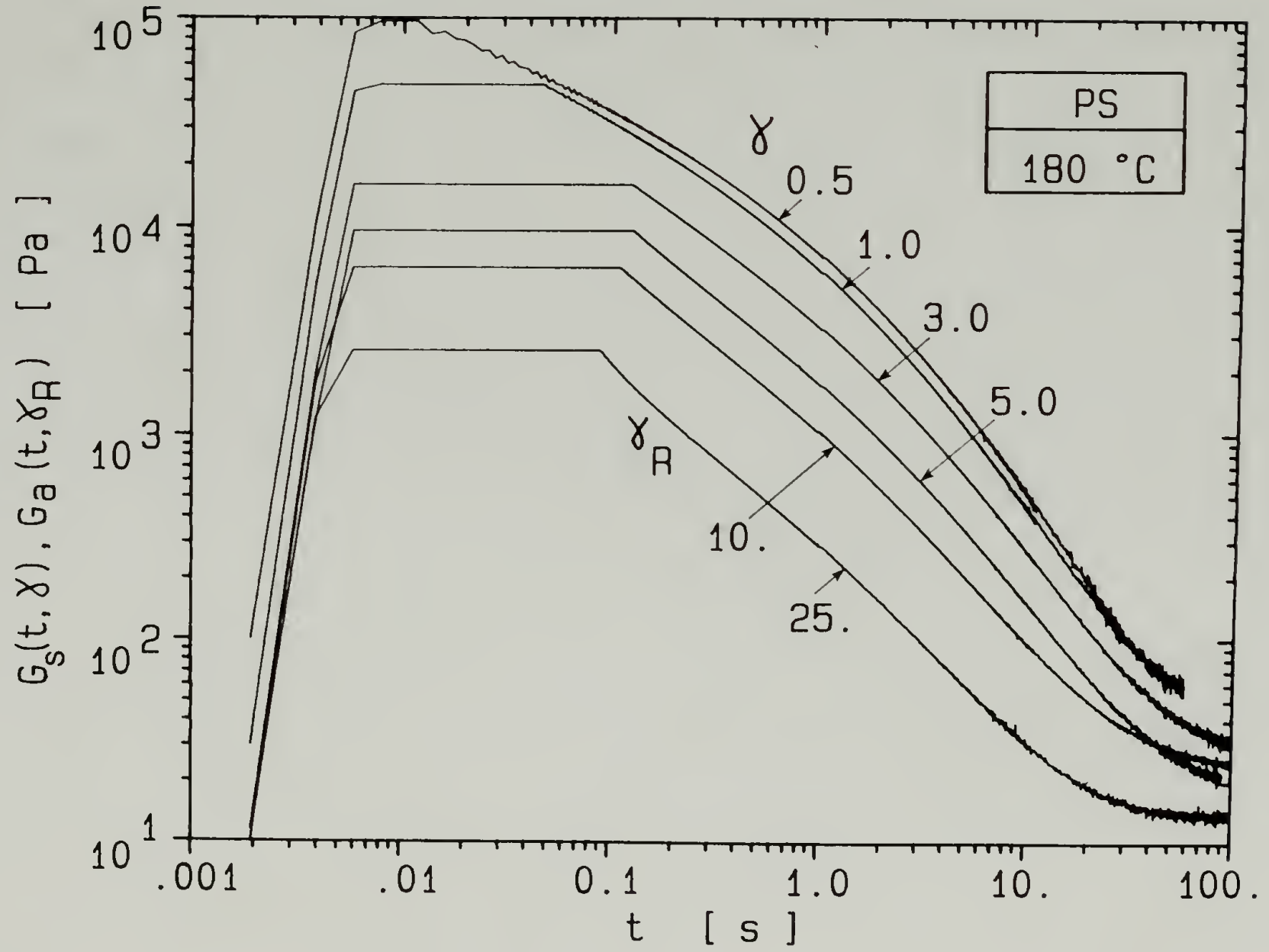

Figure 3.11. Transient shear relaxation modulus plotted directly by rheometer for PS. $G_S(t,\gamma)$ is plotted for cone-and-plate geometry ($0.5 \leq \gamma \leq 5.0$) and $G_a(t,\gamma_R)$ is plotted for parallel disk geometry (γ_R=10 and 25).

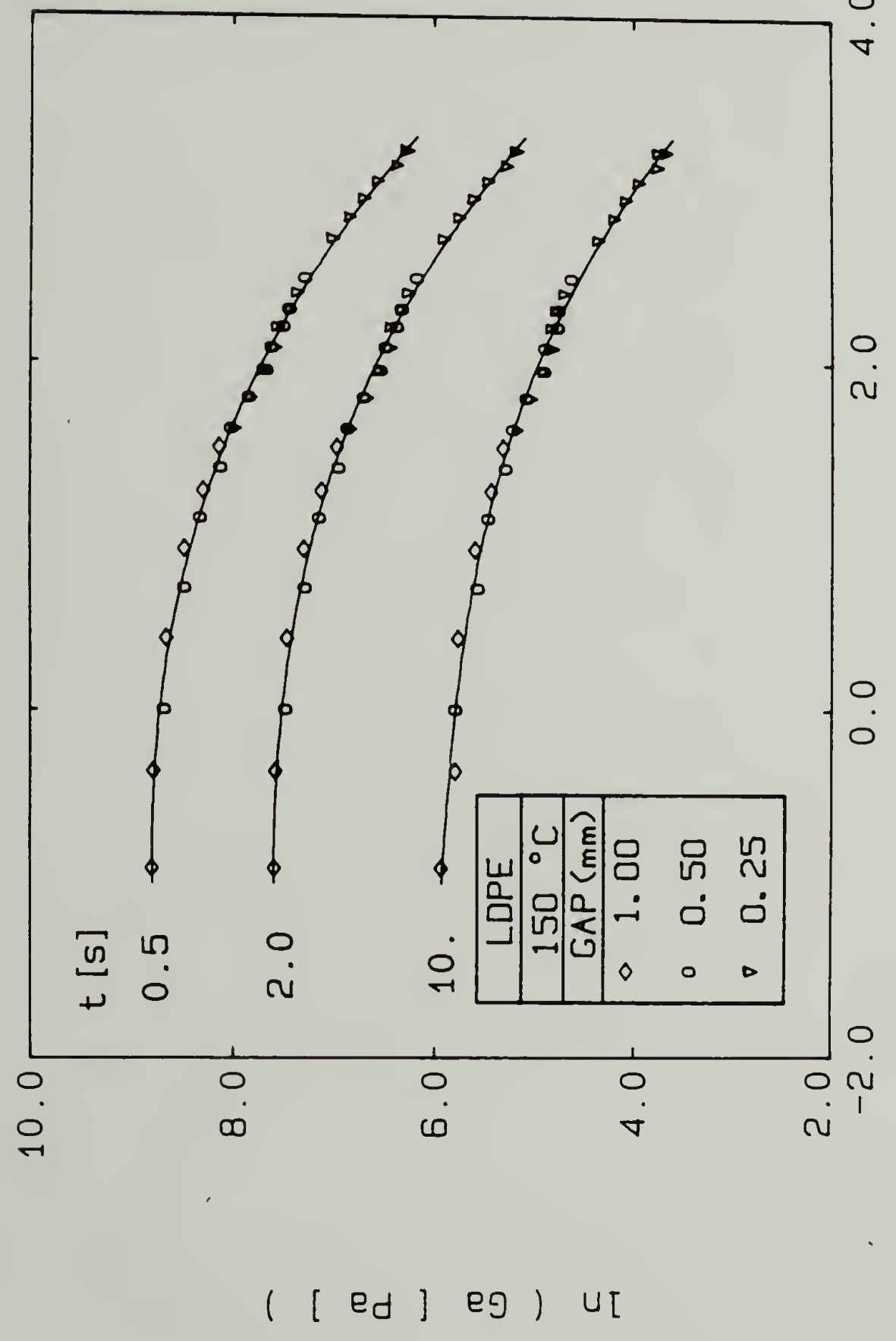

Figure 3.12. Apparent modulus as a function of strain from parallel disk experiments for LDPE. The solid lines were fit by a 3rd order polynomial.

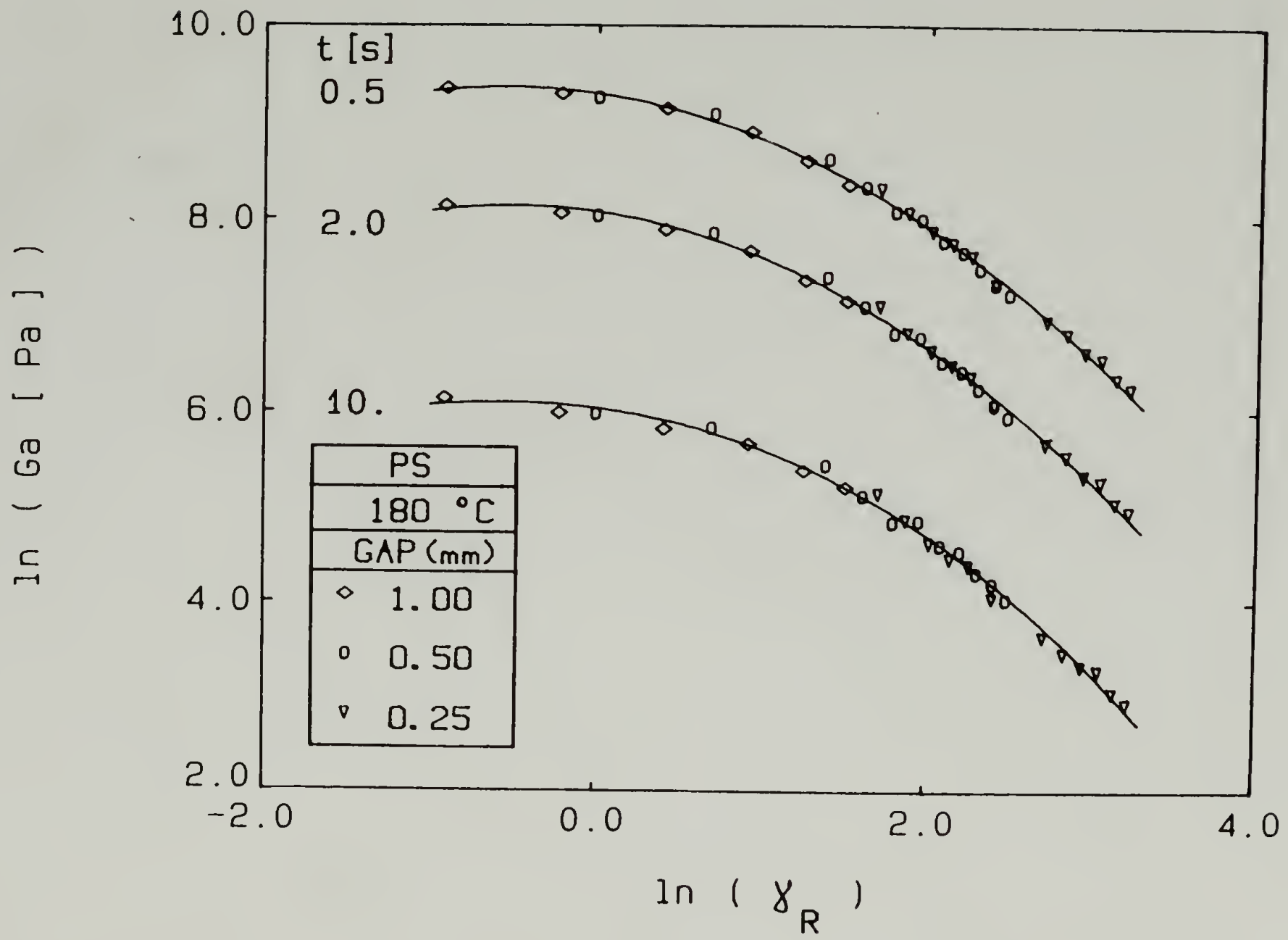

Figure 3.13. Apparent modulus as a function of strain from parallel disk experiments for PS. The solid lines were fit by a 3rd order polynomial.

moduli and the apparent moduli are compared in Figures 3.14 and 3.15. At large strains, the corrected moduli are significantly lower than the apparent moduli.

The relaxation moduli determined from the non-homogeneous strain in the parallel-disk agree well with the relaxation moduli which were obtained from the cone-and-plate geometry. Figures 3.16 and 3.17 show a superposition of the two sets of experimental data.

Several of the measured relaxation moduli, from both geometries, are shown in Figures 3.18, 3.19 and 3.20. The solid line is the relaxation modulus of linear viscoelasticity as calculated from Eq. (2.42) and the relaxation spectrum of Table 3.3. The oscillations in the calculated curve are due to the choice of a discrete spectrum. The data at the lowest strain, γ=0.2, are described well by the linear viscoelastic theory.

3.2.4.3 Capillary rheometry. A high pressure capillary rheometer (Göttfert, Rheograph 2001) was used to obtain steady shear viscosities of high shear rates for the three polymers studied. The rheometer consists of a heated barrel having an inside diameter of 20 mm on which different size capillary dies can be mounted at the bottom end. The barrel has three heating zones and is capable of temperatures up to 400$\pm$0.1°C. An electro-hydraulic linear amplifier transfers a microprocessor controlled rotation of a stepping motor into a constant linear speed of the piston. Piston speeds between 0.0001 and 20 mm/s can be selected. Interchangeable dies having capillary diameters of 1 mm and lengths of 30, 20 and 10 mm were used allowing apparent shear rates of

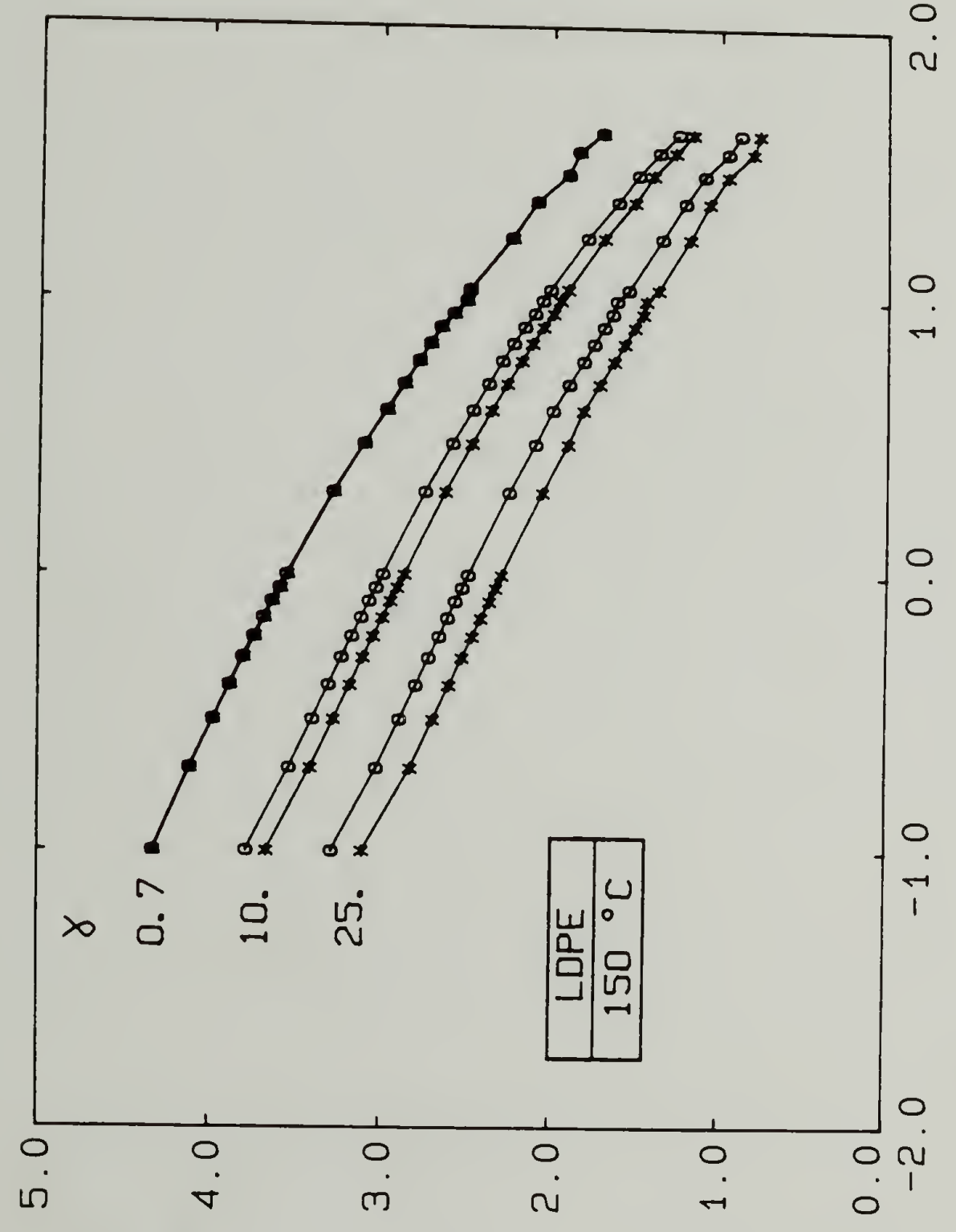

Figure 3.14. Correction of transient apparent shear relaxation modulus for non-homogeneous strain for LDPE.

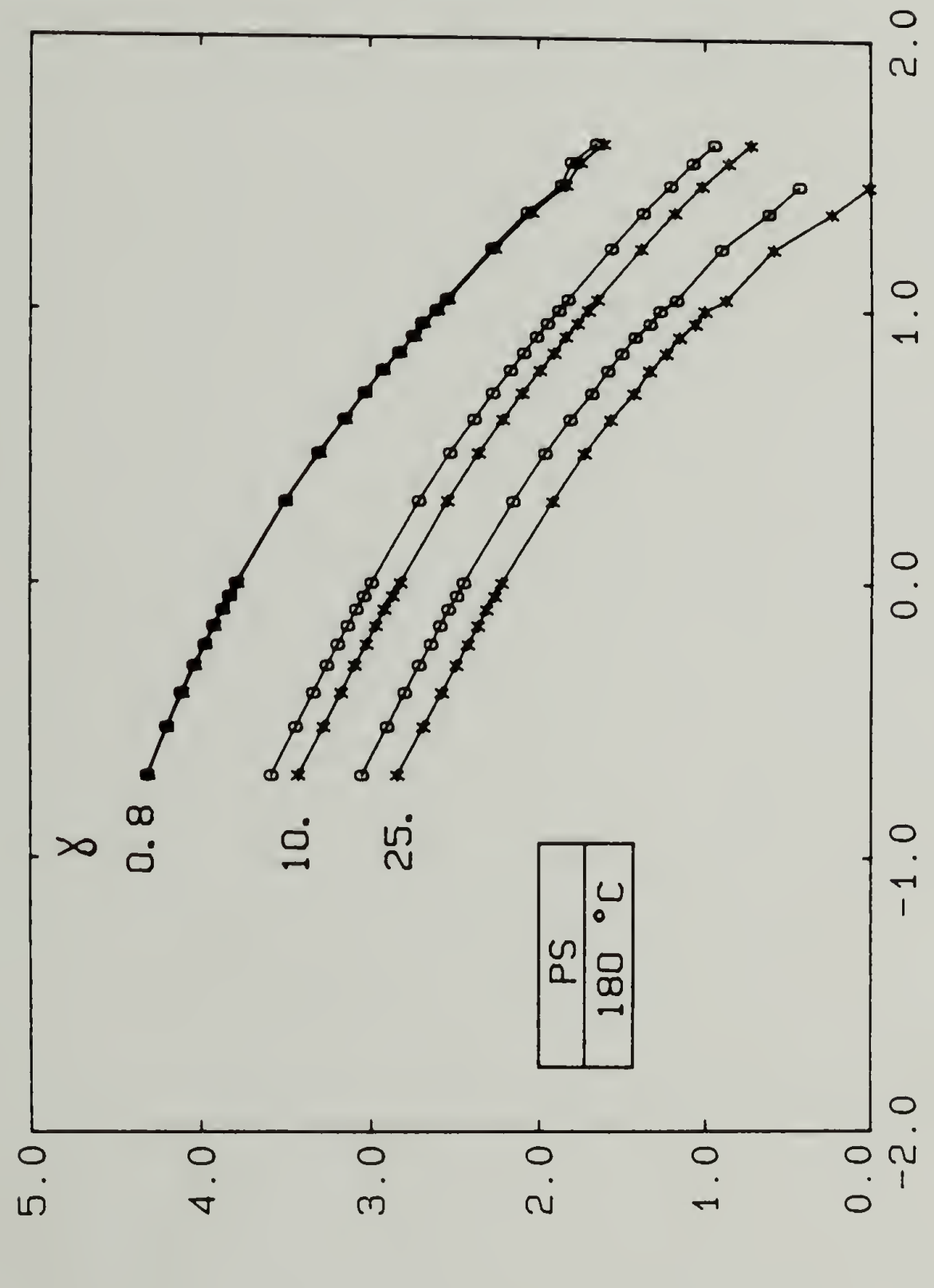

Figure 3.15. Correction of transient apparent shear relaxation modulus for non-homogeneous strain for PS.

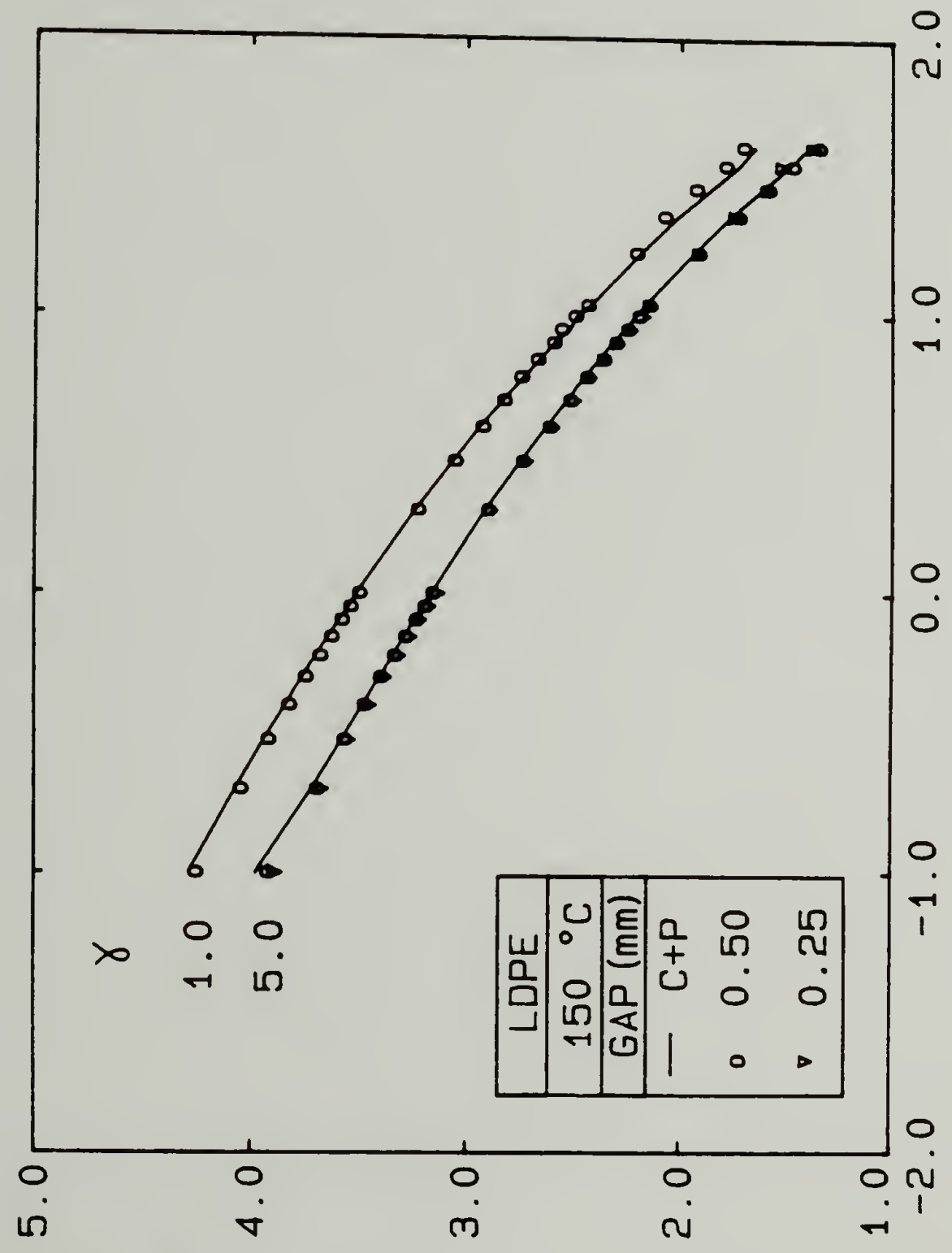

Figure 3.16. Comparison between shear relaxation modulus measured with parallel disks and cone-and-plate geometries for LDPE.

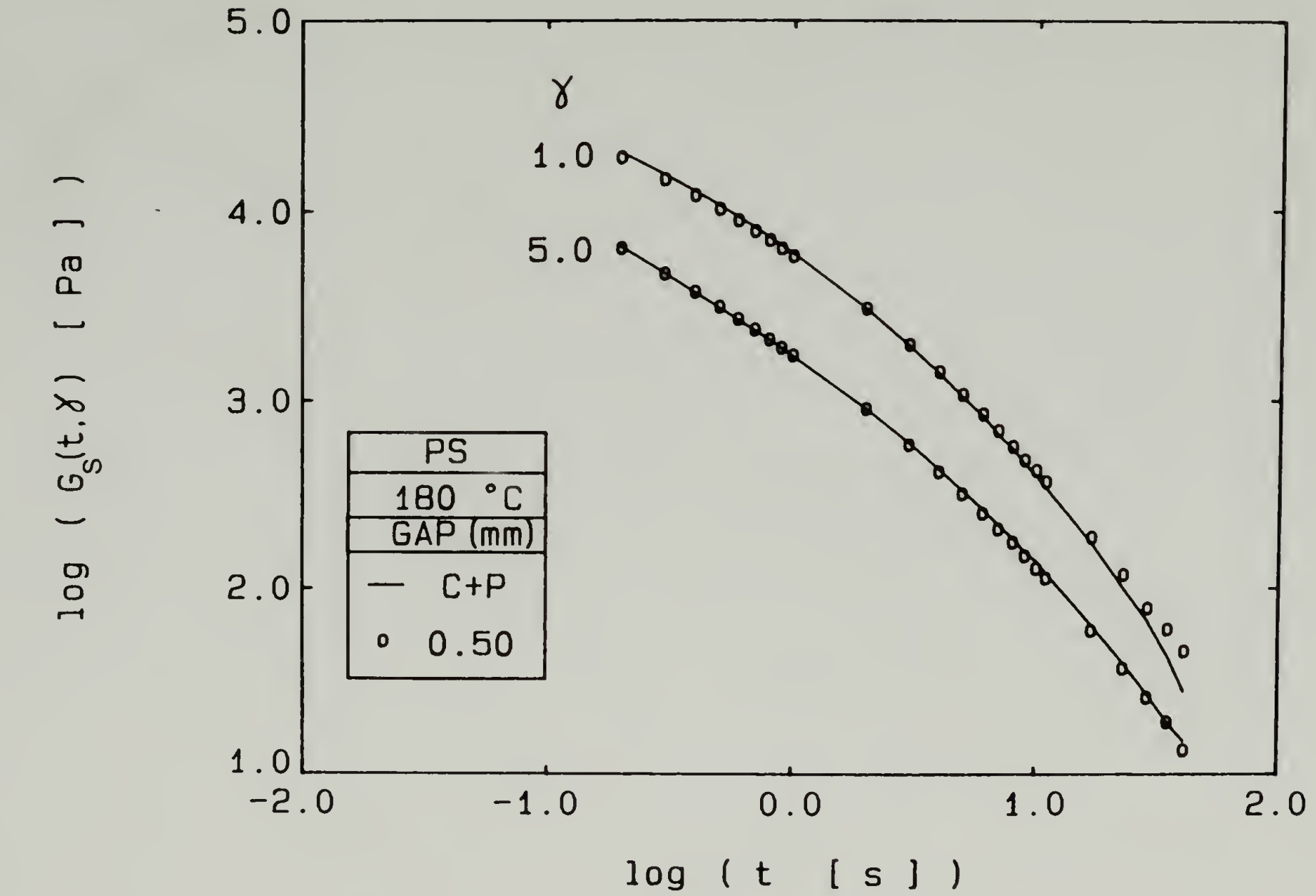

Figure 3.17. Comparison between shear relaxation modulus measured with parallel disks and cone-and-plate geometries for PS.

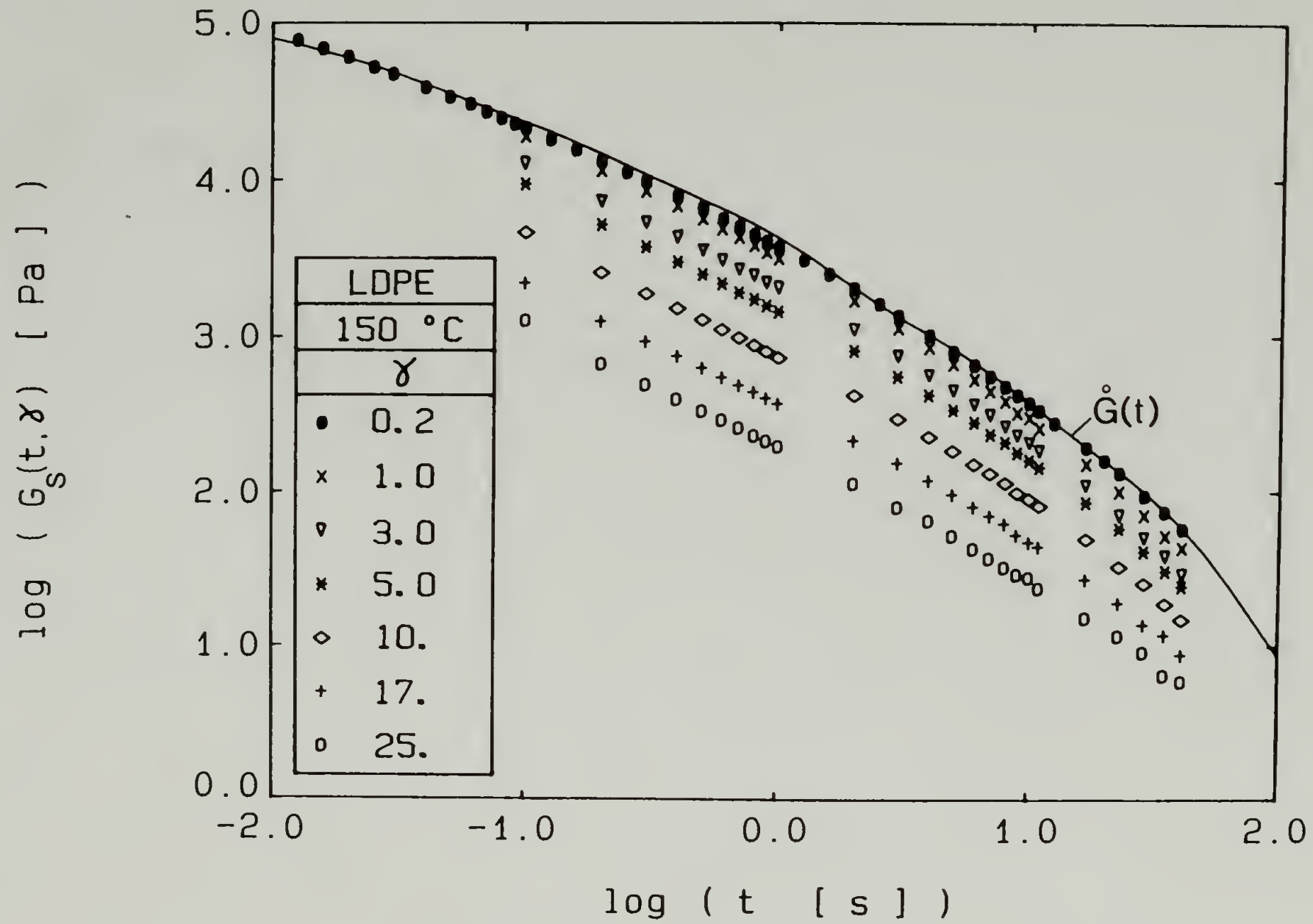

Figure 3.18. Transient shear relaxation modulus of LDPE. The solid line is $\mathring{G}(t)$ calculated from Eq. (2.42) using the values in Table 3.3.

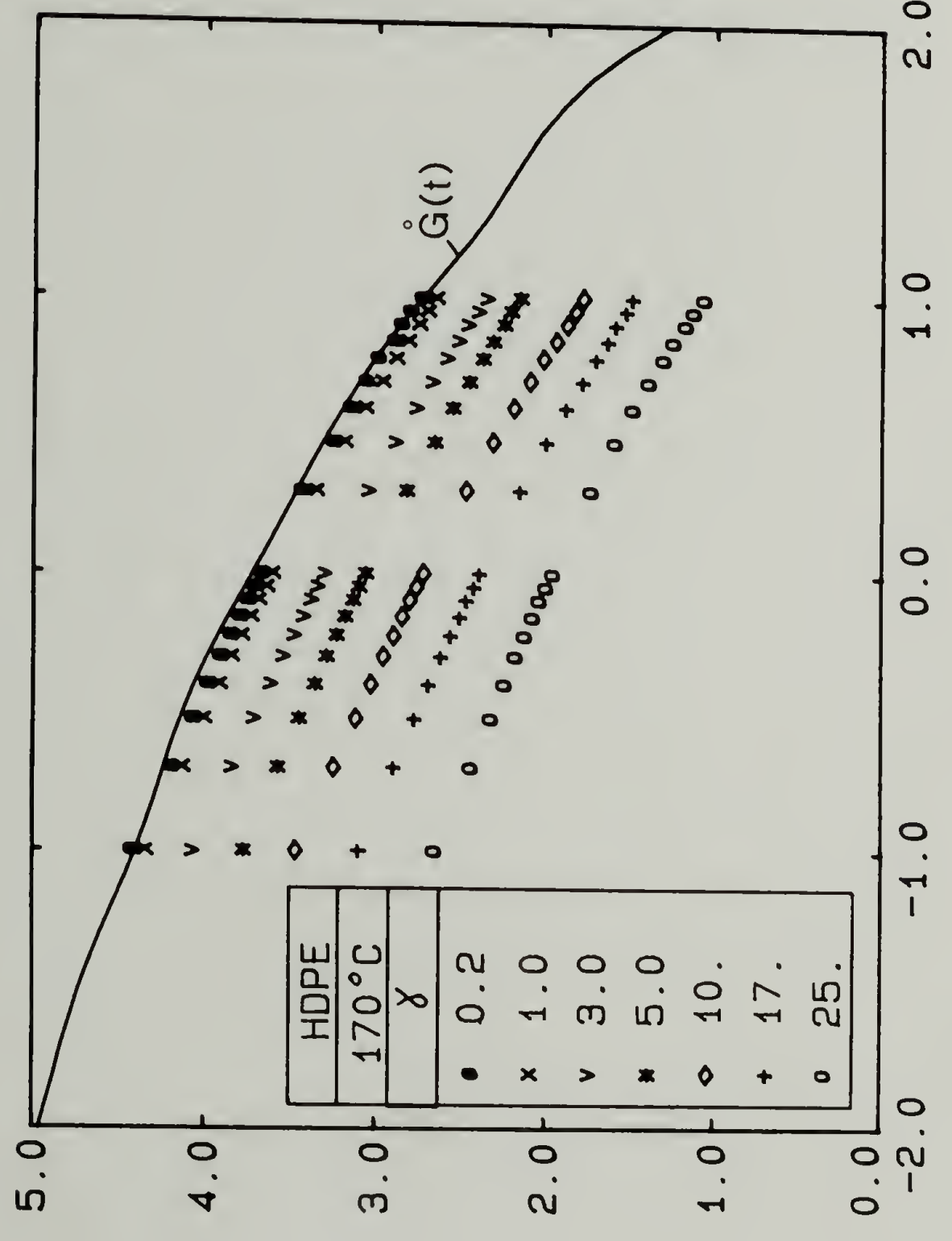

Figure 3.19. Transient shear relaxation modulus of HDPE. The solid line is $\mathring{G}(t)$ calculated from Eq. (2.42) using the values in Table 3.3.

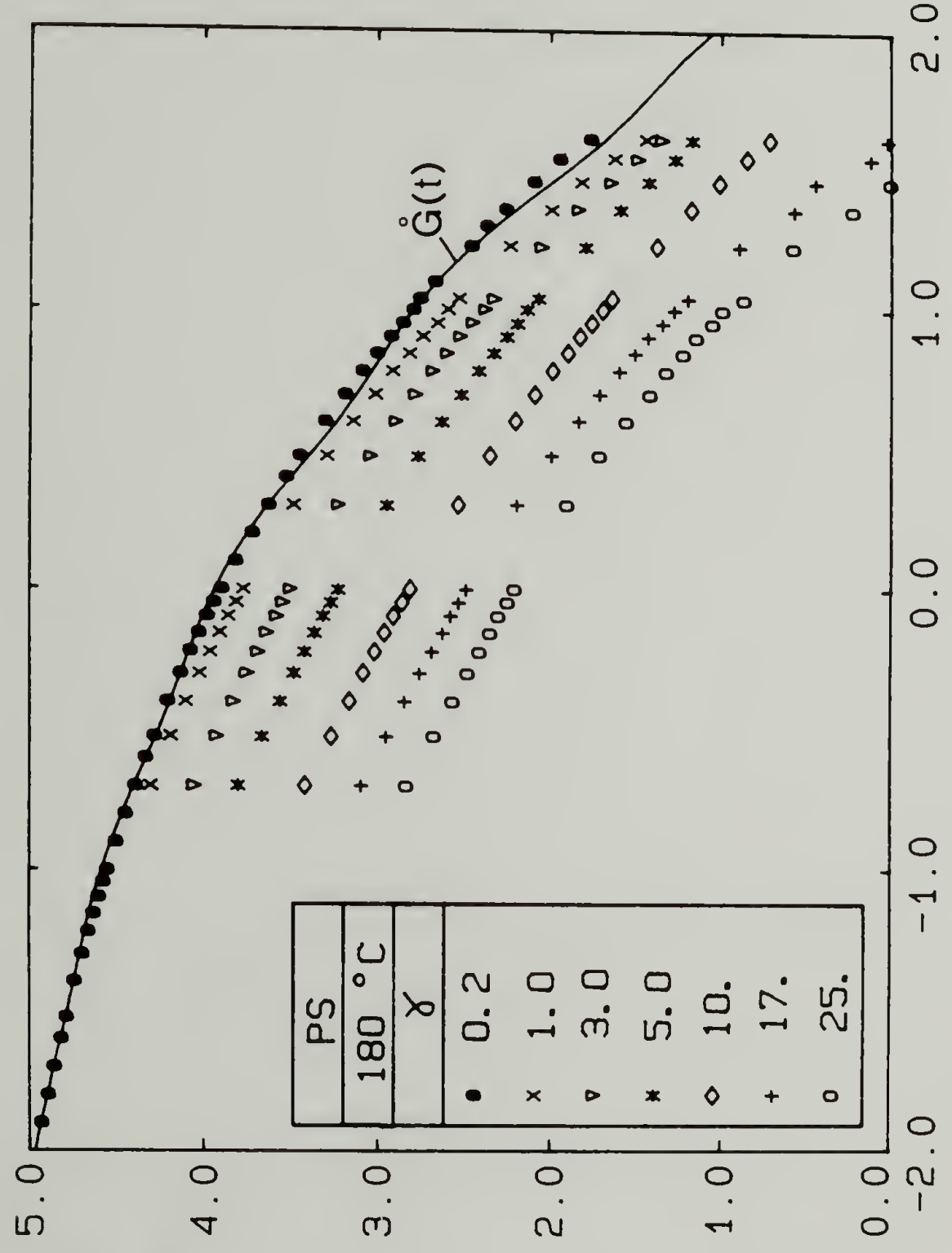

Figure 3.20. Transient shear relaxation modulus of PS. The solid line is $\mathring{G}(t)$ calculated from Eq. (2.42) using the values in Table 3.3.

$3.2\times10^{-1}<\dot{\gamma}_a<6.4\times10^{4}$ s^{-1} to be attained. A melt pressure transducer with a nominal measuring range of 100 MPa was used to measure the melt pressure just before the capillary entrance.

Steady shear viscosities were obtained for the three polymers for $10^{1}<\dot{\gamma}_a<10^{4}$ s^{-1}. The entrance pressure, P_e, was measured for nine different volume flow rates in all three capillary dies. The end correction factor in Eq. (3.32) was found from the Bagley plots shown in Figures 3.21, 3.22 and 3.23. The shear stress at the wall was evaluated and the shear rate at the wall was calculated from Eq. (3.30) and Figure 3.24. The measured steady state shear viscosities are listed in Table 3.5.

3.2.5 Discussion

3.2.5.1 Step strain experiments. The strain dependent network theory for polymer melts discussed in Section 2.4, as applied to step shear (Laun, 1978), suggests that the shear relaxation modulus can be factored into a time dependent function, the linear viscoelastic relaxation modulus, $\overset{\circ}{G}(t)$, and a strain function, $h_s(\gamma)$,

$$G_s(t,\gamma) = \overset{\circ}{G}(t)h_s(\gamma) \qquad (3.33).$$

The strain function approaches unity at small strains and decreases monotonically as the strain increases.

The strain function of the three polymers has been determined by shifting the curves of Figures 3.18, 3.19 and 3.20 vertically upward until they coincide with the linear viscoelastic curve. The magnitude of the shift, $h_s(\gamma)$, is plotted in Figures 3.25, 3.26 and 3.27. The

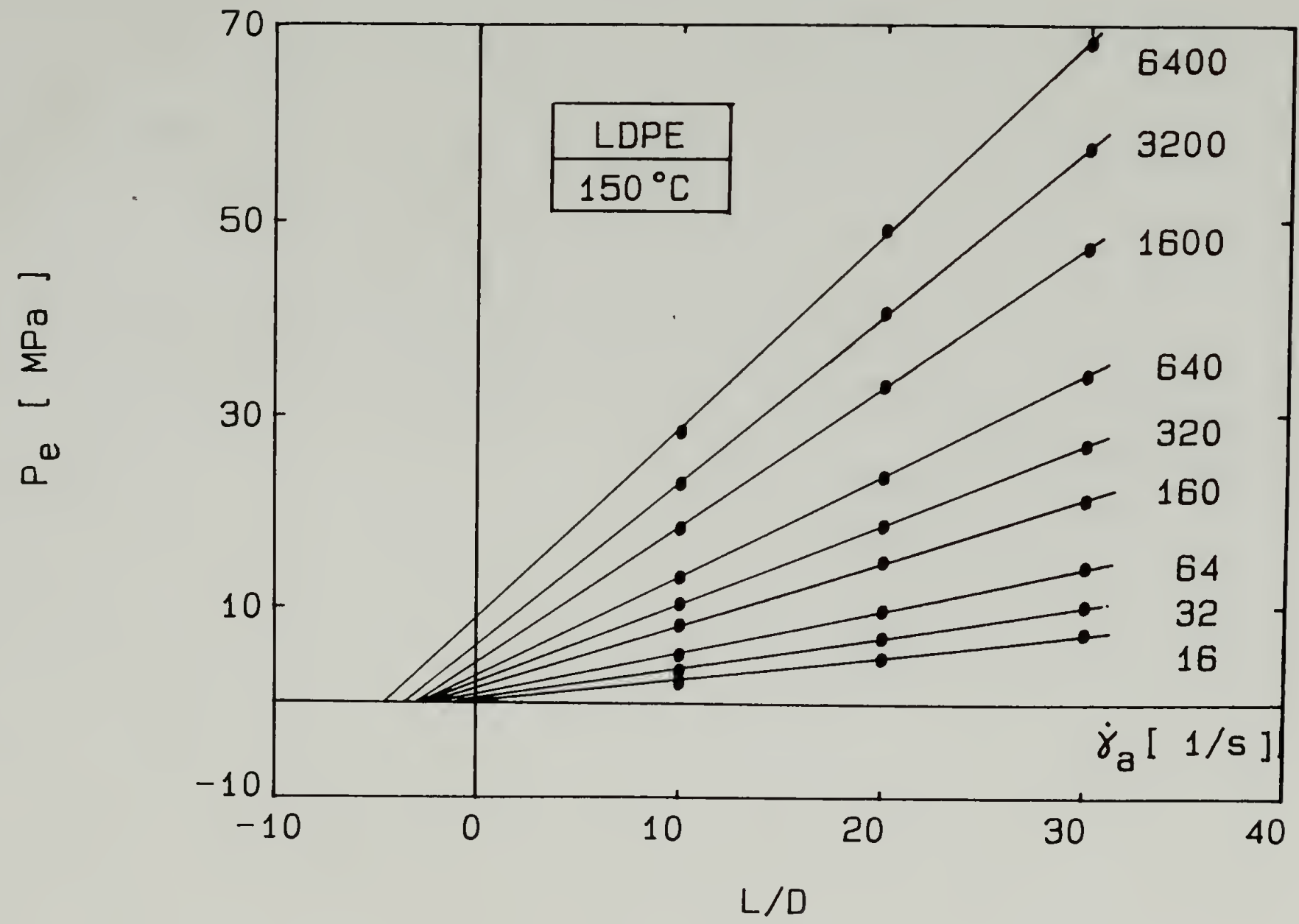

Figure 3.21. Bagley plot of LDPE.

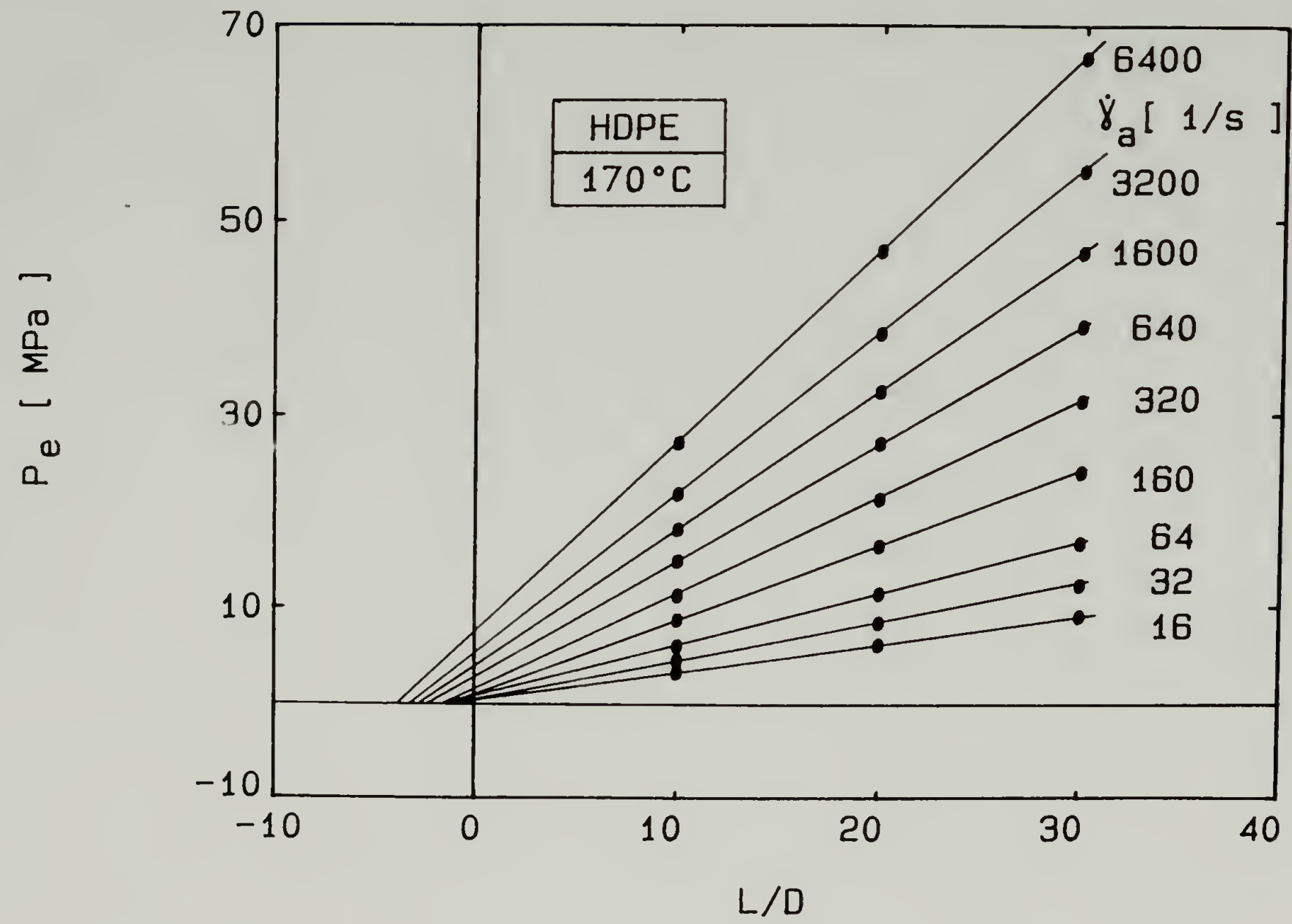

Figure 3.22. Bagley plot of HDPE.

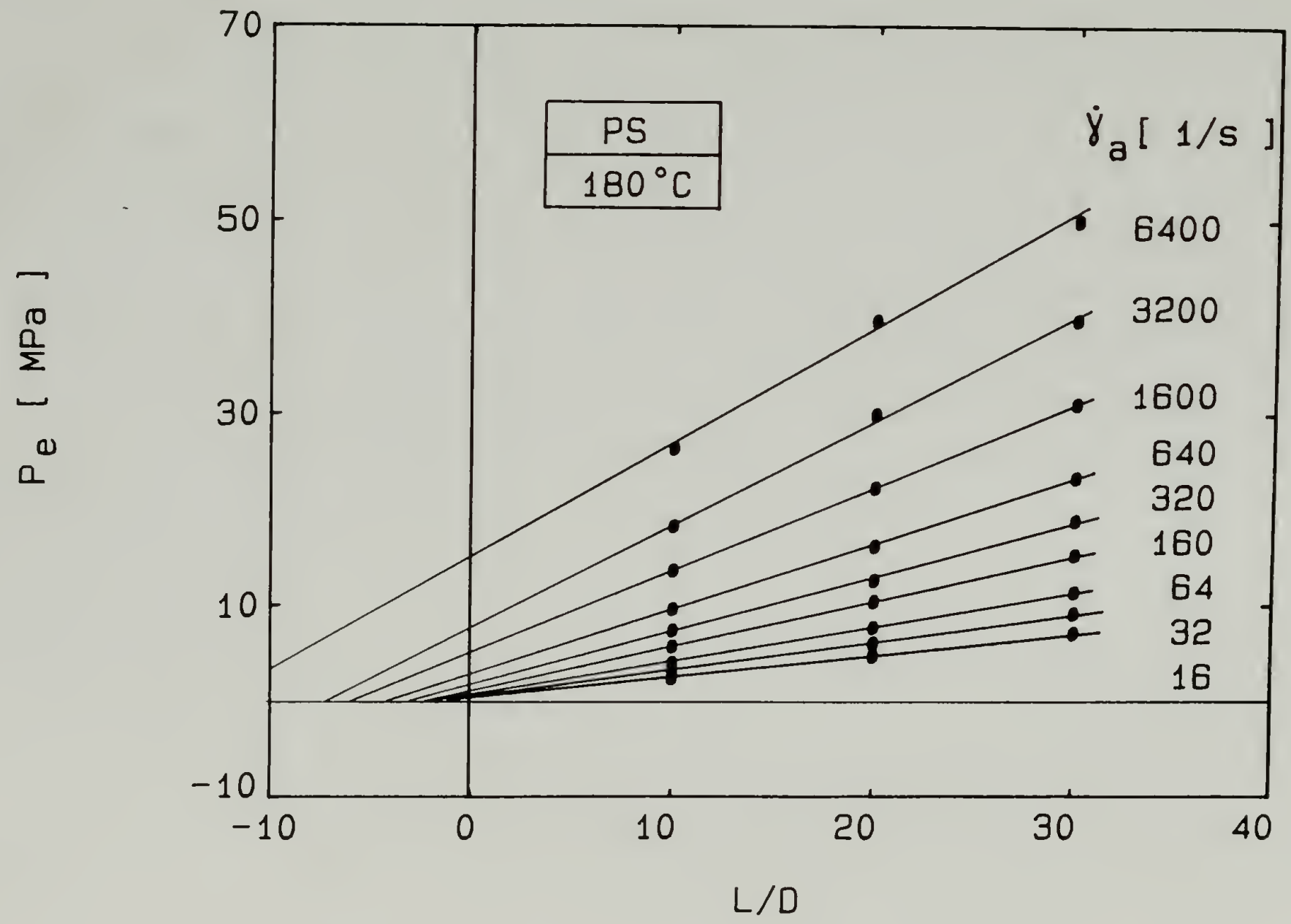

Figure 3.23. Bagley plot of PS.

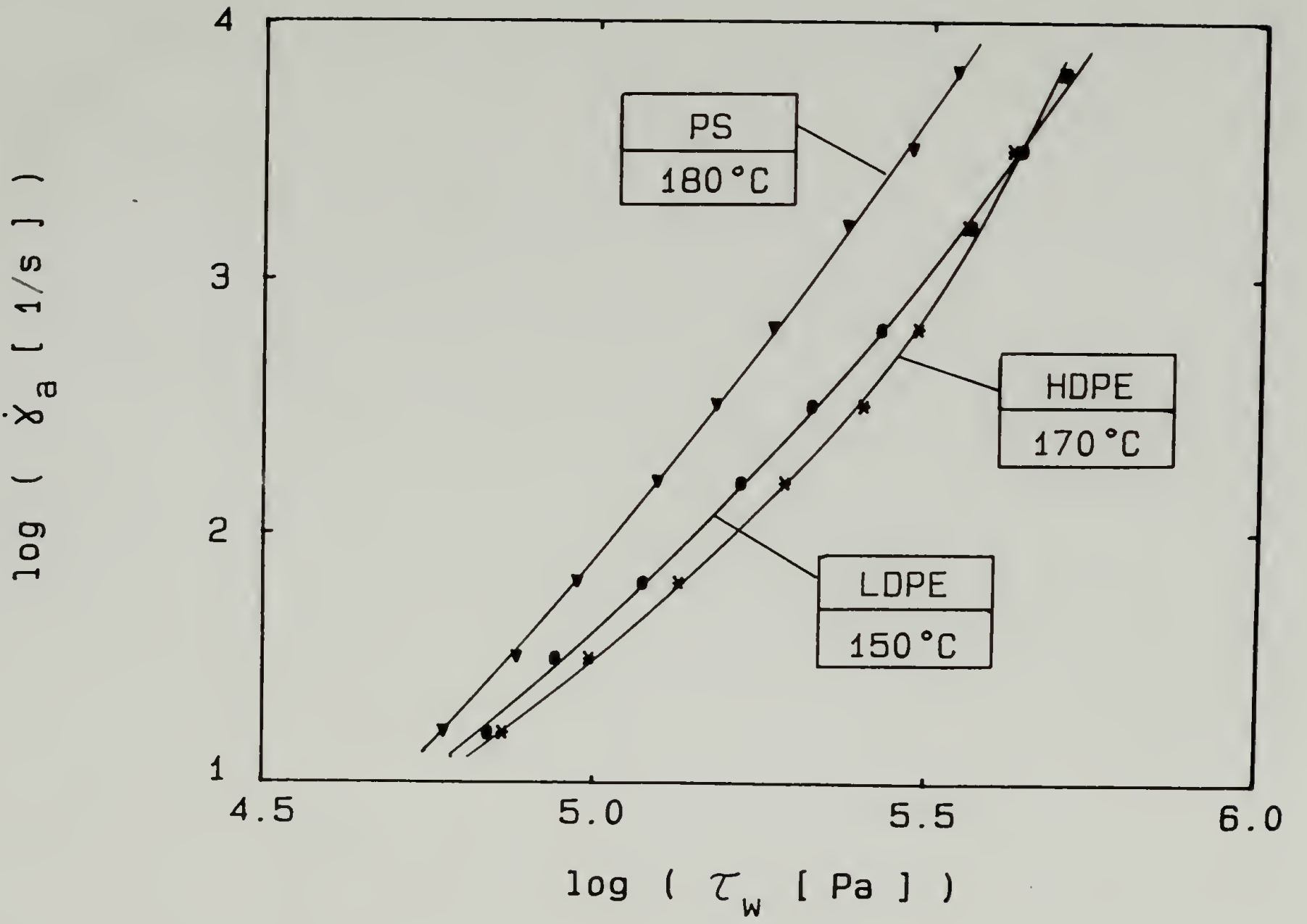

Figure 3.24. Apparent shear rate as a function of wall shear stress for capillary flow experiments.

Table 3.5. Steady shear viscosities obtained from capillary flow experiments.

LDPE 150°C		PS 180°C		HDPE 170°C	
$\dot{\gamma}_w$ [s^{-1}]	η_s [Pa·s]	$\dot{\gamma}_w$ [s^{-1}]	η_s [Pa·s]	$\dot{\gamma}_w$ [s^{-1}]	η_s [Pa·s]
20.5	3380.	23.3	2550.	21.2	3450.
41.5	2110.	48.6	1570.	41.6	2360.
85.1	1400.	99.8	944.	85.5	1560.
223.	741.	257.	482.	233.	825.
462.	455.	521.	290.	512.	490.
964.	276.	1050.	174.	1110.	274.
2570.	141.	2660.	88.9	2970.	120.
5350.	80.6	5320.	55.4	5950.	70.0
11100.	45.1	10600.	32.2	13900.	35.7

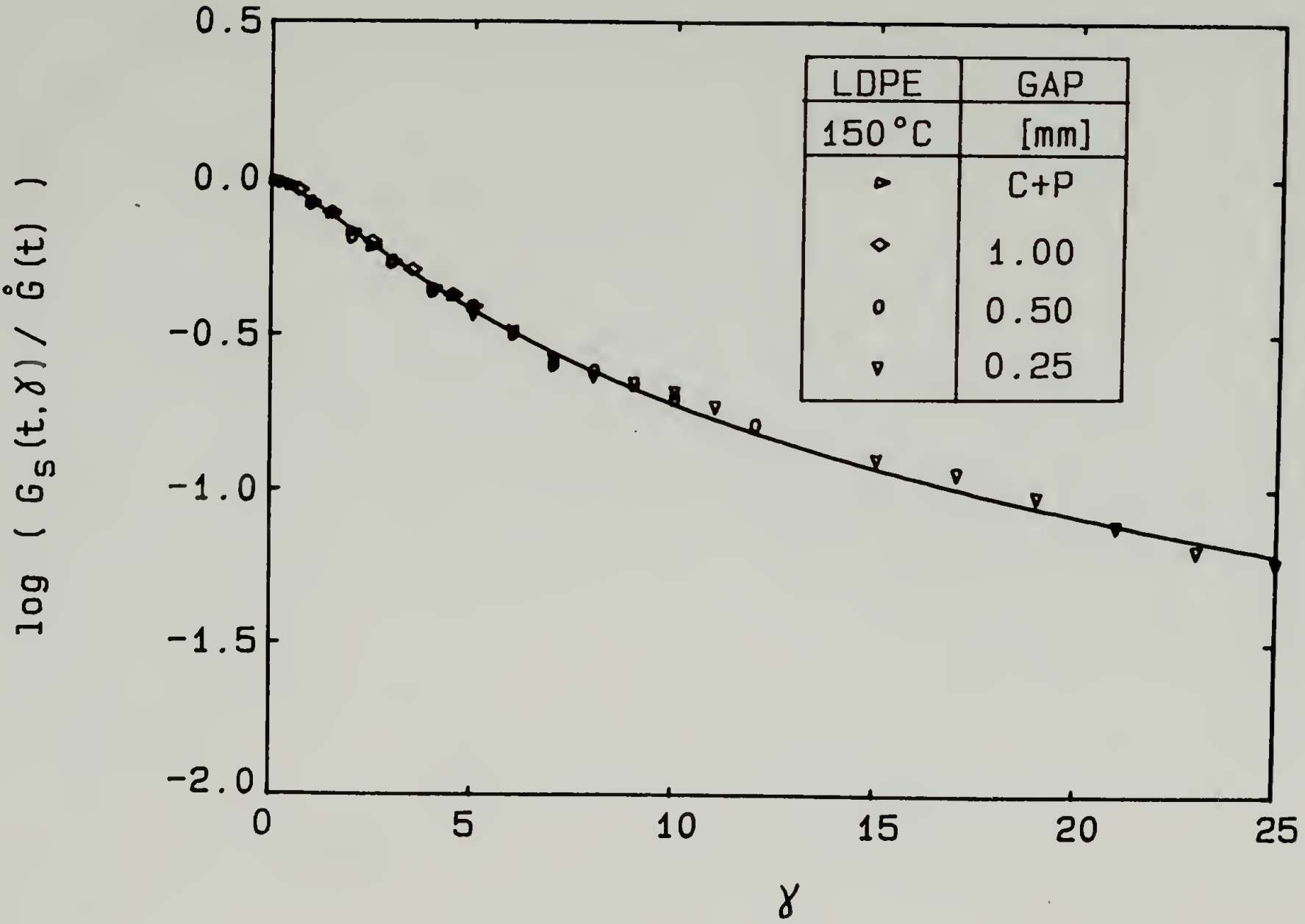

Figure 3.25. Shear strain function, h_s, of LDPE. The solid line was calculated from Eq. (3.36) using the values in Table 3.6.

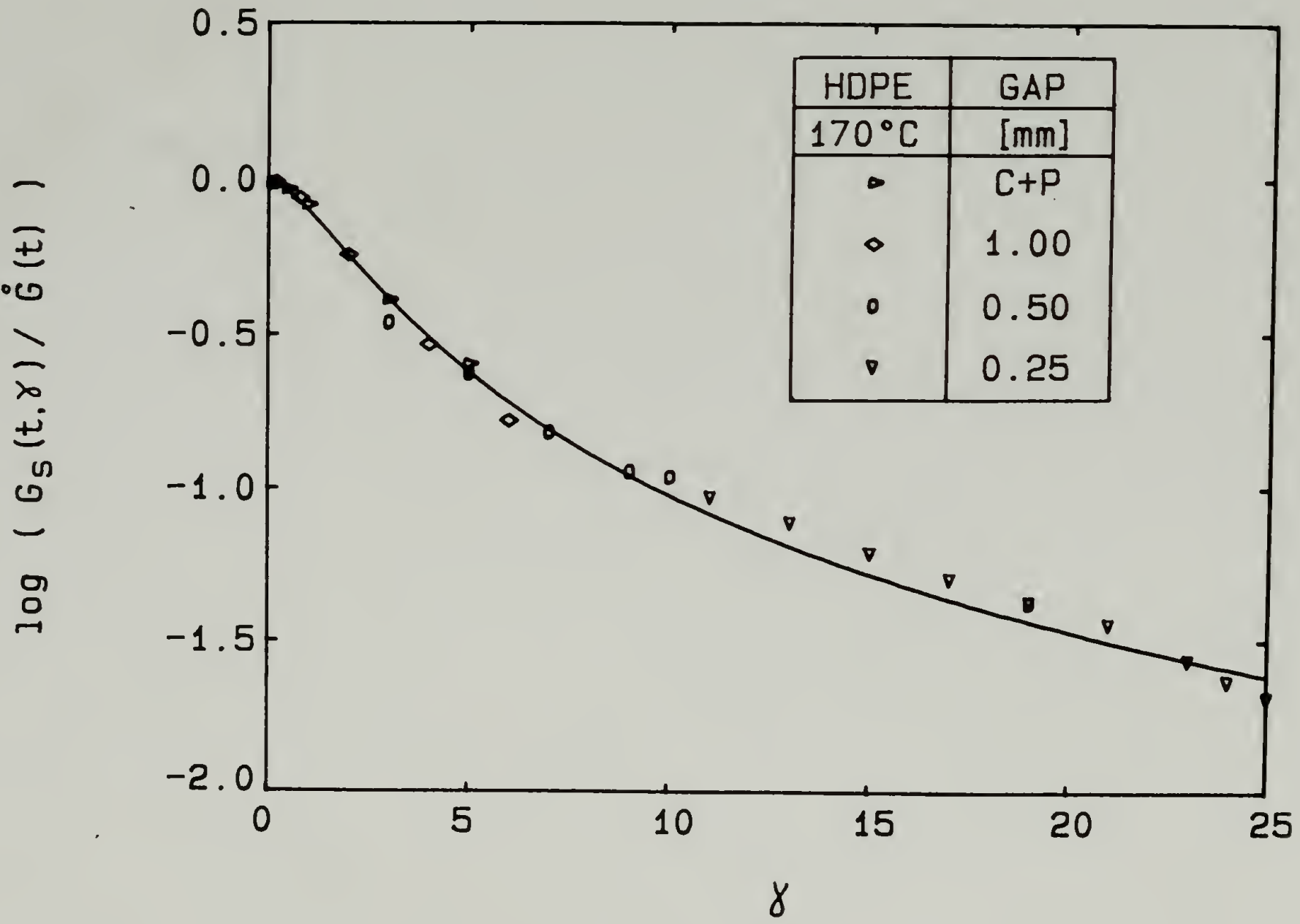

Figure 3.26. Shear strain function, h_s, of HDPE. The solid line was calculated from Eq. (3.36) using the values in Table 3.6.

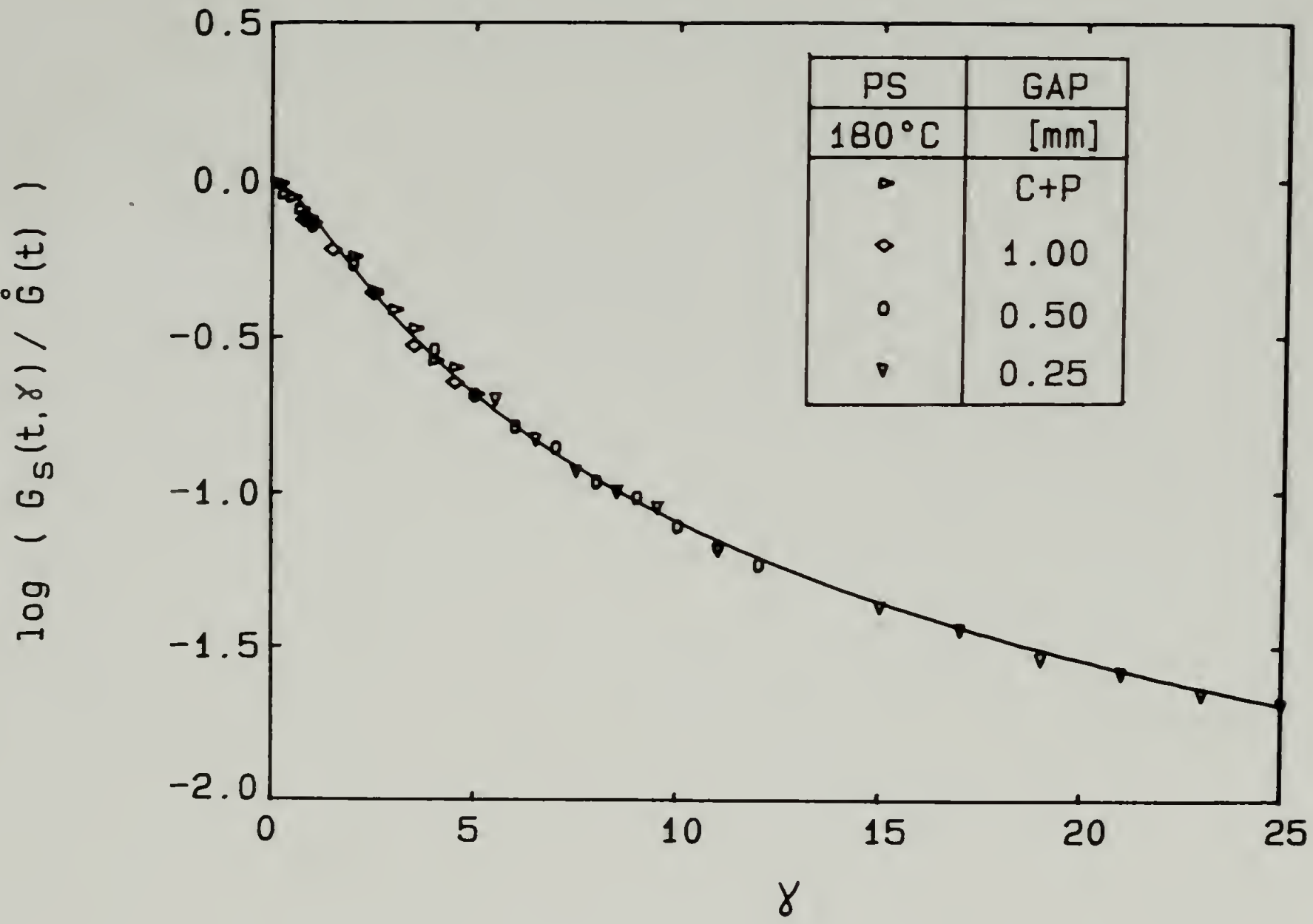

Figure 3.27. Shear strain function, h_S, of PS. The solid line was calculated from Eq. (3.36) using the values in Table 3.6.

parallel-disk data agree well with the cone-and-plate data at lower strains and continue in a smooth fashion to the large strain region. The HDPE and PS exhibit much stronger strain dependence than the LDPE.

Several forms of equations have been proposed for fitting the strain function data. Wagner (1976) proposed a single exponential function, while Osaki (1976) and Laun (1978) used the sum of two exponential functions of the form

$$h(\gamma) = f \exp(-n_1\gamma) + (1-f)\exp(-n_2\gamma) \qquad (3.34).$$

The single exponential form does not describe the large strain region as it underpredicts the data. The sum of two exponential functions gives a good fit at the larger strains but underpredicts at the small strain region where the data approach unity in a sigmoidal fashion. A sigmoidal form has been proposed by Papanastasiou et al. (1983):

$$h(\gamma) = 1/(1+a\gamma^2) \qquad (3.35).$$

This function has a sigmoidal shape but, due to the choice of γ^2 in the denominator, the experimental data is overpredicted at low strains and underpredicted at high strains. For a better fit of the data, a function is proposed where the exponent of the shear strain (or the generalized strain tensor invariant) is a material parameter

$$h(\gamma) = 1/(1+a\gamma^b) \qquad (3.36).$$

This form still contains the sigmoidal nature of Eq. (3.35), yet fits the data much better over the entire strain region. The parameter values of the different approximations appear in Table 3.6. The fit according to Eq. (3.36) is shown in Figures 3.25, 3.26 and 3.27. For

Table 3.6. Parameters for the approximation of measured shear strain function.

Approximation Function	Parameters	LDPE 150°C	HDPE 170°C	PS 180°C
$h(\gamma) = f \exp(-n_1\gamma) + (1-f)\exp(-n_2\gamma)$	f	.67	.74	.88
	n_1	.304	.447	.377
	n_2	.070	.098	.073
$h(\gamma) = \frac{1}{1+a\gamma^2}$	a	.043	-	.124
$h(\gamma) = \frac{1}{1+a\gamma^b}$	a	.172	.245	.302
	b	1.39	1.59	1.57

clarity, the comparison between the different forms of strain functional approximations is shown for LDPE and PS in Figures 3.28 and 3.29. The sum of two exponential functions and the sigmoidal functions are found to describe the shear data equally well.

3.2.5.2 Strain and time dependence of correction factor. The correction method for the parallel-disk experiments does not require separability of time and strain dependence as discussed above. The method can actually be used to experimentally check the separability assumption of Eq. (3.33), which is not generally accepted (Vrentas and Graessley, 1982; Menezes and Graessley, 1982). In the following, what is implied about the correction factor, $\chi(t,\gamma_R)$, when one considers the separability assumption, is discussed and the results are compared to the experimental findings.

The apparent relaxation modulus defined in Eq. (3.25) can be re-written substituting Eq. (3.22) for the torque and Eq. (3.33) for $G_s(t,\gamma)$:

$$G_a(t,\gamma_R) = \overset{\circ}{G}(t) \underbrace{\frac{4}{\gamma_R^4}\int_0^{\gamma_R} h(\gamma)\gamma^3 d\gamma}_{f(\gamma_R)} \tag{3.37}$$

It is then factorable into functions of time, $\overset{\circ}{G}(t)$, and of strain, $f(\gamma_R)$. Upon differentiation with respect to γ_R:

$$\frac{\partial \ln G_a(t,\gamma_R)}{\partial \ln \gamma_R} = \underbrace{\frac{\partial \ln \overset{\circ}{G}(t)}{\partial \ln \gamma_R}}_{0} + \frac{\partial \ln f(\gamma_R)}{\partial \ln \gamma_R} \tag{3.38}$$

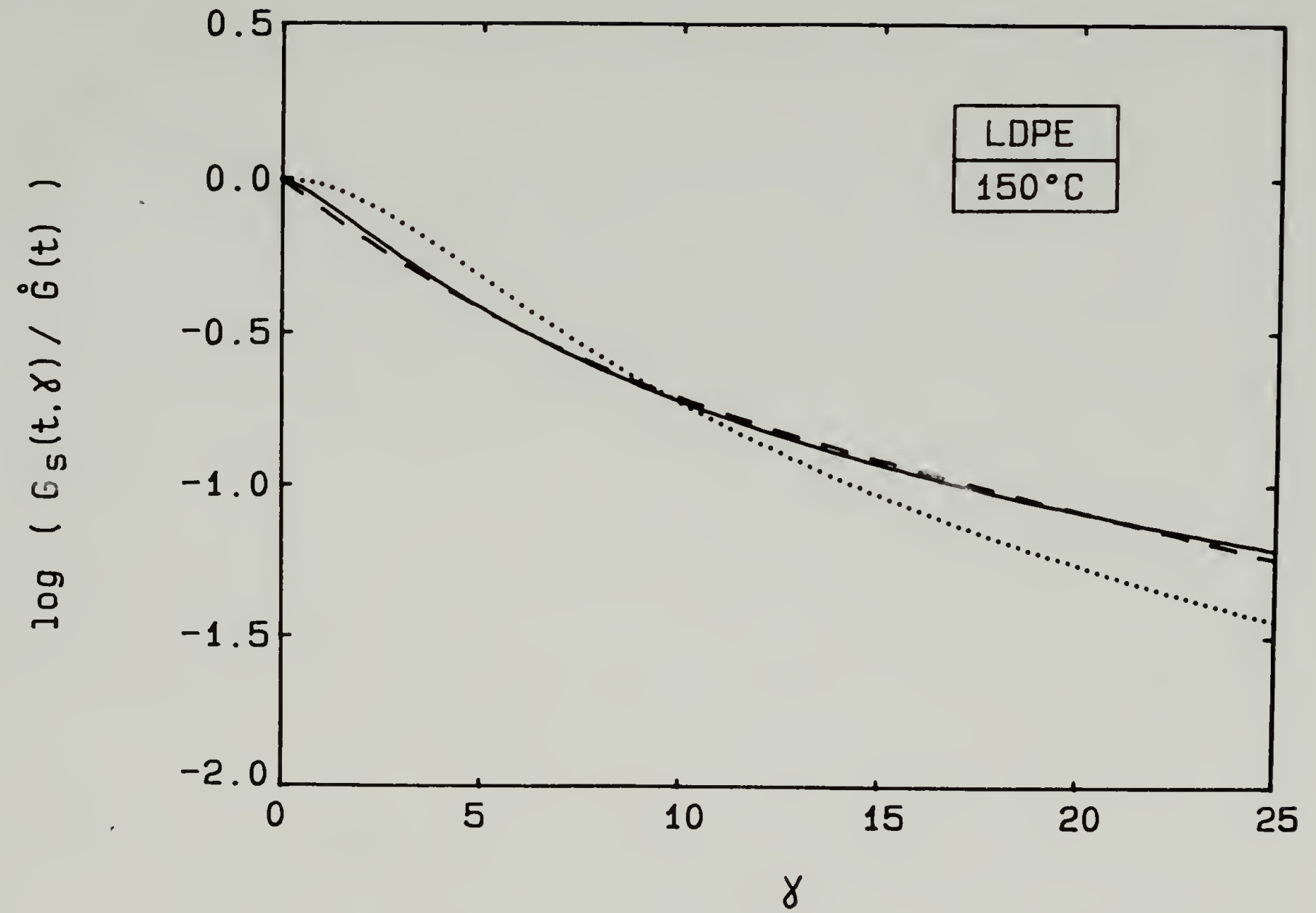

Figure 3.28. Predictions of the shear strain function of LDPE for (----) Eq. (3.34), (····) Eq. (3.35), (——) Eq. (3.36) and the values in Table 3.6.

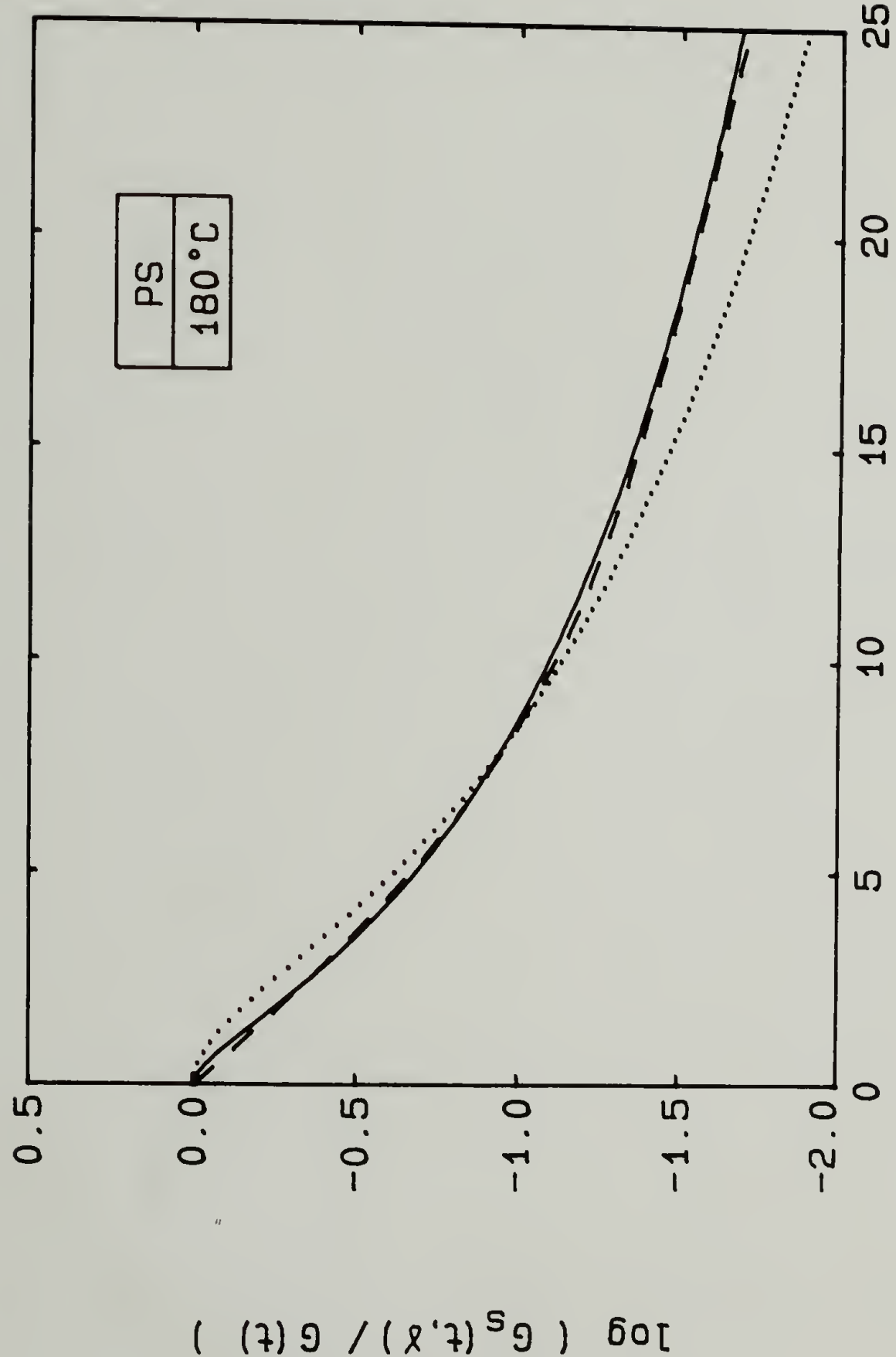

Figure 3.29. Predictions of the shear strain ... in function of PS for (----) Eq. (3.34), (••••) Eq. (3.35), (——) Eq. (3.36) and the values in Table 3.6.

the correction factor, Eq. (3.26)

$$\chi(\gamma_R) = 1 + \frac{1}{4}\frac{d \ln f(\gamma_R)}{d \ln \gamma_R} = h(\gamma_R)\gamma_R^4[4\int_0^{\gamma_R} h\gamma^3 d\gamma]^{-1} \qquad (3.39)$$

is <u>independent of time</u>.

This independence of time is verified experimentally with the data of Figures 3.12 and 3.13. The slope of the curves at various times is the same for a particular strain magnitude. The correction factor for LDPE and PS as a function of strain appears in Figure 3.30 and is seen to be independent of time from 0.5 to 10s. Some deviations at times above 10s were found in the data due to the uncertainty of G_a at long times.

Figure 3.30 also shows that the correction factor qualitatively gives the same information about the strain dependence of the polymer as the strain function (i.e., the PS has a stronger dependence on large shear strains than the LDPE). The independence of χ on time supports the validity of the separability of the relaxation modulus into time and strain dependent functions and also demonstrates that the correction method is applicable to transient experiments of this type.

The parallel-disk geometry has two advantages over the cone-and-plate geometry. First, it allows one to obtain large step strain data from rheometers having a limited angular displacement and secondly, the rise times for the step in strain are very short even at large strains due to the small angular displacement required. With a suitable choice of plate separation, H, the rise time can be made the same for all strains (about 50 ms, see Figure 3.8).

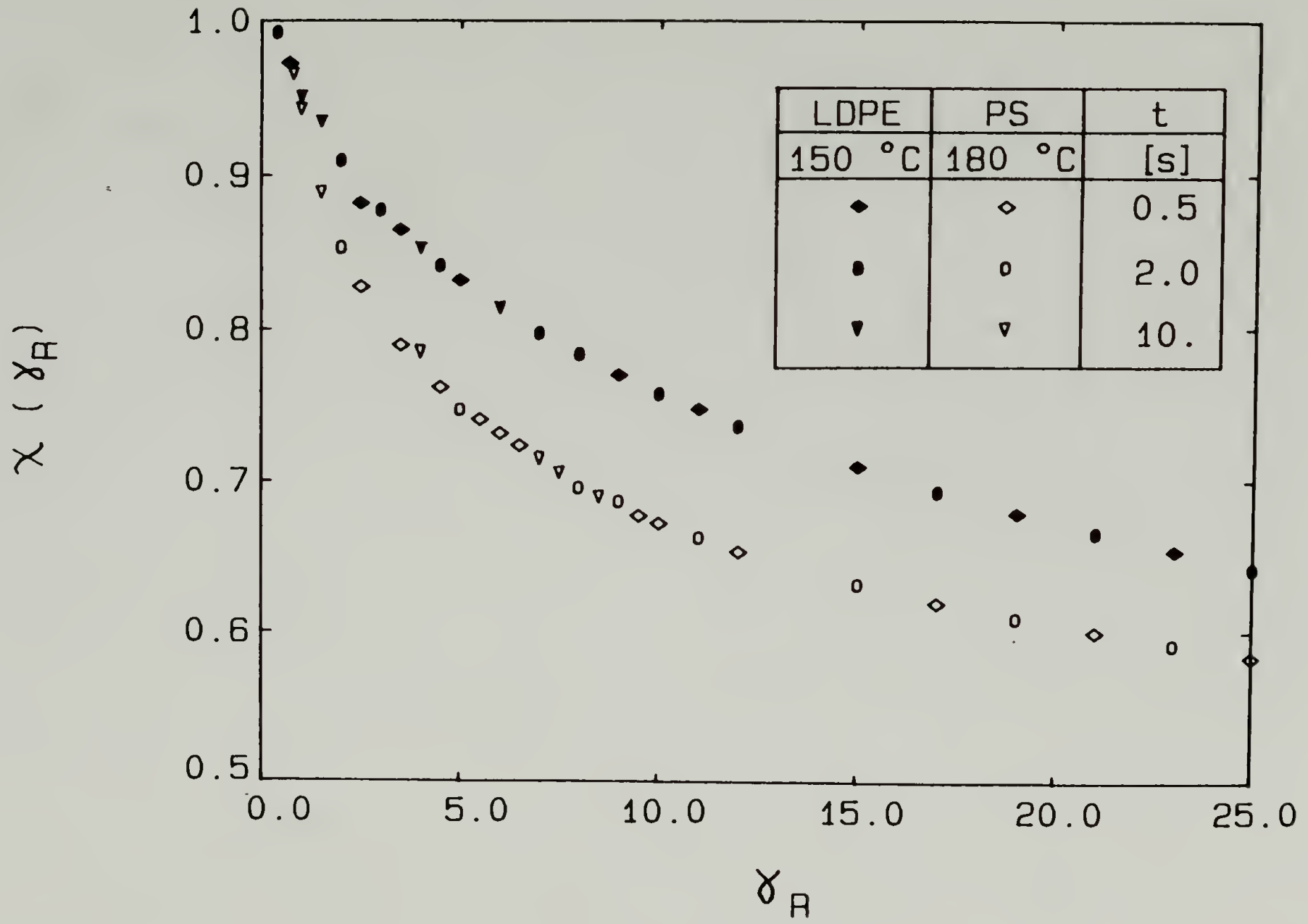

Figure 3.30. Correction factor of parallel disk experiments as a function of strain for LDPE and PS.

3.2.5.3 Predictions of constitutive equation. Once the small strain parameters of Table 3.3 were obtained from linear viscoelastic experiments and the large strain parameters of Table 3.6 were obtained from large step strain experiments, the prediction of the transient and steady state shear viscosities were calculated from the memory integral constitutive equation, Eq. (2.43).

For shear flow at constant volume, the relative Finger strain tensor is given by Eq. (2.12). A start-up experiment with a constant shear rate, $\dot{\gamma}$, is defined by

$$\gamma(t',t) = \begin{cases} \dot{\gamma}(t-t') = \dot{\gamma}s & \text{for } s<t \\ \dot{\gamma}t & \text{for } s\geq t \end{cases} \qquad (3.40)$$

where $s=t-t'$. The transient shear stress is determined from Eqs. (2.43), (2.44) and (2.50) to be

$$\sigma_{21}(t) = \int_0^t \mu(s)h(I(s))\dot{\gamma}s\, ds + \overset{\circ}{G}(t)h(I(t))\dot{\gamma}t \qquad (3.41).$$

The transient shear viscosity

$$\eta_s(t) = \sigma_{21}(t)/\dot{\gamma} \qquad (3.42)$$

was then calculated by numerical integration of Eq. (3.41) for different shear rates. Both the sum of two exponential form, Eq. (3.34) and the sigmoidal form, Eq. (3.36), of the strain function were used to compare their predictions. The predictions of the transient shear viscosity for all three polymers appear in Figures 3.31, 3.32 and 3.33. The solid lines are the predictions of the sigmoidal form of the strain function while the dashed lines are the predictions using the sum of two exponential functions. Both forms of the strain function are seen to correctly

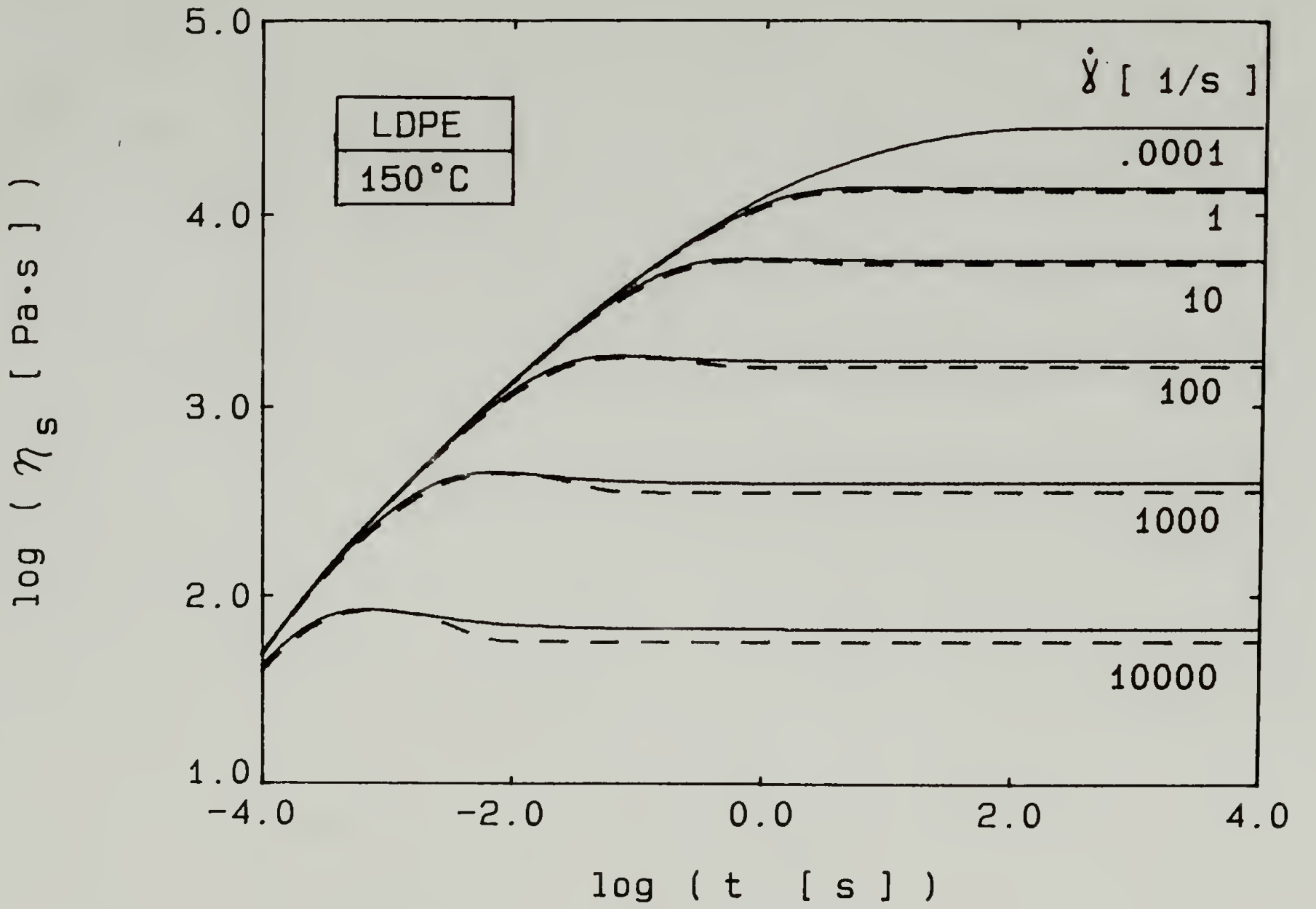

Figure 3.31. Prediction of the transient shear viscosity of LDPE according to Eq. (2.43). (——) using Eq. (3.36), (----) using Eq. (3.34).

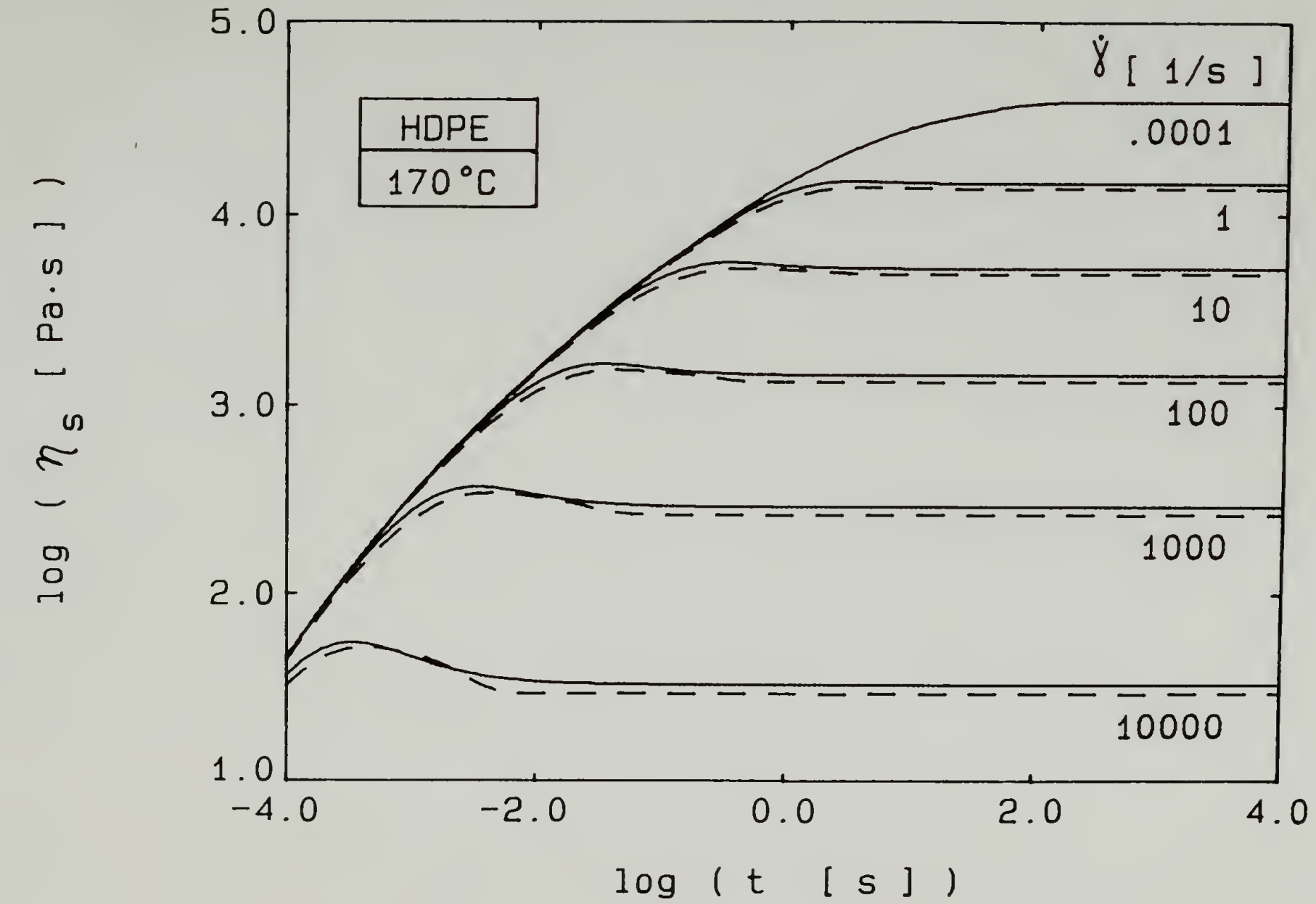

Figure 3.32. Prediction of the transient shear viscosity of HDPE according to Eq. (2.43). (——) using Eq. (3.36), (----) using Eq. (3.34).

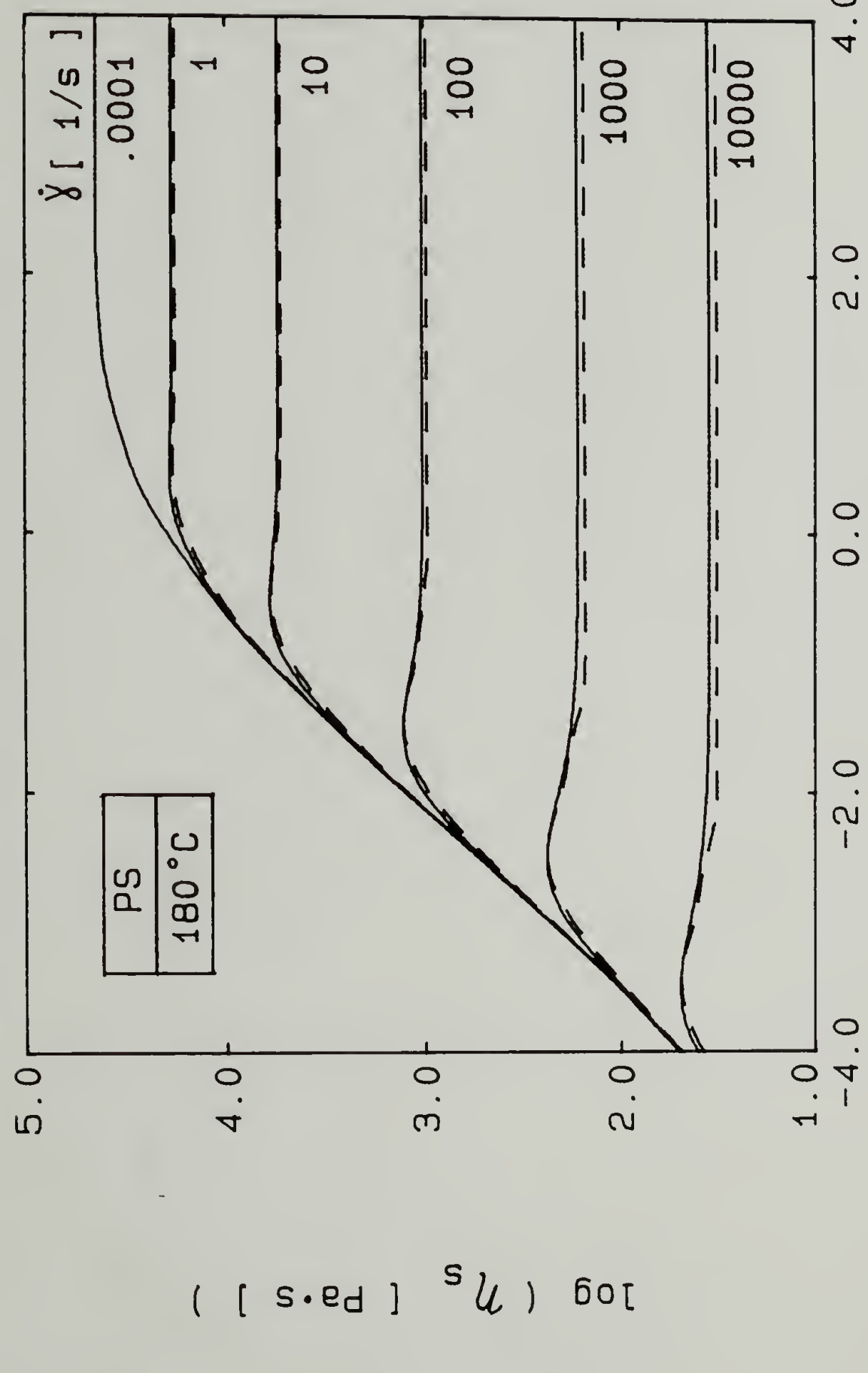

Figure 3.33. Prediction of the transient shear viscosity of PS according to Eq. (2.43). (——) using Eq. (3.36), (----) using Eq. (3.34).

predict a stress overshoot which is observed for many polymer melts and then predict a constant shear viscosity at long times for all three polymers. The exponential form of the strain function predicts a lower transient shear viscosity at each shear rate because the strain function decreases more rapidly at very high strains for an exponential function than for a sigmoidal function.

Although no transient shear data were available for the three polymers to check the predictions of Eq. (2.43) at short and intermediate times, the predictions at long times were compared to the steady state shear viscosities at high shear rates obtained from the capillary flow experiments and the complex viscosities at low and intermediate shear rates obtained in the oscillatory shear experiments through the use of the Cox-Merz relation (Cox and Merz, 1958)

$$\eta_s(\dot{\gamma}) \simeq |\eta^*(\omega)| \quad \text{for } \omega=\dot{\gamma} \tag{3.43}.$$

The experimental data of Table 3.5 and the complex viscosities calculated according to Eq. (3.7) from the data in Figures 3.5, 3.6 and 3.7, along with the steady state predictions from Figures 3.31, 3.32 and 3.33 appear in Figures 3.34, 3.35 and 3.36 for both forms of the strain function. The Cox-Merz relation is seen to be valid for the three polymers studied and both the sigmoidal form (solid lines) and sum of two exponential form (dashed lines) of the strain function describe the steady shear viscosity adequately. Only in the case of the LDPE is the prediction of the steady shear viscosity slightly higher than the experimental data at intermediate shear rates. This seems to affect the annular flow experiments somewhat as will be discussed later.

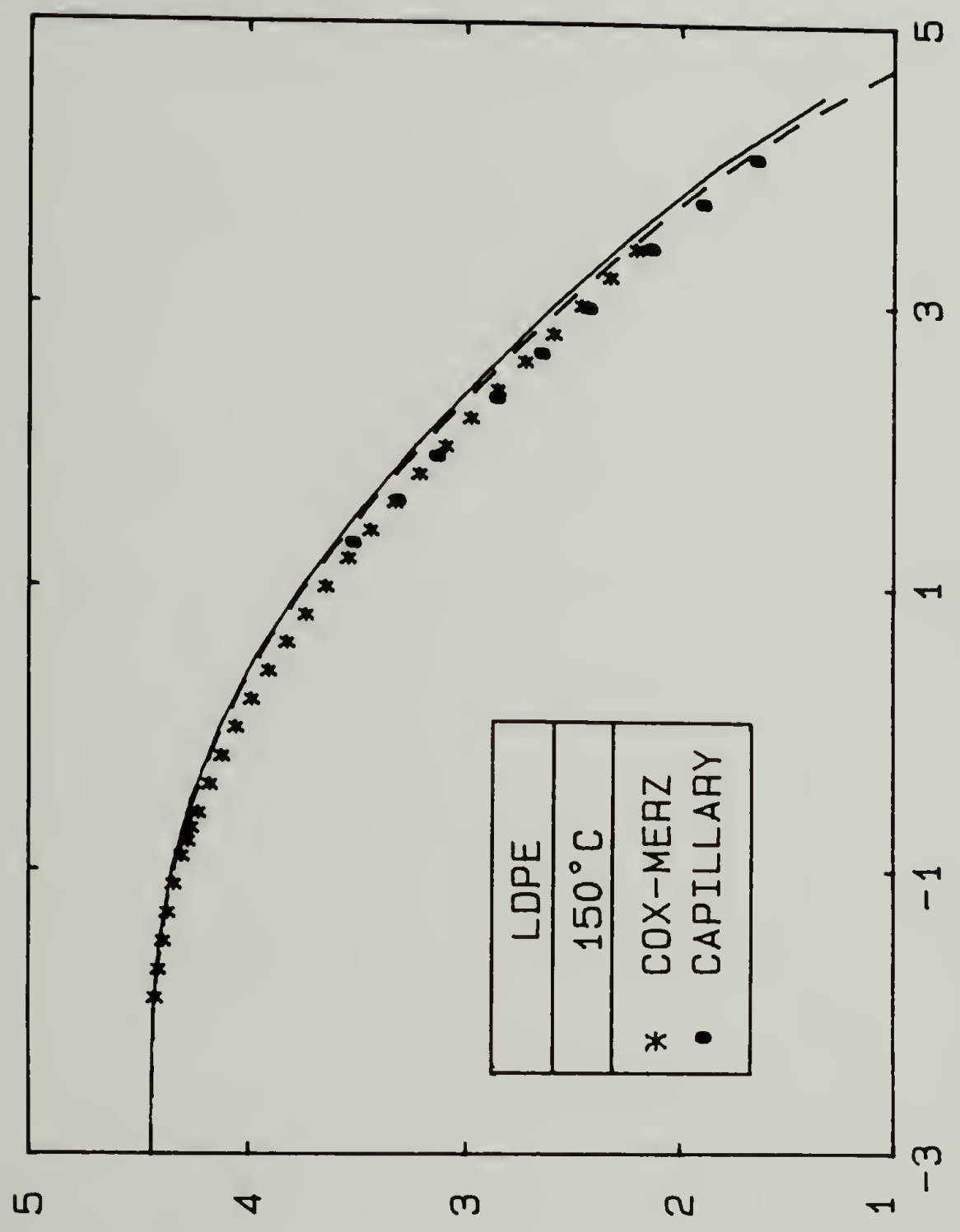

Figure 3.34. Steady shear viscosity of LDPE measured by capillary rheometry and predicted from (a) Cox-Merz relation and (b) Eq. (2.43) with (----) using Eq. (3.34) and (——) using Eq. (3.36).

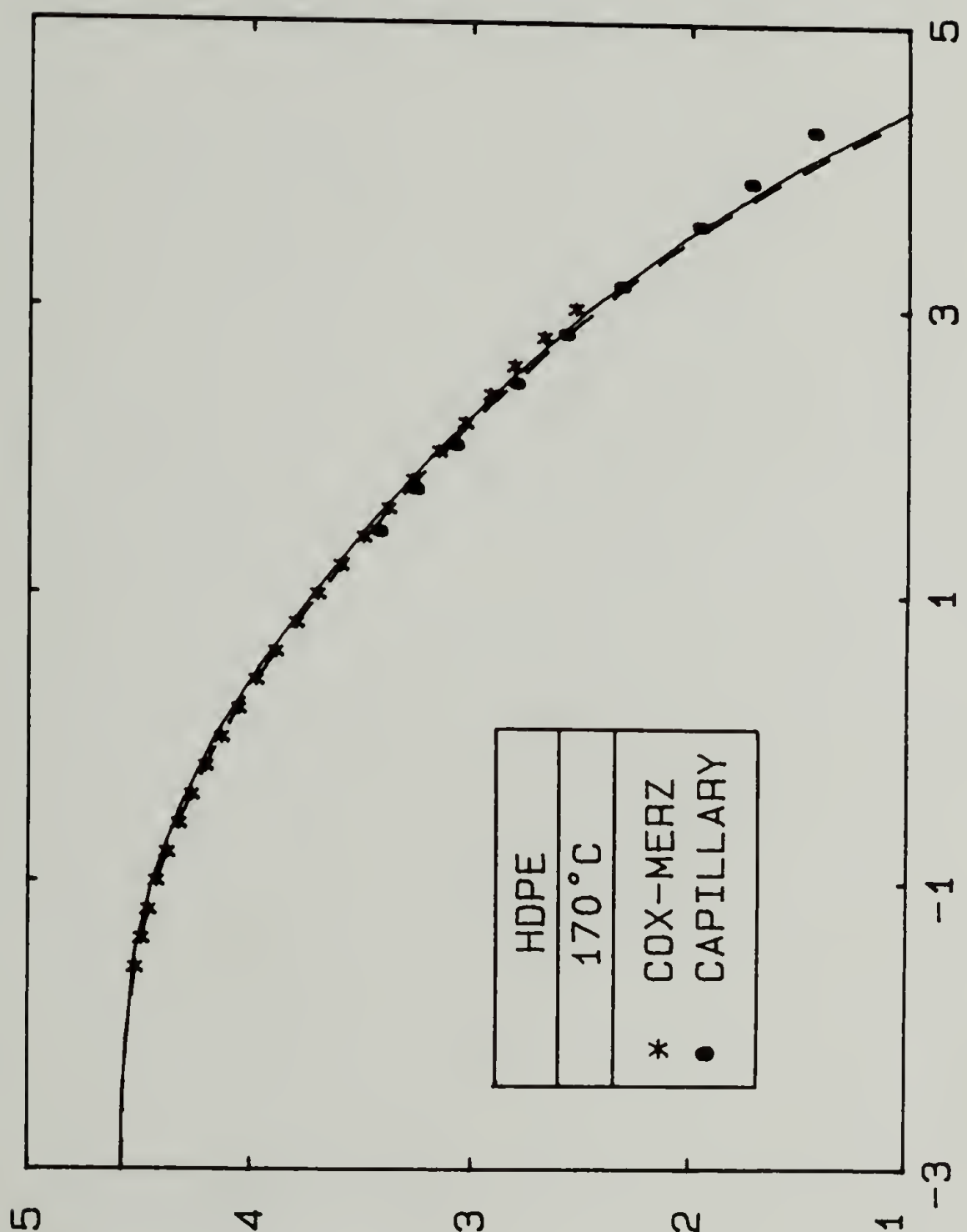

Figure 3.35. Steady shear viscosity of HDPE measured by capillary rheometry and predicted from (a) Cox-Merz relation and (b) Eq. (2.43) with (----) using Eq. (3.34) and (——) using Eq. (3.36).

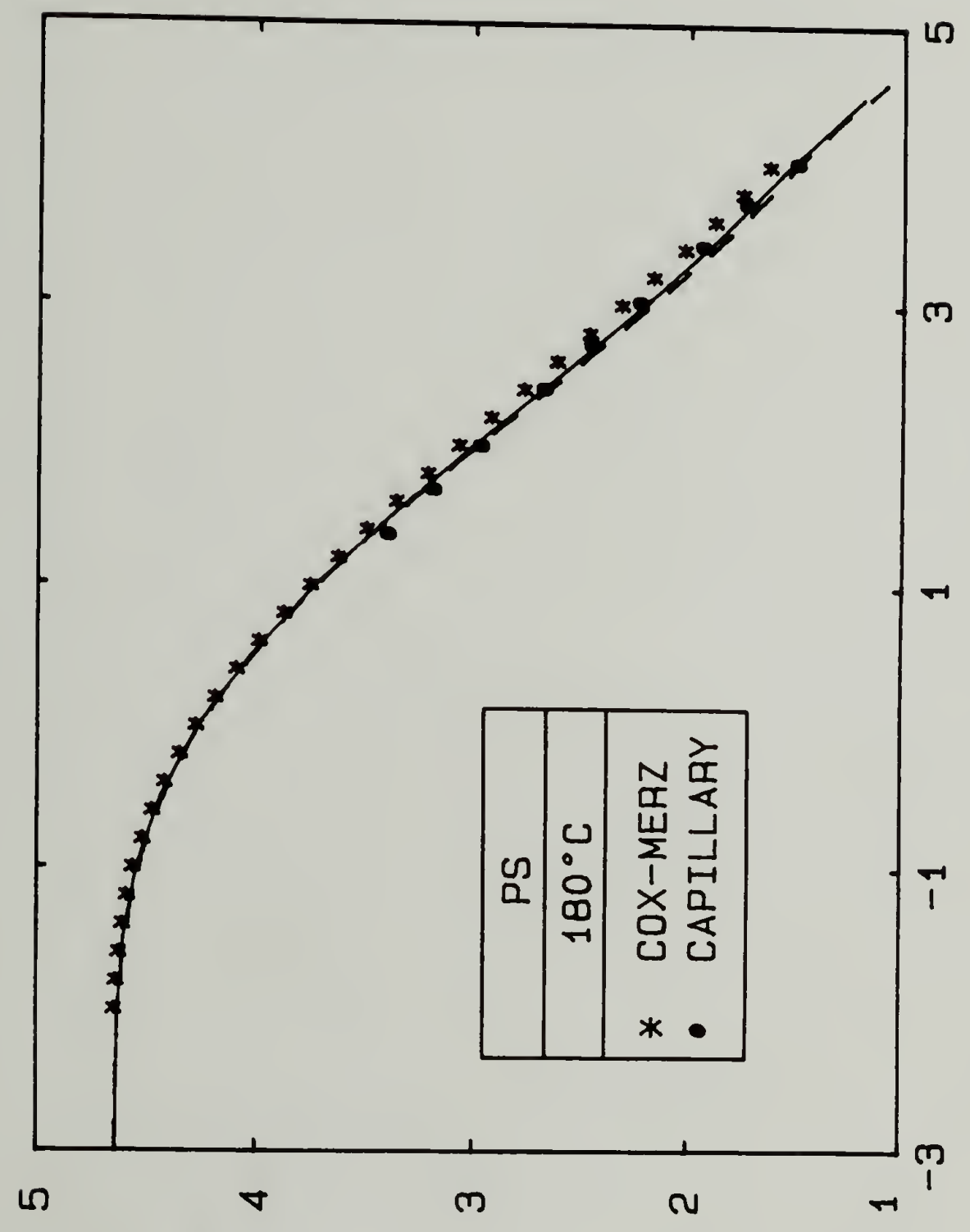

Figure 3.36. Steady shear viscosity of PS measured by capillary rheometry and predicted from (a) Cox-Merz relation and (b) Eq. (2.43) with (----) using Eq. (3.36).

As can be seen from the shear rheometry data, the strain dependent memory integral equation of Eq. (2.43) gives a good description of the shear behavior of polymer melts and with just a few experiments the shear rheology is completely determined. In order to obtain a complete rheological characterization for process modeling, the extensional rheological behavior must also be obtained experimentally.

3.3 Equibiaxial Extensional Rheometry

Research in extensional rheology has occurred primarily in the last two decades and several reviews appear in the literature (Cogswell, 1972; Dealy, 1978; Petrie, 1979). To date four methods have been used to study biaxial extension: sheet inflation, axisymmetric stagnation flow, sheet stretching, and lubricated squeezing. Three of these methods appear in Figure 3.33.

Sheet inflation involves the extension of a thin polymer sheet by means of an inert gas (Denson and Gallo, 1971; Joye et al., 1972 and 1973; Bailey, 1974; Maerker and Schowalter, 1974; DeVries et al., 1977) or a silicon oil (Denson and Hylton, 1980; Rhi-Sausi and Dealy, 1981). A hemi-spherical bubble was inflated by applying gas at different pressure on both sides of a sheet. The deformation was measured optically and the stress in the sheet was determined from the local bubble curvature and the pressure difference. Both the stress and strain rate were changing with time. The use of an incompressible silicon oil as the inflating medium and a control system for the inflation rate has enabled constant rate experiments to be performed using this technique.

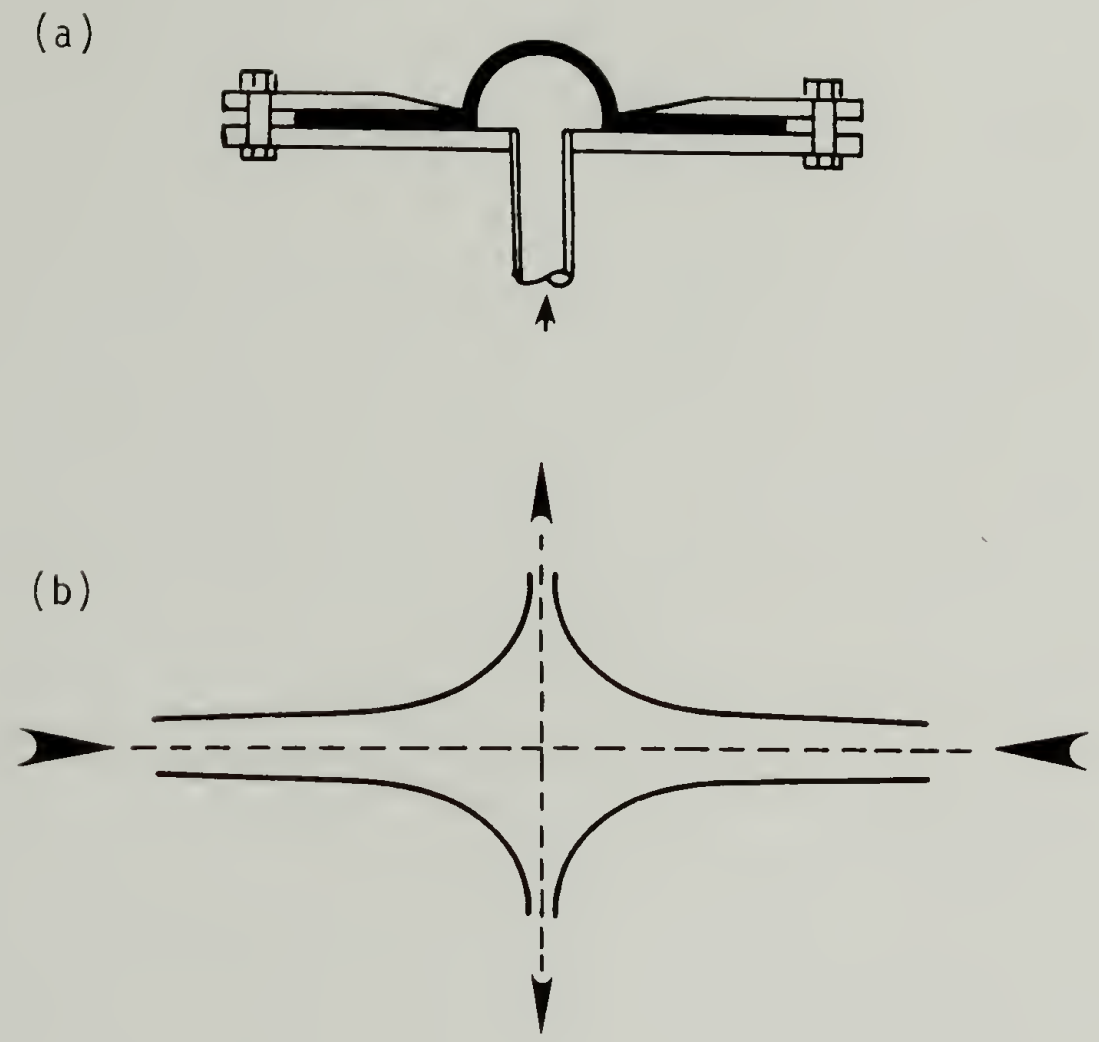

Figure 3.37. Existing biaxial rheometers. (a) Sheet inflation (Joye et al., 1972). (b) axisymmetric stagnation flow (van Aken and Janeschitz-Kriegl, 1980). (c) sheet stretching (Meissner et al., 1981).

Controlled biaxial extension, however, is restricted to the area near the pole of the bubble.

Constant biaxial strain rates were achieved in an axisymmetric stagnation flow device (van Aken and Janeschitz-Kriegl, 1980 and 1981) in which two impinging fluid streams are guided by lubricated trumpet shaped walls (Winter et al., 1979). Flow birefringence was measured in the plane of symmetry and the force which tended to separate the trumpets was measured simultaneously. Polystyrene melts were investigated at constant strain rates.

A sheet stretching device consisting of eight rotary clamps has also been used to obtain biaxial extensional data (Stephenson and Meissner, 1980; Meissner et al., 1981). The biaxial deformation with this device is homogeneous throughout the sample. Constant strain rate data for polyisobutylene at room temperature have been reported. High temperatures, as needed for polymer melt rheology, are difficult to obtain and to control due to the design of the rheometer.

These techniques require very sophisticated equipment, large samples, careful sample preparation, and are limited to certain temperature ranges. The experiments are also limited to constant stress and/or constant strain rates.

Recently, the lubricated squeezing technique has been developed to generate equibiaxial extensional flow (Chatraei et al., 1981; Frank, 1983). A small sample of viscous material is compressed between two lubricated parallel disks as shown in Figure 3.38. This technique has the advantages of simple geometry, small sample size, fast experiments,

LUBRICATED SQUEEZING
BETWEEN PARALLEL DISKS

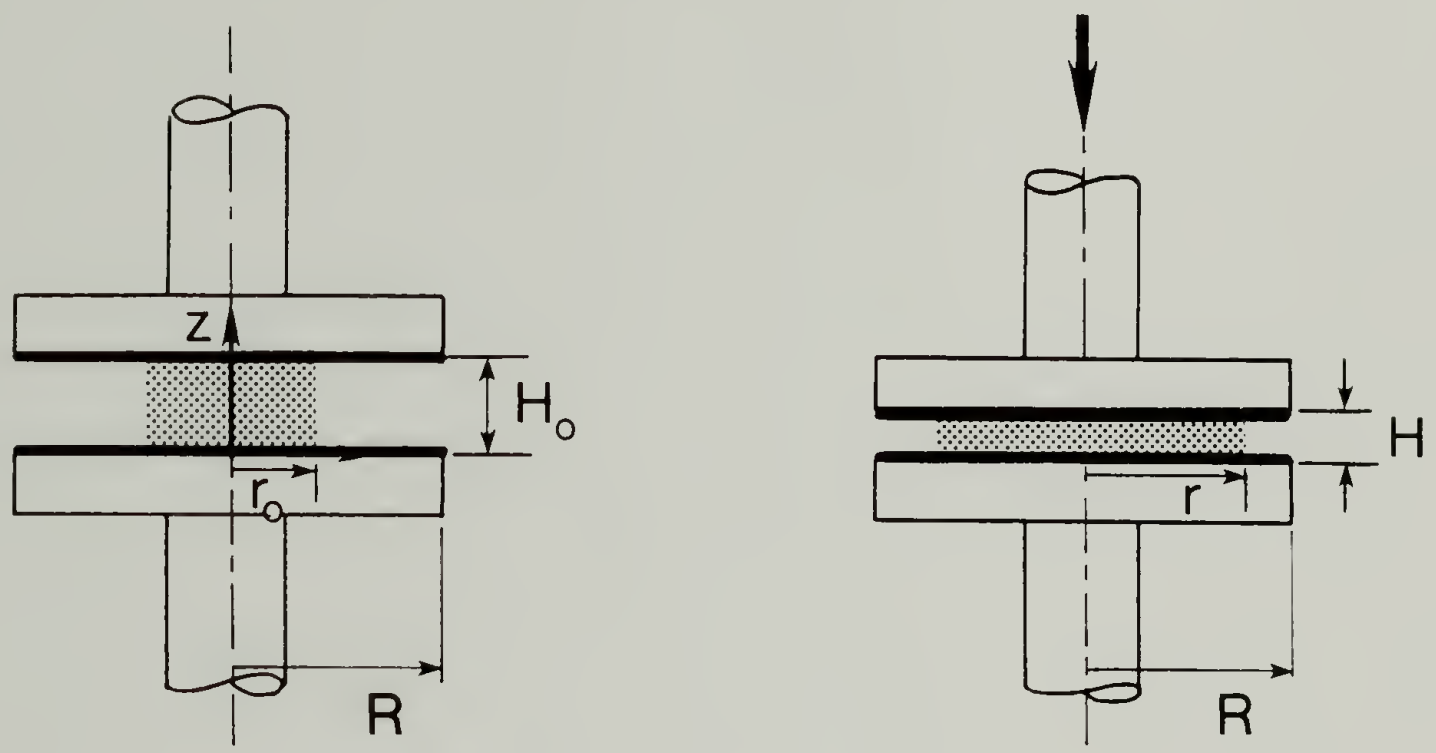

Figure 3.38. Sketch of lubricated squeezing geometry.

and a broad range of temperature control. Another important advantage and a main focus of this dissertation is the ability to perform step strain in equibiaxial extension (Papanastasiou et al., 1983) in addition to constant stress and constant strain rate experiments. The equibiaxial extensional step strain experiment is discussed next.

3.3.1 Step Strain in Equibiaxial Extension

Just as in the step shear experiment, a test sample is placed into the rheometer and the system is kept at rest until the sample is completely relaxed to the stress free state. At time t=0, a finite extensional strain is "instantaneously" applied and held constant thereafter. The resulting normal stress difference is measured as it relaxes with time. The result of the measurement is the time and strain dependent extensional relaxation modulus

$$G_e(t,\varepsilon_a) = \frac{[\sigma_{11}-\sigma_{22}](t,\varepsilon_a)}{C_{11}^{-1} - C_{22}^{-1}} = \frac{\sigma_{11}-\sigma_{22}}{e^{2\varepsilon_a}-e^{-\varepsilon_a}} \qquad (3.44).$$

If the strain is a compression (equibiaxial extension) then the extensional relaxation modulus can be written in terms of the equibiaxial extensional strain as defined in Eq. (2.25):

$$G_e(t,\varepsilon_b) = \frac{\sigma_{11}-\sigma_{22}}{e^{-4\varepsilon_b}-e^{2\varepsilon_b}} \qquad (3.45).$$

In the limit of small strain, the extensional relaxation modulus and the shear relaxation modulus become equal to the relaxation modulus of linear viscoelasticity, Eq. (2.42),

$$\lim_{\varepsilon_b \to 0} G_e(t,\varepsilon_b) = \frac{\sigma_{22}-\sigma_{11}}{6\varepsilon_b} = \lim_{\gamma \to 0} G_s(t,\gamma) = \mathring{G}(t) \qquad (3.46).$$

This relation allows the novel extensional flow experimental results to be checked against the small strain shear data of Section 3.2.

As mentioned in Section 3.2.5, the strain dependent network theory for polymer melts suggests that the relaxation modulus can be factored into time and strain dependent functions. The shear data of Section 3.2.4.2 support this assumption as well as other data in the literature (Laun, 1978; Lin, 1984). However, no step strain data were available for testing the separability assumption in extensional flow. Due to the inability of uniaxial extensional rheometers to reliably produce a rapid step in extensional strain, no uniaxial step strain data exist, so Wagner (1978) used a different method to obtain data for the extensional strain function. An extensional strain function was calculated from uniaxial extensional stress-growth experiments at constant rate of strain by differentiation and subsequent integration of the constitutive equation of Eq. (2.43). The extensional strain function obtained by this method was found to depend not only on the extensional strain but also slightly on the rate of extension.

With lubricated squeezing, a method is now available to perform step strain experiments in equibiaxial extension and determine the extensional strain function directly. If the separability assumption holds, the extensional relaxation modulus can be decomposed

$$G_e(t,\varepsilon_a) = \overset{\circ}{G}(t)h_e(\varepsilon_a),\ h_e \leq 1 \tag{3.47}$$

in the same manner as the shear relaxation modulus was in Eq. (3.33).

As a test of the separability assumption, the extensional relaxation modulus and the shear relaxation modulus should have the same shape (i.e., the ratio of the moduli is independent of time). This will be discussed further along with the experimental results.

A sketch of the lubricated squeezing test geometry is shown in Figure 3.38. A disk-shaped sample of polymer is placed between two lubricated parallel disks. Assuming that the material is incompressible and that the deformation is homogeneous (i.e., the shear deformation occurs only in the lubricant layer and the polymer melt undergoes only equibiaxial extensional flow), the axisymmetric strain rate and strain are

$$\dot{\varepsilon}_a = \frac{1}{H}\frac{dH}{dt} \tag{3.48}$$

and

$$\varepsilon_a = \ln(H/H_o) \tag{3.49}$$

where H_o,H are the initial and instantaneous sample thicknesses respectively. The equibiaxial strain, ε_b, is obtained from Eq. (2.25). The normal stress difference is obtained from the relations

$$\sigma_{rr} - \sigma_{zz} = F/(\pi r^2(t)) \quad \text{for } r \leq R \quad \text{(partial filling)} \tag{3.50}$$

$$\sigma_{rr} - \sigma_{zz} = F/\pi R^2 \quad \text{for } r \geq R \tag{3.51}$$

where F is the force on the disks, r is the instantaneous sample radius and R is the radius of the disks.

The instantaneous sample radius is determined assuming constant density:

$$r(t) = r_o[H_o/H(t)]^{1/2} \tag{3.52}$$

where r_o=r(t=0).

3.3.2 Experimental Procedure and Results

A linear rheometer (Rheometrics RDS-LA) was used for the experiments. The rheometer has a linear motor mounted for vertical displacement on which various test fixtures can be attached. Disks of 25 mm and 10 mm diameter were used. The test fixtures are surrounded by an air-convection oven and temperatures up to 250°C are easily obtainable. The temperature can be controlled to ±0.5K. A transducer with selectable nominal ranges of .1 Nm, .2 Nm and .5 Nm was used to measure the axial forces. A microprocessor controls the strain signal to the motor. A data handling system stores the measurement of the resulting strain and force for subsequent analysis.

Silicon oils (General Electric, "Viscasil" silicones) were used as the lubricating medium. The choice of a suitable lubricant is essential in generating a homogeneous extensional deformation. The ratio of zero shear viscosities between sample and lubricant was the criterion for selecting a suitable lubricant. A ratio of 500 to 1000 seems to give the best lubrication (Tovstiga, 1983). Polymer and lubricant viscosities appear in Figure 3.39. Viscasil 600K was used as the lubricant for PS while Viscasil 300K was used for both LDPE and HDPE.

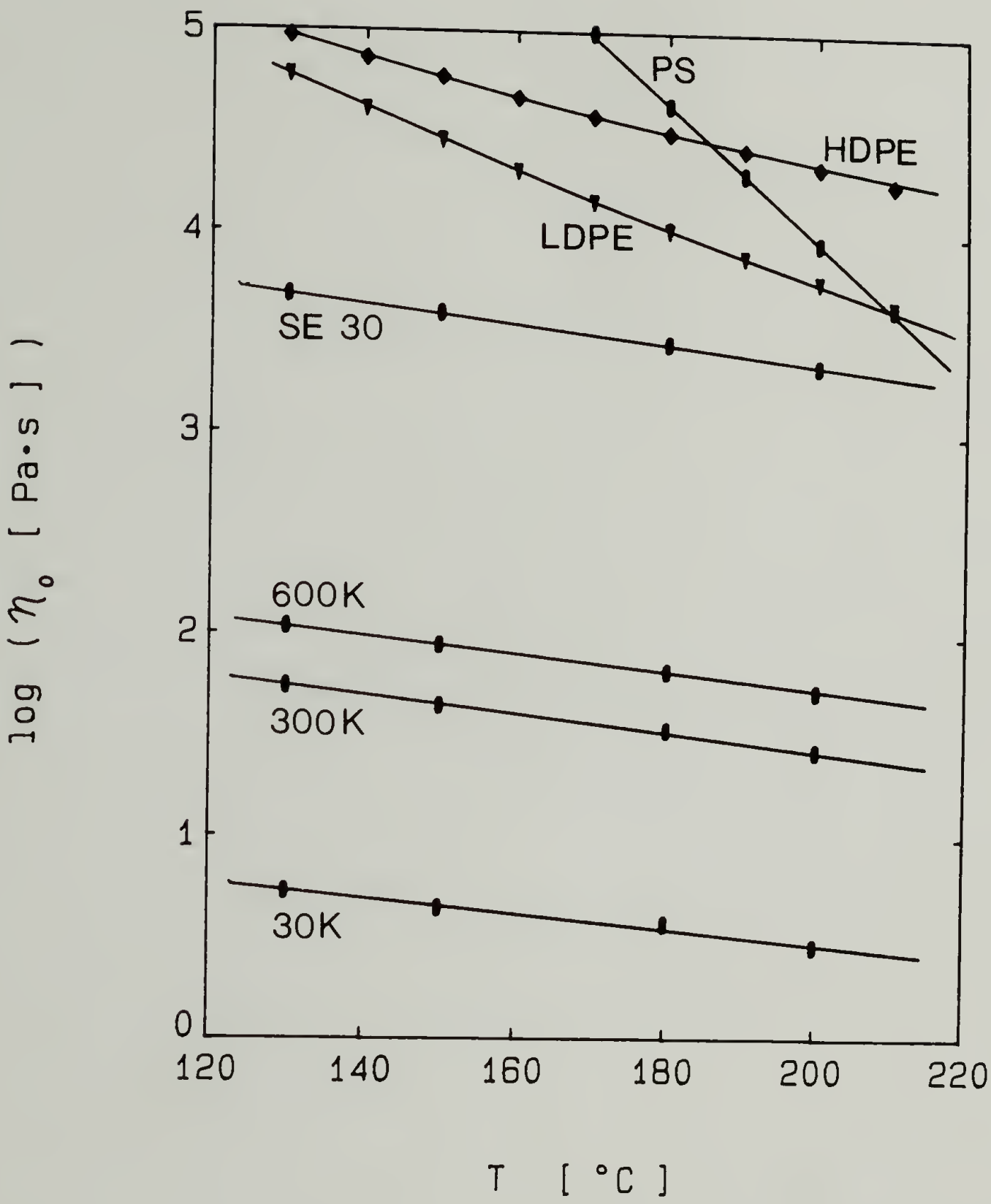

Figure 3.39. Zero shear viscosities of polymer samples and lubricants as a function of temperature.

The actual experiments proceeded as follows. The parallel disk fixtures were heated to the desired temperature, the oven was opened and a layer of lubricant approximately 0.06 mm thick was applied to the top and bottom disks by means of a wooden spatula. The lubricant layer was about 1% of the sample thickness. The sample thickness can therefore be approximated by the separation of the disks. The polymer sample (consisting of two preformed disks, stacked to give a total initial sample thickness, $H_o \sim 5mm$) was centered on the bottom disk and the top disk was lowered until it just contacted the sample. The sample was heated to the desired temperature and held there for at least five minutes before the test was started to ensure complete melting and relaxation of any residual stresses present due to the sample preparation. The initial disk separation, H_o, was measured and the test begun. The resulting transient axial force was then recorded.

Two types of experiments were performed: (1) stress relaxation after a step in equibiaxial extensional strain and (2) stress growth at constant equibiaxial extension rate.

3.3.2.1 Equibiaxial step strain. Stress relaxation experiments after a step in equibiaxial extensional strain were performed up to $\varepsilon_b = 2.3$. The 25 mm disks were used for $\varepsilon_b < 0.47$ and the 10 mm disks for $0.35 < \varepsilon_b < 2.30$. The equibiaxial extensional strain was measured by removing the deformed sample after the stress had relaxed to below the accuracy of the force transducer (after approximately 200 s), wiping any remaining lubricant from the disk surfaces, bringing the disks into

contact, and measuring the change in disk displacement after the temperature re-equilibrated to the test value.

For the step strain experiment, a rapid rise time is desired in order to avoid corrections to the resultant stress relaxation (Laun, 1978). The motor response for a step in strain was extremely fast as seen in Figure 3.40. Rise times of less than 0.20 ms were obtained for even the highest strain of ε_b=2.3. Rise times of this magnitude do not significantly affect the stress response at $t \geq 0.4$ s. These rise times are considerably faster than those obtained in shear step strain experiments, see Figure 3.8.

The stress response after various steps in strain is shown in Figures 3.41, 3.42 and 3.43. The horizontal regions at short times are due to the force transducer range being exceeded at the start of the experiments. Even though the transducer range was exceeded during some tests, there was not an appreciable offset at long times. However, at long times and small strains, some scatter in the data occurs due to the inaccuracy of the transducer at force levels less than 5×10^{-4} Nm. This scatter is more pronounced for the LDPE than for HDPE or PS. For $\varepsilon_b > 1.6$, the effectiveness of the lubrication is seen to diminish as evidenced by the very high force levels at short times and abrupt dips in the force at longer times. Also any slight disk movements at very high strains, $(H_o-H)/H_o > 0.96$, showed up as instabilities in the force measurements. Therefore, due to the limits of the transducer range and the loss of effective lubrication, stress relaxation data over two time

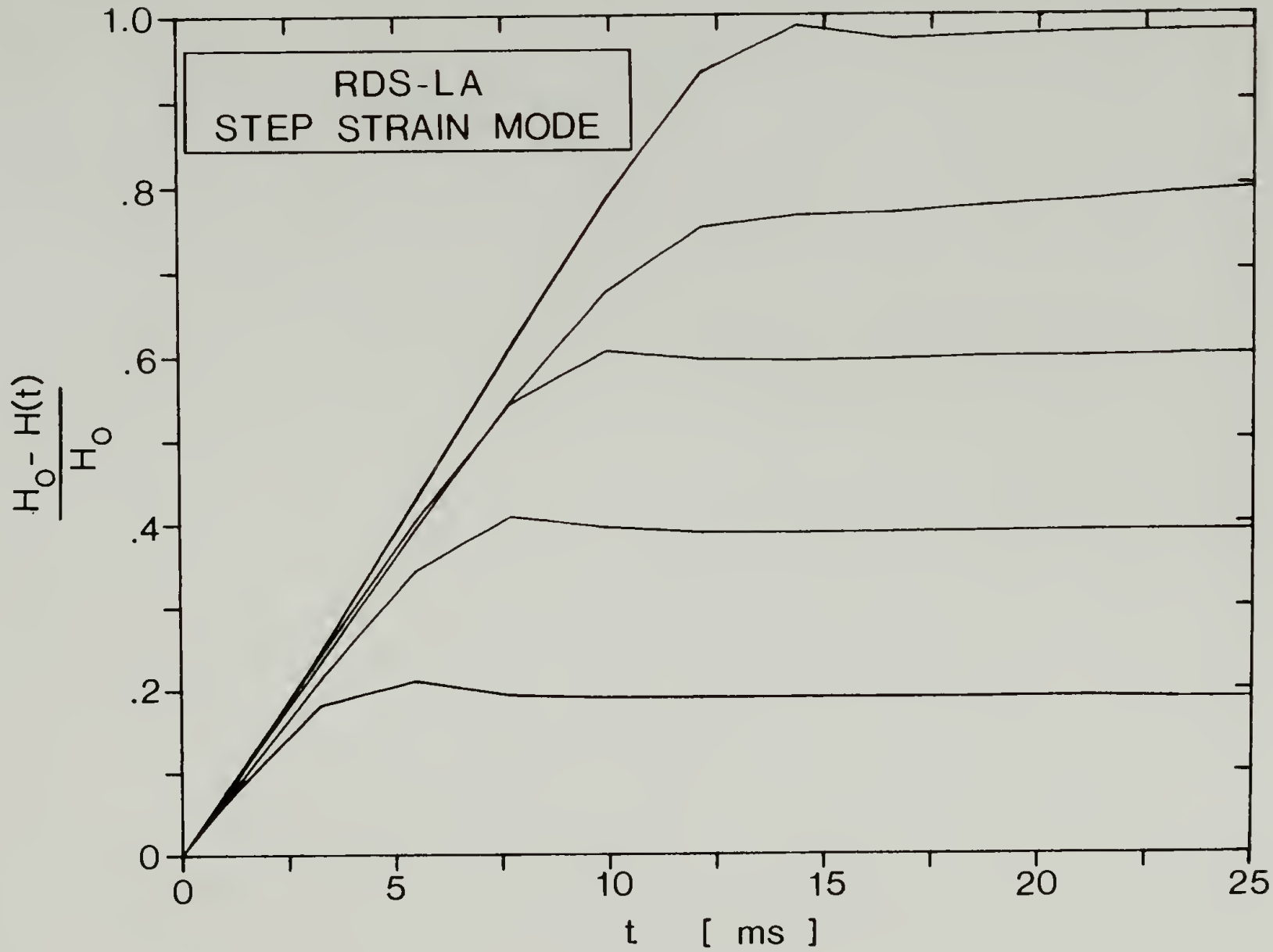

Figure 3.40. Measured plate separation as a function of time for step strain experiment on RDS-LA.

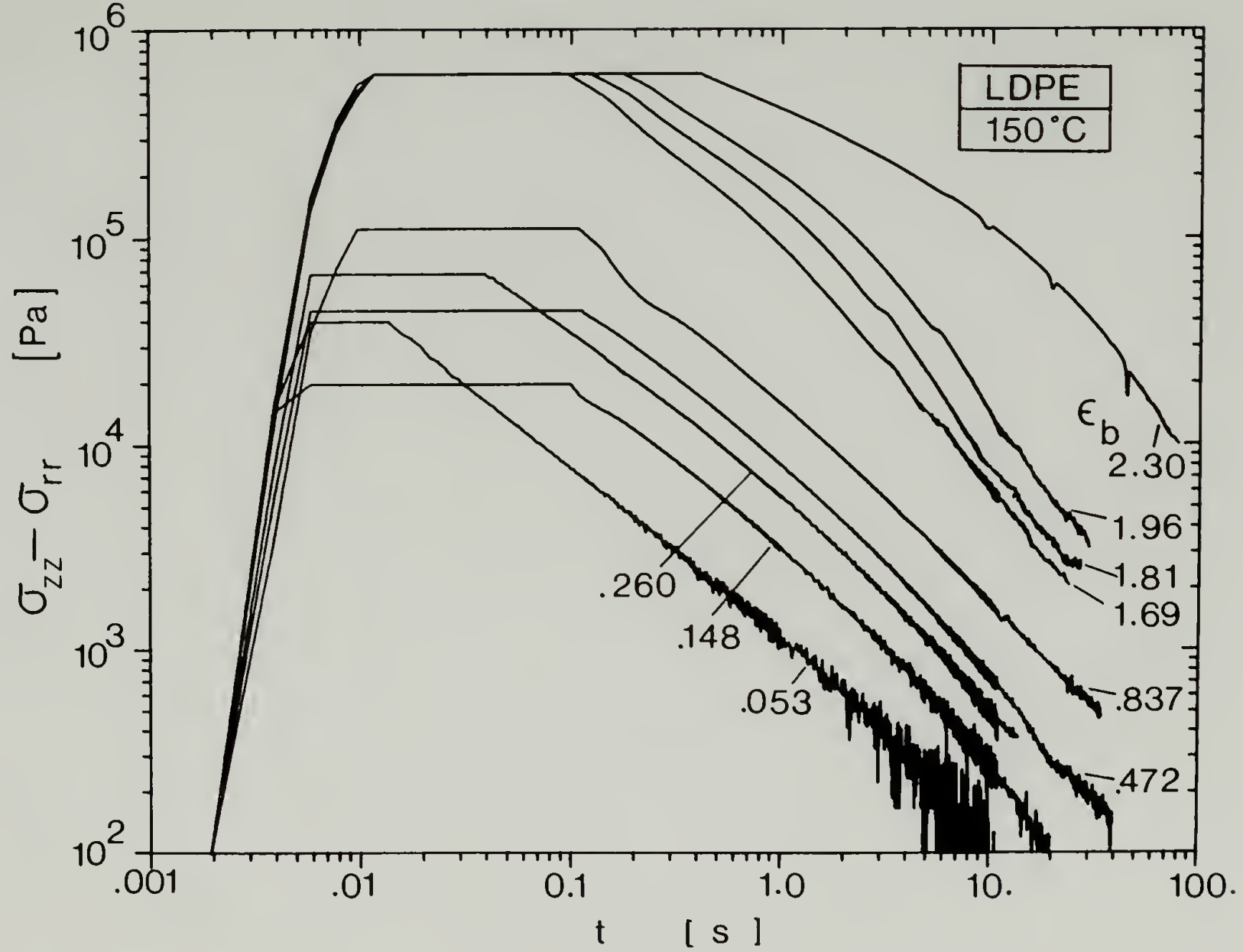

Figure 3.41. Transient stress relaxation measured by RDS-LA for LDPE.

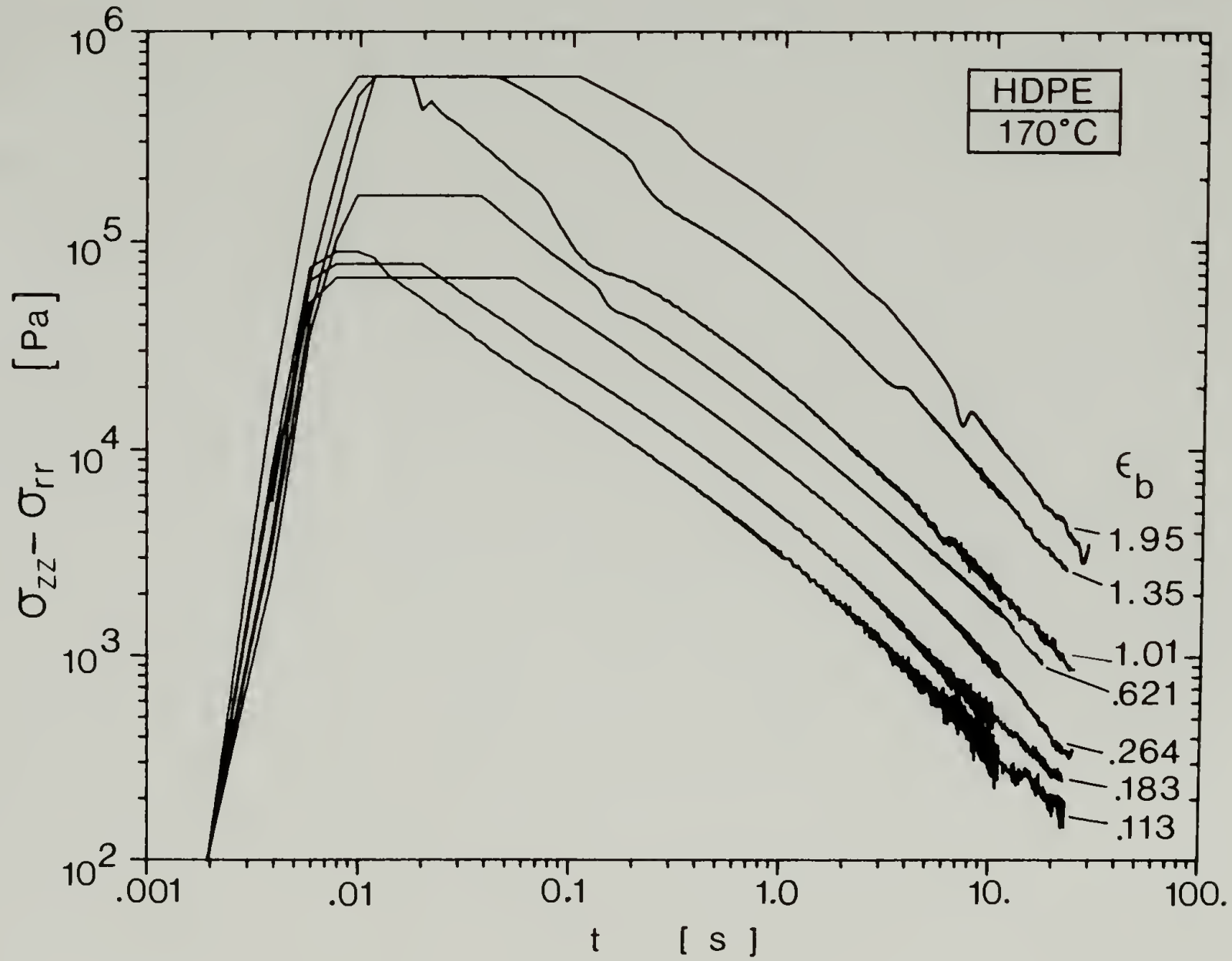

Figure 3.42. Transient stress relaxation measured by RDS-LA for HDPE.

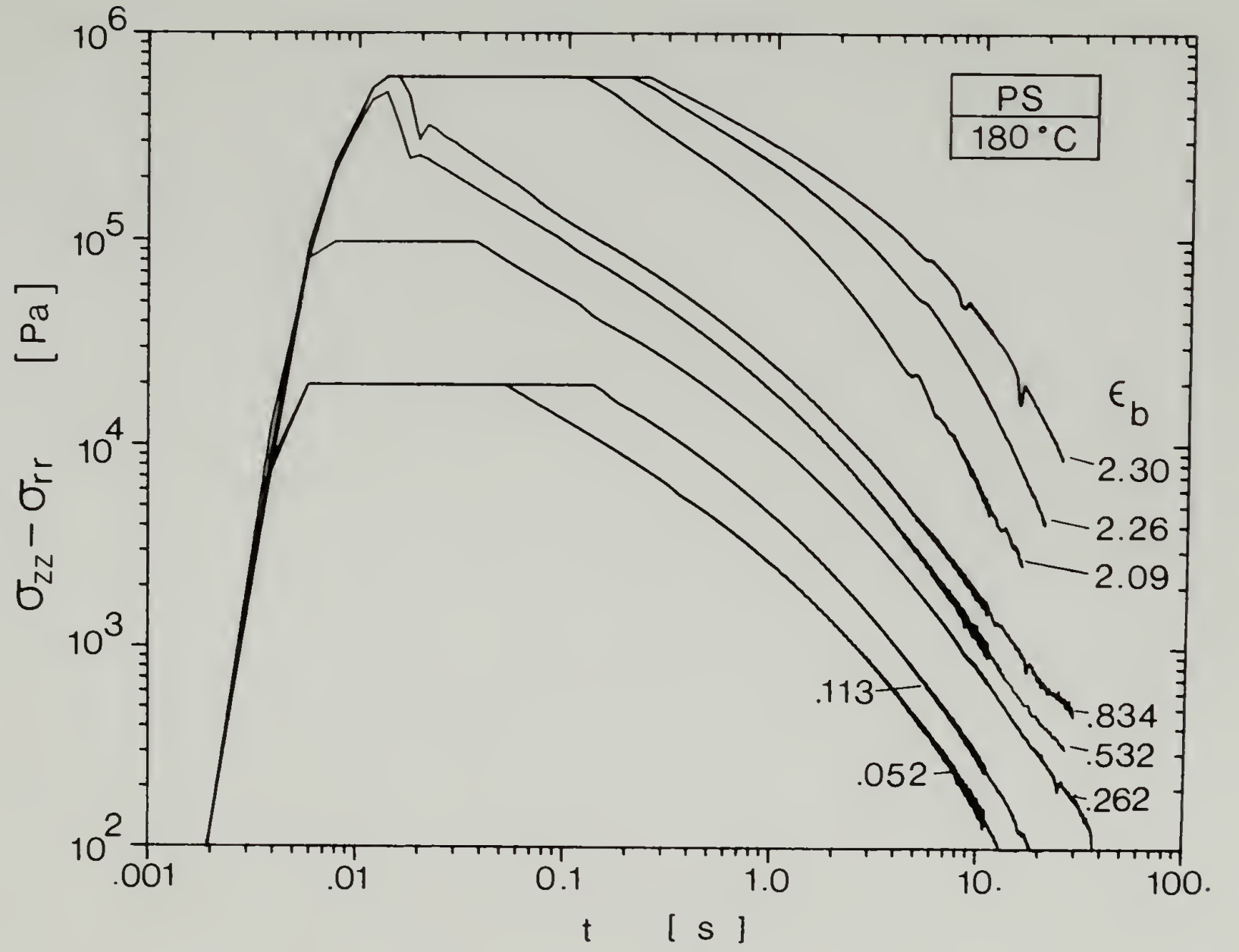

Figure 3.43. Transient stress relaxation measured by RDS-LA for PS.

decades, $0.1 \leq t \leq 10$ s, and for strains $\varepsilon_b \leq 1.5$ were considered reliable.

The transient strain dependent extensional relaxation modulus was calculated from Eq. (3.45) and the measured transient stress relaxation at various equibiaxial strains of Figures 3.41, 3.42 and 3.43. The results appear in Figures 3.44, 3.45 and 3.46 where only the data at a few strains are presented for clarity. The solid line in Figures 3.44, 3.45 and 3.46 is the relaxation modulus of linear viscoelasticity as calculated from Eq. (2.42) and the relaxation spectrum of Table 3.3. The data clearly show that, indeed, the extensional relaxation modulus is equal to the linear viscoelastic relaxation modulus as the equibiaxial strain approaches zero.

3.3.2.2 Constant extension rate. Stress growth at constant equibiaxial strain rate experiments were also performed. In order to generate a constant rate in the lubricated squeezing experiment, the disks must approach each other in a logarithmic manner based on the initial separation of the disks, see Eqs. (3.48) and (3.49). A substantial discrepancy was found between the actual strain and the prescribed strain for any particular prescribed extension rate. The actual strain is obtained from the actual disk separation ($\ln(H/H_o)$) while the prescribed strain is obtained from the prescribed extension rate at a particular time, ($\dot{\varepsilon}_b t$), see Figure 3.47. This problem in the motor displacement response prohibits the attainment of a constant extension rate without some modification of the experimental procedure. This deviation from constant extension rate is especially severe at higher strains and is due to the incorrect programming of the motor displacement based on the

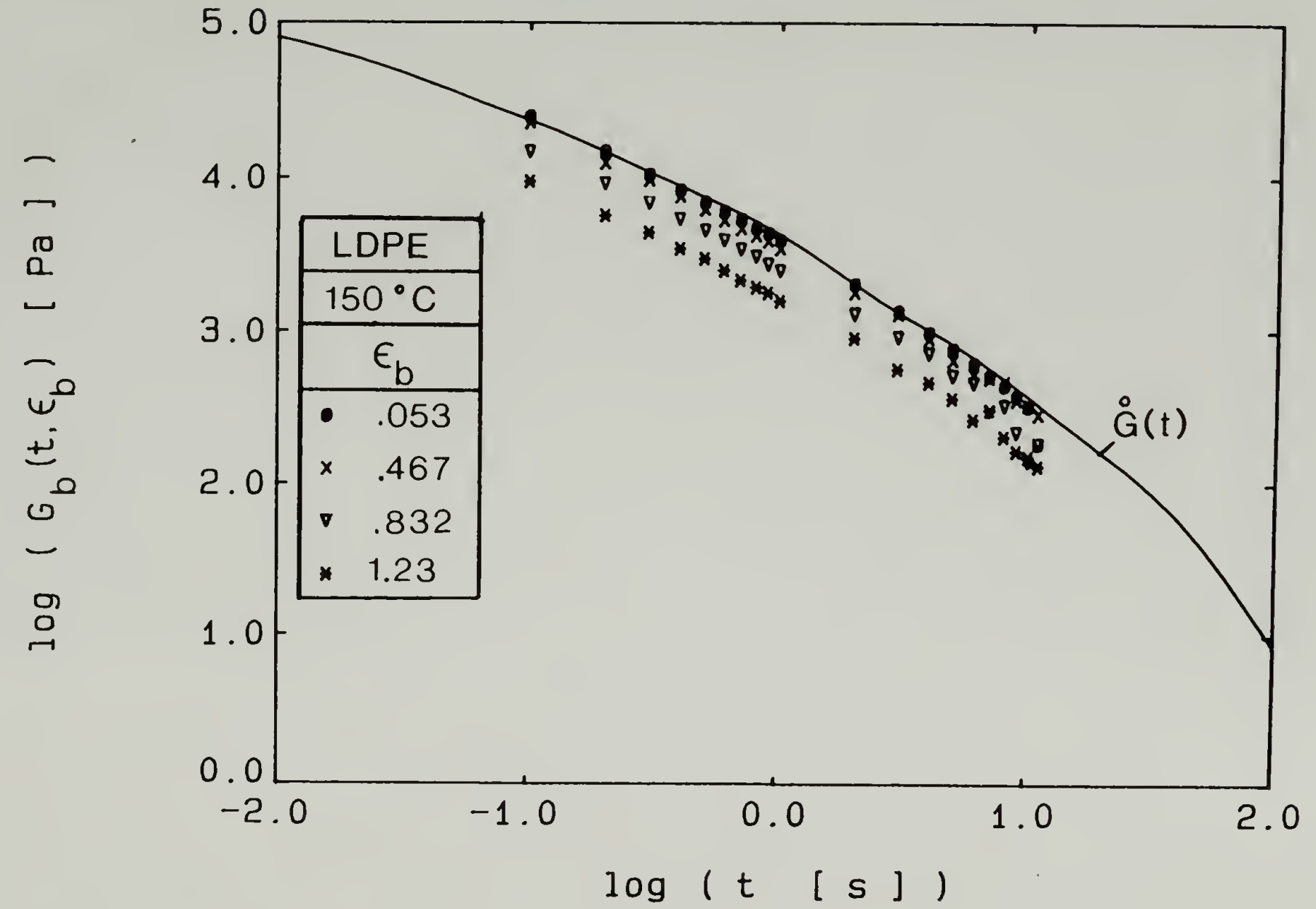

Figure 3.44. Transient extensional relaxation modulus of LDPE. The solid line is $\mathring{G}(t)$ calculated from Eq. (2.42) using the values in Table 3.3.

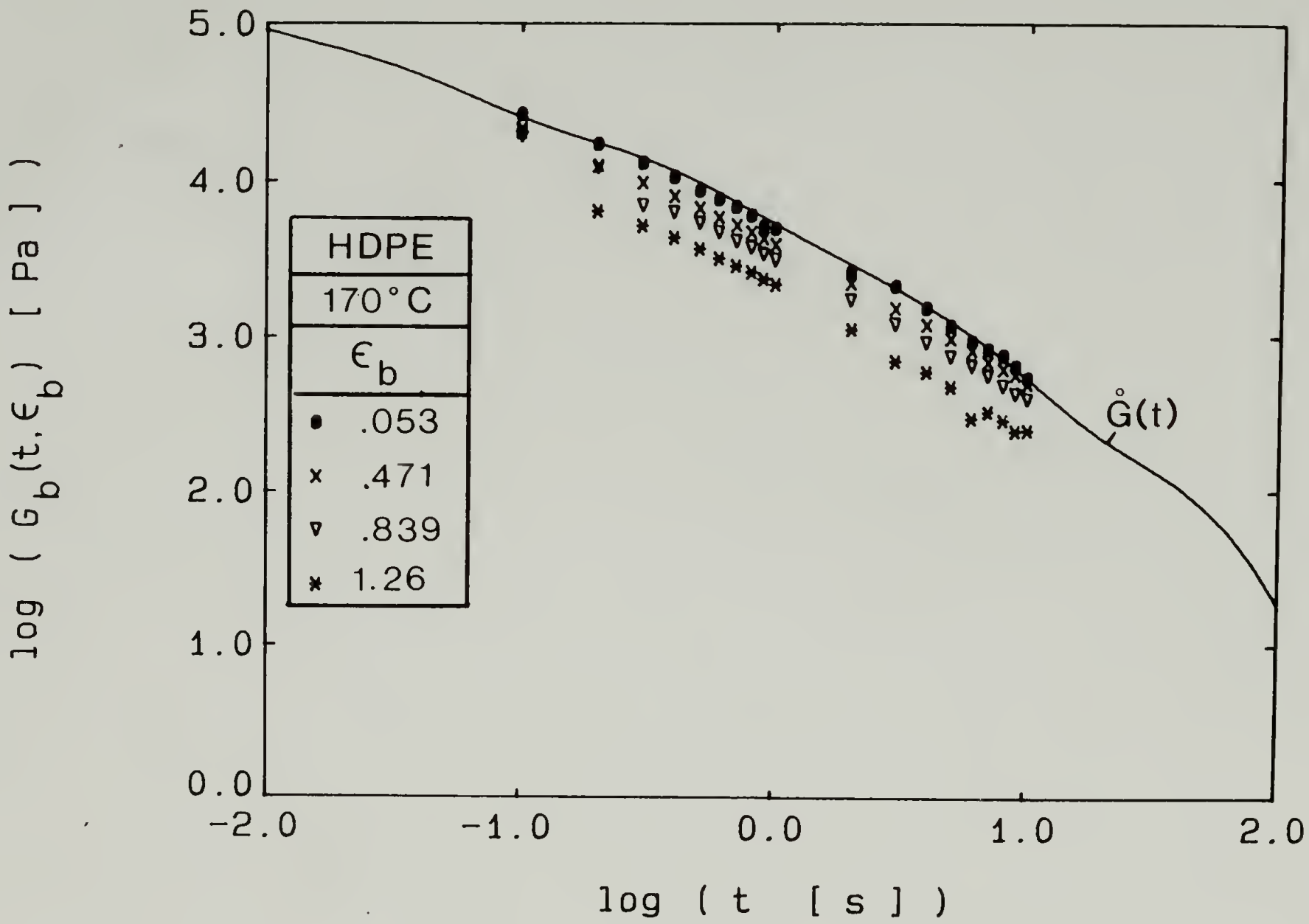

Figure 3.45. Transient extensional relaxation modulus of HDPE. The solid line is $\mathring{G}(t)$ calculated from Eq. (2.42) using the values in Table 3.3.

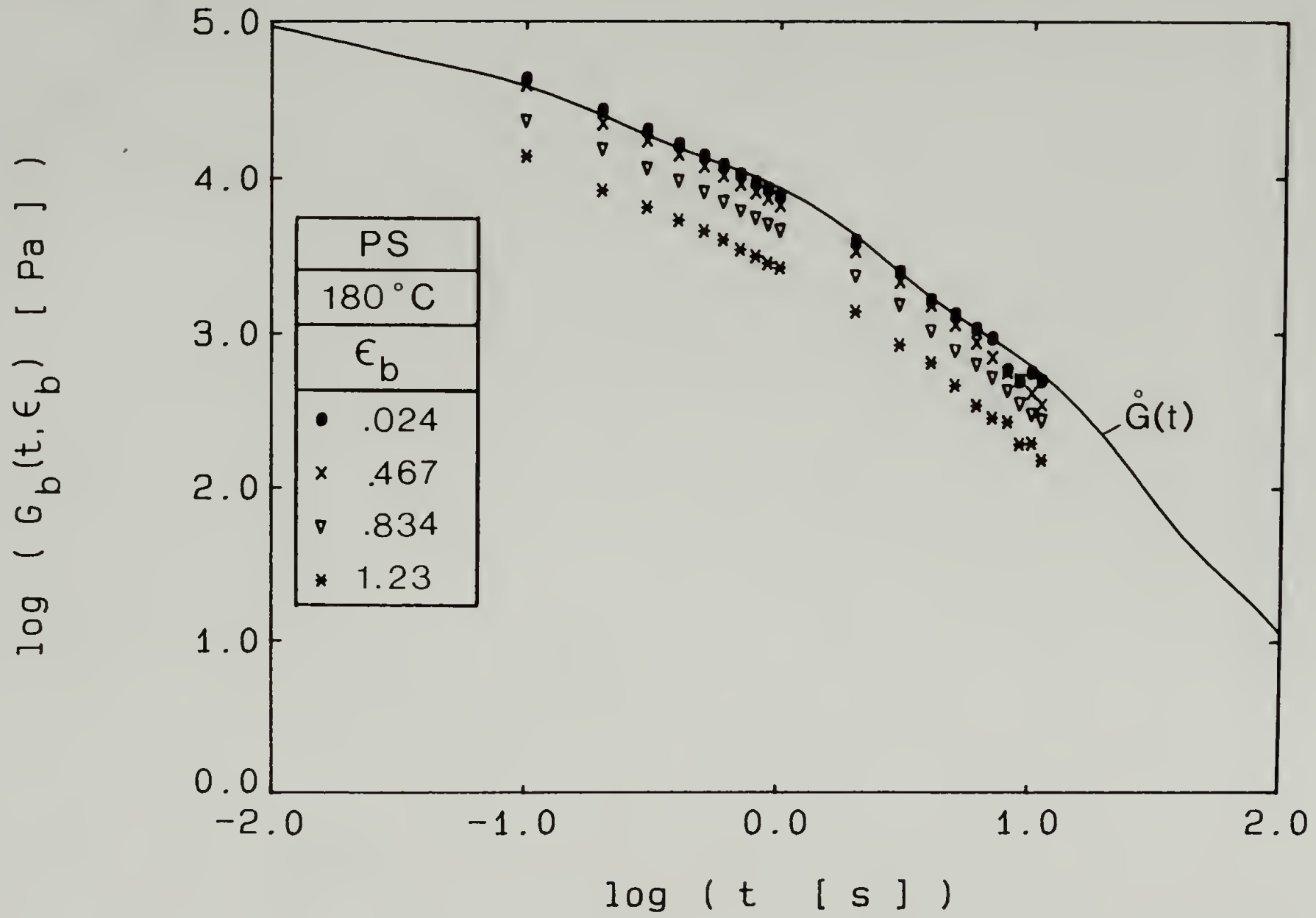

Figure 3.46. Transient extensional relaxation modulus of PS. The solid line is $\mathring{G}(t)$ calculated from Eq. (2.42) using the values in Table 3.3.

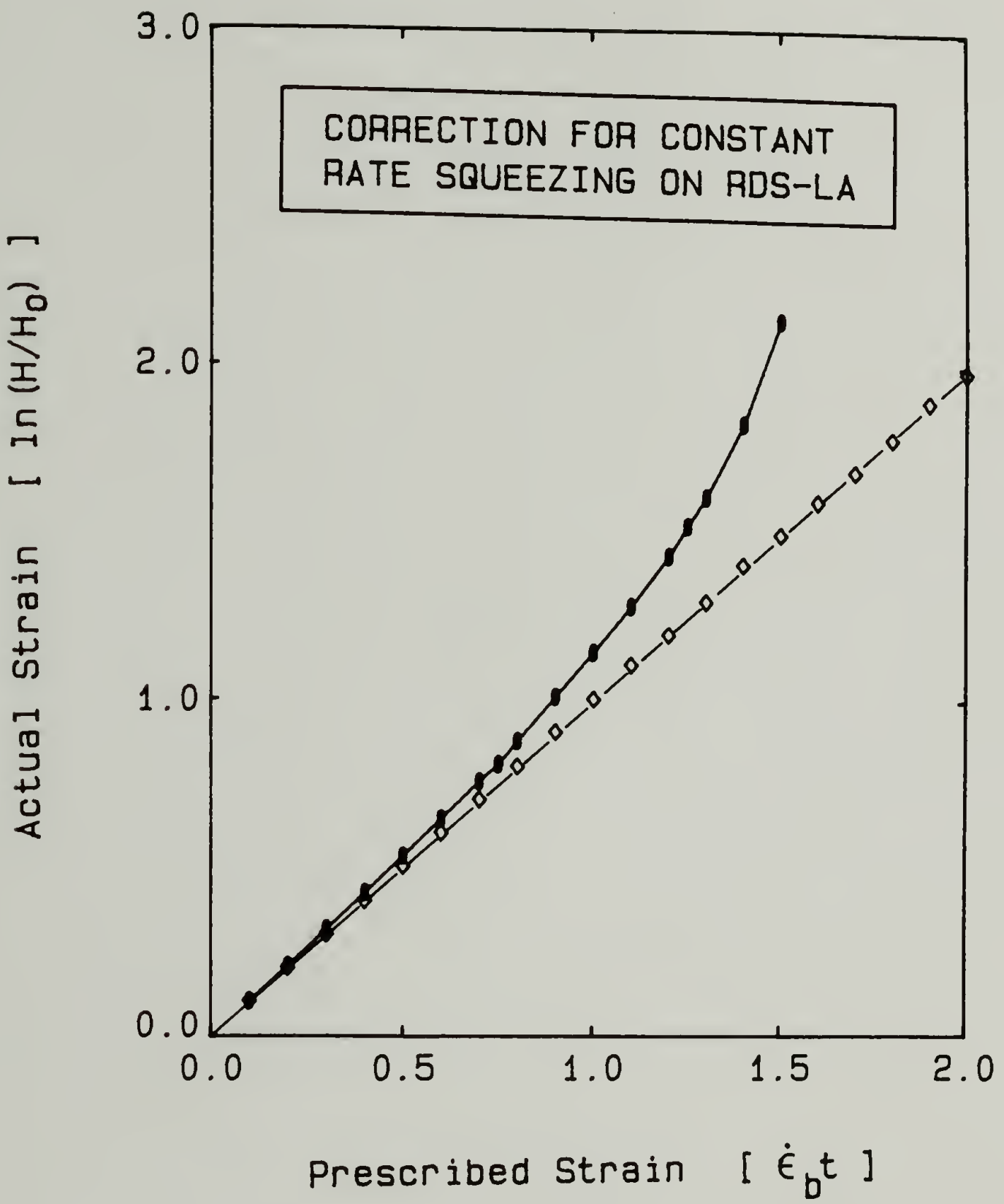

Figure 3.47. Actual plate separation as a function of prescribed strain for constant extension rate squeezing experiment on RDS-LA.
(O——O) before correction
(◇ — ◇) after correction according to Eq. (3.53).

initial disk separation, H_o. Fortunately, this error can be resolved and a constant extension rate obtained by inputting a corrected sample height for the motor control according to the following relation:

$$H_{o,corr} = 0.9467\ H_o \qquad (3.53).$$

This correction method allows a constant extension rate to be generated and is the same for all extension rates.

Constant extension rate experiments were performed for $0.01 \leq \dot{\varepsilon}_b \leq 0.5 s^{-1}$. A changing area technique similar to the one described by Frank (1983) was used. The technique involves using a sample that has an initial diameter less than the disk diameter and taking into account the changing area of the sample on the disk surface when calculating the stress from the force measurements as the experiment progresses. Figures 3.48, 3.49 and 3.50 show the transient equibiaxial extensional viscosity

$$\eta_b(t,\varepsilon_b) = [\sigma_{rr}-\sigma_{zz}](t)/\dot{\varepsilon}_b \qquad (3.54)$$

measured for the three polymers using the lubricated squeezing technique.

3.3.3 Discussion

In order to obtain reliable equibiaxial extensional rheological data, the effectiveness of the lubrication in the step strain experiment and constant rate experiment must be discussed.

3.3.3.1 Step strain experiments. The lubrication is effective in removing the shear stress at the top and bottom surfaces of the polymer sample as evidenced by the shape of the relaxation modulus curves. This

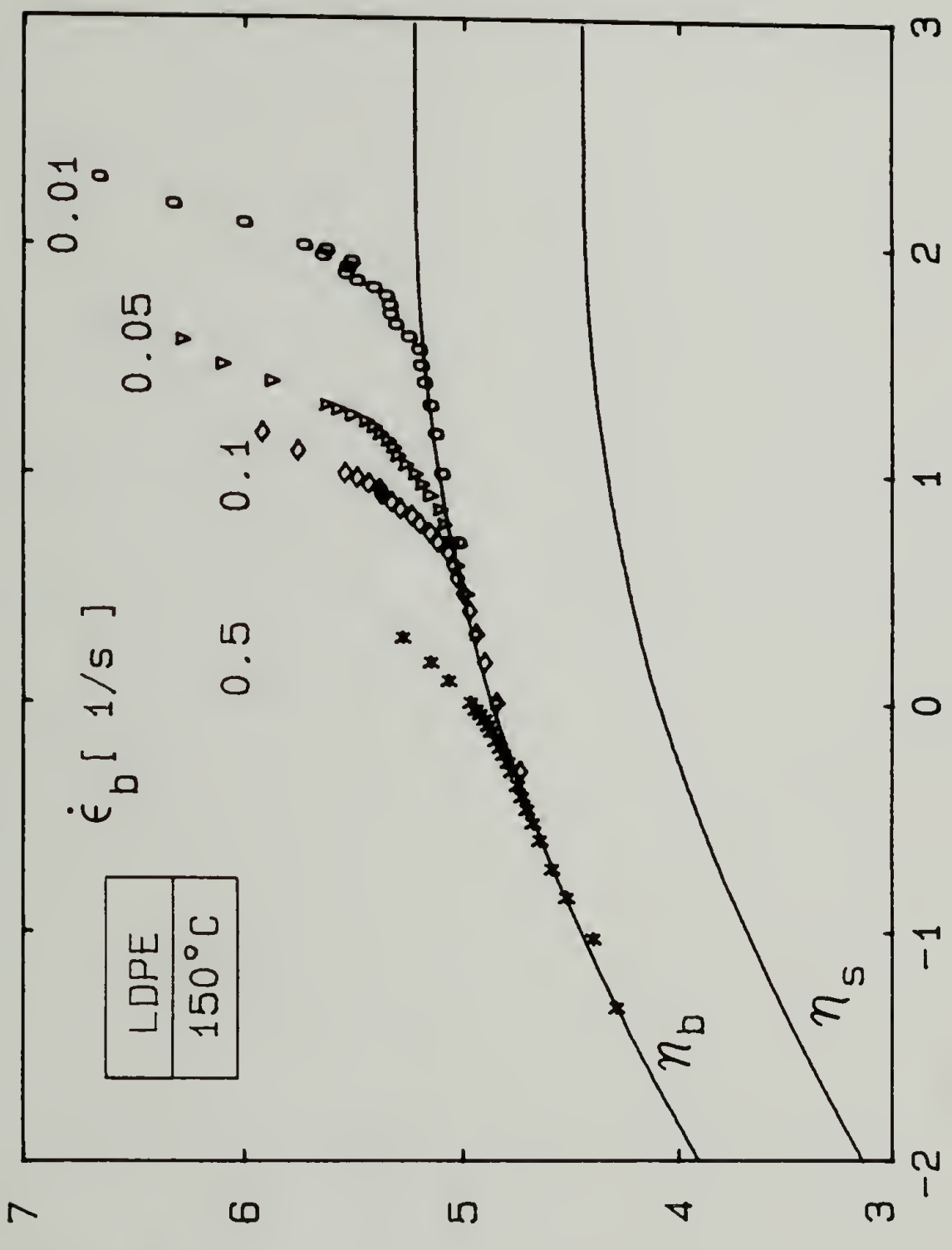

Figure 3.48. Transient equibiaxial extensional viscosity of LDPE measured with RDS-LA.

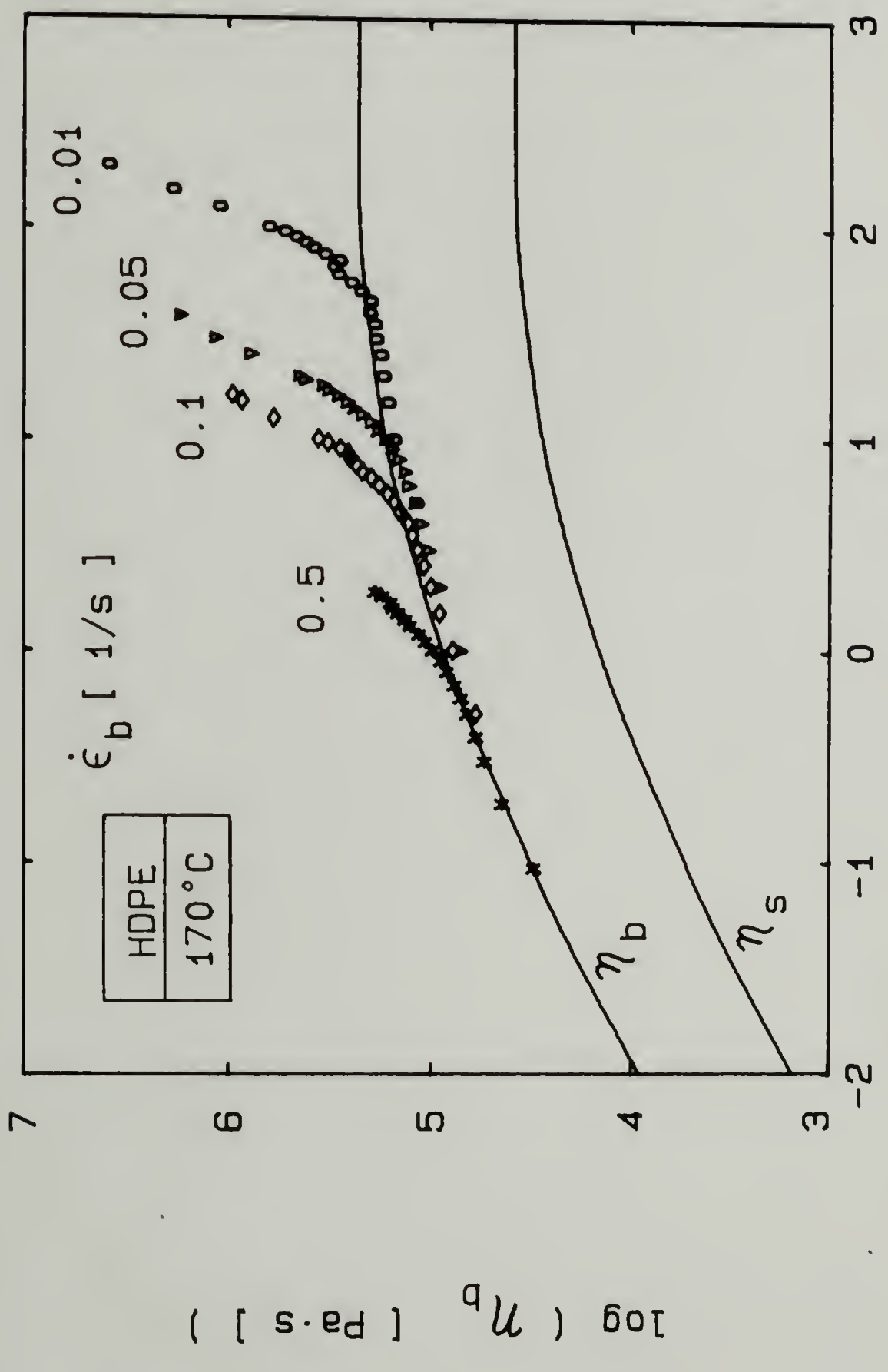

Figure 3.49. Transient equibiaxial extensional viscosity of HDPE measured with RDS-LA.

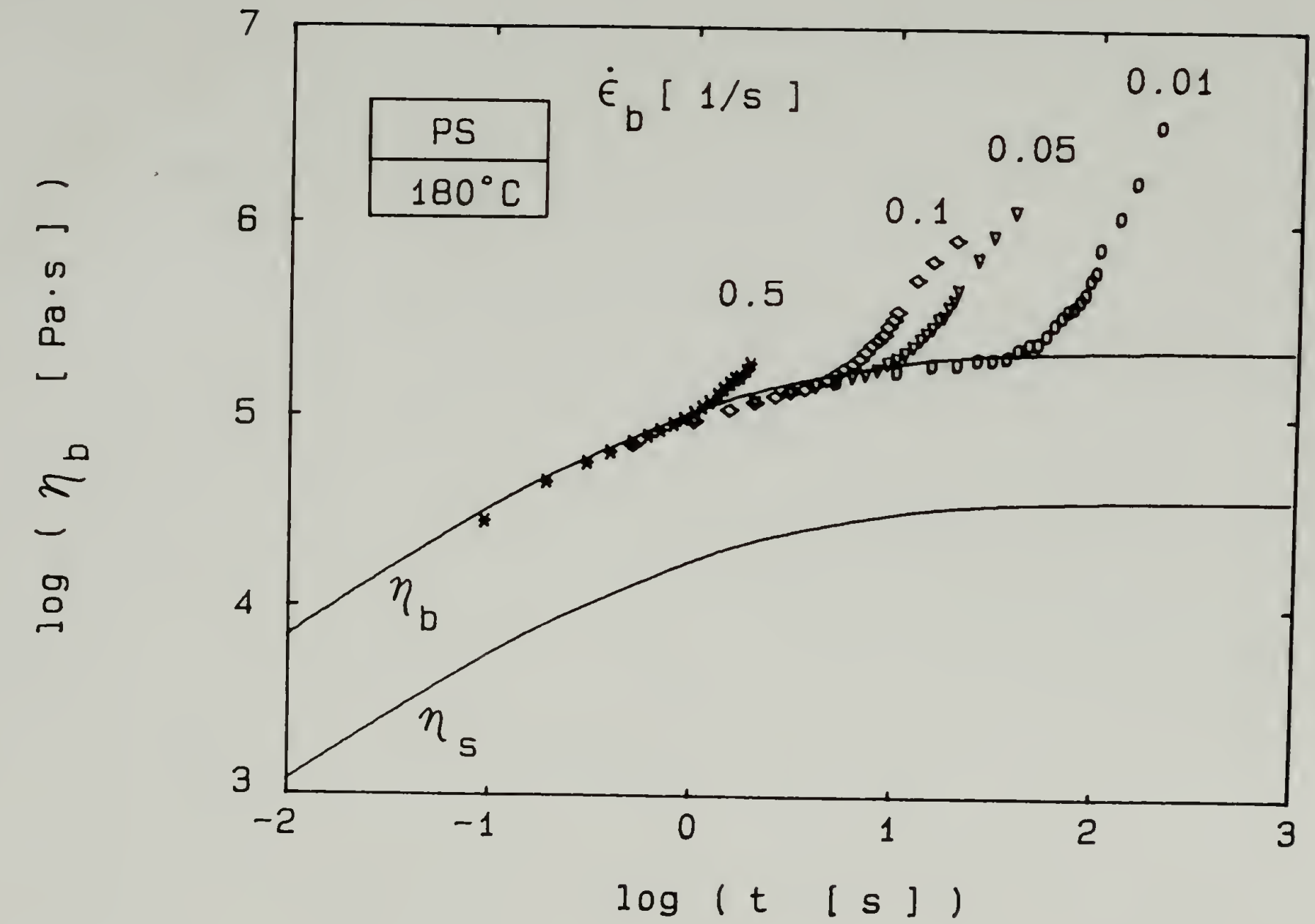

Figure 3.50. Transient equibiaxial extensional viscosity of PS measured with RDS-LA.

is argued with the following observations: the measured extensional relaxation moduli show distinctively different shapes for all three polymers, yet the shapes are identical to their respective shear relaxation moduli obtained from shear step strain experiments and from the linear viscoelasticity theory. One might expect different shapes between the shear and extensional relaxation modulus curves if the lubrication was poor in the squeezing experiment. The data, up to moderate strains, indicate that a true material response was measured in the equibiaxial extensional step strain experiment and equibiaxial extension was indeed achieved through effective lubrication. However, some loss in effectiveness of lubrication was seen at high strains, $\varepsilon_b > 1.6$ (very small final disk separations), where the shape of the stress relaxation curves change significantly as seen in Figures 3.41, 3.42 and 3.43. The curves exhibit unexpectedly high stress levels at short times along with several dips in the curves at long times. These features are attributed to the loss of effective lubrication as the sample thickness is reduced below 4% of its initial value.

The extensional modulus curves not only have the same shape but decrease as the strain increases. This supports the separability of the extensional relaxation modulus into a product of two independent functions of time and strain, Eq. (3.47). The strain function, h_e, for equibiaxial extension has been obtained by shifting the modulus data of Figures 3.44, 3.45 and 3.46 vertically upwards until they coincide with the linear viscoelastic modulus. The resultant values for the extensional strain function vs. the equibiaxial strain appear in Figures

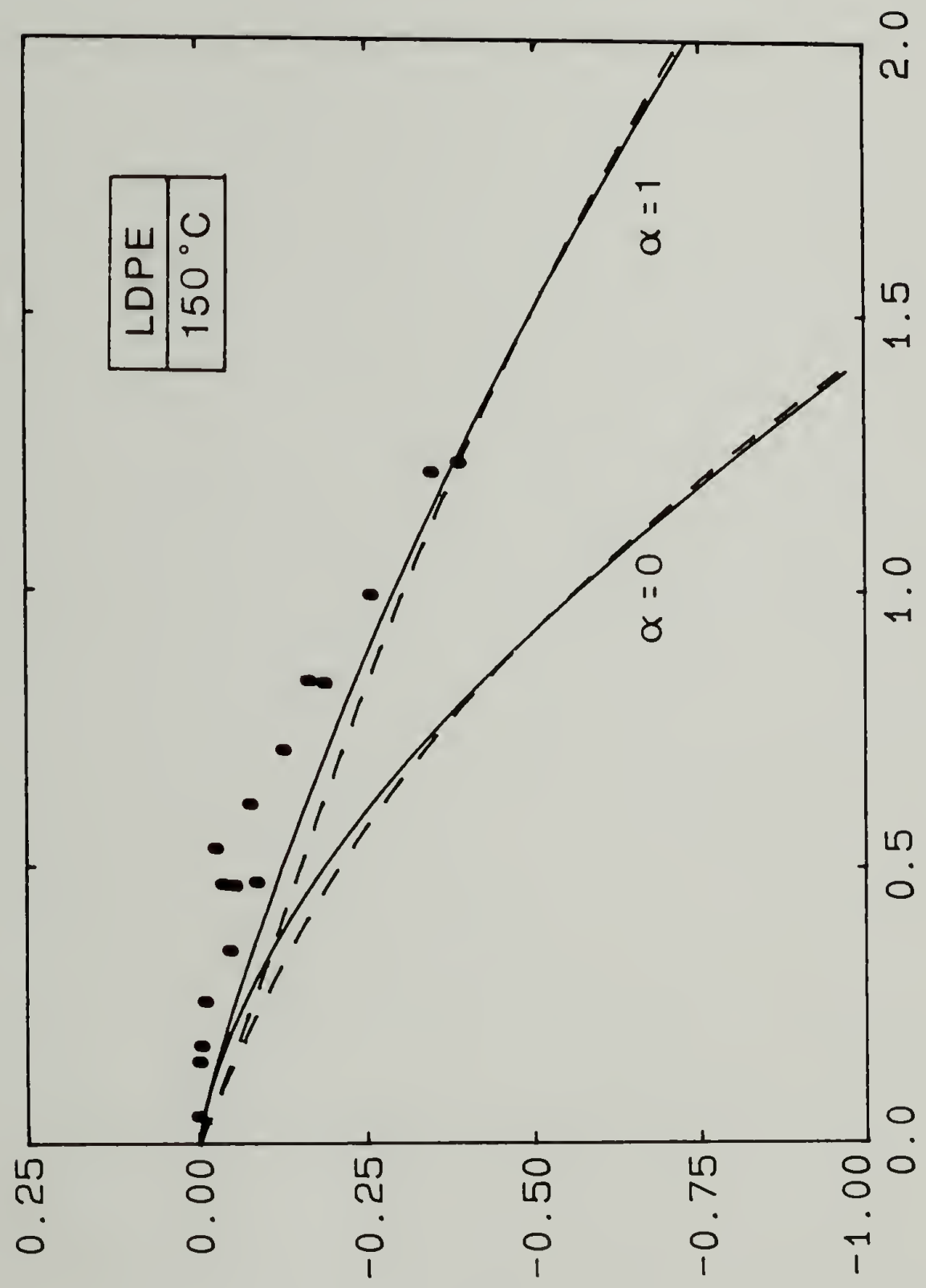

Figure 3.51. Extensional strain function, h_e, of LDPE in equibiaxial extension. (——) from Eq. (3.56) and (- - -) from Eq. (3.55) using the values in Table 3.6.

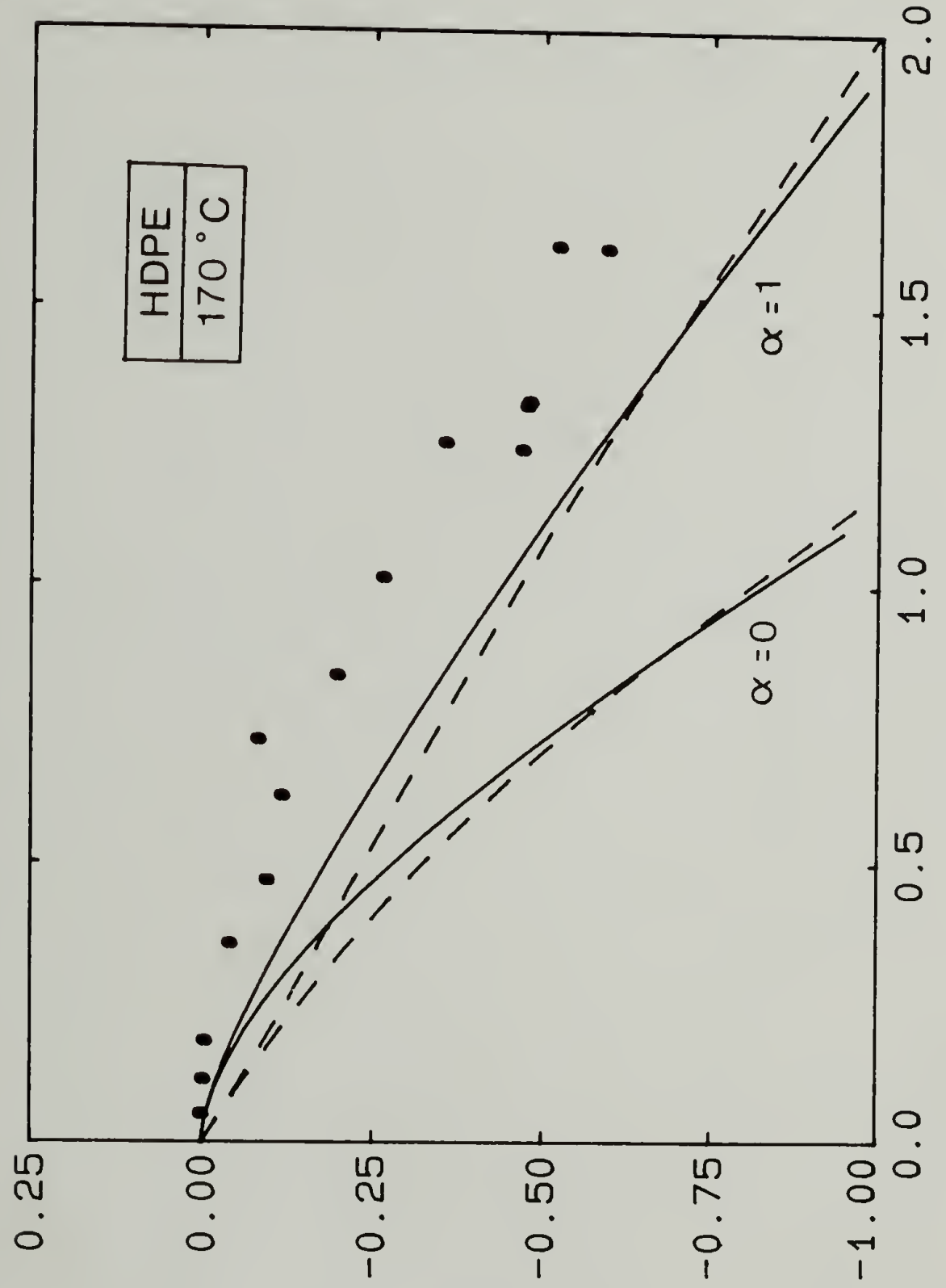

Figure 3.52. Extensional strain function, h_e, of HDPE in equibiaxial extension. (——) from Eq. (3.56) and (----) using the values in Table 3.6.

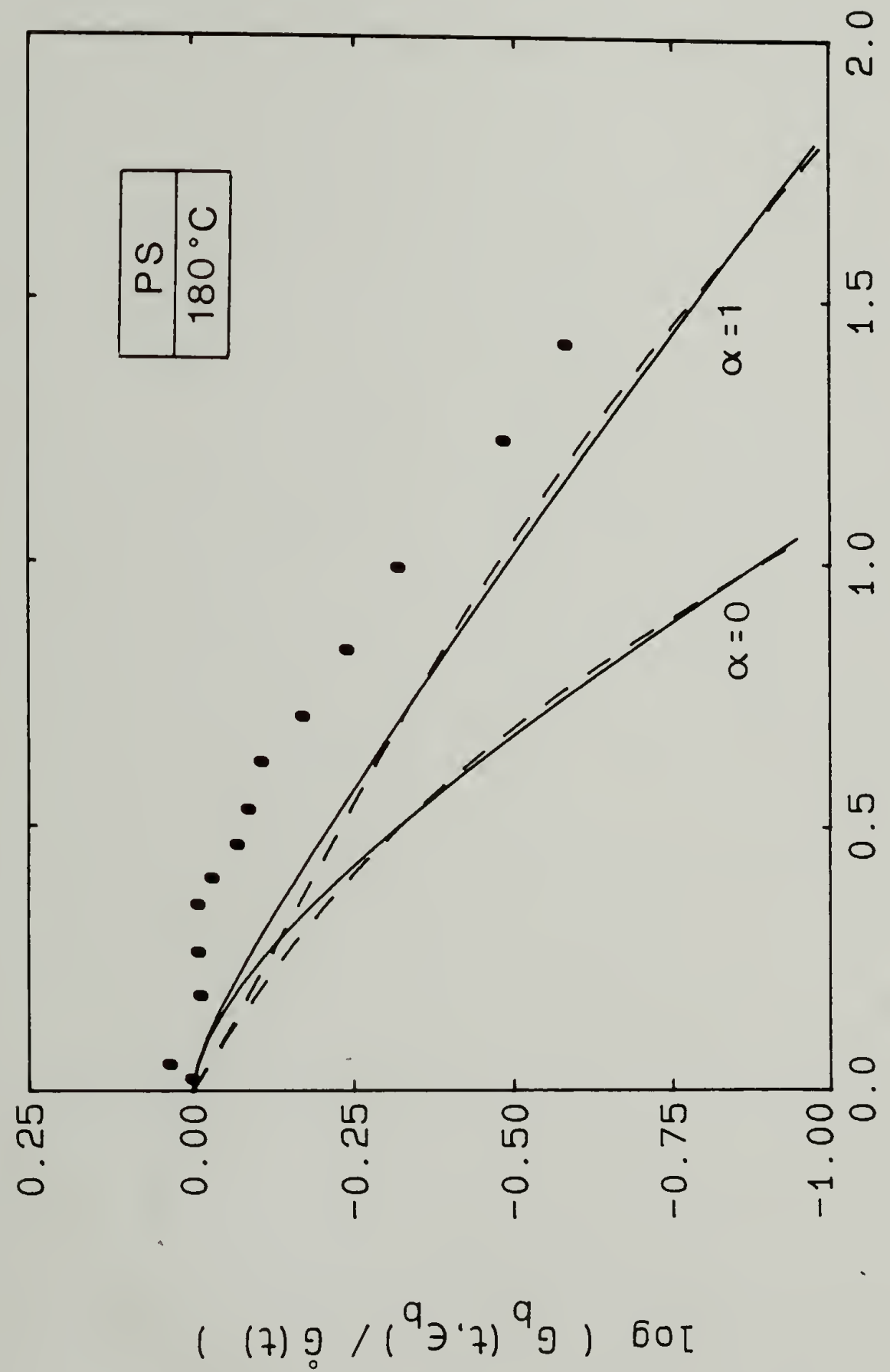

Figure 3.53. Extensional strain function, h_e, of PS in equibiaxial extension. (——) from Eq. (3.56) and (- - -) from Eq. (3.55) using the values in Table 3.6.

3.51, 3.52 and 3.53 and are seen to monotonically decrease as the equibiaxial strain increases. Due to the nonparallelism of the relaxation modulus curves at high strains, accurate values for the extensional strain function for equibiaxial extension could not be obtained beyond ε_b=1.5 or ε_a=-3.0.

As already observed with the shear strain function h_s, the extensional strain function decreases more rapidly for HDPE and PS than for LDPE although the difference between them is not as great as for the shear strain function.

A generalized strain function that describes both shear and extension, Eq. (2.50), was used to analyze the extensional strain function for equibiaxial extension. This generalized strain function can be written as

$$h(I(\varepsilon_b)) = f \exp(-n_1\sqrt{I(\varepsilon_b)-3} + (1-f)\exp(-n_2\sqrt{I(\varepsilon_b)-3}) \quad (3.55)$$

where $I(\varepsilon_b)$ is given by Eq. (2.49). The sigmoidal form as shown in Eq. (3.36) for the shear strain function can also be formulated for the generalized invariant I and applied to equibiaxial extension to become

$$h(I(\varepsilon_b)) = [1+a(I(\varepsilon_b)-3)^{b/2}]^{-1} \quad (3.56).$$

The prediction of the extensional strain function using the proposed generalized strain functions, Eqs. (3.55) and (3.56) and the parameters of Table 3.6 have also been plotted in Figures 3.51, 3.52 and 3.53. Data from the shear step strain experiments predict an extensional strain function for equibiaxial extension between the curves α=0 and α=1. The measured extensional strain function for equibiaxial

extension, $h_e(I(\varepsilon_b))$, although lying slightly above, is described best by the curve with α=1. Just as with the shear strain function, the sigmoidal form of the extensional strain function, Eq. (3.56), describes the small strain data better than the form having a sum of two exponentials, Eq. (3.55).

The extensional strain function for uniaxial extension of an LDPE melt was found to be described best by $\alpha \approx 0$ for a generalized strain invariant given by Eq. (2.48), $h_e(I(\varepsilon_a))$ (Wagner, 1979). It is seen from Eqs. (2.22), (2.23), (2.27) and (2.28) that for positive values of the respective strains ε_a and ε_b, the respective invariants are related as follows:

$$I_1(\varepsilon_a) = I_2(\varepsilon_b) \tag{3.57}$$

$$I_2(\varepsilon_a) = I_1(\varepsilon_b) \tag{3.58}$$

at values of $\varepsilon_b = |\varepsilon_a/2|$.

This relationship causes the extensional strain function for equibiaxial extension, $h_e(I(\varepsilon_b))$ with α=1, to be identical to the extensional strain function for uniaxial extension, $h_e(I(\varepsilon_a))$ with α=0 at comparable values of $\varepsilon_b = |\varepsilon_a/2|$. This identity is easily seen when one plots the extensional strain function for equibiaxial extension now in terms of the axisymmetric strain along with the extensional strain function for uniaxial extension as shown in Figure 3.54. The experimental data for equibiaxial extension of the LDPE obtained above also appear in Figure 3.54 and strongly suggest that the extensional strain function has the same values for axisymmetric extension and axisymmetric compression if one assumes that $\alpha \approx 0$ for uniaxial extension (Wagner, 1979).

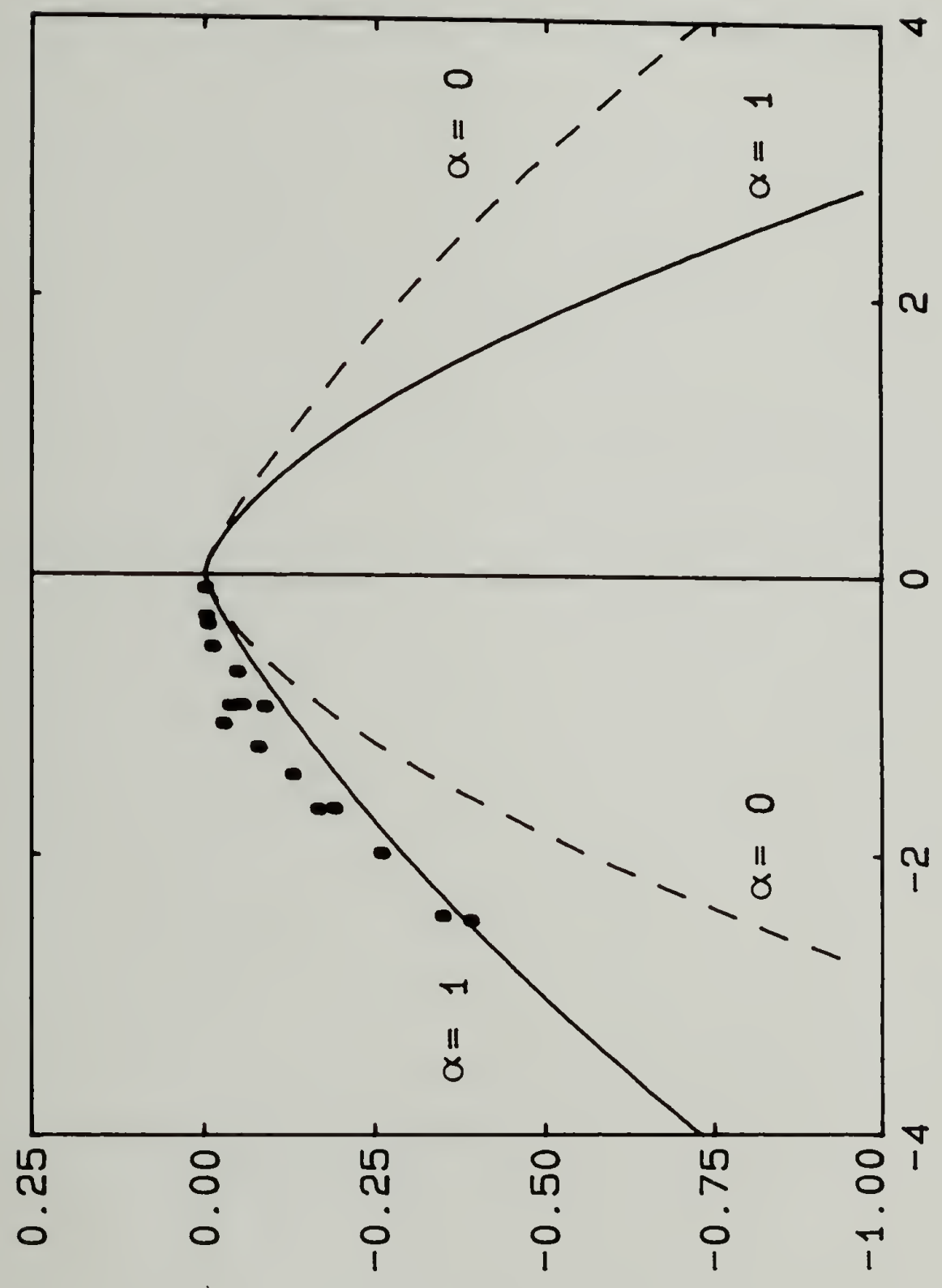

Figure 3.54. Extensional strain function, h_e, as a function of the axisymmetric strain for LDPE. Lines are calculated from Eqs. (2.48) and (3.56) and the values in Table 3.6, with (——) α=1 and (----) α=0.

Using the above notation, two different generalized strain invariants $I(\varepsilon_b)$ and $I(\varepsilon_a)$ along with two different material parameters α=1 and α=0 are required to describe the extension strain function for axisymmetric extension and compression. A more simple notation can be formulated by allowing the generalized strain invariant I to be a function of the absolute value of the axisymmetric strain, $|\varepsilon_a|$. Therefore only one value of α and one generalized strain function is required

$$h_e(I(|\varepsilon_a|)) \text{ with } \alpha=0, = \begin{cases} h_e(I(\varepsilon_a)) \text{ with } \alpha=0 \\ h_e(I(\varepsilon_b)) \text{ with } \alpha=1 \end{cases} \qquad (3.59).$$

This relationship had been assumed by Wagner and Stephenson (1979) for describing the elastic recoil behavior after uniaxial extension. A best fit was found between the prediction of a modified rubberlike liquid constitutive equation using the assumption of irreversibility of network disentanglements and their experimental data for the recoverable extensional strain when they used the relation of Eq. (3.59). No biaxial data were available for the LDPE which they considered.

3.3.3.2 Prediction of constitutive equation. The results of the stress growth at constant equibiaxial extension rate, $\dot{\varepsilon}_b$, were analyzed by applying the memory integral constitutive equation of Eq. (2.43).

For equibiaxial extension at constant volume, the relative Finger strain tensor is given in Eq. (2.26). The start-up experiment with constant equibiaxial extension rate $\dot{\varepsilon}_b$ is defined by

$$\varepsilon_b(t,t') = \begin{cases} \dot{\varepsilon}_b(t-t') = \dot{\varepsilon}_b s & \text{for } s<t \\ \dot{\varepsilon}_b t & \text{for } s \geq t \end{cases} \qquad (3.60)$$

where s=t-t'. A normal stress difference can be determined from Eqs. (2.43), (2.44) and (2.50) to be

$$[\sigma_{22}-\sigma_{11}](t) = \int_o^t \mu(s)h(I(s))[e^{-4\dot{\varepsilon}_b s} - e^{2\dot{\varepsilon}_b s}]ds$$

$$+ \overset{\circ}{G}(t)h(I(t))[e^{-4\dot{\varepsilon}_b t} - e^{2\dot{\varepsilon}_b t}] \qquad (3.61).$$

The equibiaxial extensional viscosity, Eq. (3.54), was then calculated by numerical integration of Eq. (3.61) for different extension rates and forms of the strain function.

The measured equibiaxial viscosity appears in Figures 3.48, 3.49 and 3.50 where the solid lines are the predictions of Eq. (2.43) in the linear viscoelastic limit using the constants in Table 3.3. The lower curve is the shear viscosity $\eta_s(\dot{\gamma}=0.0001\ s^{-1})$ and the upper curve is $\eta_b(\dot{\varepsilon}_b=0.0001\ s^{-1})$. It can be shown from linear viscoelastic theory that in the limit of small strain $\eta_b=6\eta_s$. At low extensional strains and for all the measured extension rates, the measured equibiaxial viscosity then becomes slightly less than the linear viscoelastic limit. At $\varepsilon_b \approx 0.85$, the measured equibiaxial viscosity begins to rise above the linear viscoelastic limit and continues to rise to very high values at large strains. The strain at which this deviation occurs increases slightly as the extension rate increases. This behavior has been seen in other constant rate lubricated squeezing experiments (Frank, 1983). This deviation has been attributed to the loss of effective lubrication and is seen for several different polymer melts. Two other lubricants having shear viscosities a decade higher and lower than the Viscasil

300K and 600K were used and the measured equibiaxial viscosity at low strains was considerably higher than those reported in Figure 3.48, but approached the same measured viscosity at high strains indicating that, regardless of the lubricant, the effectiveness of the lubrication may be lost and the response at high strains is due to the extra force needed to shear the polymer sample.

This possible loss of effective lubrication in the constant rate experiment occurs at a slightly lower strain than in the step strain experiment. It seems that at these relatively low extension rates the lubricant has a chance to squeeze out at lower strains, whereas for the step strain experiment, the extension occurs so fast (very short rise times) that the lubricant does not have enough time to squeeze out and therefore the effectiveness of the lubrication remains until higher strains.

A rise in biaxial viscosity at large strains has also been seen by others who have not used the lubricated squeezing technique. Both Stephenson and Meissner (1980) with the sheet stretching device and Rhi-Sausi and Dealy (1981) with a sheet inflation biaxial rheometer, where lubrication effects are absent, report biaxial viscosities which increase at high strains. However, other experimental difficulties at high strains make it difficult to analyze the data. Better methods of obtaining high strain data are surely needed.

Even though experimental data at large strains are difficult to obtain it is instructive to look at the predictions of the equibiaxial viscosity for the various forms of the strain function obtained from the

step strain experiments. The predictions of the equibiaxial viscosity appear in Figures 3.55, 3.56 and 3.57 for $\dot{\varepsilon}_b$=0.1 s^{-1}. The three curves marked L, S and E correspond to the following choice of $h(I(\varepsilon_b))$:

L - Lodge rubberlike-liquid constitutive equation; $h(I(\varepsilon_b))$=1.

S - Sigmoidal form of strain function; $h(I(\varepsilon_b))$ as given by Eq. (3.56) with α=1.

E - Exponential form of strain function; $h(I(\varepsilon_b))$ as given by Eq. (3.55) with α=1.

The prediction of $\eta_b(t)$ from the Lodge rubberlike-liquid equation is seen to follow the linear viscoelastic limit at small strains then rise sharply at $\varepsilon_b \approx 1$ and continue to rise to an infinite viscosity similar to the uniaxial extensional viscosity (Wagner, 1976). The prediction with the sigmoidal form of $h(I(\varepsilon_b))$ is seen to follow the linear viscoelastic limit at small strains, level off to a viscosity below the linear viscoelastic limit at intermediate strains and then rise in a dramatic manner to an infinite viscosity at large strains. The form of $h(I(\varepsilon_b))$ containing the sum of two exponential functions predicts an equibiaxial viscosity similar to the sigmoidal form up to intermediate strains as would be expected from Figures 3.51, 3.52 and 3.53 where the functions are nearly identical up to ε_b=2. However, at ε_b>4 the exponential form of $h(I(\varepsilon_b))$ predicts a constant value of η_b that is less than the linear viscoelastic limit. This feature occurs because the exponential form of $h(I(\varepsilon_b))$ decreases much more rapidly at large strains than the sigmoidal form and is able to cancel out the exponentially increasing part of Eq. (3.61) due to the equibiaxial strain. The

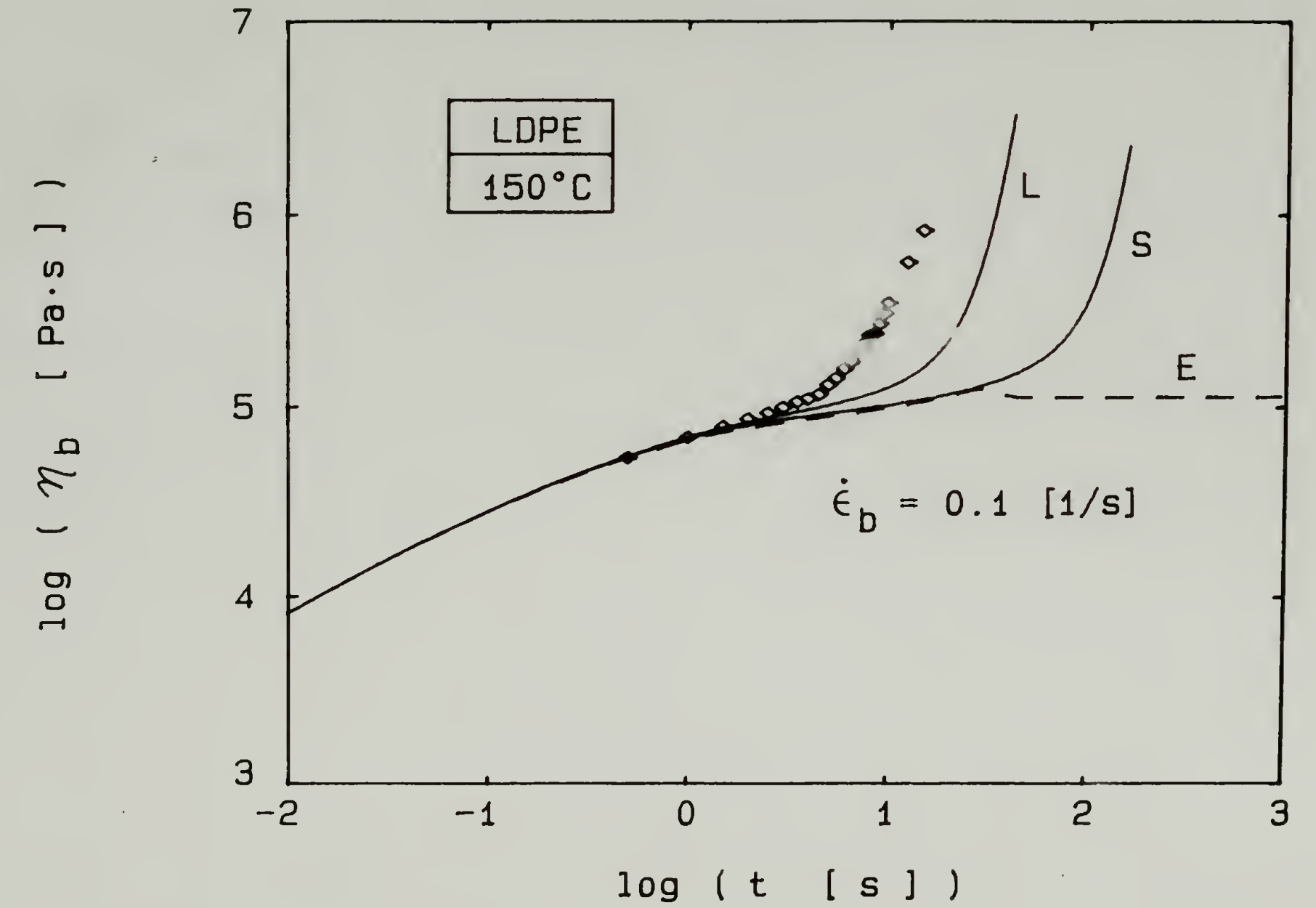

Figure 3.55. Prediction of the transient equibiaxial viscosity of LDPE according to Eq. (2.43). See text for explanation of lines L, S and E.

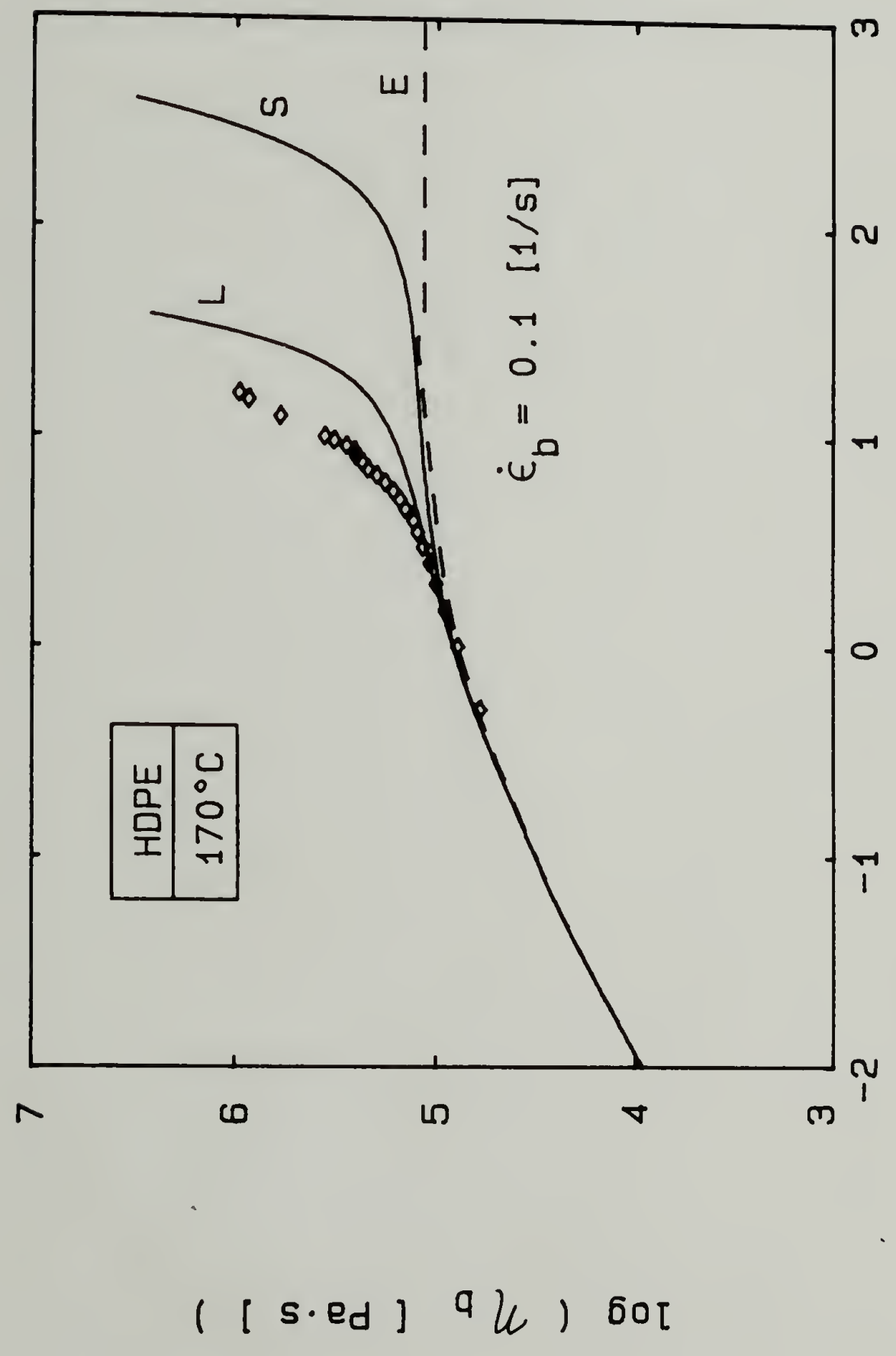

Figure 3.56. Prediction of the transient equibiaxial viscosity of HDPE according to Eq. (2.43). See text for explanation of lines L, S and E.

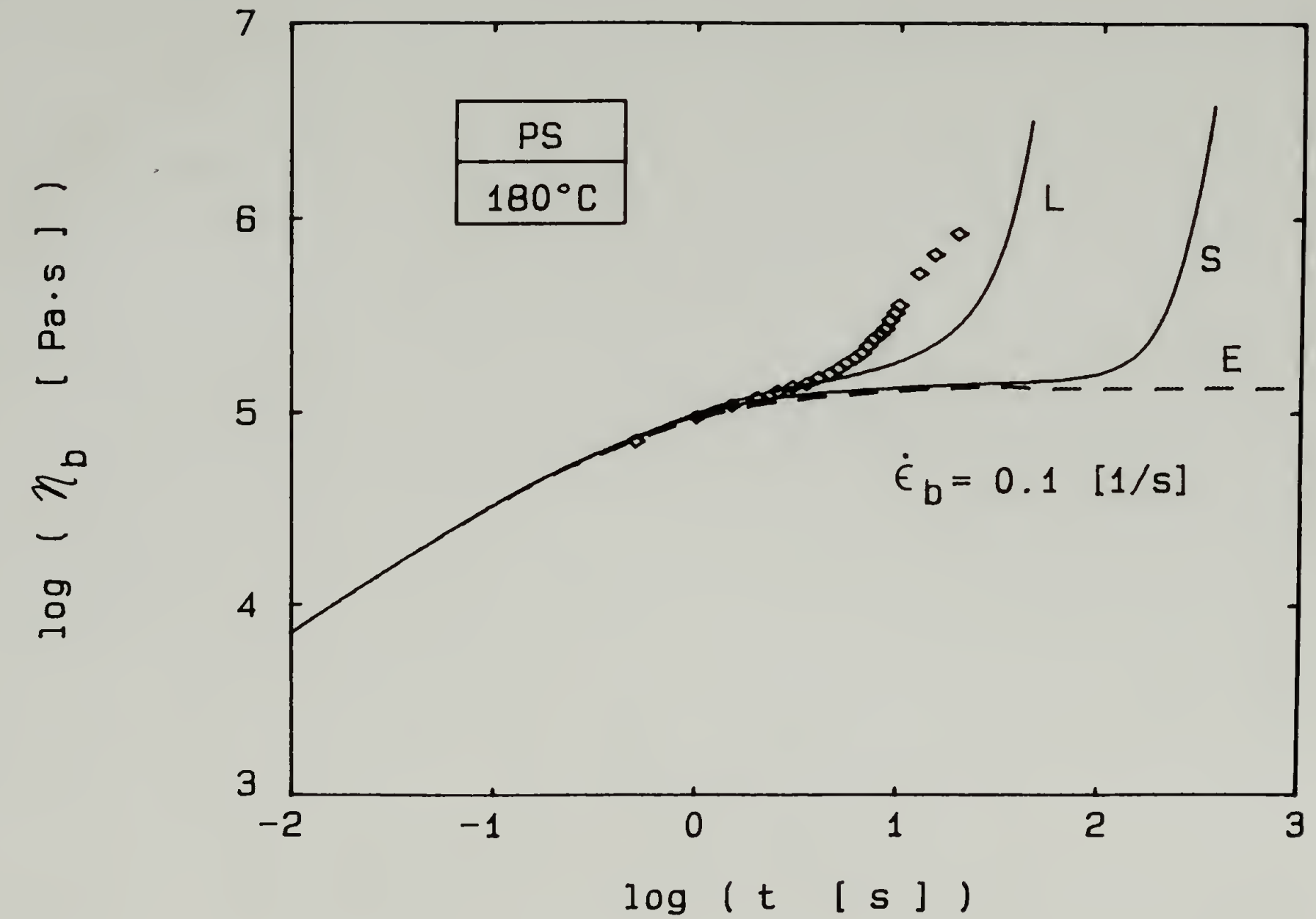

Figure 3.57. Prediction of the transient equibiaxial viscosity of PS according to Eq. (2.43). See text for explanation of lines L, S and E.

measured equibiaxial viscosity is described well by the memory integral constitutive equation up to intermediate strains.

C H A P T E R I V

PROCESS MODELING OF AXISYMMETRIC FLOW

The modeling of processing flows consists of three main steps. First an appropriate constitutive equation is chosen and the required rheological parameters are experimentally determined. An appropriate constitutive equation should describe both steady state and transient behavior of polymer melts in shear and extension. Secondly, the strain history of material elements at some point in the flow is determined. The entire strain history of a material element is obtained by first determining the approximate kinematics and temperature field of the flow from experimental measurements or by means of established modeling techniques. The material elements are then tracked along pathlines to obtain the required strain history. The final step is the calculation of the desired stress distributions using the appropriately chosen constitutive equation. These three steps are described in detail in this chapter.

4.1 Determination of Rheological Parameters

An appropriate constitutive equation for modeling axisymmetric flows is the memory integral constitutive equation as described in the second chapter. The equation has been well tested for polymer melts in shear and extension as well as transient and steady flows. Both the linear viscoelastic (small strain) and non-linear (large strain) rheological parameters in both shear and extension have been determined for

the polymers under study using the rheometric techniques described in the third chapter.

4.2 Determination of Strain History

The strain history of material elements in annular flow was determined by calculating the approximate kinematics of annular flow from established modeling techniques and then tracking the material elements along their pathlines.

4.2.1 Kinematics of Annular Flow

Integral constitutive equations are most suited for stress calculations when the kinematics of the process flow are known. The kinematics of annular flows can be calculated utilizing well established numerical solution procedures (Winter, 1977).

The assumptions used in the calculation of the velocity field in annular dies of changing cross-section are:

(a) During flow, the polymer melt has a constant temperature and density.

(b) The flow in a specific cross-section of a tapered section is identical to the flow in a parallel channel of the same cross-section. This is equvalent to the lubrication approximation which is valid for gradual changes in tapered sections.

(c) The local shear stress is determined from the local steady shear rate and the corresponding steady shear viscosity. This is valid since any steady flow near a rigid surface, assuming no slip at the surface, reduces to shear flow.

(d) The rheological parameters do not depend on the pressure.

Using these assumptions the kinematics for annular flow were calculated. The annular flow geometry is shown in Figure 4.1 and is described in cylindrical coordinates (z,r,Θ). The axial velocity is v_z and the inner and outer radii of the flow channel are r_i and r_o respectively. The z-component of the stress equation of motion becomes

$$\partial p/\partial z = (1/r)\partial(r\sigma_{rz})/\partial r \tag{4.1}$$

with the assumption of steady shear flow. The shear stress, σ_{rz}, is determined from the relation

$$\sigma_{rz} = \dot{\gamma}\eta_s(\dot{\gamma}) \tag{4.2}$$

where the local shear rate is

$$\dot{\gamma} = \partial v_z/\partial r \tag{4.3}$$

and the local viscosity is calculated from the memory integral constitutive equation, Eq. (2.43), as applied to steady shear flow

$$\eta_s(\dot{\gamma}) = \int_{-\infty}^{\infty} \mu(t',t)h(I(t',t))(t-t')dt' \tag{4.4}.$$

When a memory function having a discrete relaxation spectrum and a strain function having the form of the sum of two exponential functions is used in Eq. (4.4), the steady shear viscosity can be solved analytically to obtain

$$\eta_s(\dot{\gamma}) = \sum_{i=1}^{M} \sum_{j=1}^{2} f_j\lambda_i g_i/(1+n_j\lambda_i|\dot{\gamma}|)^2 \tag{4.5}$$

where $f_1=f$ and $f_2=(1-f)$; f being the material parameter in Eq. (3.34). If the sigmoidal form of the strain function is used in Eq. (4.4), the

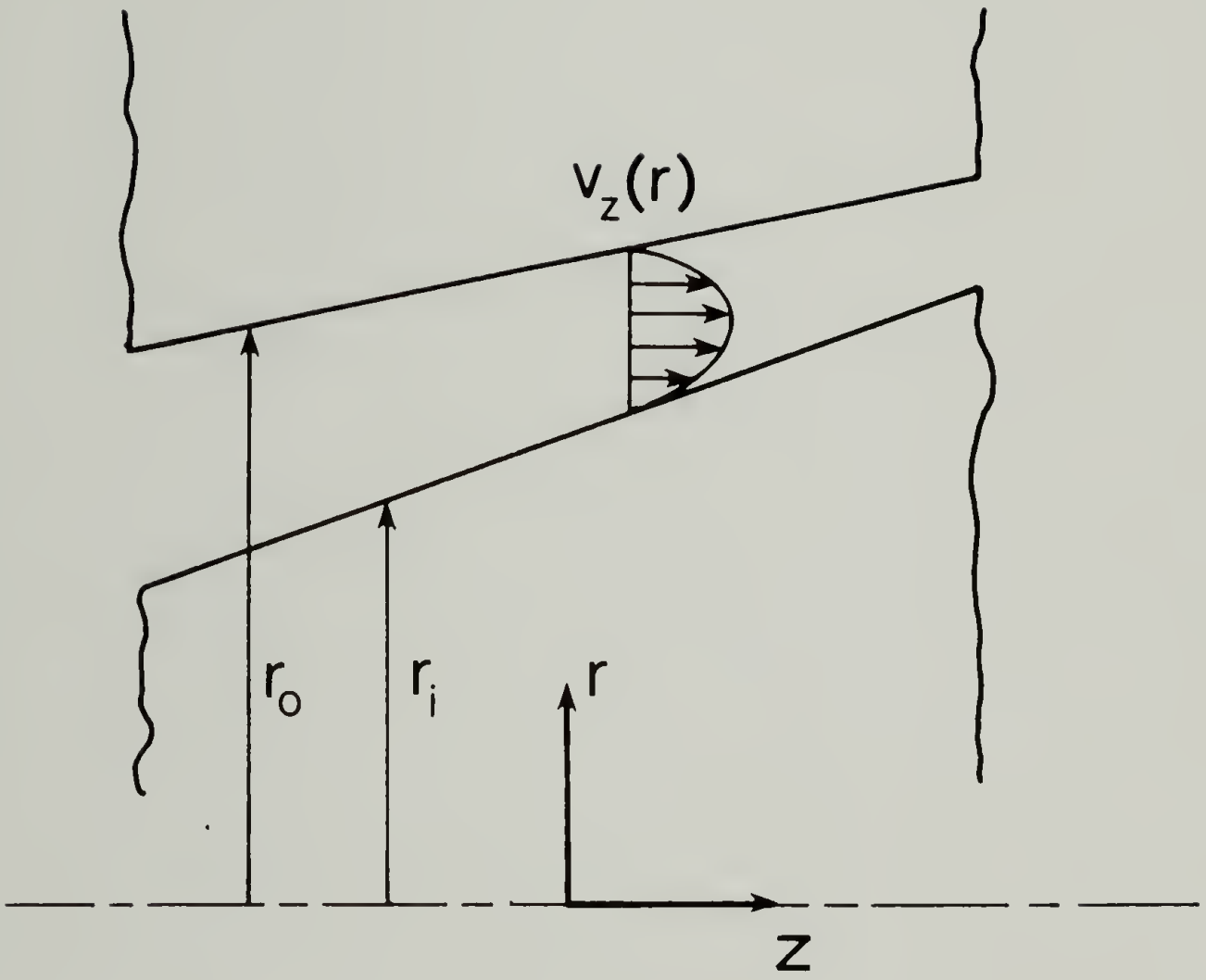

Figure 4.1. Annular flow geometry.

steady shear viscosity function itself must be solved numerically requiring much more computation time. It should be noted that the constitutive equation used to calculate the stress is the same one used to calculate the kinematics. The steady shear viscosity function obtained from the integral constitutive equation is preferable to the simple power-law equation since it gives a much better description of the low shear rate region by predicting a zero-shear viscosity.

Velocity profiles are then calculated numerically at various cross-sectional positions to give a complete velocity field in the die flow channel. For a more detailed discussion of the velocity field determination see Winter and Fischer (1981).

The kinematics are then used to calculate the deformation of a material element along its pathline. In order to do this, a tracking procedure must be used.

4.2.2 Tracking of Material Elements

The strain history of a material element is completely defined if the kinematics of its flow is known. The strain history is expressed by six time dependent components of the Finger strain tensor. In numerical calculations, the quantitative description of the strain history is somewhat complicated since the velocity field is available only as discrete values at specified initial grid points. A tracking procedure is needed for calculating the components of the Finger strain tensor for the particular flow.

A detailed description of the tracking procedure for material elements in all types of steady axisymmetric flows is given by Winter

(1982). This tracking procedure is applied to the steady flow through annular dies having tapered sections. A given velocity field of steady axisymmetric flow is needed for the tracking procedure. In this study, the approximate kinematics, as discussed in the previous section is sufficient. Material elements are then tracked along their pathlines. For steady axisymmetric flows the pathlines and streamlines are identical and are given by

$$\Psi(r) = \int_{r_i}^{r} \rho v_z(r) r dr \Big/ \int_{r_i}^{r_o} \rho v_z(r) r dr \qquad (4.6).$$

The streamline has a value of zero at the inner wall and unity at the outer wall of the flow channel.

The strain is described by an orthonormal coordinate system, $\underline{x}_i$, that translates and rotates with the material elements as they move along their pathlines. A sketch of such a deforming material element is shown in Figure 4.2. The components of the coordinate system are: $\underline{x}_1$ in the flow direction (tangent to pathline), $\underline{x}_2$ normal to an axisymmetric stream surface and $\underline{x}_3$ in the stream surface normal to $\underline{x}_1$ and $\underline{x}_2$.

The flow is viewed as a superposition of shear flow and extensional flow where one of the principal planes of the extensional component is at the same time a shear surface of the shear component. The components of the Finger strain tensor are obtained from the relationships developed in Section 2.1. For the material element pictured in Figure 4.2, the material vectors are

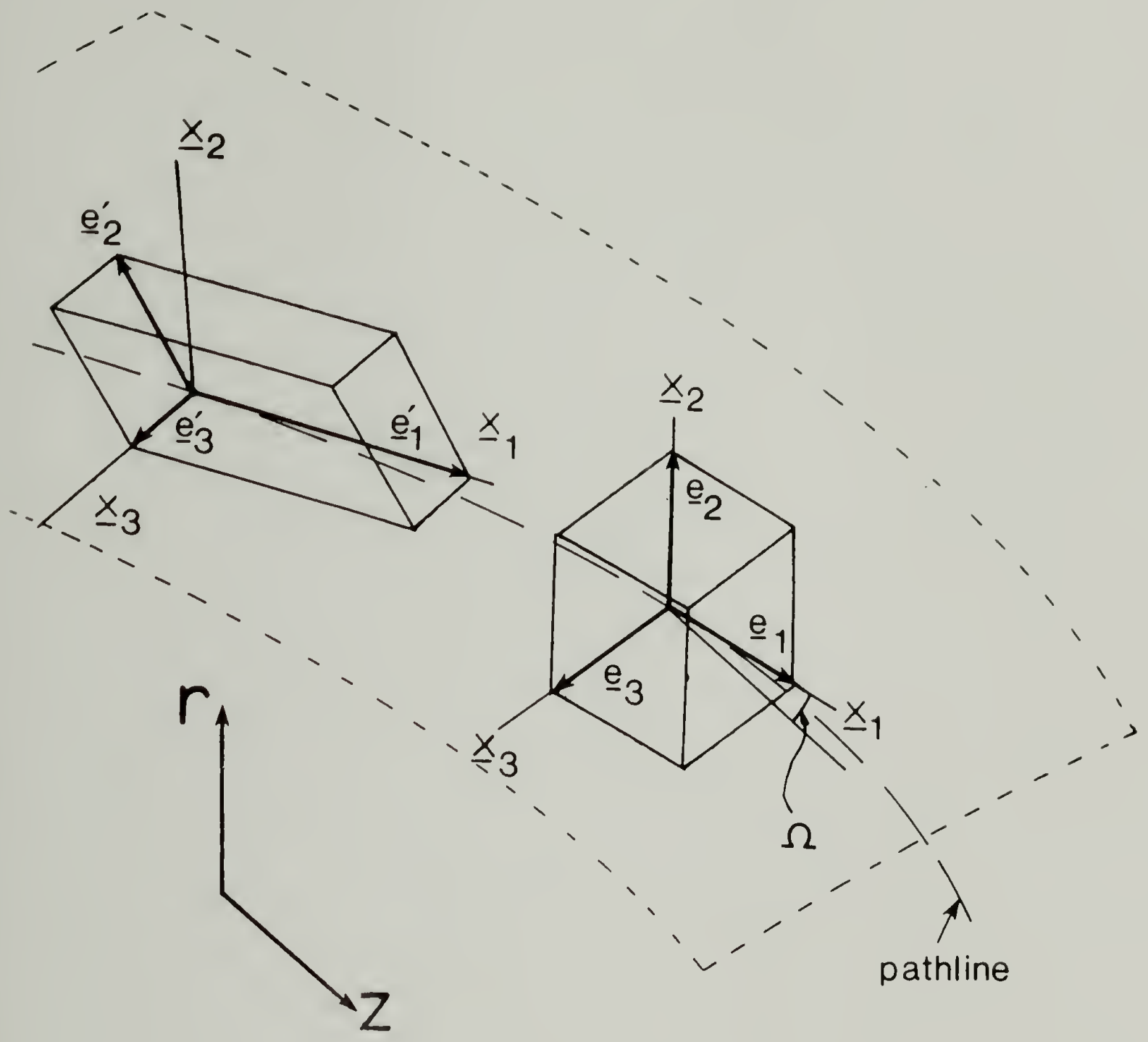

Figure 4.2. Deforming material element in axisymmetric flow.

$$\underline{e}_1' = (L_1^{-1},0,0) \tag{4.7}$$

$$\underline{e}_2' = (-\gamma L_2^{-1},L_2^{-1},0) \tag{4.8}$$

$$\underline{e}_3' = (0,0,L_3^{-1}) \tag{4.9}.$$

The Finger strain tensor for <u>shear</u> and <u>extension superimposed</u> is then, from Eqs. (2.2) and (2.3)

$$\underline{\underline{C}}^{-1}(t',t) = \begin{pmatrix} (1+\gamma^2)L_1^2 & -\gamma L_1 L_2 & 0 \\ -\gamma L_1 L_2 & L_2^2 & 0 \\ 0 & 0 & L_3^2 \end{pmatrix} \tag{4.10}$$

The quantity L_1 is the stretch in the pathline direction given by

$$L_1(t',t)_\Psi = v_1(t)/v_1(t') \tag{4.11}$$

where v_1 is the velocity tangent to the streamline for axisymmetric flow and the subscript Ψ denotes that the strain is evaluated on each streamline. The quantity L_3 is the stretch in the circumferential direction given by

$$L_3(t',t)_\Psi = r(t)/r(t') \tag{4.12}$$

where r is the radius of the streamline. The stretch L_2 is the change in separation of neighboring stream surfaces and is given by

$$L_2(t',t)_\Psi = \rho(t')/(\rho(t)L_1L_3) \tag{4.13}.$$

The shear strain γ is the tangent of the shear angle and is given by

$$\gamma(t',t)_\Psi = \frac{L_2(t',t)}{L_1(t',t)} \int_{t'}^{t} \left(\frac{L_1(t'',t)}{L_2(t'',t)} \dot{\gamma}_{21}(t'') \right)_\Psi dt'' \tag{4.14}.$$

One interesting result of Eq. (4.14) is that the shear strain not only depends on the shear rate, $\dot{\gamma}_{21}$, but also on the stretches L_1 and L_2. This equation for the shear strain was not used in the initial modeling calculations of flow through extrusion dies (Winter and Fischer, 1981). For dies of constant annular cross-section ($L_1=L_2=L_3=1$), Eq. (4.14) reduces to the equation used in the previous reference and for dies having very little contribution to the extensional deformation the results are not significantly different. However, for dies producing significant amounts of extensional deformation, the improved shear strain relationship is required. This improved tracking procedure is used in this study.

The components of the Finger strain tensor are evaluated for each streamline in a coordinate system which is tilted by an angle

$$\Omega = \tan^{-1}(v_r/v_z) \tag{4.15}$$

with respect to the z-axis of the global cylindrical coordinate system of the flow. The residence time of the material element on the streamline is

$$(t-t')_\Psi = \int_{z'}^{z} (v_z^{-1})_\Psi dz \tag{4.16}.$$

4.3 Calculation of the Stress State of a Material Element

Now that the rheological parameters of the polymer are known and a tracking procedure has been developed to determine the strain history, the calculation of the stress distributions inside annular extrusion

dies is accomplished by using the memory integral constitutive equation of Eq. (2.43). The stress state of a material element at some axial position in the dies is calculated by numerical integration of Eq. (2.43) back along the streamlines towards the inlet of the die. The integration is performed along each streamline so, due to the upstream history, a distribution of the stress tensor and not simply an average stress along the flow channel is obtained.

The streamlines are divided into small time intervals which are determined by the initial choice of the axial grid size. The contribution to the total stress is then obtained for each interval going back towards the entrance to the die. If, during the course of the integration of the stress acting on the material element over all the time intervals, the contribution to the total stress becomes sufficiently small, the remaining contribution to the integral is disregarded and the integration along that streamline is terminated.

The stress calculation is therefore terminated when either of two criteria is met. The first criterion requires that the calculation is terminated if the contribution to the component of normal stress in the direction of flow from the last interval is approximately less than 0.001% of the total normal stress in the direction of flow at that point in the integration. The component of the normal stress in the flow direction is chosen as a criterion because it contains a squared dependency of both the shearing and stretching components in the Finger strain tensor and it therefore continues to contribute to the total stress longer than the shear stress. This criterion allows the complete

stress due to the upstream history to be determined for all the components. This criterion is usually met for streamlines that are close to the walls of the die where there are large shear strains which cause the strain function in the constitutive equation to rapidly decrease and subsequently cause the contribution of the stress over a particular time interval to become insignificant.

The second criterion is more obvious and requires that the integration be terminated when the inlet of the die is reached and the last grid point is encountered. This criterion is often met for streamlines that are near the center of the flow channel where the total accumulated shear strain tends to be small and therefore the strain function does not decrease to zero in such a rapid manner. The question of whether the stress calculated up to that point is a true description of the total stress for a material element along that streamline, or whether the deformation in the flow channel prior to the die entrance has an appreciable contribution to the total stress must be addressed. In order to investigate this question, a method for estimating the additional contribution to the total stress due to the flow in channels upstream of the die entrance was formulated. This method gives an upper bound for the stress contribution upstream of the die entrance.

4.3.1 Stress Contribution Upstream of the Die Entrance

To estimate the contribution to the total stress of a material element due to deformation upstream of the die entrance, two assumptions are made:

(a) The material elements on each streamline are at a constant temperature prior to the die entrance. This temperature is the same as the temperature of the first material element on the same streamline that is at the die entrance.

(b) The material elements do not have any relative deformation between the die entrance and all prior times. In other words, the values of the relative Finger strain tensor and the strain function are constant and equal to the values for the material element on the same streamline that is just at the die entrance.

In reality there is some finite deformation between the die entrance and all prior states but these assumptions were made to simplify the analysis and give an upper bound for the estimation of the contribution to the total stress upstream of the die entrance. This estimation is now discussed in more detail.

Consider a die flow channel where t is the time at some position inside the die and t* is the time at the die entrance. In order to calculate the stress at time t inside the extrusion die, Eq. (2.43) is written as

$$\underline{\underline{\sigma}}(t) = -p\underline{\underline{I}} + \int_{-\infty}^{t^*} \mu(t',t)h(I(t',t))\underline{\underline{C}}^{-1}(t',t)dt'$$

$$+ \int_{t^*}^{t} \mu(t',t)h(I(t',t))\underline{\underline{C}}^{-1}(t',t)dt' \qquad (4.17).$$

The second integral in Eq. (4.17) is over the time interval (t*,t) and is the contribution to the total stress that is calculated by the

integration over the grid points in the die. The first integral in Eq. (4.17) is the additional stress contribution upstream of the die entrance, over the time interval $(-\infty,t^*)$ and is given by

$$\underline{\underline{g}}_A(t) = \underline{\underline{g}}(t)-p\underline{\underline{I}} = \int_{-\infty}^{t^*} \mu(t',t)h(I(t',t))\underline{\underline{C}}^{-1}(t',t)dt' \qquad (4.18).$$

Now assuming that the material element has a constant temperature and that there is no relative deformation upstream of the die entrance, the strain function and the Finger strain tensor become independent of time and are taken outside the integral. Eq. (4.18) can then be rewritten as

$$\underline{\underline{g}}_A(t) = h(I(t-t^*))\underline{\underline{C}}^{-1}(t^*,t) \int_{-\infty}^{t^*} \mu(t',t)dt' \qquad (4.19).$$

The integral in Eq. (4.19) is seen to be nothing more than the linear viscoelastic modulus evaluated at $(t-t^*)$. This yields the equation that is used in the modeling procedure to estimate the upper bound of the extra stress contribution upstream of the die entrance

$$\underline{\underline{g}}_A(t) = \overset{\circ}{G}(t-t^*)h(I(t-t^*))\underline{\underline{C}}^{-1}(t^*,t) \qquad (4.20).$$

An upper bound is given since $\overset{\circ}{G}$ and h are exponentially decaying functions of the time interval $(t-t^*)$ and the strain; whereas, the components of the Finger strain tensor can, at most, be quadratically increasing functions of the strain. Therefore even if a larger time interval (and hence strain) is used (i.e., numerically integrating even further upstream of the die entrance than the initial axial grid choice) the value for the extra stress contribution would be less. This method was developed for use in the modeling of flow through extrusion dues but

is applicable to other processing flows as well, although the information obtained must be analyzed carefully for each particular flow process.

4.3.2 Computer Program for Stress Calculations

A computer program written in FORTRAN was used to numerically calculate the stresses in annular flow. The program uses an algorithm for numerical quadrature to evaluate the integral of Eq. (2.43) by means of the modeling procedure of this chapter. The calculations were performed on a Digital, Inc. (PDP 11/34) computer. A flow chart of the program showing the important subprogram units appears in Figure 4.3. The code for the major program units appears in Appendix B.

The main program, DIEB, handles the input of the rheological parameters, density parameters, die geometry, grid size and the processing parameters of temperature and mass flow rate. Up to 40 axial grid points, corresponding to time intervals, and 21 radial grid points, corresponding to the number of streamlines, may be selected. The various steps of the modeling procedure have been separated into subroutines, with the main program calling these as needed. This division enables changes to the program to be easily made for other processing flows, for improvement of the various steps in the modeling or for including different forms of any of the functions. After the processing parameters and other input data have been read in by the main program, discrete values of axial velocity at every grid point are calculated.

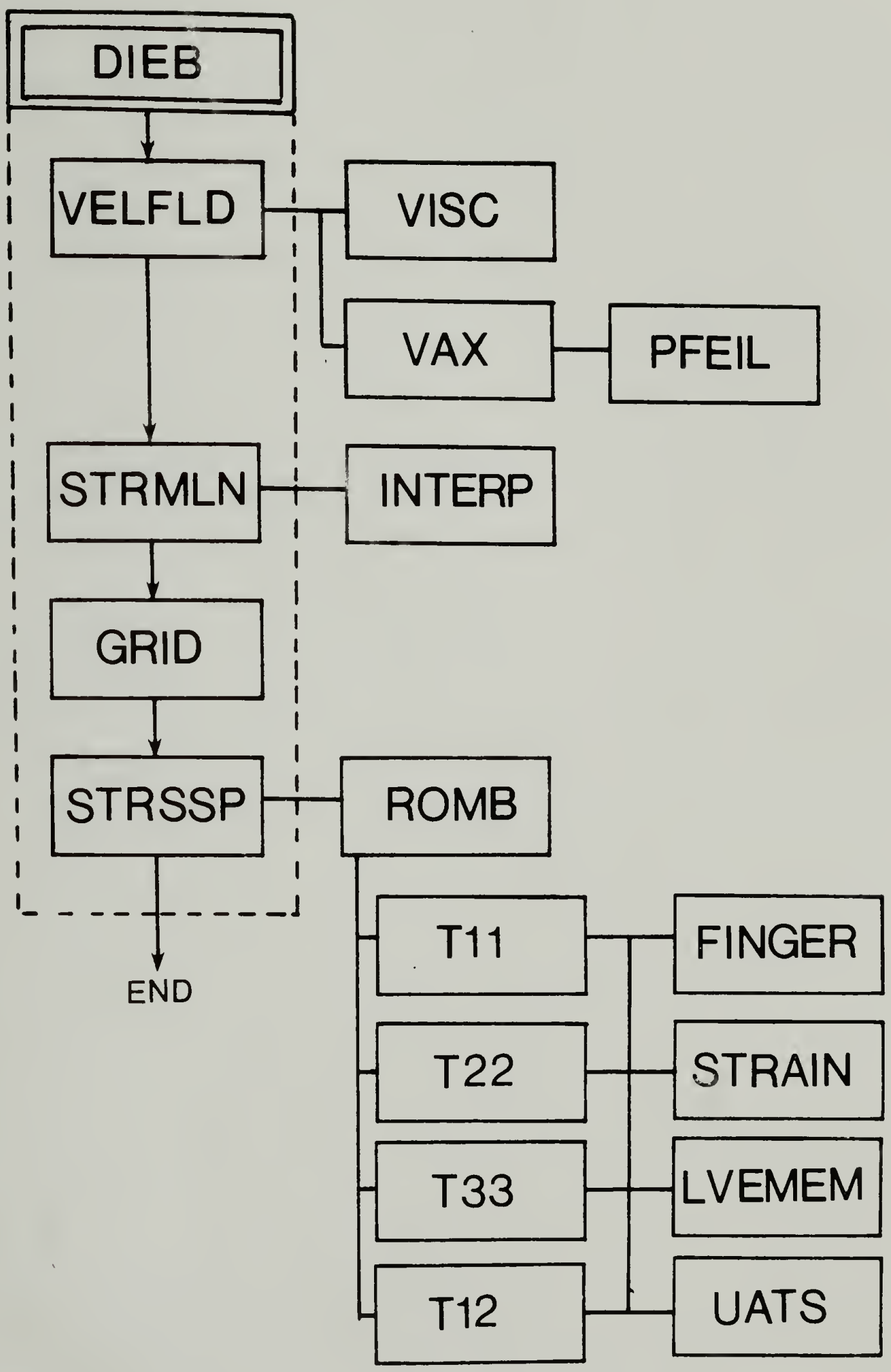

Figure 4.3. Flow chart of computer program for calculating stress distributions in annular extrusion dies.

The subroutine VELFLD calculates the velocity field in the annular flow channel using the procedure outlined in Section 4.2.1. A finer radial grid of 61 points is used to calculate the axial velocity distribution at each cross-section. The function subprogram VISC contains the desired function for the steady shear viscosity of Eq. (4.4). The subroutines VAX and PFEIL are then called to calculate the axial velocity distribution (Winter, 1977). After the kinematics have been determined, the discrete values of velocity and radius are determined for the streamlines of the flow.

The subroutine STRMLN calculates the radial positions, axial velocities, local shear rates and residence times for material elements on each streamline inside the die channel. Only 21 of the 61 discrete axial velocities in the radial direction determined by VELFLD are used. Therefore the stress of material elements on nineteen streamlines (both the streamlines Ψ=0 and Ψ=1 at the walls are not calculated since v_z=0 on the bounding surfaces) are eventually calculated. The discrete values on the streamlines are obtained by interpolating between the values on the original radial grid when a streamline is found to be between two of the original radial grid points. This is done by the subroutine INTERP. The positions of the original radial grid points may be changed in which case new radial grid point positions are assigned to correspond to the streamline positions. The number of grid points, however, stays the same. Having established the streamlines of the flow, the stretches, shear angle and residence times of the material elements are determined.

The subroutine GRID calculates the values of the stretches from Eq. (4.11), (4.12), and (4.13), the shear strain, from Eq. (4.14), and the residence times, from Eq. (4.16), of a material element at each grid point along the streamlines. Having determined the strain history of the material elements, the stress is now calculated.

The stress state of a material element on a streamline at a desired point in the die is calculated by the subroutine STRSSP. The function subprogram ROMB solves the integration problem using a cautious Romberg extrapolation procedure to find an acceptable estimate of the subfunctions T11, T22, T33 and T12 over a given time interval. The subfunctions T11, T22, T33 and T12 correspond to the three normal stresses and the shear stress respectively. The subroutine FINGER calculates the components of the Finger strain tensor, the subroutine STRAIN calculates the strain function, the subroutine LVEMEM calculates the non-isothermal linear viscoelastic memory function and the subroutine UATS calculates the shift factors and non-isothermal time interval at points between the limits of integration of the interval. Both the strain functional, Eq. (2.51), as given by the irreversibility assumption and the stress contribution upstream of the die entrance, as discussed in the previous section, are included in the subroutine STRSSP.

After the stresses have been calculated for each streamline, the remainder of the main program DIEB calculates a retardation angle due to the average flow birefringence across the gap and provides a printout of the stress distributions as a function of dimensionless radial position. The flow birefringence calculations are discussed in the next chapter.

C H A P T E R V

ANNULAR DIE FLOW

The modeling of annular extrusion was chosen for study because it is a fundamental part of polymer shaping processes such as film blowing, blow molding, and pipe extrusion. One advantage of studying the flow in annular dies is that various amounts of extensional deformation can be imposed on the flowing polymer just by the addition of diverging and/or converging sections in the die. Thus extensional flow can be studied in these types of dies. One disadvantage is that there are always large shear deformations superimposed due to the bounding walls of the channel. This superposition makes the flow a complex mixture of shear and extension. Nonetheless, this complex flow is of technological interest and the availability of a modeling technique to quantitatively describe the state of the polymer at the die exit would be a major contribution to the field of process modeling.

The state of the polymer at the die exit has a large influence on the swelling of the extrudate (Orbey, 1983), the bubble shapes in film blowing and blow molding, and the mechanical properties in the solid state. This chapter describes the experimental measurement of the state of orientation due to the upstream flow history in annular dies of differing cross-sections. The measurement of the stress state at the die exit, using a flow birefringence technique, is compared with the predictions from the modeling calculations.

5.1 Flow in Converging and Diverging Annular Dies

Three annular dies, having different channel geometries, were chosen for flow experiments and appear in Figure 5.1. Die I has a constant annular cross-section from the entrance region to the die exit. Die II has a converging section, and Die III has a diverging section immediately before the die exit. The annular die produces only a shearing deformation in the flow (except for the small region near the die entrance); whereas, the converging and diverging dies produce a complex flow having both shear and extensional deformations superimposed. The converging and diverging sections of Dies II and III taper to the same constant annular dimensions of Die I so the effect that these sections have on the flow in a downstream annulus can be investigated.

The exit region of the dies consists of glass components which have the same annular dimensions of Die I. The glass annulus is required for optical studies inside the die. The measured flow birefringence is related to an average normal stress difference through the stress-optical law. Measurements of flow birefringence are compared to the modeling calculations. The flow birefringence is measured at some distance downstream of the converging and diverging sections to see what effects these sections have on the internal stress field. By analysis of these three types of dies (straight annular, converging and diverging), the flow in dies having a combination of these sections is more easily understood. This understanding helps one not only in analyzing the performance of existing dies but also in the design of new extrusion dies.

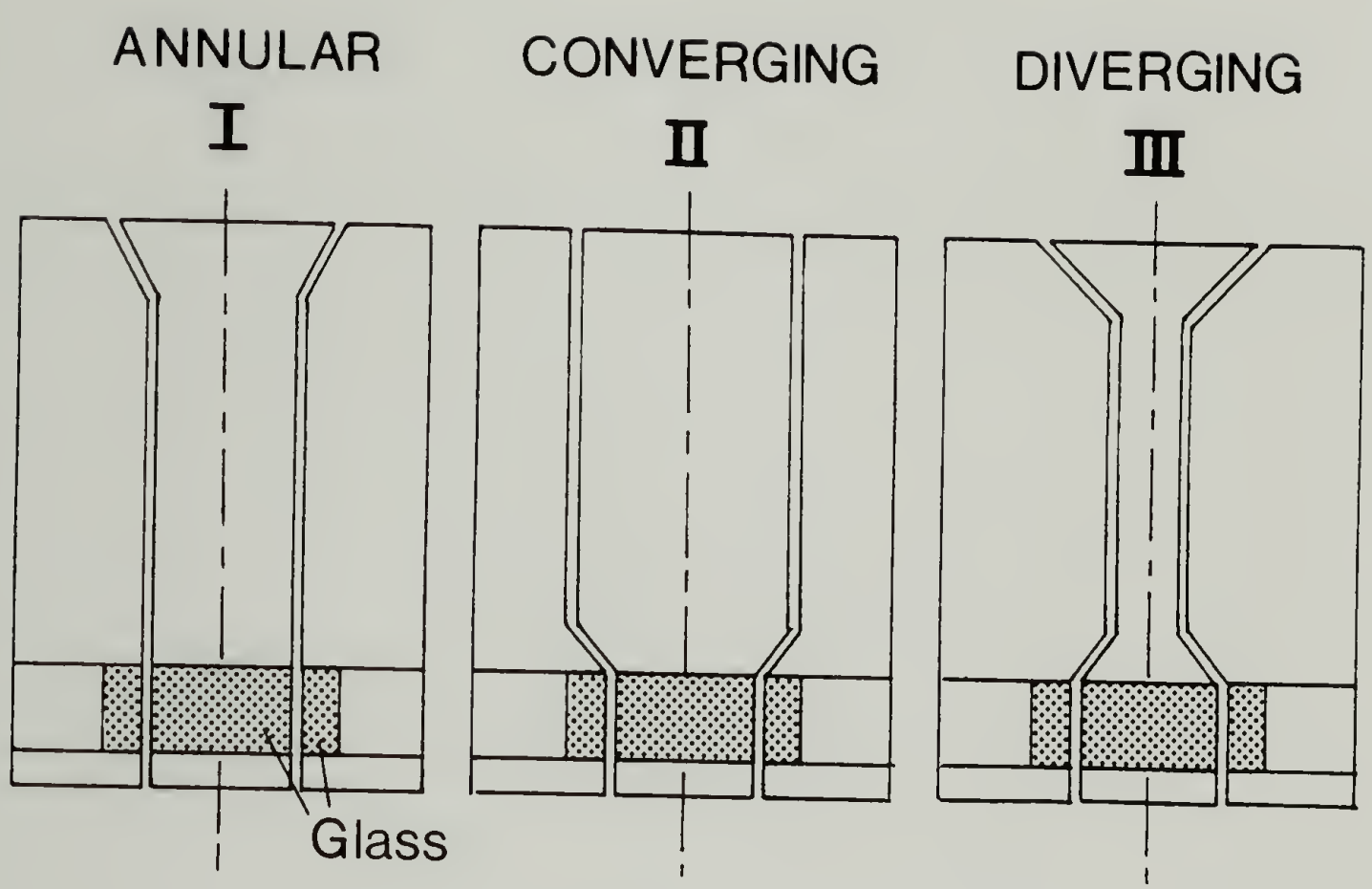

Figure 5.1. Die designs used in flow experiments.

When designing extrusion dies for a specific process, three major aspects are often of interest. First, a knowledge of the pressure required to generate specific flow rates is desired to specify the size and power requirements of the extruder and to estimate the production rates for specific polymers. Secondly, the deformation history of a material element through the die is needed to indicate if there are any regions of high deformation or long residence times which may be extremely important in the degradation of highly deformation or temperature sensitive polymers. Finally, the stress state at various positions in the die is of considerable interest, especially near the exit, since the stress state is associated with molecular orientation, which in turn may affect the final mechanical properties of the resultant part. Preliminary calculations obtained from the modeling procedure were used as a guide in the design of suitable annular dies which were used for the flow experiments.

5.1.1 Pressure Drop Calculations

Pressure drop calculations were performed using the equations developed for the determination of the kinematics of annular flow which were presented in Section 4.2.1. The stress equation of motion is determined from Eq. (4.1) for each small interval dz and the total pressure drop, ΔP, is obtained by integrating over the entire axial length of the die channel to obtain

$$\Delta P = P^* - P_o = \int_{z_o}^{z^*} (\partial p/\partial z)dz \tag{5.1}$$

where "o" indicates the die exit and "*" indicates the die entrance.

Three different models were used for calculating the steady shear viscosity function found in Eq. (4.2). The first was the power-law or Ostwald-deWaele model

$$\eta_s(\dot{\gamma}) = \eta^o|\dot{\gamma}/\dot{\gamma}^o|^{n-1};\ \eta^o = \eta_s(\dot{\gamma}^o) \tag{5.2}$$

where $\dot{\gamma}^o$ is a reference shear rate and n is the dimensionless power-law exponent. The second model used was the Carreau model

$$\eta_s(\dot{\gamma}) = (\eta_o - \eta_\infty)[1+(\lambda\dot{\gamma})^2]^{(n-1)/2} + \eta_\infty \tag{5.3}$$

where η_o is the zero-shear-rate viscosity, η_∞ is the infinite-shear-rate viscosity, λ is a time constant and n is the dimensionless power-law exponent. Both of these models are described by Bird et al. (1977a).

The third model for the steady shear viscosity was obtained from the same memory integral constitutive equation used to calculate the stress in the subsequent calculations and is given by Eq. (4.4). Since both the sigmoidal and sum of two exponential forms of the strain function in the memory integral constitutive equation predict similar steady shear viscosities as seen in Figures 3.34, 3.35 and 3.36, the form having the sum of two exponential functions was used in the velocity field calculation because it can be solved analytically. This functional form for the steady shear viscosity is given by Eq. (4.5). Using these considerations, the calculated pressure drop in the three dies was compared to experimental measurements.

5.1.2 Strain History and Stress Calculations

The strain history that a material element experiences is extremely important for many processing applications. The measure of the strain history is found in the components of the Finger strain tensor which consist of the various stretches in three mutually perpendicular directions and the shear strain. The stretches and shear strains are found for a material element on each streamline using the tracking procedure described in Section 4.2.2. By inspection of these stretches and shear strains at positions inside the die, a quantitative description of the deformation history is obtained, regardless of the choice of constitutive equation.

Due to the geometry of annular flow, the most convenient direction to measure the flow birefringence is in the shearing plane (1-3 plane), which will be discussed in more detail in the next section. Because of this particular measurement direction, the three dies were designed specifically to maximize the difference between the expected flow birefringence in the 1-3 plane. In order to achieve this, a large difference between the normal stress difference in the shearing plane, $(\sigma_{11}-\sigma_{33})$, for the three different dies was required.

By inspection of the relative Finger strain tensor for annular flow, Eq. (4.10), it is seen that to maximize the difference between C_{11}^{-1} and C_{33}^{-1} the dies should have large differences in the axial stretches, L_1 and circumferential stretches, L_3, assuming that the shear is similar in all three dies. For constant annular dies there is no stretching, but in diverging and converging dies the stretches L_1 and

L_3 can be increased or decreased by the particular design of the geometry. With these considerations in mind, preliminary calculations of the stress distributions were made to aid in the design of the dies which were used in this study. The specific dies are described in detail in the experimental section of this chapter.

The specifics of the stress calculations are now discussed in terms of the various coordinate systems of (z,r,Θ), $(1,2,3)$ and $(1',2',3')$ all of which are shown in Figure 5.2. The components of the stress tensor are found by solving the integral constitutive equation for a material element on a particular streamline. The stress components are therefore calculated for the local coordinate system of the deforming material element on a pathline, $(1,2,3)$. If the annular section where the stress is calculated has a constant cross-section, then the local coordinate system of the material element $(1,2,3)$ and the global coordinate system for axisymmetric flow (z,r,Θ) are coincident (Ω=0 radians).

In order to determine the principal stress components of the stress tensor, which is required to analyze the flow birefringence measurements, the stress components in the $(1,2,3)$ coordinate system are transformed by use of the rotation matrix

$$\underline{\underline{R}} = \begin{pmatrix} \cos\phi & \sin\phi & 0 \\ -\sin\phi & \cos\phi & 0 \\ 0 & 0 & 1 \end{pmatrix} \tag{5.4}$$

and the relation

$$\underline{\underline{\sigma}}' = \underline{\underline{R}}^{-1} \cdot \underline{\underline{\sigma}} \cdot \underline{\underline{R}} \tag{5.5}$$

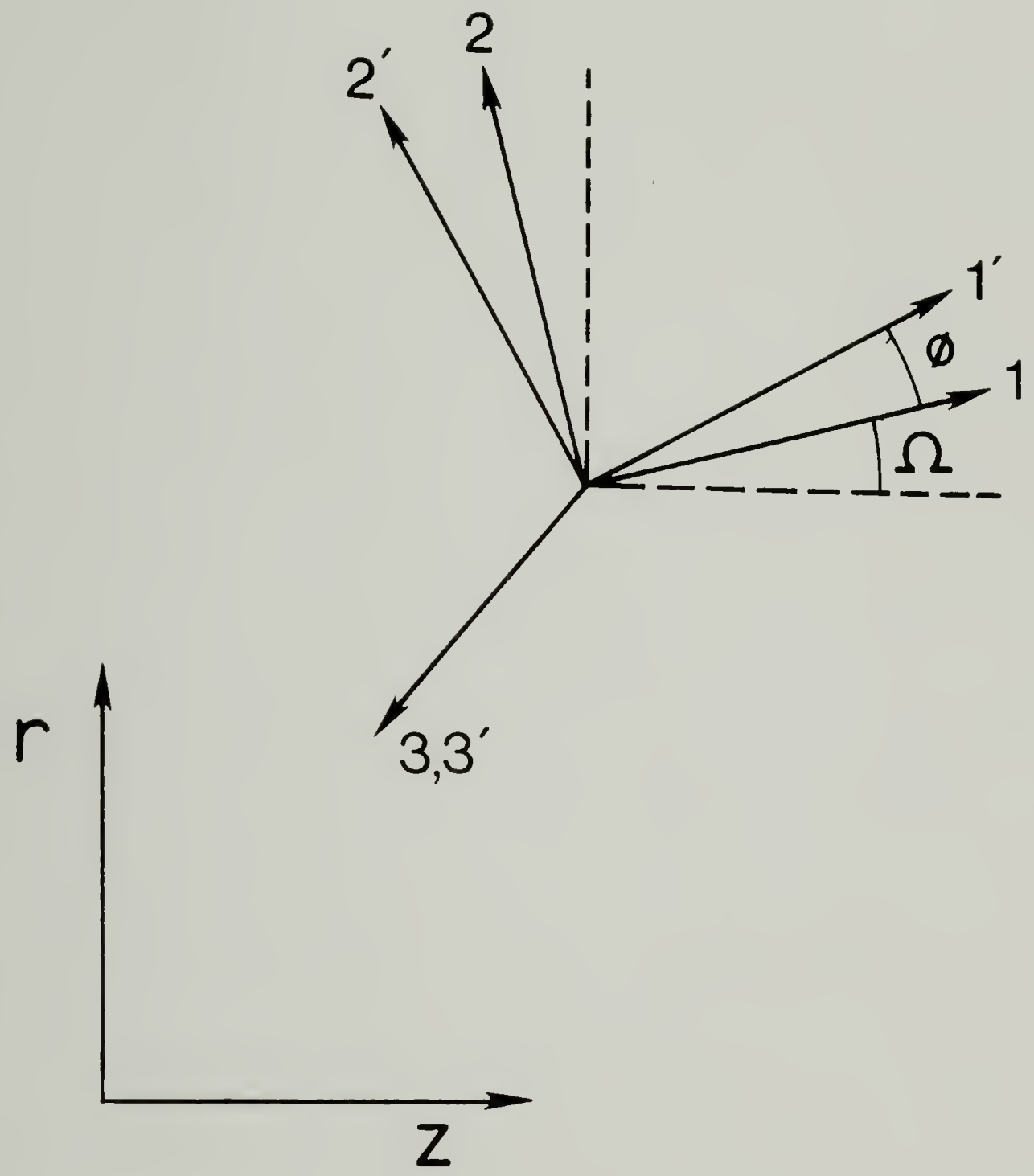

Figure 5.2. Coordinate systems in annular die flow.
(z,r,Θ) global cylindrical coordinate system of axisymmetric flow
(1,2,3) local coordinate system of the material element on a pathline
(1',2',3') local principal coordinate system of the material element

where $\underline{\sigma}'$ is the principal stress tensor which consists only of diagonal components.

The angle ϕ is obtained from the relation

$$\tan 2\phi = 2\sigma_{21}/(\sigma_{11}-\sigma_{22}) \qquad (5.6).$$

The components of the principal stress tensor are then found to be

$$\sigma'_{11} = \sigma_{11}\cos^2\phi + \sigma_{22}\sin^2\phi + 2\sigma_{21}\sin\phi\cos\phi \qquad (5.7)$$

$$\sigma'_{22} = \sigma_{11}\sin^2\phi + \sigma_{22}\cos^2\phi - 2\sigma_{21}\sin\phi\cos\phi \qquad (5.8)$$

$$\sigma'_{33} = \sigma_{33} \qquad (5.9)$$

$$\sigma'_{21} = \sigma'_{12} = 0 \qquad (5.10).$$

In summary, for the annular die flow experiments, the stress components are calculated for each streamline (in the (1,2,3) coordinate frame) and transformed to the principal coordinate frame (1',2',3'). Once the principal stress components are evaluated the results are compared to the flow birefringence measured across the annular gap.

5.1.3 Flow Birefringence Across an Annular Gap

The use of the flow birefringence technique, along with the stress-optical law, to measure stress levels in polymer processing flows has been discussed in the second chapter. This technique is used to measure an average normal stress difference inside the annular extrusion dies. A sketch of the flow birefringence measuring technique appears in Figure 5.3. A polarized monochromatic laser light beam passes through the outer glass, the flowing polymer, another piece of glass, another channel of melt, another layer of glass, and finally through another

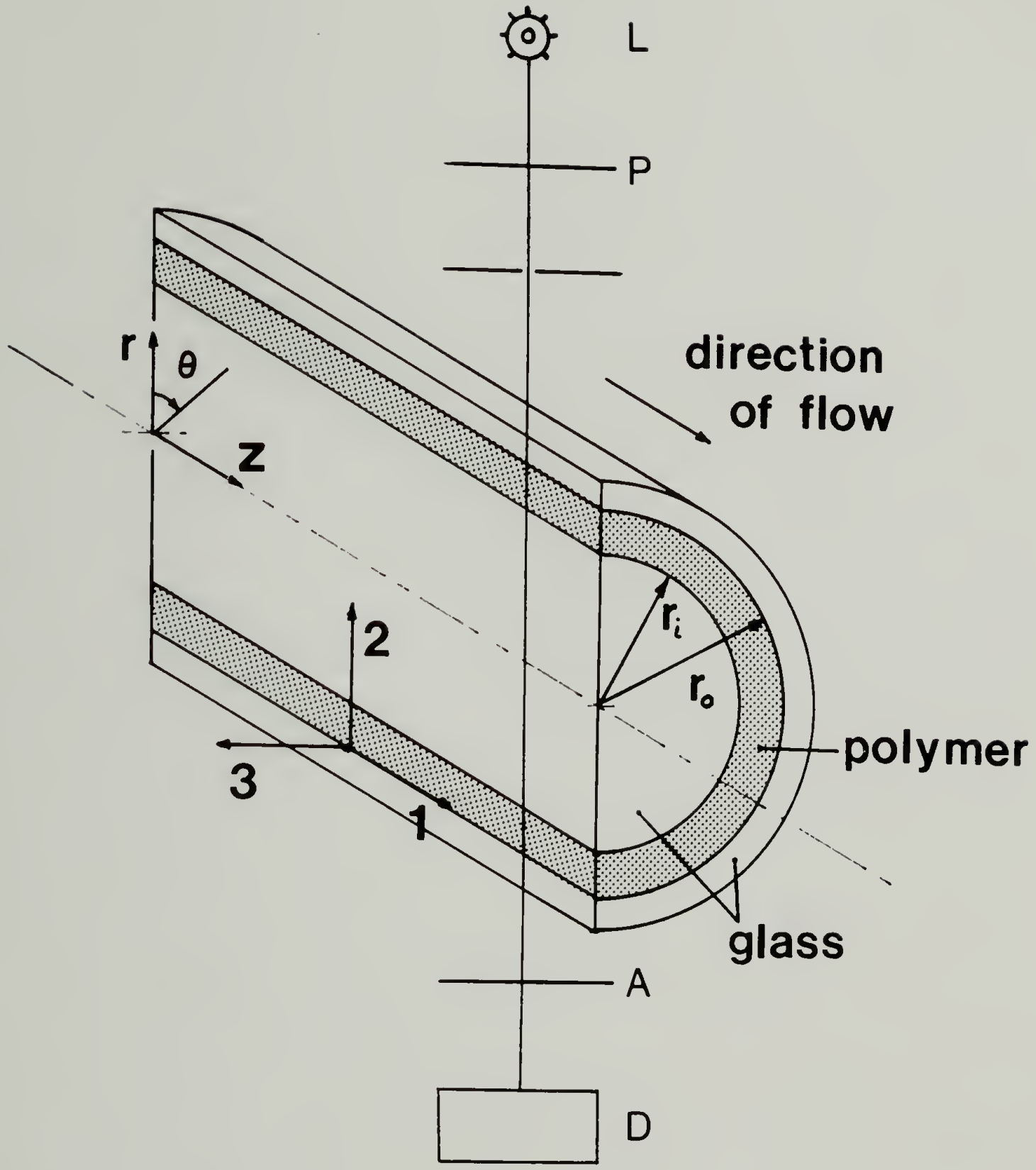

Figure 5.3. Flow birefringence measurement in annular flow. Light beam is along the 2-direction perpendicular to the 1-3 plane. L - laser, P - polarizer, A - analyzer, D - photomultiplier detector.

polarizer set at 90° to the first (called an analyzer) after which the intensity is measured. Since the pieces of glass form an annular flow channel of constant cross-section, the coordinate system of the streamlines, (1,2,3), and the global coordinate system, (z,r,Θ), are coincident. The beam is directed radially along the 2-direction, so the measurements are taken perpendicular to the 1-3 plane which is the shearing plane of the flow. The first measurements of the flow birefringence of a polymer melt were, in fact, carried out in the 1-3 plane of shear flow (Dexter et al., 1961). A sandwich device was used to measure the flow birefringence as a function of shear rate and temperature. A slit apparatus was also developed for measuring an average flow birefringence in the 1-3 plane (Wales, 1976). In this case the beam passes through two channels of melt so twice the signal is measured.

Assuming that the flow birefringence is constant along an optical path length, L_p, the retardation angle, δ (the angle of phase difference between the transmitted light in the principal directions), for the light beam perpendicular to the 1-3 plane is

$$\delta = 2\pi L_p[n_1-n_3]/\lambda_o \qquad (5.11)$$

where λ_o is the wavelength of the laser light in vacuum and $[n_1-n_3]$ is the difference of the principal refractive indices in the 1- and 3-directions. The previous equation presumes that the birefringence is constant over the entire optical path, but since the stress field is non-homogeneous across the annular gap, the direction of the principal axes of the stress (and the refractive index, from the stress-optical

law) changes and hence the birefringence varies over the optical path. Therefore, Eq. (5.11) must be replaced by the integral relationship for the total retardation angle

$$\delta_T = 4\pi/\lambda_o \int_{r_o}^{r_i} [n_1 - n_3](r)\, dr \tag{5.12}$$

where r_o and r_i are the outer and inner radii of the flow channel from which an average birefringence in the 1-3 plane can be defined as

$$n_{13} = \lambda_o \delta_T / [4\pi(r_o - r_i)] \tag{5.13}$$

where δ_T is experimentally measured.

To relate the retardation angle measured with the flow birefringence technique to the stress difference distribution predicted from the modeling, a procedure for calculating the retardation angle for a situation where the optic axis changes across the optical path must be used.

The correct measurement of the birefringence in a non-uniform medium is given by Ong et al. (1974). For the situation where the birefringent medium is of variable refractive index and optic axis orientation, a complex Jones matrix procedure must be used to obtain the true total retardation angle, δ_T. A discussion of Jones matrix calculations is given by Shurcliff (1962) and Theocaris and Gdoutos (1979). The total retardation angle is obtained as follows.

Consider a point, P, somewhere in the annular flow channel as shown in Figure 5.4 where the coordinate system of the flow is (1,2,3) and the principal coordinate system is (1',2',3'). The optical

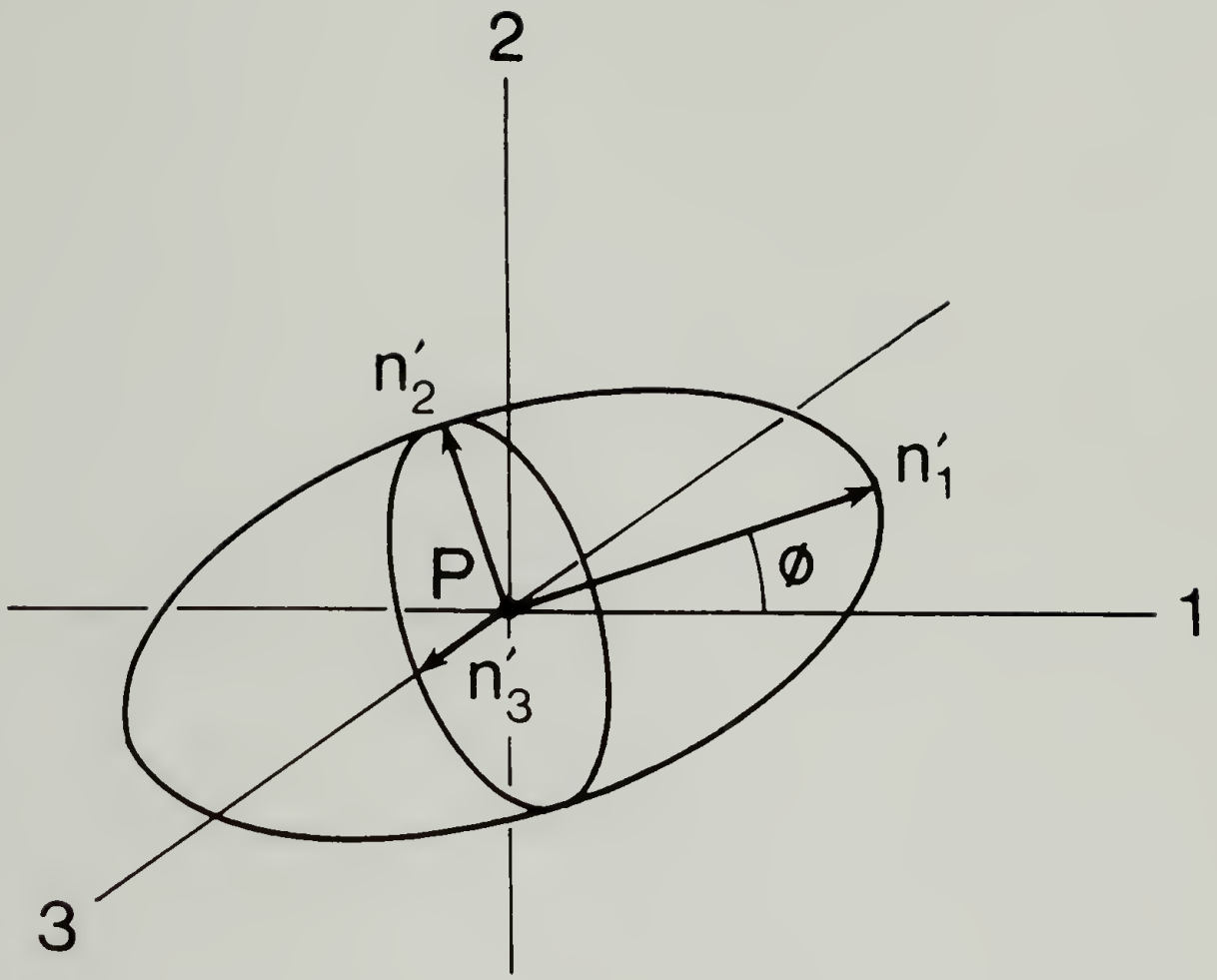

Figure 5.4. The refractive index ellipsoid at some point, P, in an annular flow channel. Light beam is along the 2-axis and perpendicular to the 1-3 plane. The principal refractive indices are coaxial with the principal stress components and related by the stress-optical law.

properties of this point P are represented by the indicatrix tensor

$$\underline{\underline{N}}' = \begin{pmatrix} (n_1')^{-2} & 0 & 0 \\ 0 & (n_2')^{-2} & 0 \\ 0 & 0 & (n_3')^{-2} \end{pmatrix} \tag{5.14}$$

where n_1', n_2' and n_3' are the principal refractive indices. In terms of the coordinate system of the flow, n_3' always lies along the 3-axis and n_1' and n_2' lie in the 1-2 plane at an angle ϕ to the 1-axis. The indicatrix tensor in the coordinate system of the flow is then

$$\underline{\underline{N}} = \underline{\underline{R}}^{-1} \cdot \underline{\underline{N}}' \cdot \underline{\underline{R}} \tag{5.15}$$

where $\underline{\underline{R}}$ is the rotation tensor given in Eq. (5.4).

The indicatrix tensor then becomes

$$\underline{\underline{N}} = \begin{pmatrix} (n_1')^{-2}\cos^2\phi+(n_2')^{-2}\sin^2\phi & [(n_1')^{-2}-(n_2')^{-2}]\cos\phi\sin\phi & 0 \\ [(n_1')^{-2}-(n_2')^{-2}]\cos\phi\sin\phi & (n_1')^{-2}\sin^2\phi+(n_2')^{-2}\cos^2\phi & 0 \\ 0 & 0 & (n_3')^{-2} \end{pmatrix} \tag{5.16}.$$

The section of the indicatrix ellipsoid in the 1-3 plane is given by

$$N_{11}x_1^2 + 2N_{13}x_1x_3 + N_{33}x_3^2 = 1 \tag{5.17}$$

and its principal axis is inclined to the 3-axis by an angle, ψ, where

$$\tan 2\psi = 2N_{13}/(N_{11}-N_{33}) \tag{5.18}.$$

The principal refractive indices in the 1-3 plane are

$$n_1 = \left[(N_{11}+N_{33}) - \frac{N_{11}-\cos^2\psi(N_{11}+N_{33})}{1-2\cos^2\psi} \right]^{-1/2} \tag{5.19}$$

and

$$n_3 = \left[\frac{N_{11}-\cos^2\psi(N_{11}+N_{33})}{1-2\cos^2\psi} \right]^{-1/2} \tag{5.20}.$$

From Eq. (5.16), $N_{13}=0$. Consequently from Eq. (5.18), $\psi=0$ radians from which the principal refractive indices in the 1-3 plane for the annular geometry now become

$$n_1 = [(n_1')^{-2}\cos^2\phi + (n_2')^{-2}\sin^2\phi]^{-1/2} \tag{5.21}$$

and

$$n_3 = [(n_3')^{-2}]^{-1/2} \tag{5.22}.$$

Now, assuming that the flow channel can be divided into m thin layers, within which the refractive index is assumed to be constant; the retardation angle of the jth layer is

$$\delta_j = |n_1-n_3|[2\pi(r_o-r_i)]/\lambda_o m \tag{5.23}.$$

The effect of a thin layer of the birefringent polymer melt on the incident light wave can be represented by a two-by-two complex Jones matrix. The appropriate matrix for annular flow is

$$A_j = \begin{pmatrix} \cos(\delta_j/2) + i\sin(\delta_j/2) & 0 \\ 0 & \cos(\delta_j/2) - i\sin(\delta_j/2) \end{pmatrix} \tag{5.24}.$$

The effect over the entire channel gap is obtained from the product of all the matrices for the m layers

$$B = (A_m)(A_{m-1})(A_{m-2})\ldots(A_2)(A_1) \tag{5.25}.$$

From the matrix B, the total retardation angle is calculated as

$$\delta_T = \cos^{-1}[(B_{11}+B_{22})/(2\cos\omega_p)] \tag{5.26}$$

where

$$\omega_p = \tan^{-1}[(B_{21}-B_{12})/(B_{11}+B_{22})] \tag{5.27}.$$

By multiplying all the A_j matrices together one finds that, for the annular flow under consideration, $B_{21}=B_{12}=0$, and by substituting B_{11} and B_{22} into Eq. (5.26) the total retardation angle is simply the sum of the retardation angles in each thin layer of constant refractive index

$$\delta_T = \sum_{j=1}^{m} \delta_j \tag{5.28}.$$

Now, by using the stress-optical law of Eq. (2.59), the principal refractive indices in the indicatrix tensor, Eq. (5.14), are calculated from the stress components determined from the process modeling. The resulting predictions of the total retardation angle, obtained from the procedure developed above, are then compared to the measurements obtained from the flow birefringence experiments.

5.2 Experimental Procedure and Results

5.2.1 Polymers Investigated

The two polymers used in the annular flow experiments were described in Section 3.1. Both the LDPE and PS were used for the pressure drop measurements while only the LDPE was used for the flow birefringence measurements. The LDPE was chosen for the flow birefringence

measurements because of its high transparency and less tendency to trap bubbles in the melt state than the PS.

The melt density of the LDPE and PS was measured with a capillary rheometer by filling the barrel with polymer, heating to the desired temperature, allowing the polymer to equilibrate then extruding at a very low constant piston speed and weighing the amount of polymer extruded in a known period of time. The extrusion pressures never exceeded 2MPa. The melt densities appear in Figure 5.5. The density parameters of Eq. (2.56) appear in Table 5.1.

The parameters for the power-law model and the Carreau model of the steady shear viscosity were determined from Figures 3.34 and 3.36. They are also listed in Table 5.1.

Since the stress-optical coefficients of the particular polymers studied were not available, values from the literature for similar polymers were obtained (Wales, 1976) and are listed in Table 5.1. The stress-optical coefficient was reported to be constant for LDPE of varying molecular weight, molecular weight distribution, non-linear rheological behavior and temperatures.

5.2.2 Extrusion Dies

The annular extrusion dies used in the flow experiments were designed from the considerations mentioned in Section 5.1.2. A sketch of the die is shown in Figure 5.6. All pieces of the die were fabricated from steel except for the glass windows. The die consists of six main pieces: (a) an adapter which attaches the die body to the high pressure capillary rheometer barrel which is described in Section 3.2.4.3,

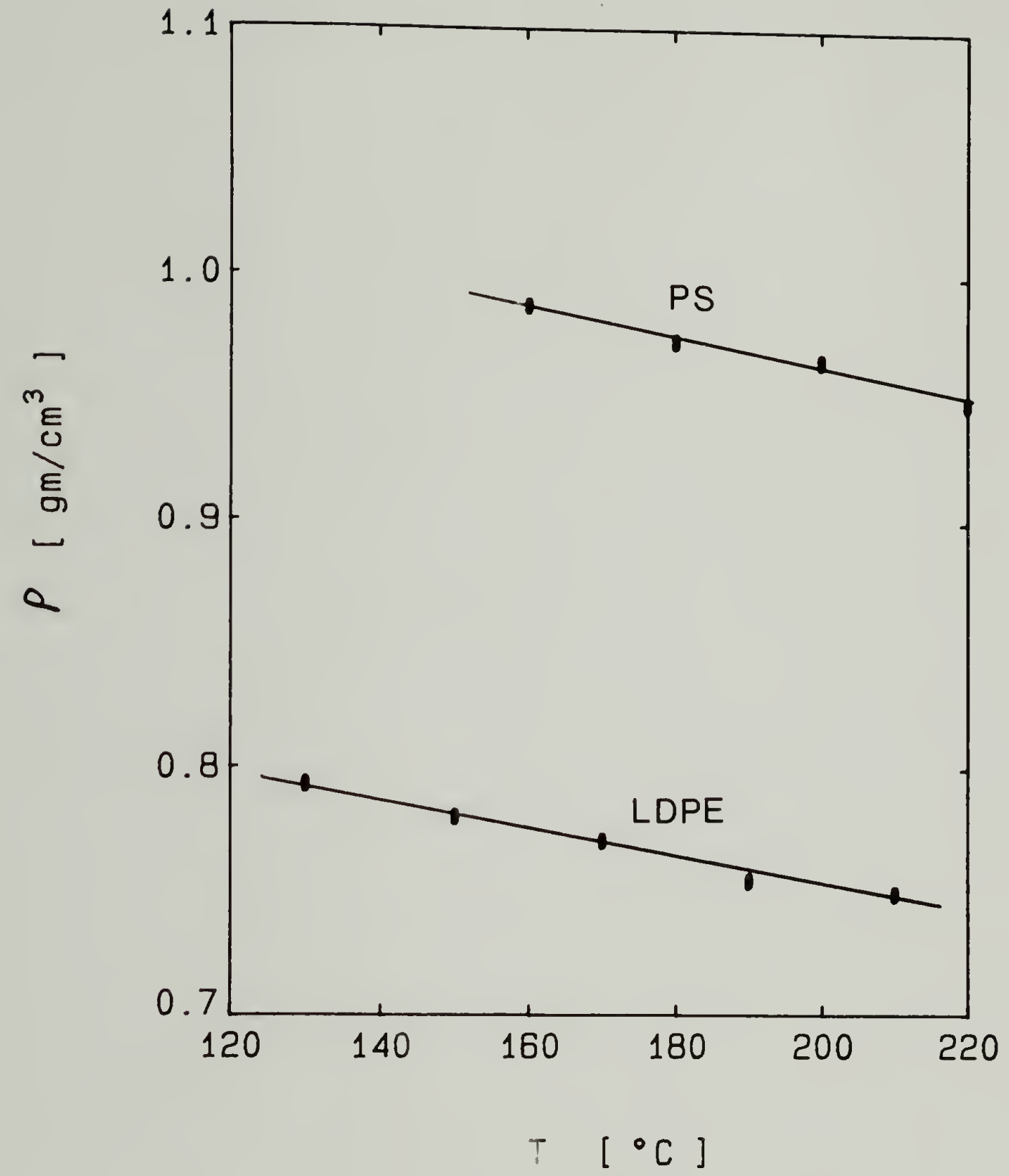

Figure 5.5. Melt density as a function of temperature.

Table 5.1. Density and rheological parameters of polymers used in die flow experiments.

	Polymers	
	LDPE	PS
Reference temperature, T_o [°C]	150	180
Density parameters of Eq. (2.56)		
Reference density, ρ_o [g/cm^3]	0.781	0.974
Coefficient of cubical expansion, β [K^{-1}]	7.27×10^{-4}	6.21×10^{-4}
Power-law parameters of Eq. (5.2)		
Reference shear rate, $\dot{\gamma}^o$ [s^{-1}]	100	100
Reference viscosity, η^o [Pa·s]	1.306×10^3	1.086×10^3
Power-law exponent, n	0.434	0.294
Carreau Model parameters of Eq. (5.3)		
Infinite-shear-rate viscosity, η_∞ [Pa·s]	0	0
Zero-shear-rate viscosity, η_o [Pa·s]	2.81×10^4	4.47×10^4
Time constant, λ [s]	2.09	2.06
Stress-optical Coefficient,* C [Pa^{-1}]	2.1×10^{-9}	-4.1×10^{-9}

*Values obtained from Wales (1976).

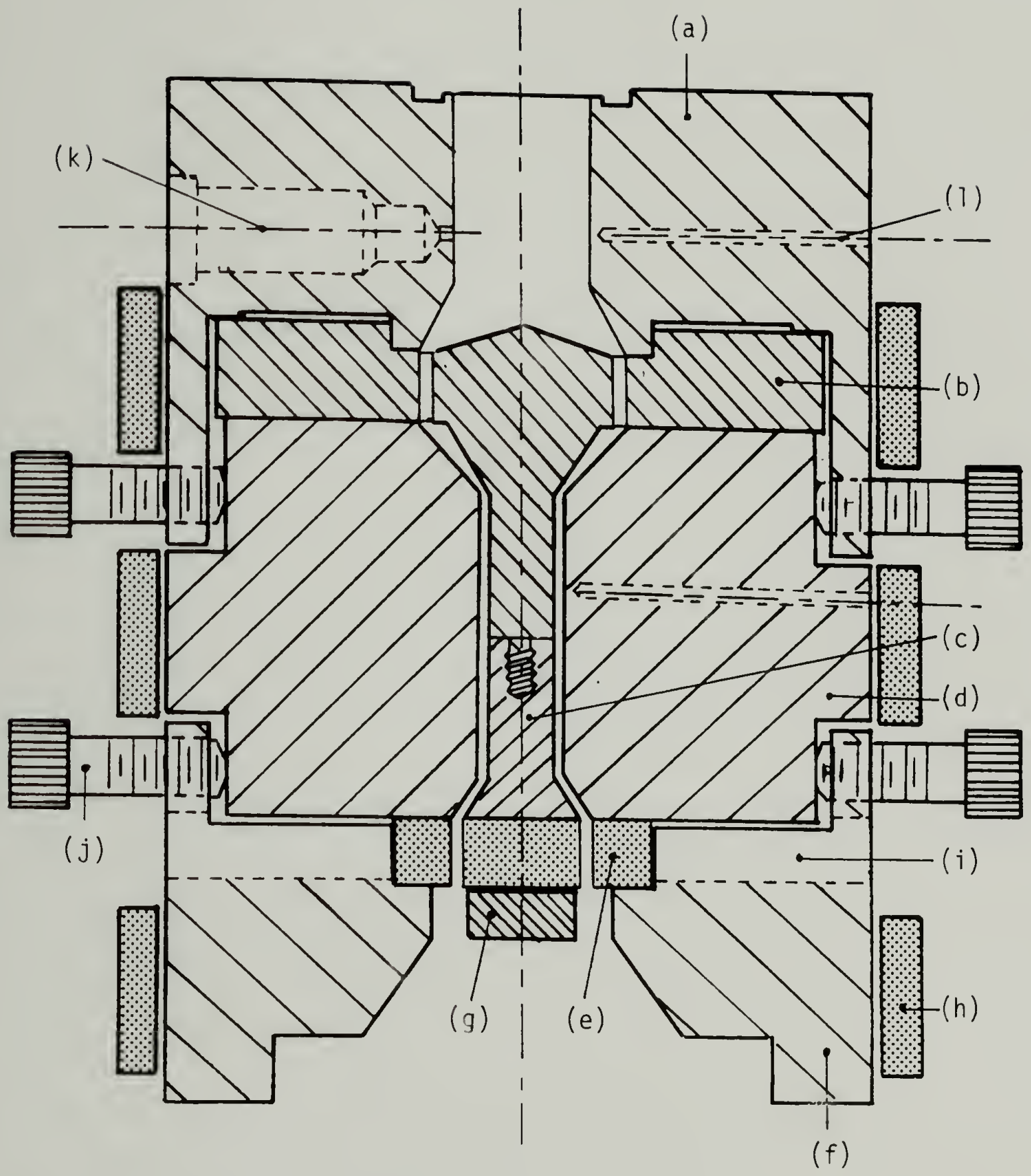

Figure 5.6. Annular extrusion die assembly.
(a) adapter. (b) inner mandrel, (c) inner die body,
(d) outer die body, (e) glass windows, (f) outer end cap,
(g) inner end cap, (h) heating bands, (i) horizontal slot,
(j) centering screws, (k) melt pressure transducer,
(l) thermocouple well.

(b) an inner mandrel, (c) and (d) interchangeable inner and outer die bodies which determine the channel geometry, (e) glass windows which make up the exit region of the die, and (f) an outer end cap which holds the outer glass window in place. The inner mandrel has a threaded post on which the different inner die bodies can be mounted. By changing the inner and outer die bodies, the three different die geometries are obtained. The centering screws allow both the outer die body and the outer glass window to be centered on the inner mandrel. The outer end cap has horizontal slots cut into it to allow the light beam to pass through the glass windows for the flow birefringence measurements.

Three heating bands (Watlow, 625W @ 240V) and associated controllers (Watlow, Series 808, PID) allow temperatures of 300°C$\pm$0.5K to be attained. Thermocouple wells are situated near the outer wall of the flow channel for accurate measurements of the temperature in that region. A melt pressure transducer (Dynisco, PT462E-3M-6/18) with a range of 0-20.6 MPa is mounted just upstream of the die entrance.

The actual dimensions of the steel part of the dies are given in Figure 5.7. All the dimensions were machined to $\pm$0.025 mm. A fine surface finish was applied to the surfaces that come in contact with the polymer melt.

The glass windows are made of fused silica glass (Corning Glass, 7940 U.V. Schlieren grade) which was machined to exact specifications. A sketch of the glass pieces appears in Figure 5.8. All dimensions are $\pm$0.025 mm. The center piece is attached to the inner die body by four small screws. The outer glass piece has four ground flat surfaces,

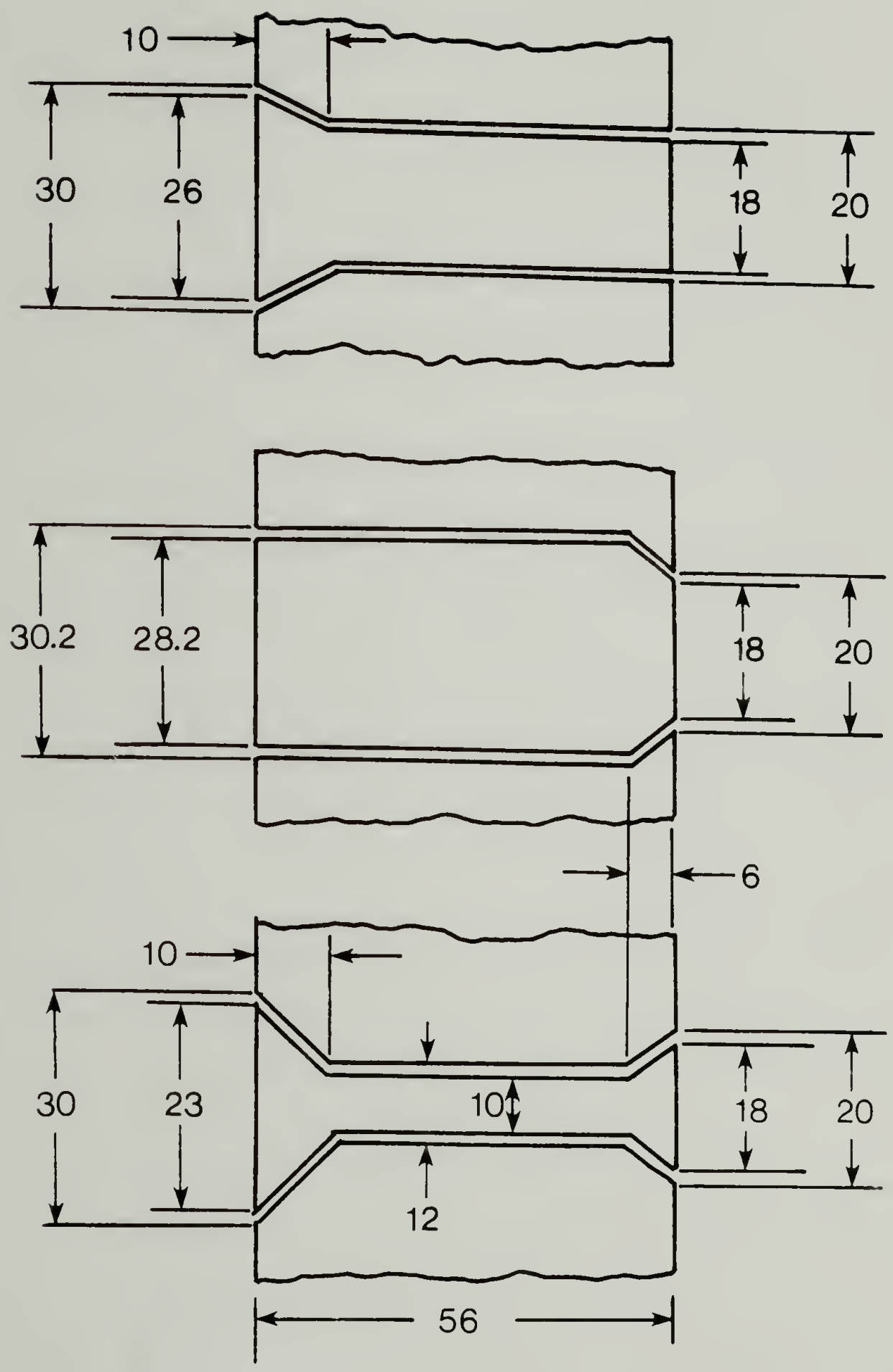

Figure 5.7. Dimensions of annular extrusion dies used in flow experiments. All dimensions are in mm.

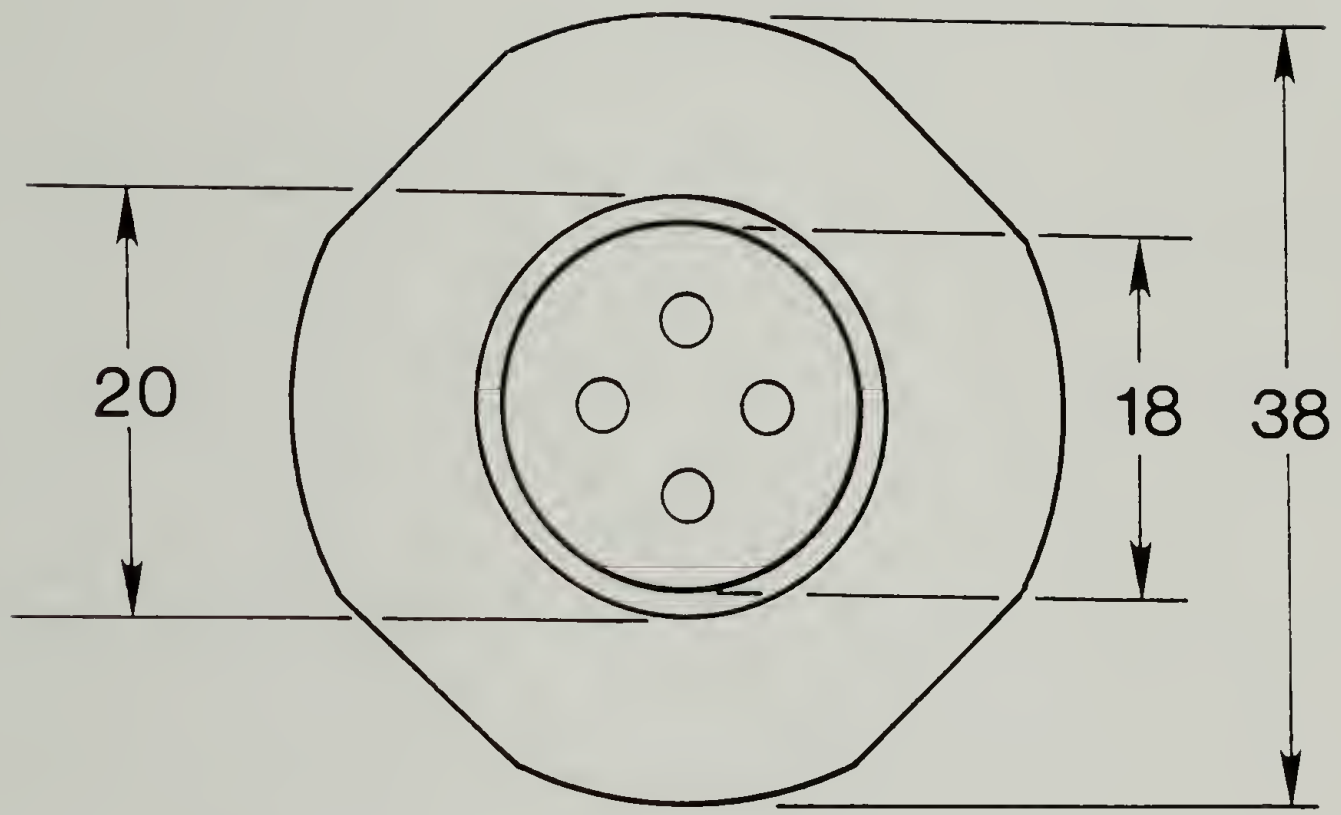

Figure 5.8. Dimensions of glass windows. All dimensions are in mm.

parallel to each other, in order to minimize any beam divergence due to a lens effect.

5.2.3 Pressure Drop Measurements

The pressure drop through the various dies with the glass exit region removed was measured by the melt pressure transducer near the entrance to the die as shown in Figure 5.6. The pressure difference between the actual location of the transducer and the die entrance was assumed to be negligible since the cross-sectional area of the piston channel is much greater than the cross-sectional area of the die channel. The atmospheric pressure at the die exit was also assumed small compared to the melt pressure at the die entrance. Therefore, from Eq. (5.1) the pressure measured by the transducer is equal to the pressure drop ΔP since $P^* >> P_o$. The volume flow rate, Q, through the dies is given by

$$Q = \pi v_p D_p^2/4 \tag{5.29}$$

where v_p is the piston speed and D_p is the piston diameter. Pressure drop data were obtained for $3.1<Q<1300$ mm^3/s.

The experimental data appear in Figures 5.9, 5.10 and 5.11 for LDPE and Figures 5.12, 5.13 and 5.14 for PS. The solid lines are the calculated pressure drops using the steady shear viscosity function, Eq. (4.5), determined from the memory integral constitutive equation and the procedure of Section 5.1.1. The dashed lines correspond to the predictions using the Carreau model and the dotted lines from the power-law relation.

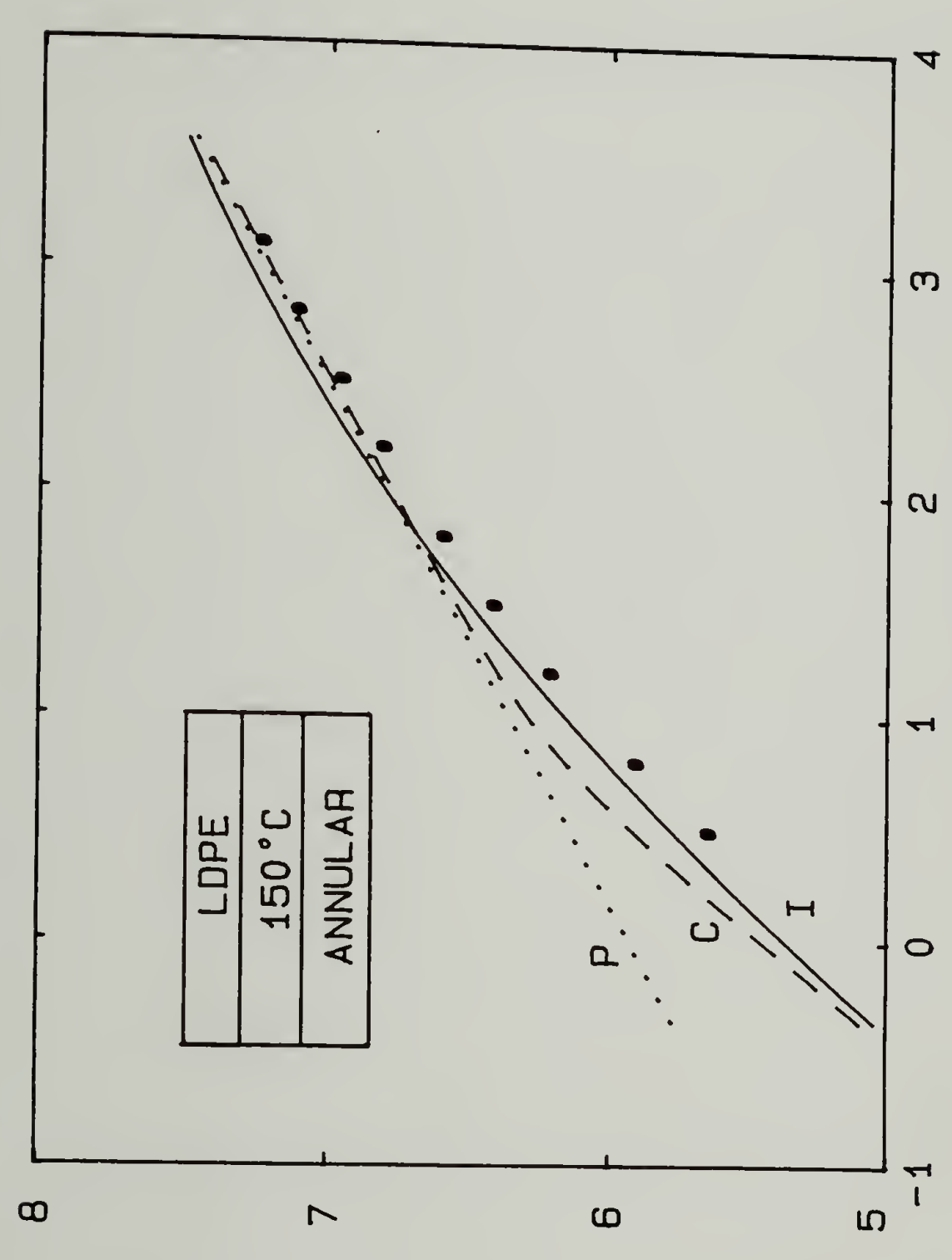

Figure 5.9. Pressure drop in annular die for LDPE.
P - Power-law model
C - Carreau model
I - Integral model

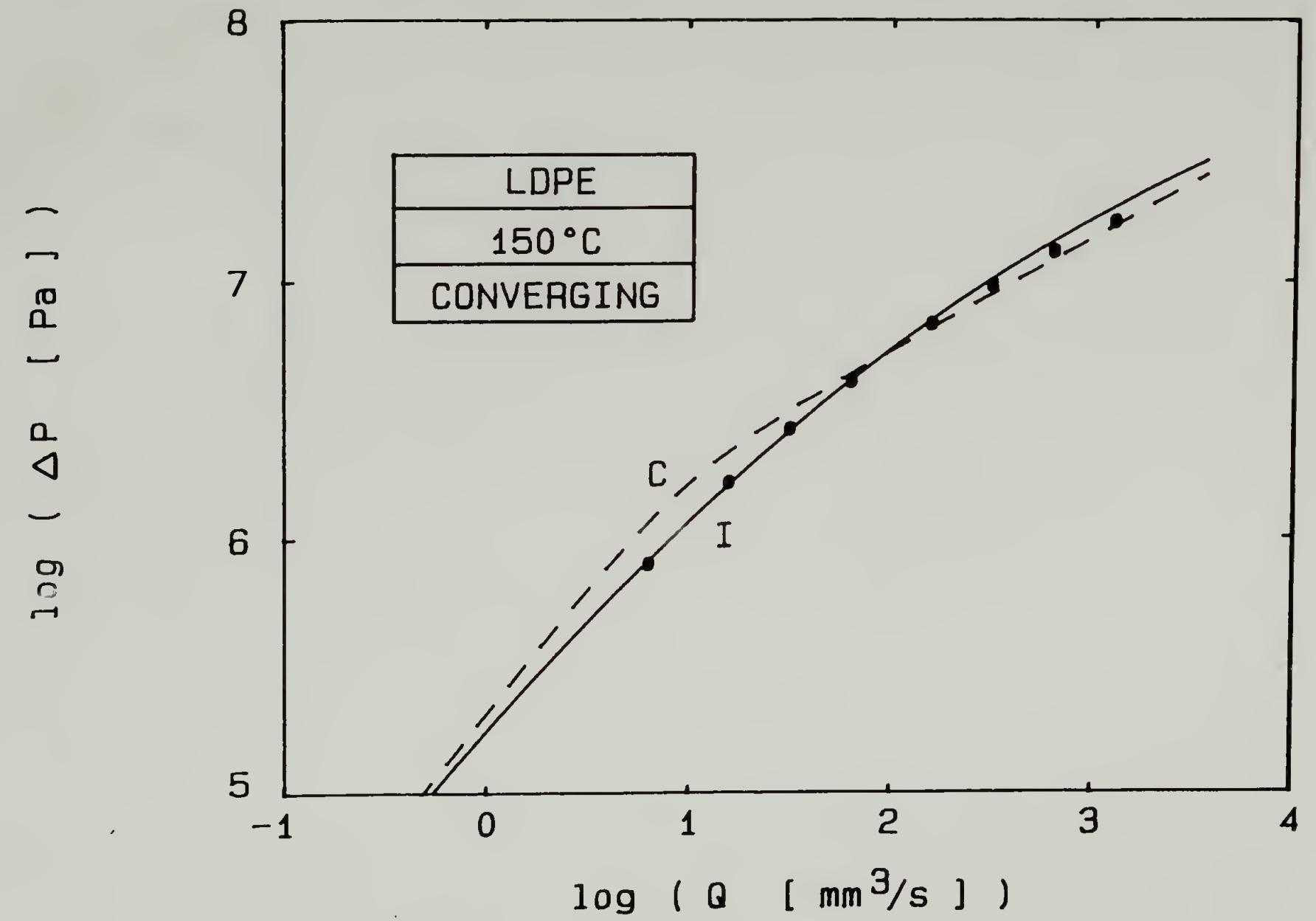

Figure 5.10. Pressure drop in converging die for LDPE.
C - Carreau model
I - Integral model

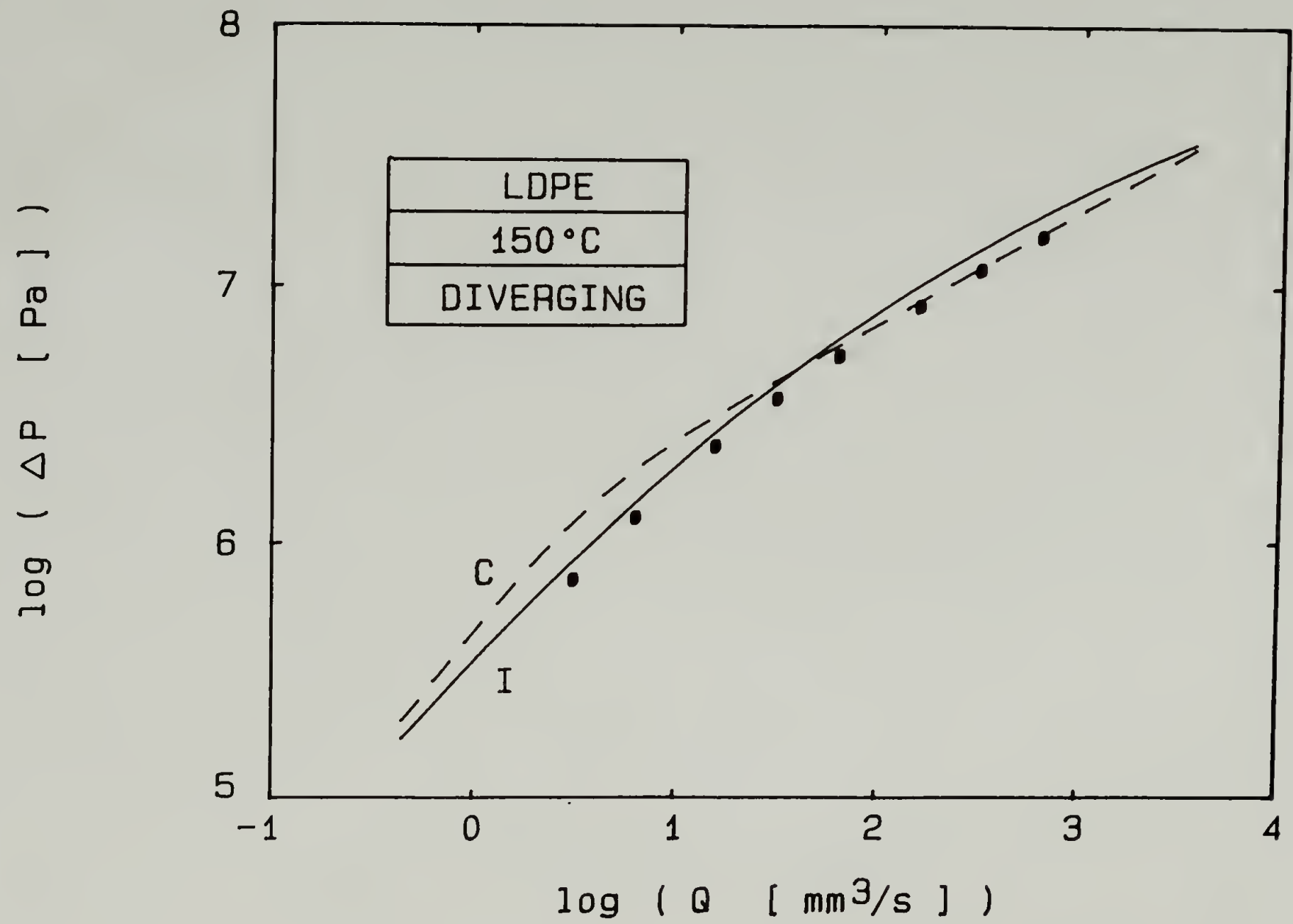

Figure 5.11. Pressure drop in diverging die for LDPE.
C - Carreau model
I - Integral model

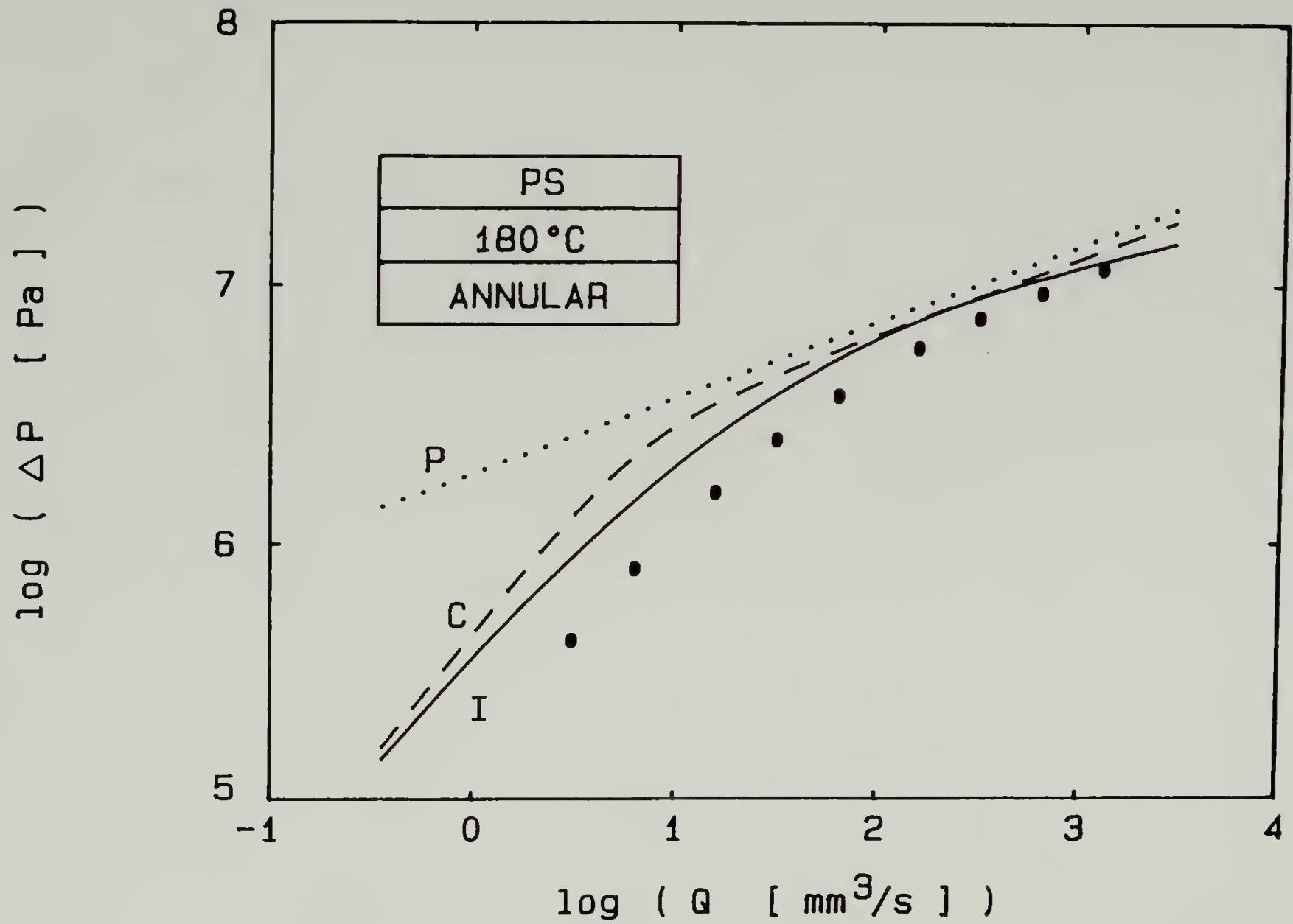

Figure 5.12. Pressure drop in annular die for PS.
P - Power-law model
C - Carreau model
I - Integral model

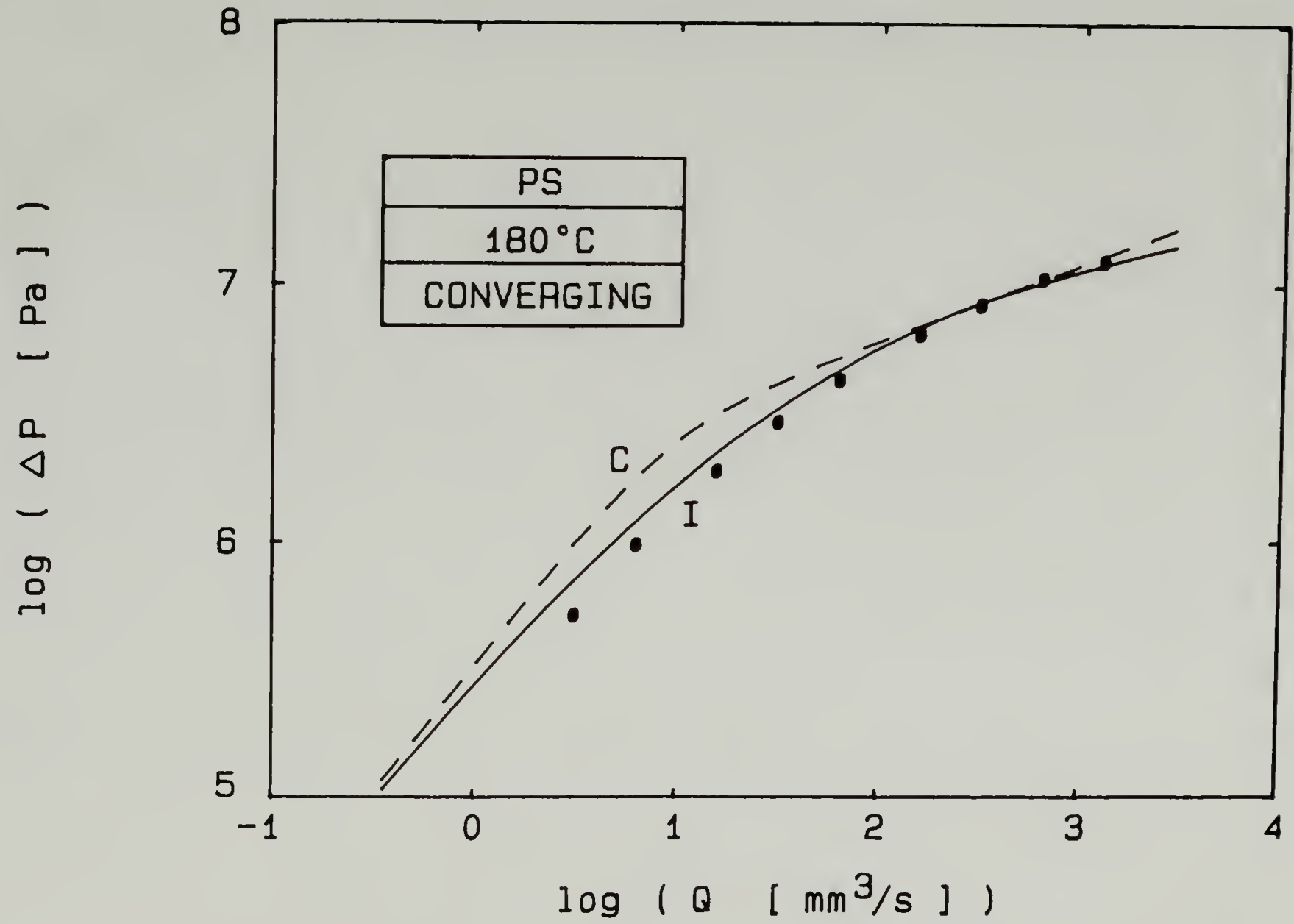

Figure 5.13. Pressure drop in converging die for PS.
C - Carreau model
I - Integral model

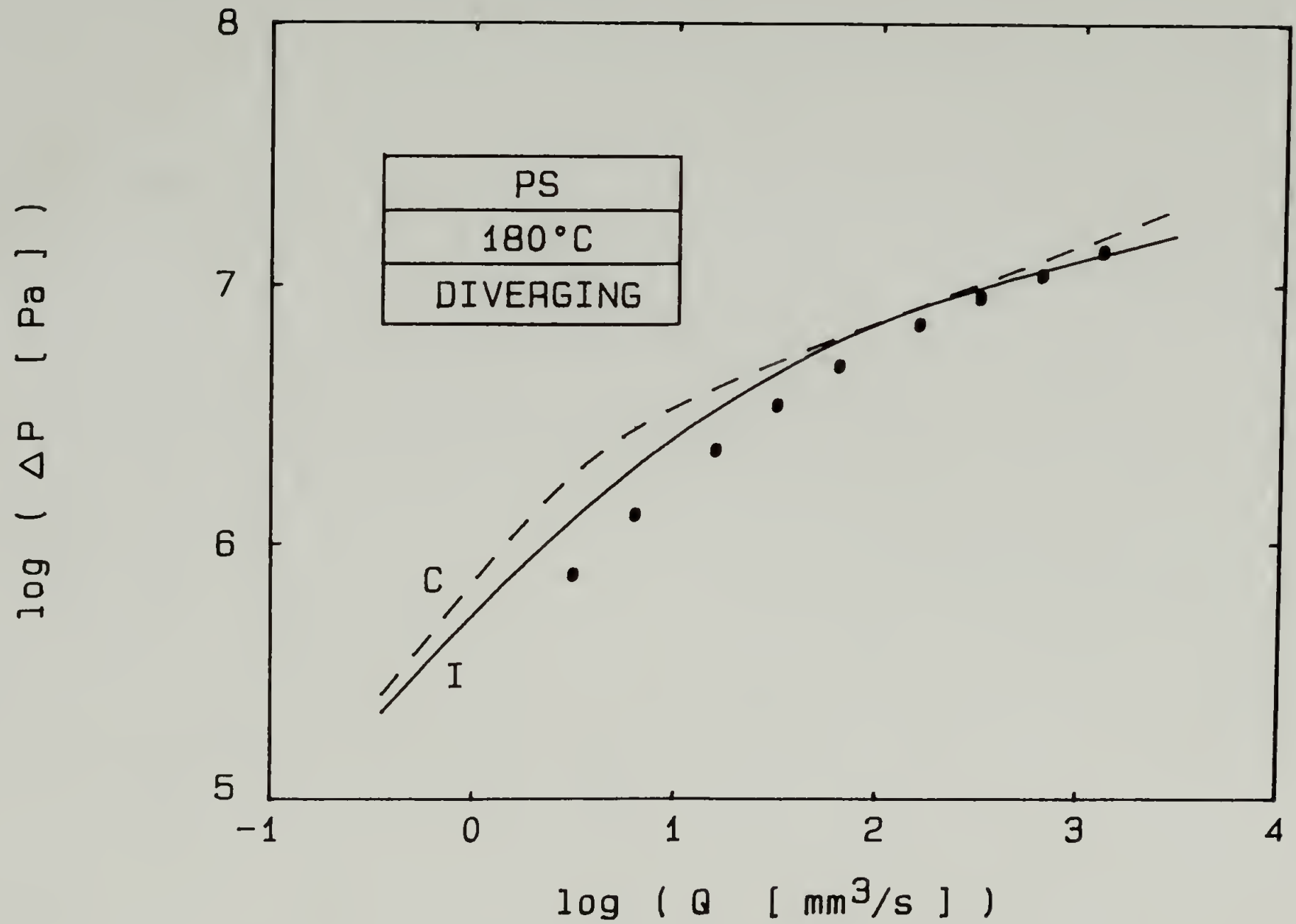

Figure 5.14. Pressure drop in diverging die for PS.
C - Carreau model
I - Integral model

There are two points to be made about the predictions of the pressure drop in the three dies. As seen from Figures 5.9 through 5.14, the memory integral constitutive equation gives the best prediction of the pressure drop in the annular dies over the entire range of flow rates. For the die of constant annular cross-section both the Carreau model and power-law model predict similar results as the integral model at high flow rates but deviate dramatically at low flow rates. This is explained by examining the ability of the models to predict the steady shear viscosity behavior. The power-law model predicts a non-constant steady shear viscosity that increases at low shear rates and hence a higher pressure drop at low flow rates. Even though the Carreau model predicts a zero-shear-rate steady shear viscosity at low shear rates, it predicts a slightly higher viscosity in the intermediate region of shear rates. This is reflected in the pressure drop calculations by the slightly higher predictions of the Carreau model at low to moderate flow rates.

Another observation to note is that, for each polymer, the pressure drops in both the converging and diverging dies are adequately predicted by the integral model. This does not reflect the choice of a particular model which predicts the rheological behavior better than another model, as much as the manner in which the approximate kinematics were determined. The agreement between the predictions and experiments indicates that the lubrication approximation used in the determination of the kinematics for the dies having the converging and diverging

sections was valid. The lack of exact agreement, however, indicates that other factors may be important.

Even though the integral model gives the best description of the pressure drops, it slightly overpredicts the experimental data over the entire range of flow rates. This phenomenon may result from using a steady shear viscosity function that slightly overpredicts the measured steady shear viscosity at intermediate rates as seen in Figure 3.34 or it may indicate that a refinement of the approximate kinematics may be necessary in order to obtain more exact agreement. This tendency to slightly overpredict the stress is observed to be more severe in the flow birefringence experiments which will be discussed later.

5.2.4 Strain History Calculations

Calculations of the strain histories and stress distributions were performed for the flow of the LDPE at 150°C at 2 mm downstream of the metal/glass interface for all three dies. The range of flow rates was $10<Q<400$ mm^3/s which corresponds to an average velocity, $\bar{v}$, in the die channel of $0.2<\bar{v}<10.5$ mm/s. The results of the stress calculations will be discussed in Section 5.3.

As mentioned previously, the strain or deformation history that a material element experiences is important and can be quantitatively described by the axial stretches and shear strains. The axial stretches and shear strains for the LDPE appear as a function of axial distance in the dies in Figures 5.15 through 5.19. A value of $z=0$ corresponds to a point 2 mm downstream of the metal/glass interface. The average velocity was $\bar{v}=2.6$ mm/s and the data are presented for material elements on

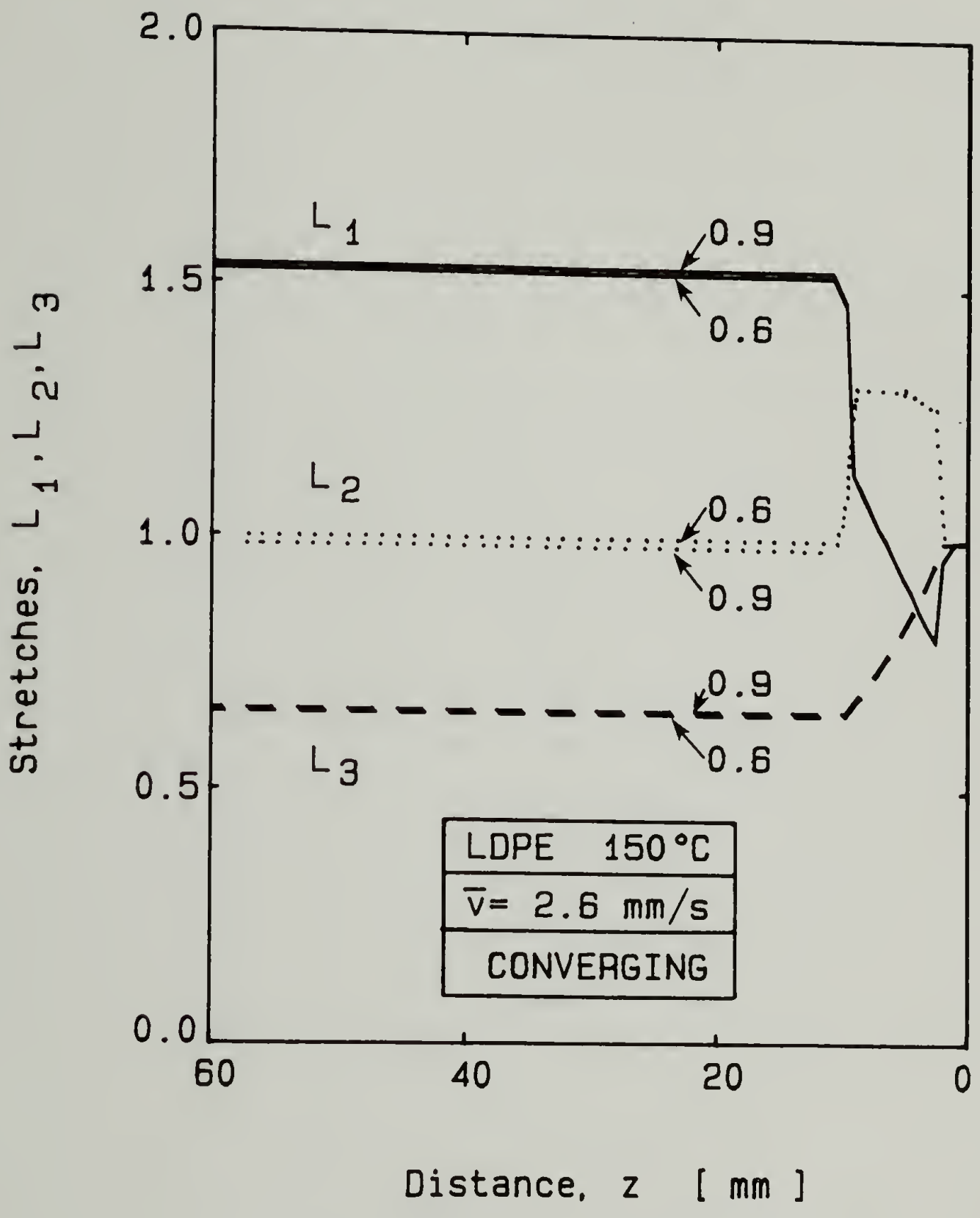

Figure 5.15. Axial stretches as a function of axial distance in converging die. Two streamlines are selected with radial positions at the die exit being $[(r-r_i)/(r_o-r_i) = 0.6$ and $0.9]$.

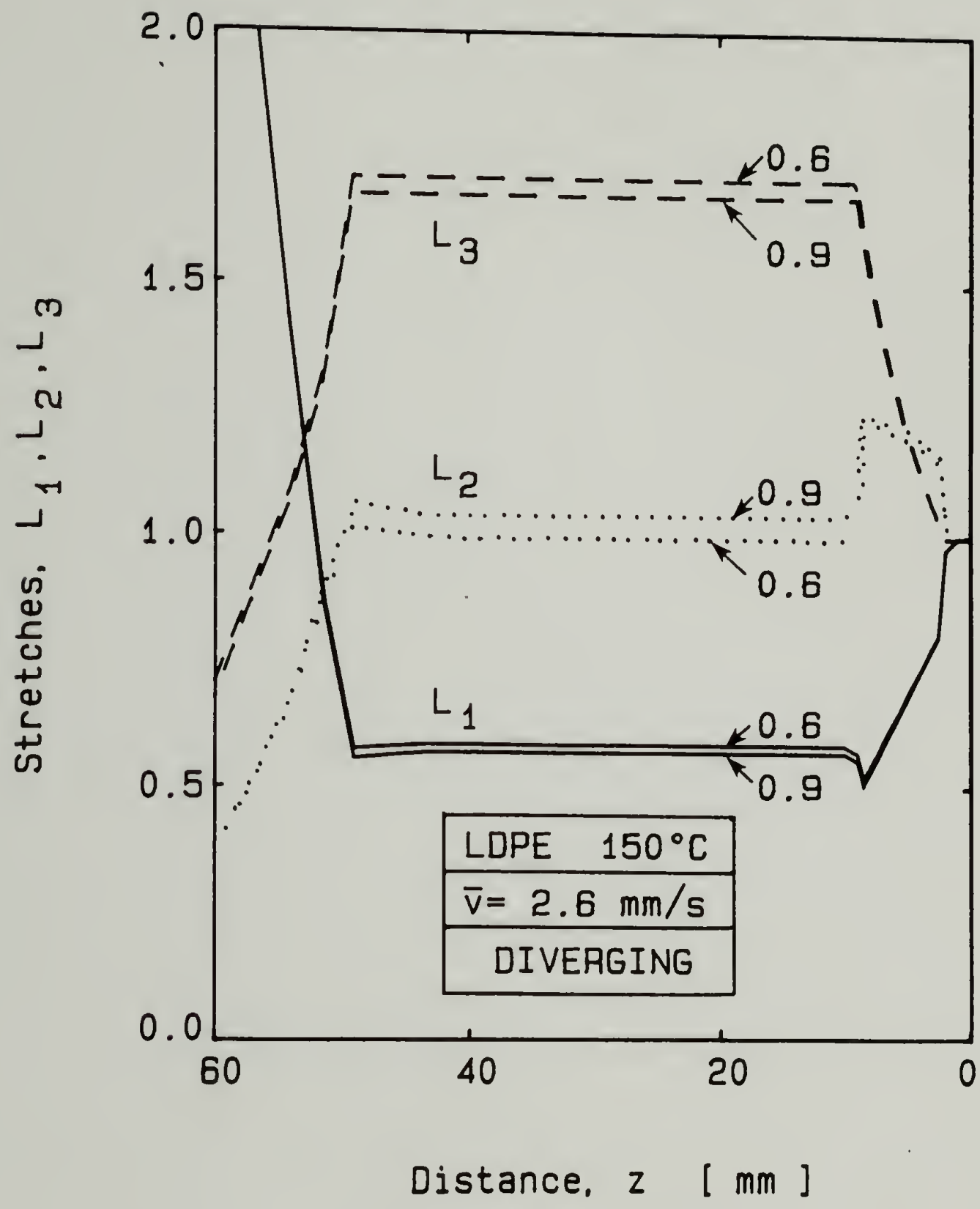

Figure 5.16. Axial stretches as a function of axial distance in diverging die. Two streamlines are selected with radial positions at the die exit being $[(r-r_i)/(r_o-r_i) = 0.6$ and $0.9]$.

two streamlines, at $(r-r_i)/(r_o-r_i)=0.9$ (near the outer wall) and 0.6 (near the center of the gap).

Some interesting results were obtained from the calculated strain history. The extensional deformation a material element experiences is presented first. For the die of constant annular cross-section there are no axial stretches ($L_1=L_2=L_3=1$) for a material element anywhere across the gap, however, the converging and diverging dies show drastically different results. As seen from Figure 5.15 for the converging die, L_2 is approximately unity (i.e., there is no stretch in that direction) and $L_1>1>L_3$ indicating that the material element is <u>elongated</u> in the flow direction and <u>compressed</u> in the circumferential direction. The axial stretches also do not depend on the streamline, so material elements near the center of the gap and near the outer wall are subjected to the same stretches. From Figure 5.16, the diverging die shows a very different deformation history. The stretch L_2 is again near unity, but $L_1<1<L_3$ indicating that the material element is <u>compressed</u> in the flow direction and <u>elongated</u> in the circumferential direction. Again, the material elements near the center of the gap and near the walls experience nearly the same stretches.

The shear deformation that a material element experiences is quite different as seen in Figures 5.17, 5.18 and 5.19. The data indicate that the shear deformation is very high near the wall where the local shear rate is the highest and very low near the center of the gap where the shear rate is the lowest. This same behavior is seen for all three

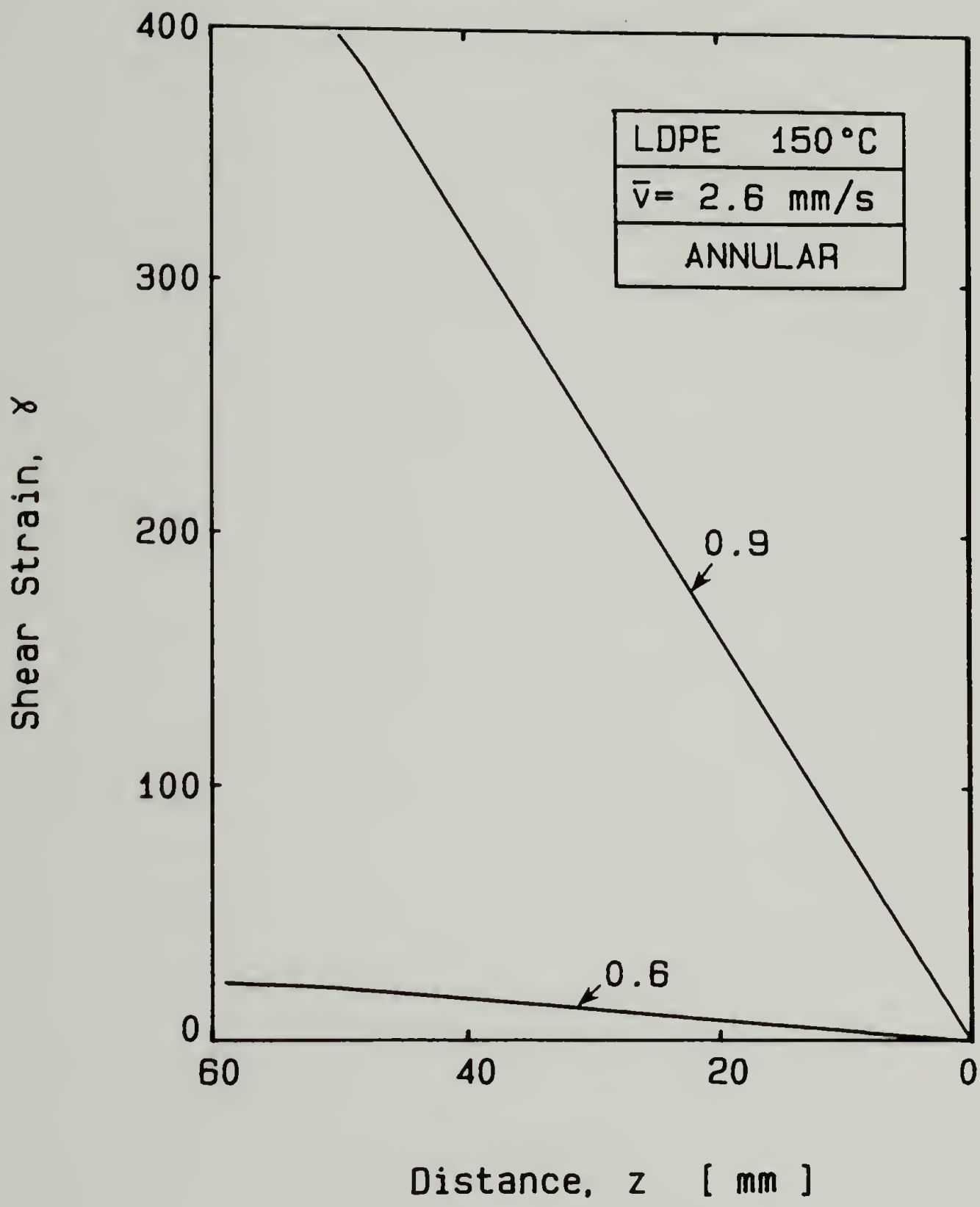

Figure 5.17. Shear strain as a function of axial distance in annular die. Two streamlines are selected with radial positions at the die exit being $[(r-r_i)/(r_o-r_i) = 0.6$ and $0.9]$.

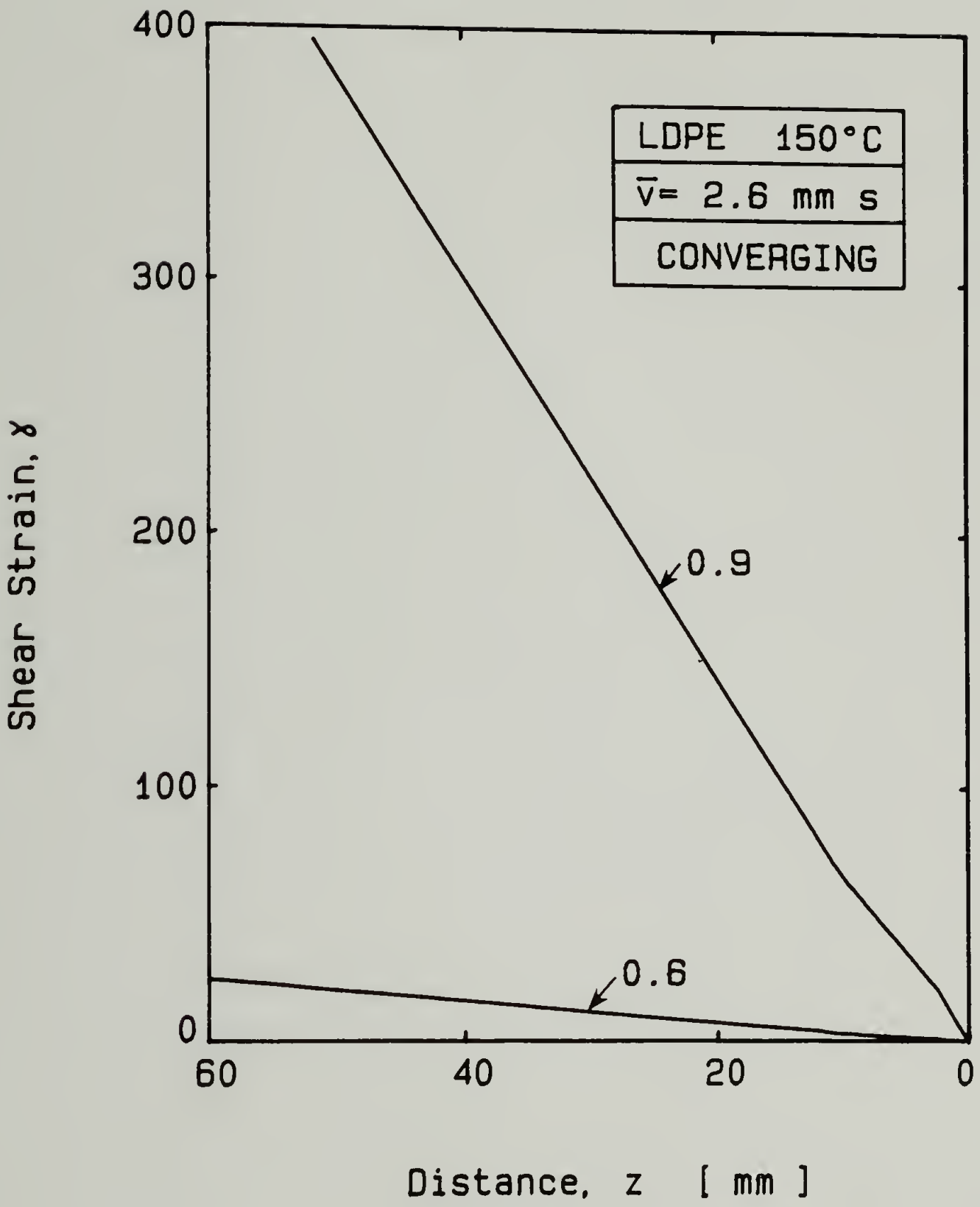

Figure 5.18. Shear strain as a function of axial distance in converging die. Two streamlines are selected with radial positions at the die exit being $[(r-r_i)/(r_o-r_i) = 0.6$ and $0.9]$.

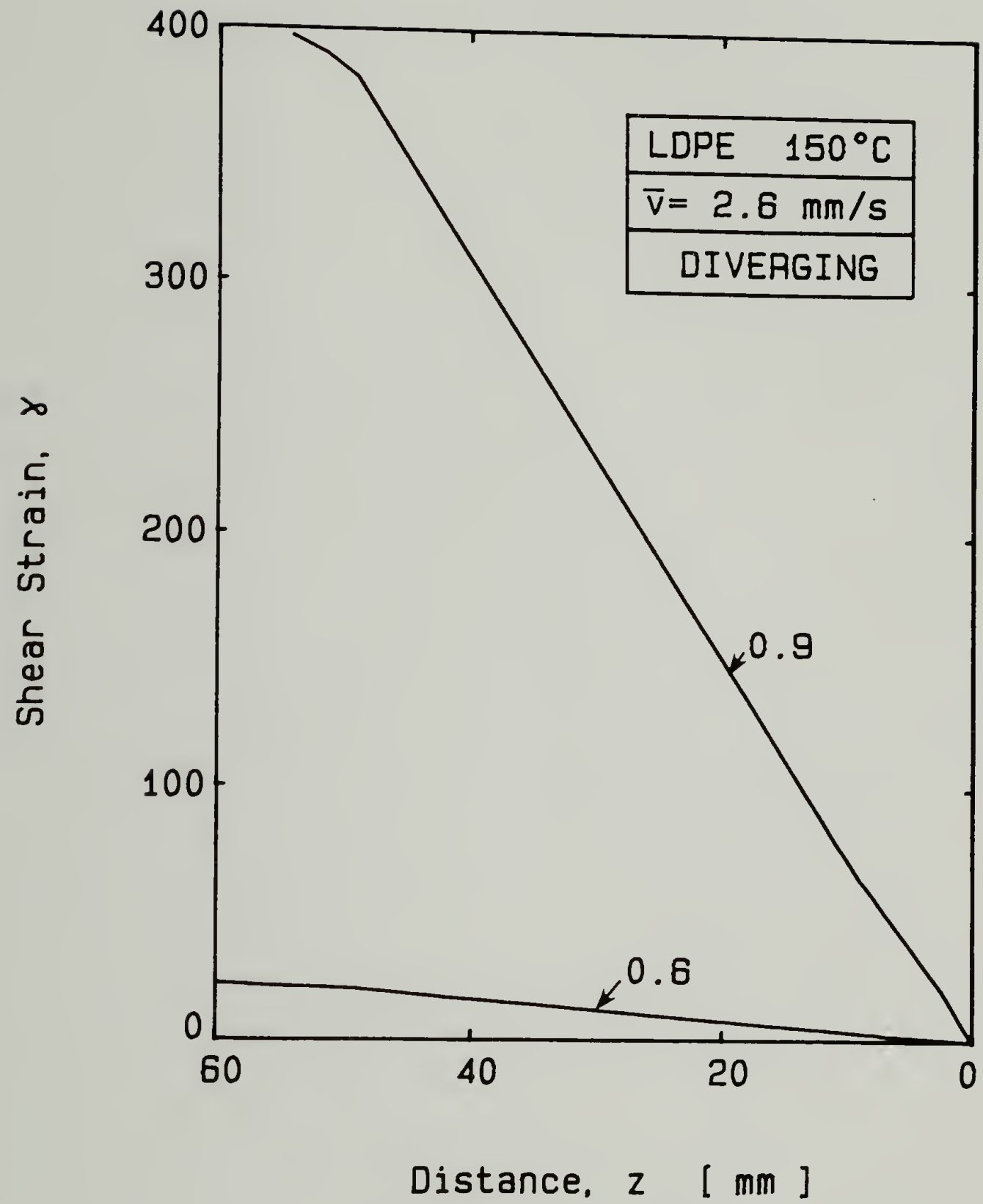

Figure 5.19. Shear strain as a function of axial distance in diverging die. Two streamlines are selected with radial positions at the die exit being $[(r-r_i)/(r_o-r_i) = 0.6$ and $0.9]$.

dies and more importantly the shear strains are very similar for all three dies.

The conclusion from the strain history calculations is that the extensional deformation is essentially the same for all material elements across the gap and is highly dependent on the die geometry; whereas, the shear deformation is essentially the same for all die geometries and is highly dependent on the position of the material element across the gap. This conclusion becomes important in explaining the measured flow birefringence data.

5.2.5 Flow Birefringence Measurements

The flow birefringence measuring system is shown in Figure 5.20. It consists of an optical bench on which a He-Ne laser (λ_o=632.8 nm) and a photomultiplier tube (PMT) (Hammamatsu, Type R777) sensitive to the wavelength of the laser are mounted. The PMT is attached to a photomultiplier detection system (Oriel). The light beam is linearly polarized, passed through neutral density filters and then a small circular aperture (d=0.5 mm) before entering the glass part of the die. The exiting beam then passes through another linear polarizer which is 90° to the first (polarization directions perpendicular) and into the PMT housing on which another circular aperture (d=5.0 mm) and a diffuser are mounted. The measured half-angle of beam divergence after exit from the die was only 0.8 mrad. The PMT was operated at -300V and the light beam intensity was adjusted with the neutral density filters to give a maximum signal of 1.8×10^{-6} amps from the PMT when the polarizers were uncrossed (polarization directions parallel).

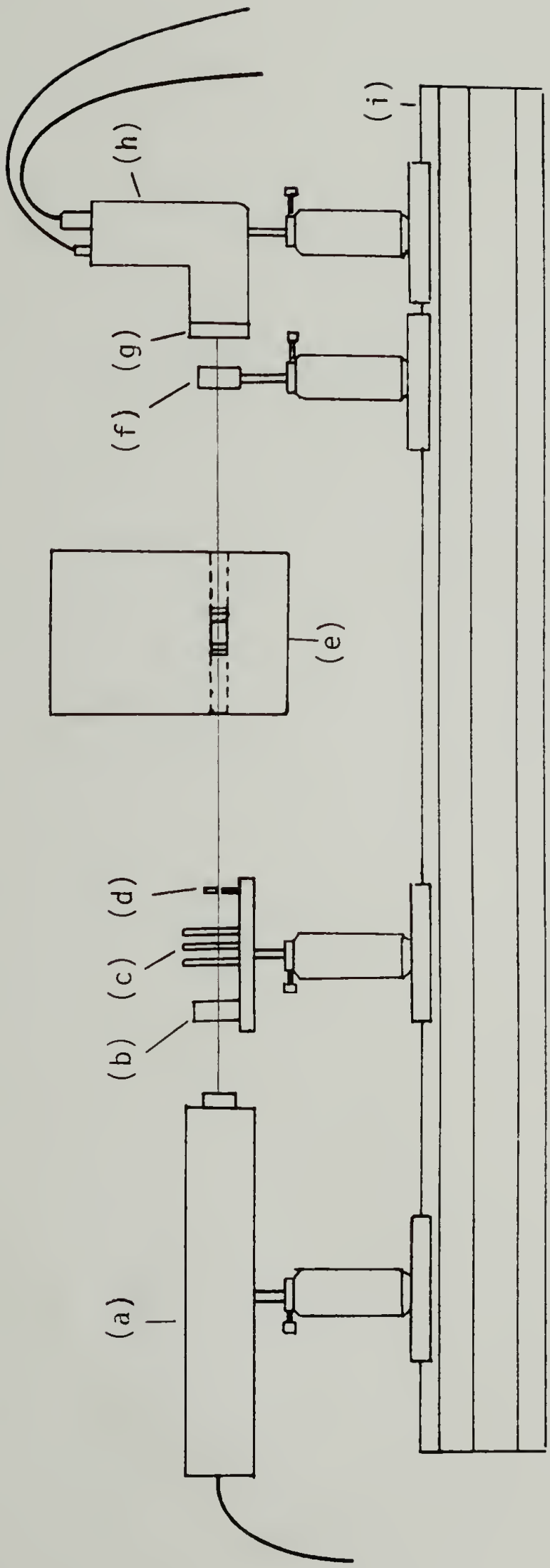

Figure 5.20. Flow birefringence measuring system.
(a) He-Ne laser, (b) polarizer, (c) neutral density filters, (d) aperture,
(e) annular die, (f) polarizer, (g) diffuser, (h) photomultiplier tube
housing, (i) optical bench.

The retardation angle due to the flow birefringence of such an experimental setup is expressed as (Janeschitz-Kriegl, 1983)

$$I = I_o \sin^2(2\beta)\sin^2(\delta_T/2) \tag{5.30}$$

where I is the transmitted intensity due to the flow birefringence, I_o is the intensity through the system with no flow and the polarizers uncrossed, and β is the angle between the direction of flow and the incident polarization direction. In this case, $\beta=\pi/4$ rad as shown in Figure 5.21.

The flow birefringence experiments proceeded as follows. The desired die was mounted in the adapter and the outer die body was centered on the inner mandrel. The center glass was then mounted onto the inner die body with four small screws. A thin sheet of teflon was placed between the inner glass and the inner end cap. There was no need to place any teflon between the glass and the inner and outer die bodies because the surfaces in contact were smooth and the extrusion pressures near the die exit were low enough that no leakage occurred. Another reason for not using any teflon between those surfaces was the desire to have as little disruption in the flow channel as possible. The outer glass piece was then mounted and centered. Small strips of teflon sheet were used on all the surfaces of the outer glass piece which came into contact with the outer end cap. The glass was tightened just less than finger tight at room temperature. The die was then heated to the operating temperature and the glass windows were tightened finger tight.

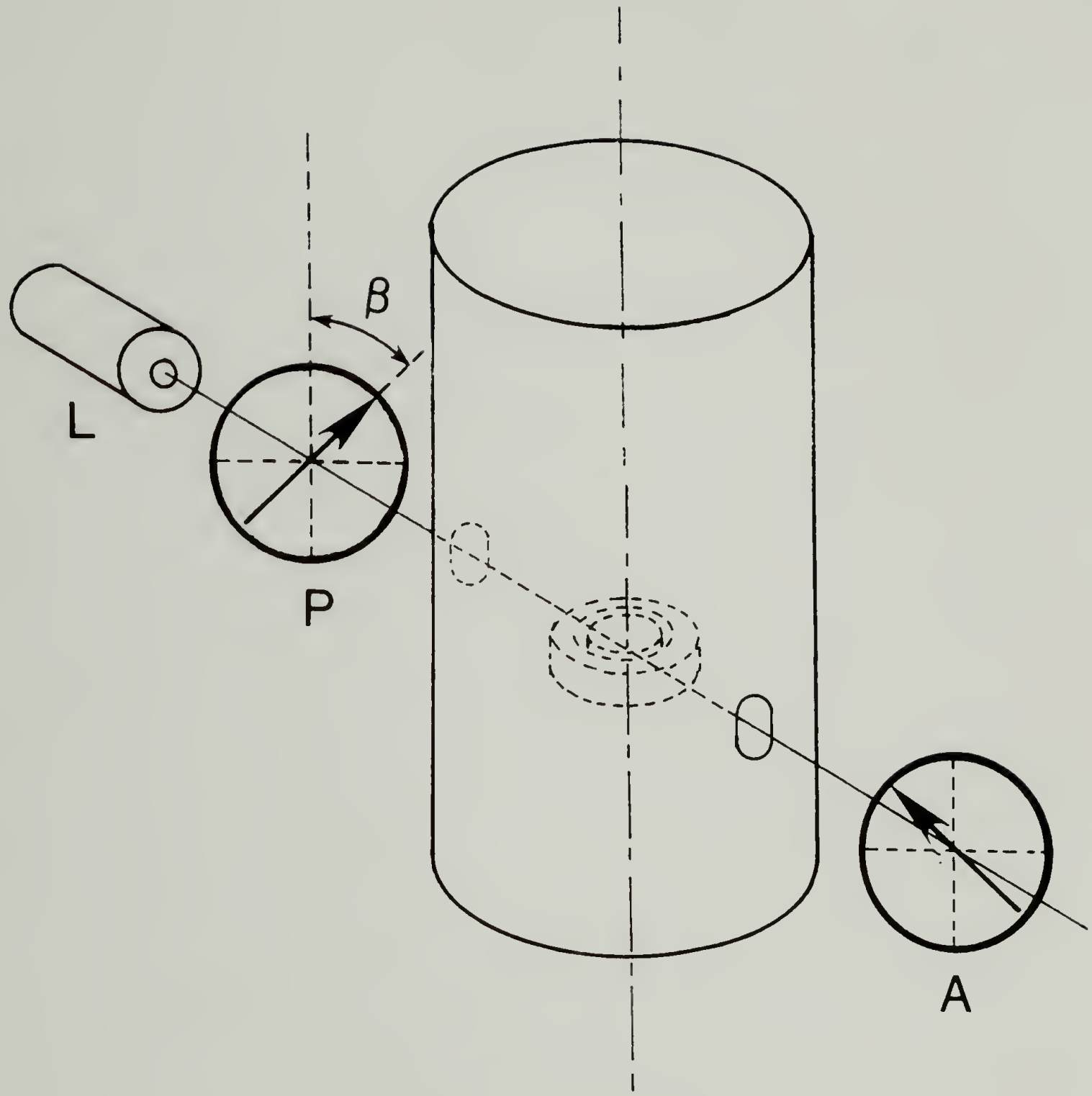

Figure 5.21. Polarization direction of light beam.

The optical bench was installed and the light beam aligned so that it entered the glass at 2 mm downstream of the metal/glass interface. The glass channel was filled with the polymer melt and allowed to equilibrate to the stressfree state. If the glass was tightened too much, a signal was measured with the flow birefringence system due to the strain birefringence of the glass. When this happened the glass tightening screws were adjusted to obtain a zero signal with no polymer flowing. The intensity level was then adjusted and the flow started. The capillary rheometer was used in these flow experiments because it produces a very constant volume flow rate and the temperature is easily and accurately controlled. The intensity of light due to the flow birefringence was measured for flow rates ranging over two and a half decades, $3<Q<630$ mm^3/s, for the three different die geometries.

The resulting intensity data appear in Figure 5.22 for the LDPE at 150°C. At low flow rates, the flow in the diverging die produced the lowest intensity ratios while the converging die produced the highest ratio. As the flow increased the intensity ratios went through maximums due to the sinusoidal dependence on the retardation angle as seen from Eq. (5.30). The data indicate that, for the range of flow rates studied, the intensity ratio data went through just one maximum which corresponds to just over one quarter of the first period or order of the retardation angle.

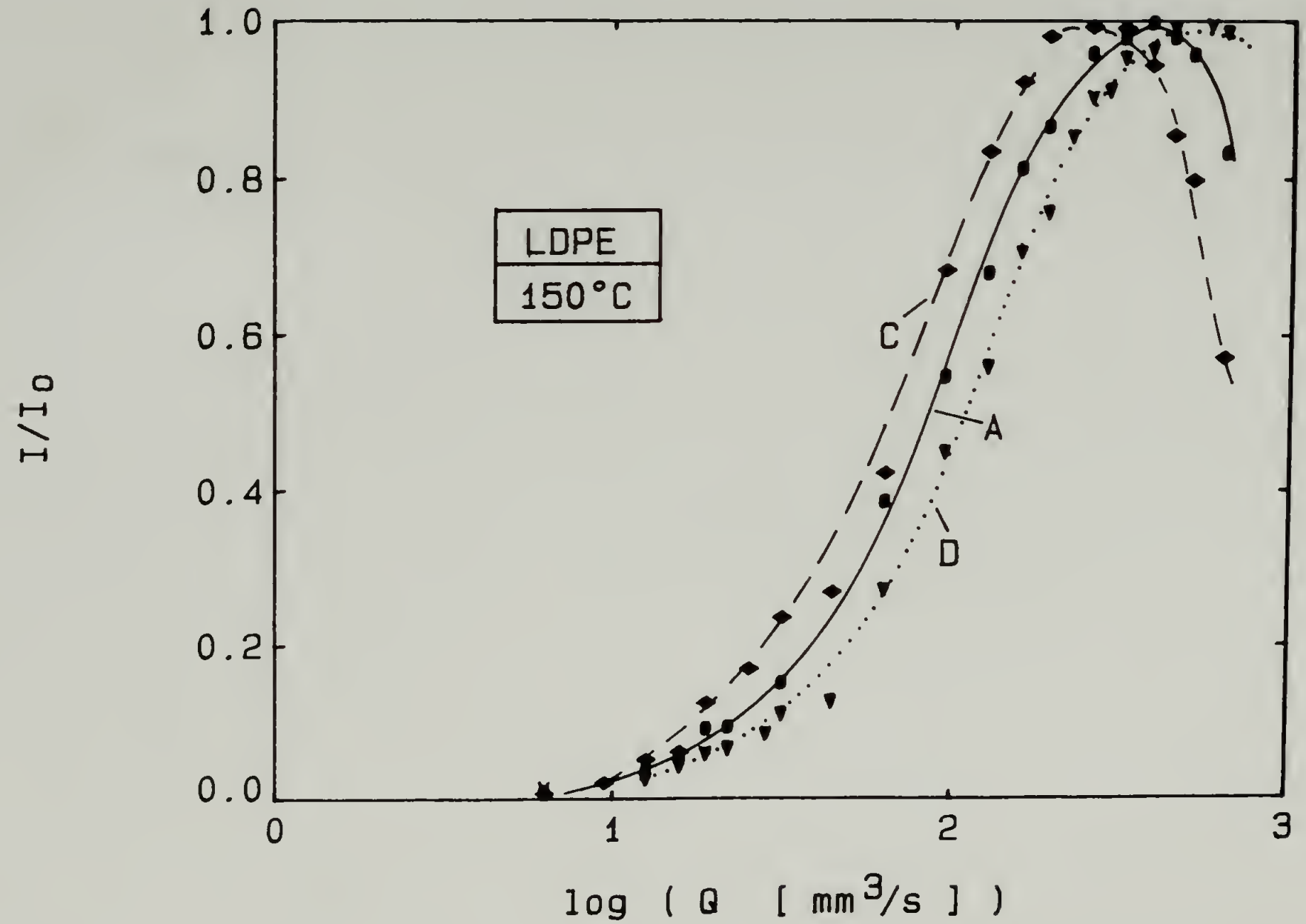

Figure 5.22. Measured intensity data as a function of flow rate for all three dies. C - Converging, A - Annular, D - Diverging.

5.3 Discussion

The generalized strain function described by the sum of two exponential functions was used in the calculations of the stress in the extrusion dies. For annular flow, the Finger strain tensor is given in Eq. (4.10) and the invariants are

$$I_1(\gamma,L_1,L_2,L_3) = (1+\gamma^2)L_1^2 + L_2^2 + L_3^2 \qquad (5.31)$$

$$I_2(\gamma,L_1,L_2,L_3) = L_1^{-2} + (1+\gamma^2)L_2^{-2} + L_3^{-2} \qquad (5.32).$$

For shear flow ($L_1=L_2=L_3=1$), $I_1=I_2$ and the calculated stresses are the same for all α. For extensional flow ($\gamma=0$), a value of $\alpha=0$ describes rheological data obtained in uniaxial extension while $\alpha=1$ describes rheological data obtained in biaxial extension as discussed in the third chapter.

The predictions of the stress distributions in the three dies are discussed in terms of the differing die geometries and the choice of the parameter α in the generalized strain function for processing flows having both shear and extensional components superimposed.

5.3.1 Predicted Stress Distributions

The predictions of the stress distributions across the die gap were obtained from the modeling procedure for the LDPE at 150°C at 2 mm downstream of the metal/glass interface (which is also the position at which the flow birefringence was measured). The strain histories for these three dies were presented in Section 5.2.4.

The contributions to the following stress distributions due to the flow upstream of the die entrance were found to be nonexistent for

streamlines close to the channel walls where the integration was terminated inside the die according to the first criterion discussed in Section 4.3. For streamlines closer to the center of the gap, some contribution to the total stress due to deformation upstream of the die entrance was calculated but it was extremely small compared to the total stress. Only for a few streamlines near the center of the gap was there any substantial contribution to the total stress from the upstream die history beyond the entrance region. The largest contribution to any of the components of the stress tensor was about 4% of the associated maximum total stress component for the streamlines at $(r-r_i)/(r_o-r_i) = 0.4$ and 0.6. This indicates that the three dies are long enough that essentially all of the deformation upstream of the die entrance region is forgotten by a material element near the die exit. That upstream history is wiped out and the stress calculated near the exit is due only to the specific deformation history in each die.

The calculated shear stress, σ_{12}, in the annulus of constant cross-section is shown in Figure 5.23 for various average velocities in the die channel. The shear stress in the converging and diverging dies was not significantly different from the shear stress in the constant annular die so the data for those dies were not shown in the figure for clarity. The fact that the shear stresses are the same supports the assumption of locally steady shear flow when determining the kinematics of the flow in the converging and diverging sections.

The normal stress differences

$$S_{23} = \sigma_{22}-\sigma_{33} \tag{5.33}$$

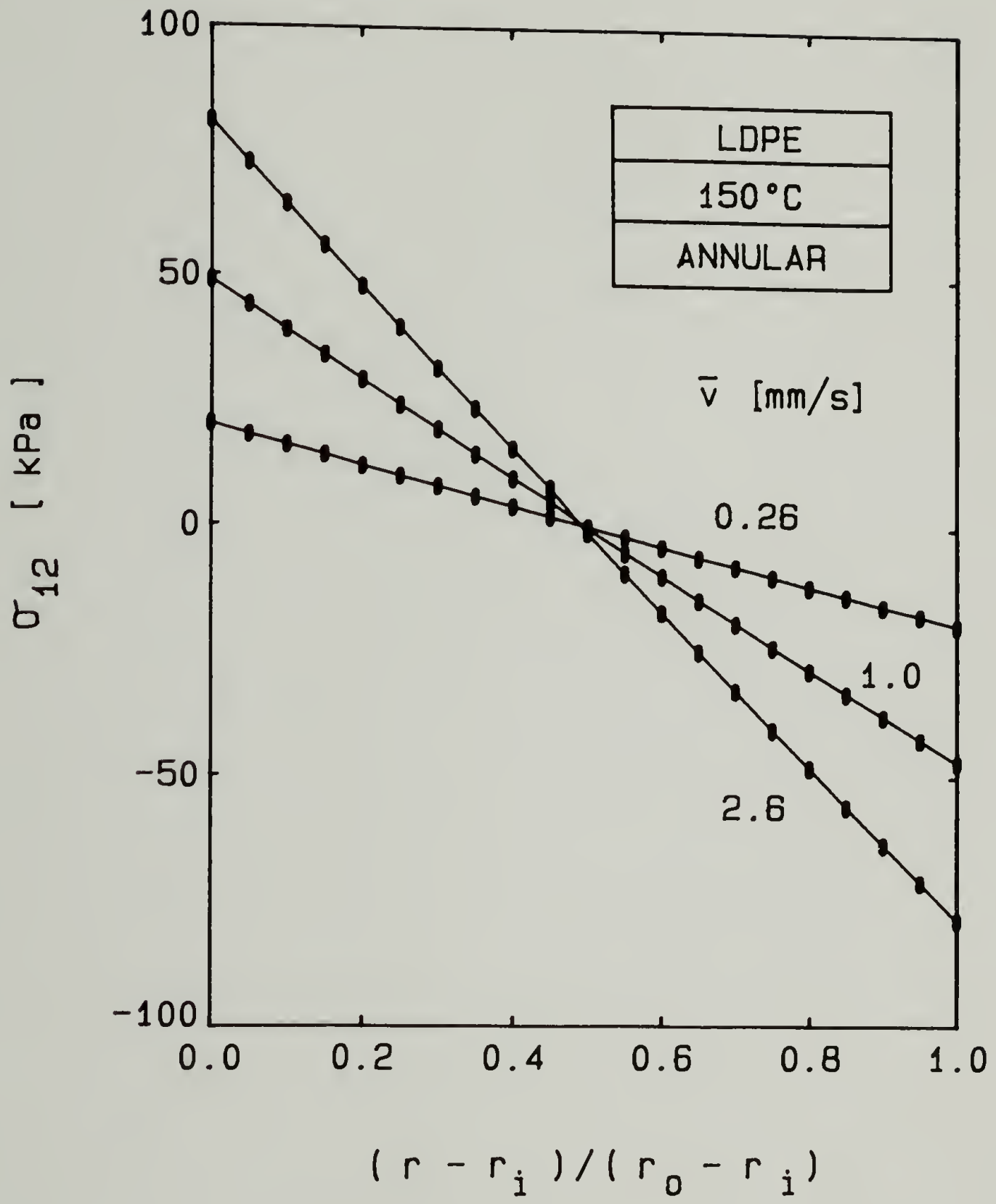

Figure 5.23. Calculated shear stress distribution, σ_{12}, in annular die.

and

$$S_{13} = \sigma_{11} - \sigma_{33} \tag{5.34}$$

were calculated to compare the normal stresses in the flow or 1-direction and the radial or 2-direction to the normal stress in the circumferential or 3-direction. The principal values of S_{13}, denoted by S'_{13}, were then calculated from Eq. (5.5) in order to analyze the flow birefringence data.

The normal stress difference, S_{23}, is plotted in Figure 5.24. The constant annular die shows $S_{23}=0$ across the entire gap due to the lack of extensional deformations in the flow ($L_1=L_2=L_3=1$) and due to the choice of constitutive equation. The memory integral constitutive equation of Eq. (2.43) utilizes the Finger strain tensor as a measure of the strain and so a second normal stress difference is not even predicted for shear flow. The converging and diverging dies do have extensional components of deformation and exhibit finite values for S_{23} across the gap. S_{23} is positive for the converging die and negative for the diverging die. A negative S_{23} indicates that the stretch in the circumferential direction is greater than the stretch in the radial direction. The S_{23} distributions for the three dies are substantially different for the three dies just as the axial stretches were different for the three dies as shown in Figures 5.15 and 5.16. Thus, an experimental measurement of this stress difference should be able to show large differences between the three geometries. However, the direct measurement of this stress difference in annular flow is extremely difficult if not impossible experimentally. Some conflicting measurements have been obtained

in rheometric flows by subtracting the other two normal stress differences, $(\sigma_{11}-\sigma_{22})$ and $(\sigma_{11}-\sigma_{33})$.

For all the dies, S_{23} approaches zero at the walls since the flow approaches steady shear flow in that region. The choice of α=0 or α=1 had little effect on the calculated S_{23} so only the values for α=1 are shown in Figure 5.24.

The principal normal stress difference, S'_{13}, is shown in Figure 5.25. The distributions are very similar for all three dies. The values are high near the walls of the channel and decrease sharply towards the center of the gap. This particular shape of the S'_{13} distribution is mainly due to the shear deformations in the dies. From the previously presented strain history calculations, the shear strain was found to be similar in all three dies. Since S'_{13} depends on σ_{11} which contains a squared term of the shear strain in the Finger strain tensor, Eq. (4.10), the distribution of S'_{13} is shear dominated. The slight differences that do exist are due to the extensional components and are distinguishable only near the center region of the channel gap. The value of α had little effect on the calculation of S_{23}, but it substantially affects the results for the S'_{13} distributions.

For the converging die, a value of α=0 gives a distribution that is higher than the distribution for the die of constant annular cross-section over most of the gap. A value of α=1, on the other hand, predicts a distribution which is nearly identical to the one calculated for the constant annular die over the entire gap.

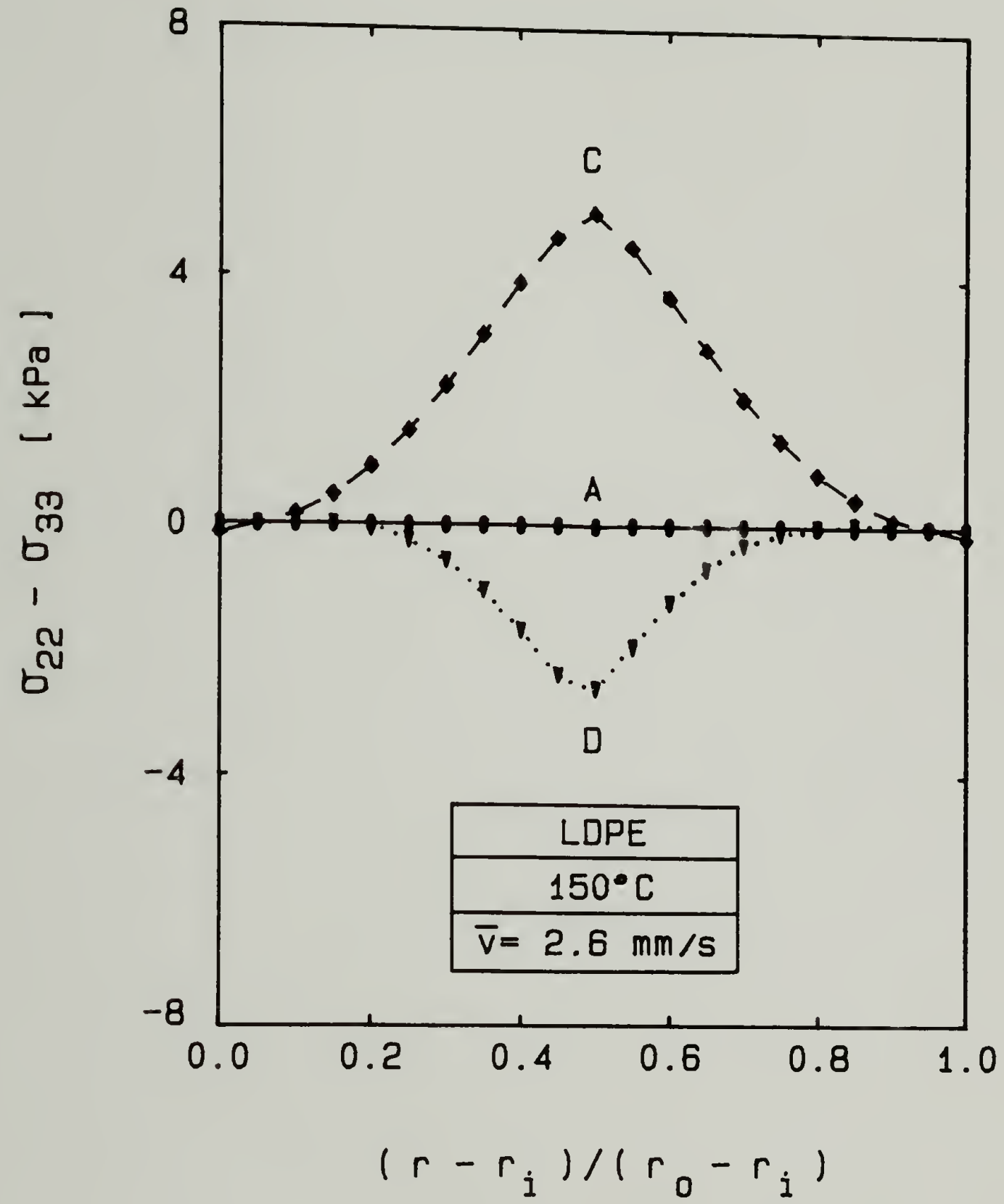

Figure 5.24. Calculated normal stress distribution, S_{23}, in all three dies. A - Annular; C - Converging, α=1; D - Diverging, α=1

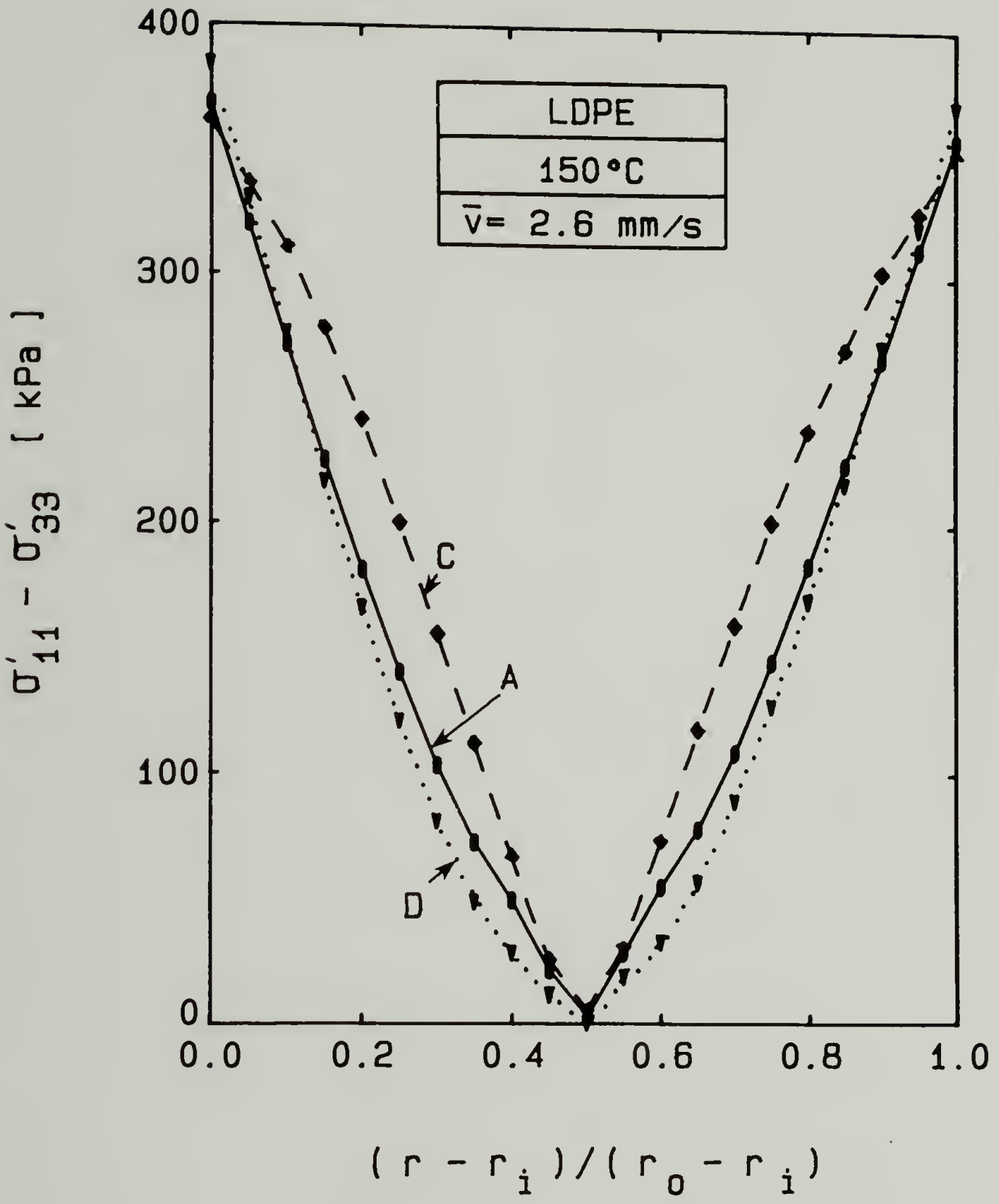

Figure 5.25. Calculated principal normal stress distributions, S'_{13}, in all three dies
A - Annular
C - Converging, α=0
D - Diverging, α=1

For the diverging die, a value of α=1 predicts a S'_{13} distribution that is lower than the constant annular die near the center of the gap and identical near the walls. A value of α=0 was also found to predict a similar distribution as for α=1 only it was slightly lower near the center.

The different predictions for the S'_{13} distribution using the two values of α=0 and α=1 raise the question of which is the more appropriate value to use to describe the flow in each die. A possible answer is arrived at by inspection of the strain history calculations and the results of the step strain experiments in equibiaxial extension presented in the third chapter.

The material elements in the converging die are subjected to the stretches $L_1 > L_2, L_3$. This deformation is similar to an <u>uniaxial</u> extension of a material element. Rheological data from the literature for LDPE (Wagner, 1979) suggest that $\alpha \approx 0$ for this type of extensional deformation and so one would expect that the distribution of S'_{13} with α=0 should give a better prediction than for α=1.

The material elements in the diverging die are, on the other hand, subjected to the stretches $L_3 > L_1, L_2$. This deformation is similar to a <u>biaxial</u> extension of a material element. The rheological data obtained in the third chapter for this LDPE suggests that for this type of extensional deformation α=1 is more appropriate and therefore one would expect that the distribution of S'_{13} with α=1 would more accurately predict the flow in the diverging die.

The comparison of these calculations to the measured flow birefringence further supports this reasoning.

5.3.2 Comparison to Flow Birefringence Results

The principal stress difference, S'_{13} was calculated for all three dies and over the same range of flow rates attained in the flow birefringence experiments. The predicted total retardation angle was then calculated using the procedures of Section 5.1.3 and the average birefringence defined in Eq. (5.13) was determined. The measured average flow birefringence was also determined for the data in Figure 5.22 from Eqs. (5.30) and (5.13). The predicted average flow birefringence is compared to the measured values in Figure 5.26.

The experimental values have a constant slope in the lower flow rate region and a gradual change in slope is notable near a volume flow rate of Q=300 mm^3/s. The leveling off of the measured flow birefringence data may be due to two phenomena.

The intensity ratio data in that region were near a maximum in the squared sine function of the retardation angle making it difficult to distinguish changes in the flow birefringence in that region of flow rate. This is seen in Figure 5.22. Also, at higher flow rates the normal forces in the radial direction may become very large and would tend to enlarge the gap between the windows. The strained windows, being made of glass, may have contributed some strain birefringence to the total signal that was independent of the upstream die geometry so the curves would all be shifted similar amounts.

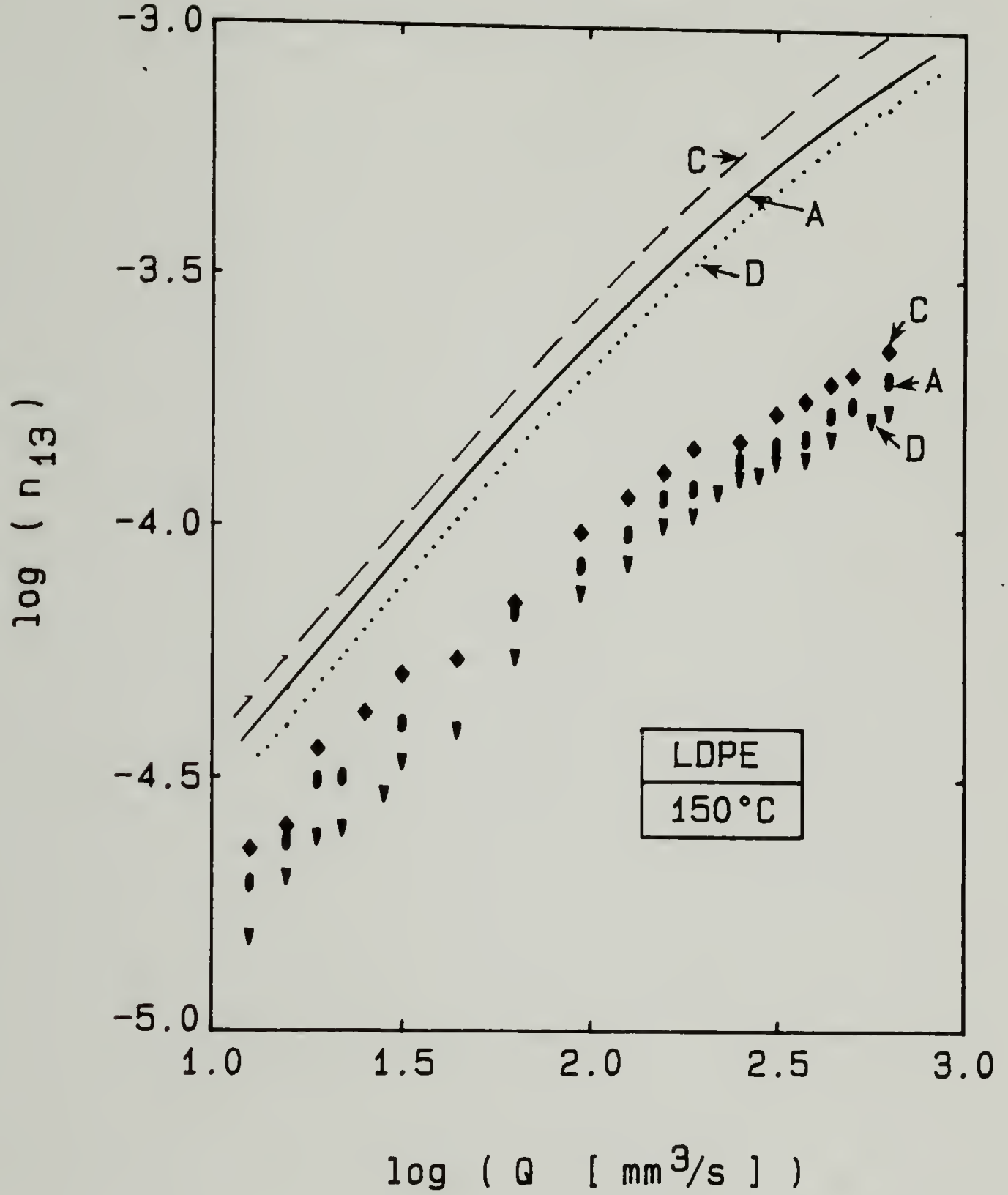

Figure 5.26. Comparison between measured (points) and predicted (lines) average flow birefringence for all three dies.
A - Annular
C - Converging, α=0
D - Diverging, α=1

The predictions of the average flow birefringence obtained from the modeling calculations are above the measured values. Even though the modeling predictions are greater than the measured values by about a factor of two which is constant for all three dies, useful information is obtainable from the data.

The modeling calculations show the same trends as the measured flow birefringence data. The slope at the low flow rates is the same for the predictions and the measured values and the relative difference in values between the three dies is about the same. These relative differences are due to the converging and diverging sections just upstream of the point of measurements and the modeling calculations were able to successfully predict these differences. The same answer to the question, that was posed in the previous section, of which value of the parameter α in the strain function is more appropriate for the converging and diverging dies, is supported by the flow birefringence data.

For the converging die, the measured flow birefringence is distinctly higher than the data obtained from the die of constant annular cross-section over the entire flow rate range. The prediction of the flow birefringence in the converging die for α=0 also is distinctly higher than the prediction from the constant annular die; whereas, the value of α=1 in the converging die predicted the same average flow birefringence as the constant annular die. This supports the choice of α=0 for describing the flow in the converging die and suggests that an uniaxial extensional deformation occurs in the die due to the converging section.

Alternatively, the measured flow birefringence for the diverging die is distinctly lower than the data obtained from the constant annular die. The relative difference between the prediction of the flow birefringence in the diverging die for α=1 and the predictions of the constant annular die is the same as the relative differences between the measured values. This suggests that a biaxial extensional type deformation occurs in the diverging section of the die channel.

Since the relative differences in the flow birefringence between the three dies is predicted by the modeling calculations and this relative difference seems to be due to the extensional deformations which are different in the three dies, the disagreeement between the absolute values of the predictions and measurements seems to be due to the shear deformation in the three dies. From Figure 5.25, the principal stress difference, S'_{13}, is seen to be similar near the walls due to the shear deformation being similar in all three dies. When calculating the total retardation angle, the large values of S'_{13} near the walls contribute the most when the integral over the entire gap is considered. If the values of S'_{13} were predicted high, the predicted average flow birefringence would also be high. The tendency of the integral model to slightly overpredict the stress for LDPE was already seen in the steady shear viscosity curves and in the pressure drop predictions. The pressure drop only depends on the shear stress which has a linear term involving the shear strain; whereas, the flow birefringence depends on the principal normal stress difference, $\sigma'_{11}-\sigma'_{33}$, which has a squared term involving the shear strain. Therefore, if the shear strain is predicted

slightly high, the predicted flow birefringence will be even higher, due to its squared dependency on the shear strain, and the predicted curves will be shifted by a constant value for all three dies because the shear strain is similar in all the dies.

For the LDPE, the shear rates near the walls of the flow channel ranged from 1.0 to 100. s^{-1} for the range of flow rates studied. From Figure 3.34, in the same region of shear rates, the integral model overpredicts the shear viscosity by a factor of 1.46. The shear stress and hence shear viscosity is directly proportional to the shear strain, γ, but the normal stress difference, S'_{13}, is dependent on the square of the shear strain, γ^2, and would therefore be overpredicted by a factor of $(1.46)^2$=2.13. This factor of 2 is in agreement with the predicted and measured values of the average flow birefringence data shown in Figure 5.26.

In summary of this chapter, the process model, using an integral constitutive equation to describe the polymer rheological behavior, adequately predicts the pressure drop through annular extrusion dies having shear and extension superimposed. The strain history in the dies was calculated and gives a quantitative description of the deformation of a material element at the die exit. The flow birefringence predicted from the modeling described the differences due to the extensional components in the three dies but was found to be higher than the measured values. This discrepancy was attributed to the significant contribution of the shear deformation which was similar in all three dies.

C H A P T E R V I

THE APPLICATION OF THE MODELING TO CHANGES OF RHEOLOGY IN ANNULAR DIES

An application of the modeling technique to the study of polymers having slightly different rheological behavior is described in this chapter. The stress state in two different annular dies is compared for the LDPE which was characterized in Chapter 3. The rheology of the LDPE was mathematically "modified" by changing some of the modulus coefficients associated with the relaxation times in the linear viscoelastic relaxation spectrum. The effect of changing the coefficients of the two longest relaxation times and the two shortest relaxation times was investigated.

6.1 Results of the Modeling Calculations

The geometries of the two dies used in this simulation appear in Figure 6.1. Die IV is similar to Die I described in the previous chapter, having a constant annular cross-section along the entire length. Die V has a long tapering section for most of the length but has the same dimensions as Die IV at the exit. The average velocity in the channel, $\bar{v}$=10 mm/s, and the temperature, T=150°C, for the LDPE was chosen to be the same for all the following examples. A value of α=1 was used in the strain function.

The ratio of the normal stress difference, $\sigma_{11}-\sigma_{22}$, to the shear stress, σ_{12}, has been used to describe the state of stress at the exit

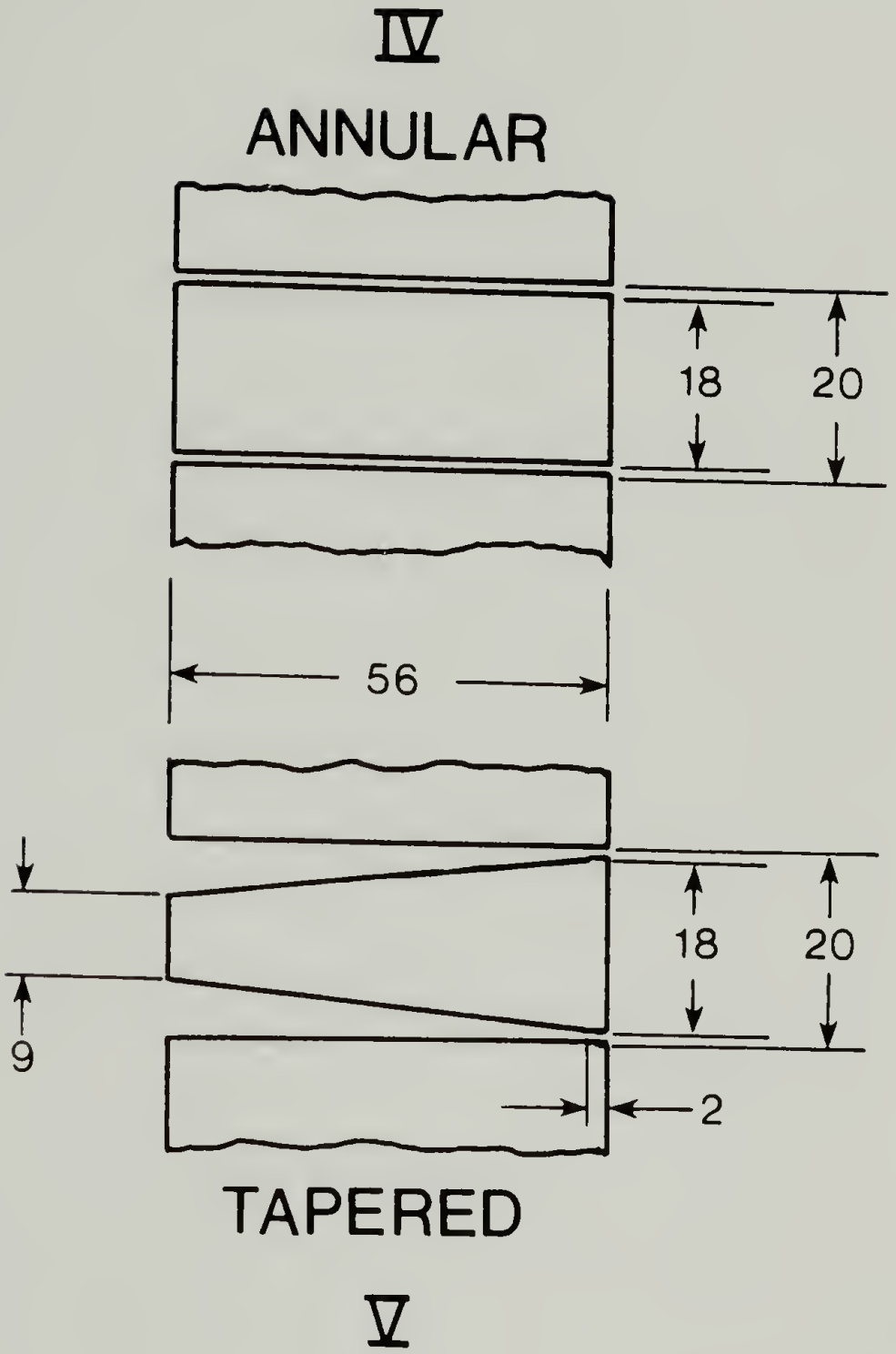

Figure 6.1. Dimensions of annular dies used in simulation experiments. All dimensions are in mm.

of the extrusion dies (Winter and Fischer, 1981). The ratio of these stresses is equal to the recoverable strain (Lodge, 1964)

$$\gamma_r = \lim_{t' \to -\infty} (\sigma_{11}-\sigma_{22})/2\sigma_{12} \qquad (6.1)$$

in steady shear flow both within and outside the linear viscoelastic region. This recoverable strain can be related to the swell of the extrudate upon leaving the die.

This stress ratio was found to be highly sensitive to small changes in die geometry due to the incorporation of extensional deformations in the flow (Winter and Fischer, 1981). The sensitivity of this stress ratio to die geometry is shown in Figure 6.2 where the results for the annular die (Die IV) and the tapered die (Die V) are compared. The stress ratio distribution is essentially symmetric about the center of the gap so the distribution is shown from the center of the gap to the outer wall. The larger stress ratio near the center of the gap for the tapered die is due to the extensional flow components produced in the tapering section. The stress ratio is small near the center of the constant annular die due to its lack of extensional components. Close to the wall, the stress ratios approach the same values for both dies because the flow approaches steady shear flow at the wall as discussed earlier. The sensitivity of this stress ratio to slight changes in the rheological behavior of the polymer is now discussed.

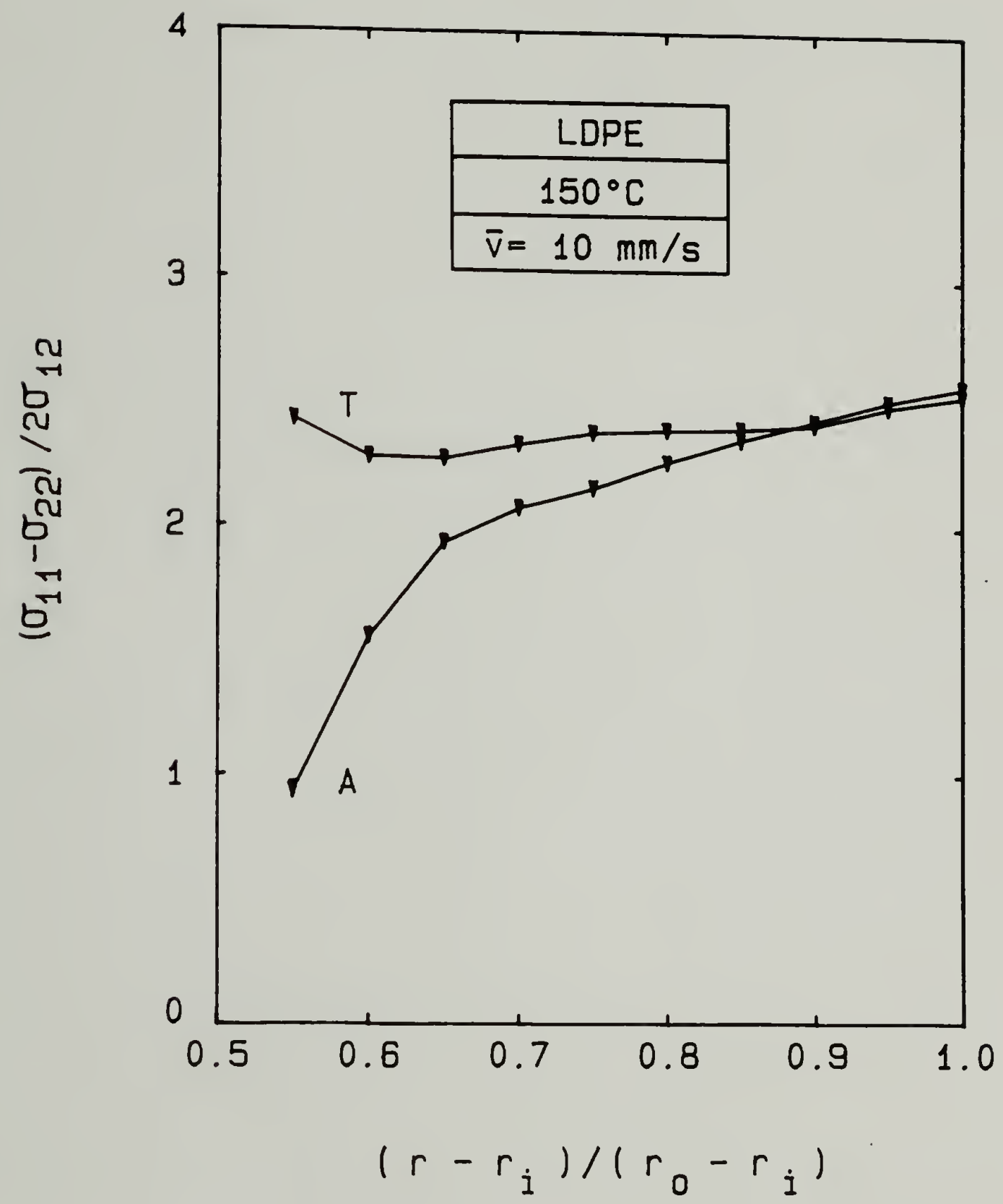

Figure 6.2. Stress ratio at the exit of extrusion dies shown in Figure 6.1
A - Annular
T - Tapered

6.2 Sensitivity to Changes of Rheology

In order to study the sensitivity of the modeling to changes in the rheological behavior of a polymer, the well characterized LDPE was mathematically "modified" by changing some of the parameters in the relaxation spectrum found in Table 3.3. The modulus coefficients of the two longest and two shortest relxation times were modified as shown in Table 6.1. In one case they were made five times greater and in the other case they were made one fifth less. By changing these coefficients, the simulated low rate and high rate steady shear properties of the LDPE were varied. The effect that these simulated changes in shear rheology have on the stress state at the exit of the two dies is now discussed.

6.2.1 Modification of Long Relaxation Time Coefficients

The modification of the long relaxation time coefficients changes the low shear rate steady shear viscosity of the LDPE as shown in Figure 6.3. The solid curve is the prediction according to the integral model using the relaxation spectrum in Table 3.3. The dashed curve is the prediction using the greater coefficients of the two longest relaxation times from Table 6.1 and the dotted curve is the prediction using the lesser values of the coefficients of the two longest relaxation times. In the following figures, G and L will indicate these simulations.

The results of the stress calculations with these modifications are shown in Figure 6.4 for the constant annular die and Figure 6.5 for the tapered die. The stress ratio near the center of both dies is

Table 6.1. Modifications to relaxation spectrum of LDPE.

Relaxation Times λ_i[s]		Modulus Coefficients g_i[Pa]		
		Unmodified (U)	Greater (G)	Less (L)
Longest	5.913×10^{1}	3.776×10^{1}	1.888×10^{2}	7.552×10^{0}
	1.817×10^{1}	3.710×10^{2}	1.855×10^{3}	7.420×10^{1}
Shortest	3.026×10^{-3}	1.371×10^{5}	6.855×10^{5}	2.742×10^{4}
	3.381×10^{-4}	3.027×10^{5}	1.513×10^{6}	6.054×10^{4}

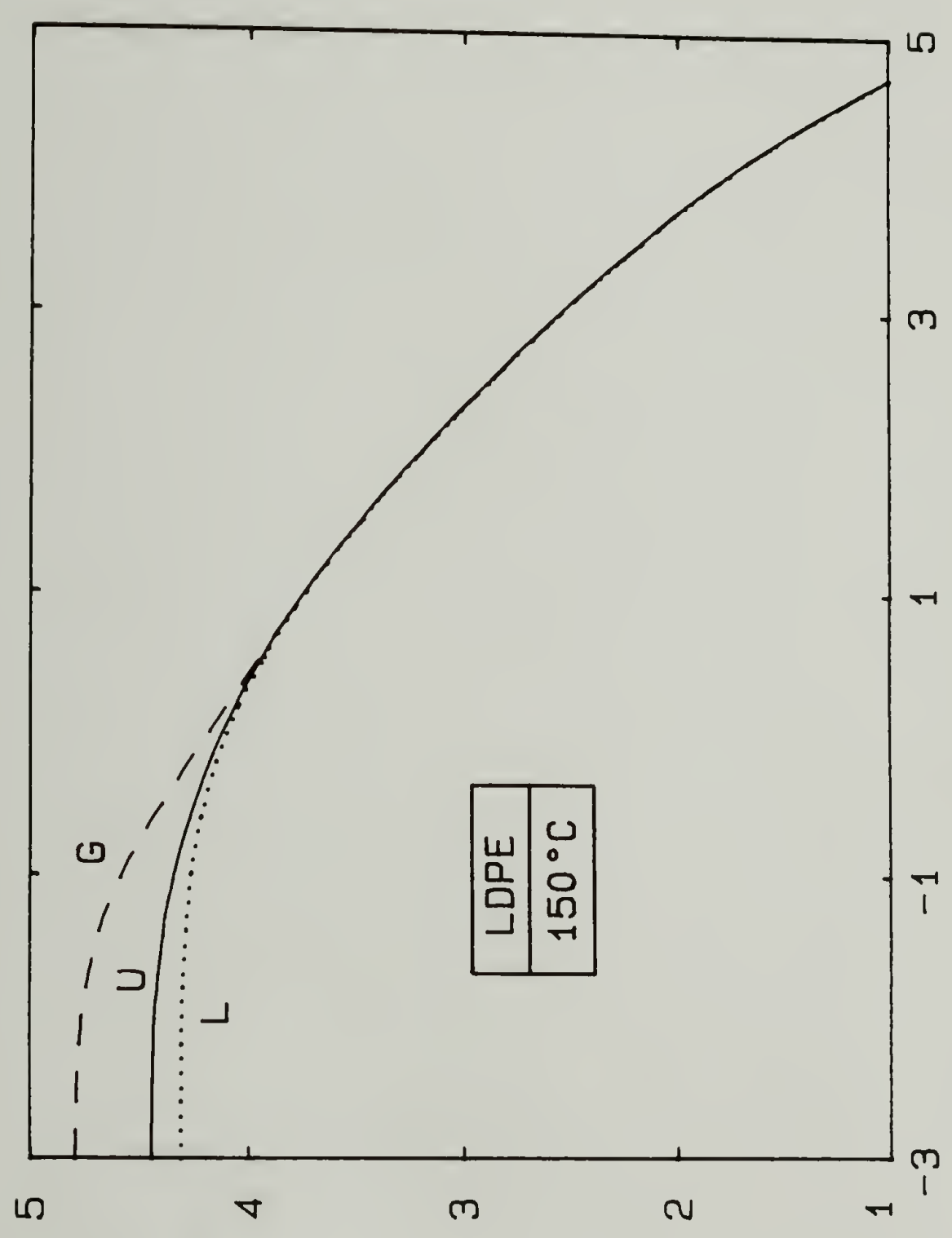

Figure 6.3. Simulated steady shear viscosity of LDPE after modification of the coefficients of the long relaxation times
G - Greater, U - Unmodified, L - Less
For description of G, U and L see text.

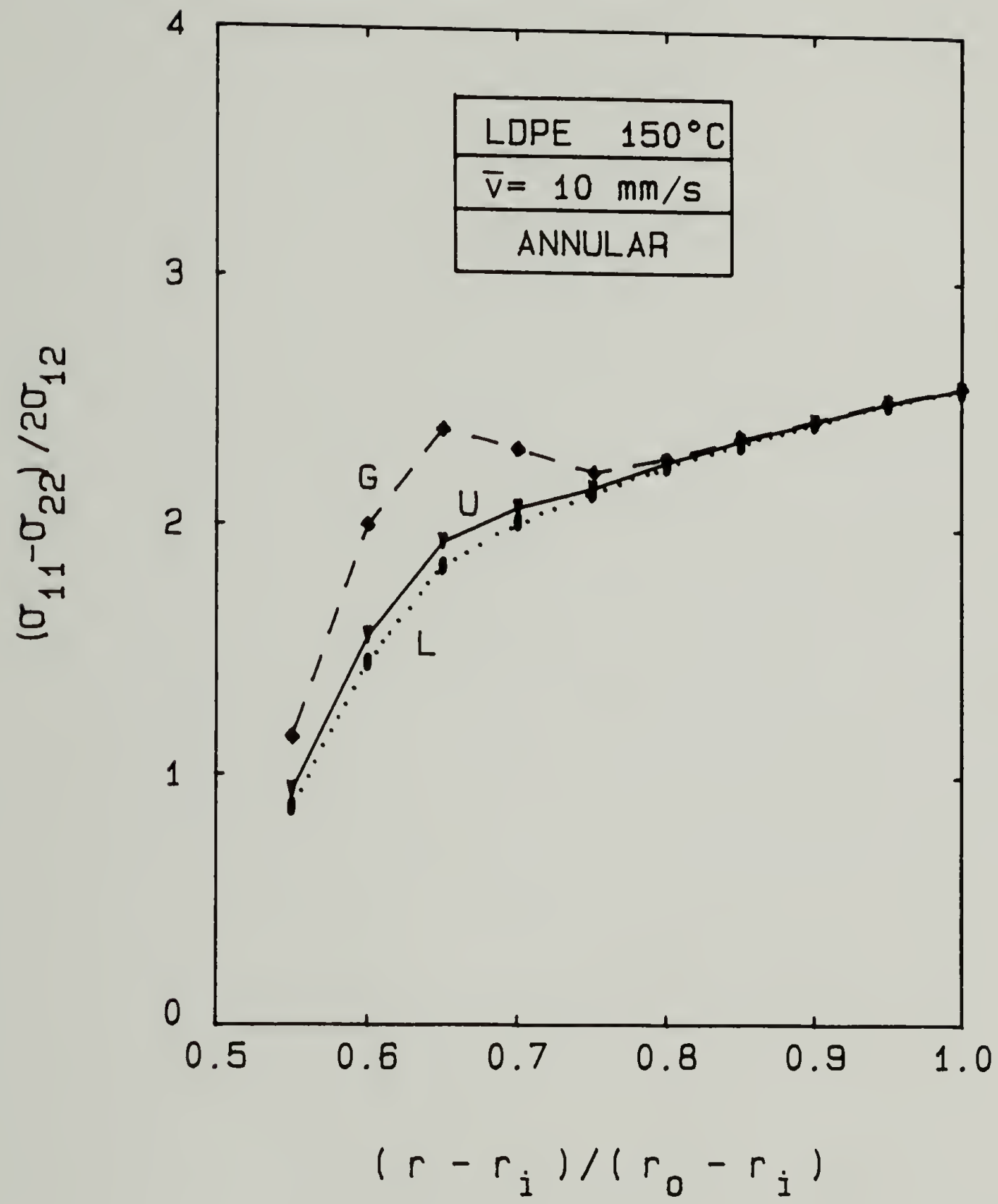

Figure 6.4. Stress ratio at the exit of annular die after modification of the coefficients of the long relaxation times
G - Greater
U - Unmodified
L - Less
For description of G, U and L see text.

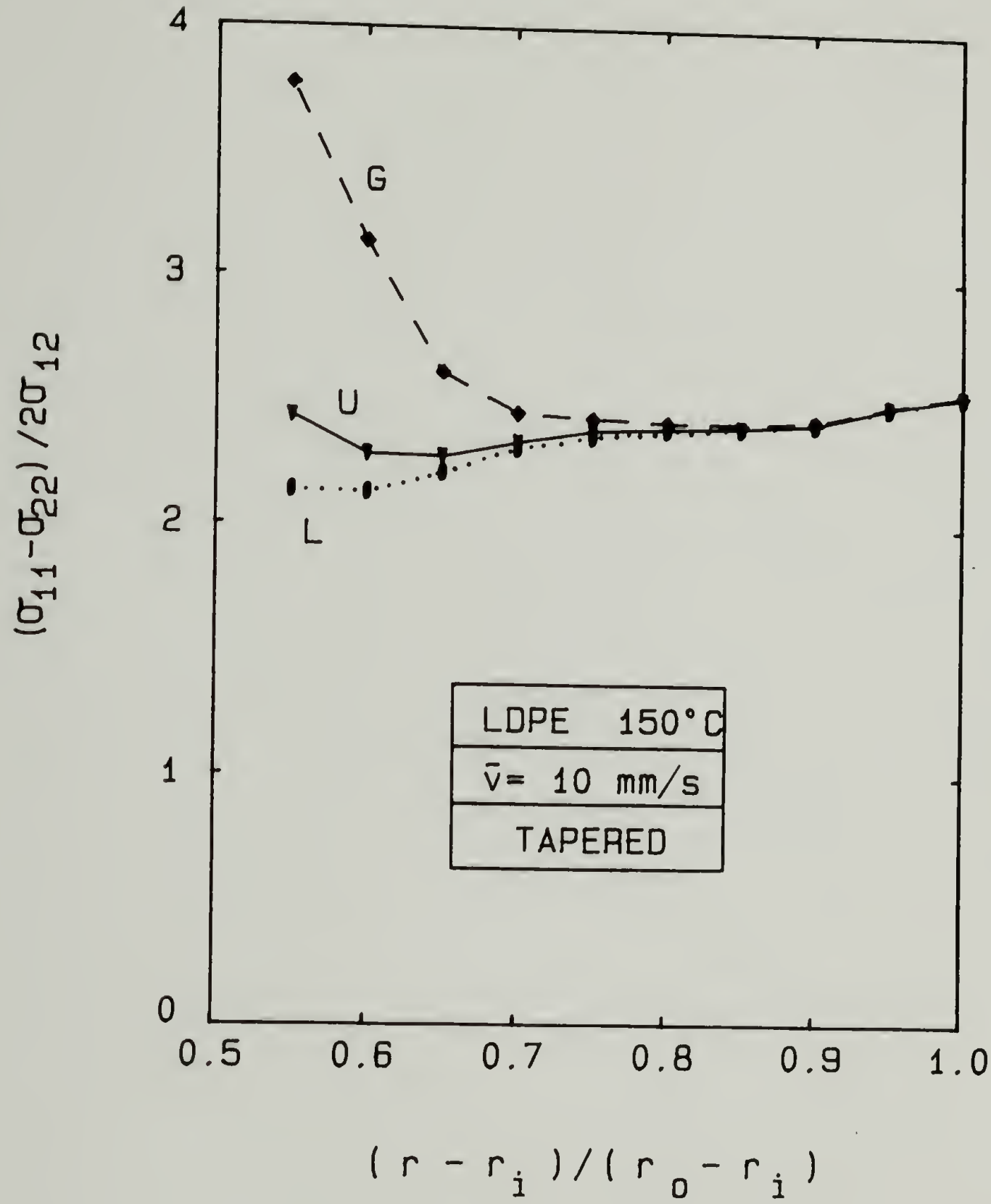

Figure 6.5. Stress ratio at the exit of tapered die after modification of the coefficients of the long relaxation times
G - Greater
U - Unmodified
L - Less
For description of G, U and L see text.

affected most by the modification of the long relaxation time coefficients. The greater coefficients predict a higher stress ratio and the lesser coefficients predict a lower stress ratio than the unmodified polymer. These changes are dramatic near the center of the channel due to the low shear rate in that region. From the steady shear viscosity predictions of Figure 6.3, the greater coefficients are seen to predict a higher shear viscosity at low shear rates which in turn predicts a higher stress ratio near the center due to the normal stress difference changing more dramatically than the shear stress. A similar argument can be made for the lesser coefficients.

The largest fraction of the polymer passes through the center of the die gap where the differences between the "modified" polymers are most pronounced. The different stress ratios are related to the swelling phenomena outside the die so the "modified" polymers may have substantially different swelling properties. Whereas the modeling indicates that the behavior of the modified polymers is much different in annular die flow, a simple characterization such as capillary rheometry would be unable to predict these differences since the high shear rate viscosity is the same for all three of the "modified" LDPE polymers. The fact that all the "modified" polymers have the same high shear rate shear viscosity is exhibited in the stress ratio calculations which show that near the walls, where the shear rate is highest, the stress ratios are the same. Therefore, it can be concluded from the modeling calculations that the characterization of the long relaxation times of a polymer melt is very important for understanding annular processing flows.

6.2.2 Modification of Short Relaxation Time Coefficients

The modification of the short relaxation time coefficients changes the intermediate and high shear rate steady shear viscosity of the LDPE as shown in Figure 6.6. The solid curve is the prediction according to the integral model as shown in Figure 6.3. The dashed curve is the prediction using the greater coefficients of the two shortest relaxation times from Table 6.1 and the dotted curve is the prediction using the lesser values of the coefficients of the two shortest relaxation times.

The results of the stress calculations with these modifications are shown in Figure 6.7 for the constant annular die and Figure 6.8 for the tapered die. For the annular die, the stress ratio near the walls is affected most by the modification of the short relaxation time coefficients. Contrary to the modification of the longest relaxation time coefficients, the greater coefficients predict a lower stress ratio and the lesser coeffieients predict a higher stress ratio than the unmodified polymer for the modification of the shortest relaxation time coefficients. These changes are dramatic near the walls of the channel due to the high shear rate present in that region. As seen in Figure 6.6, the greater coefficients predict a higher shear viscosity at high shear rates which in turn predicts a lower stress ratio near the wall due to the shear stress changing more dramatically than the normal stress difference. A similar argument can be made for the lesser coefficients.

Similar behavior is seen for the tapered die except even the stress ratios near the center of the gap are different for the "modified" polymers.

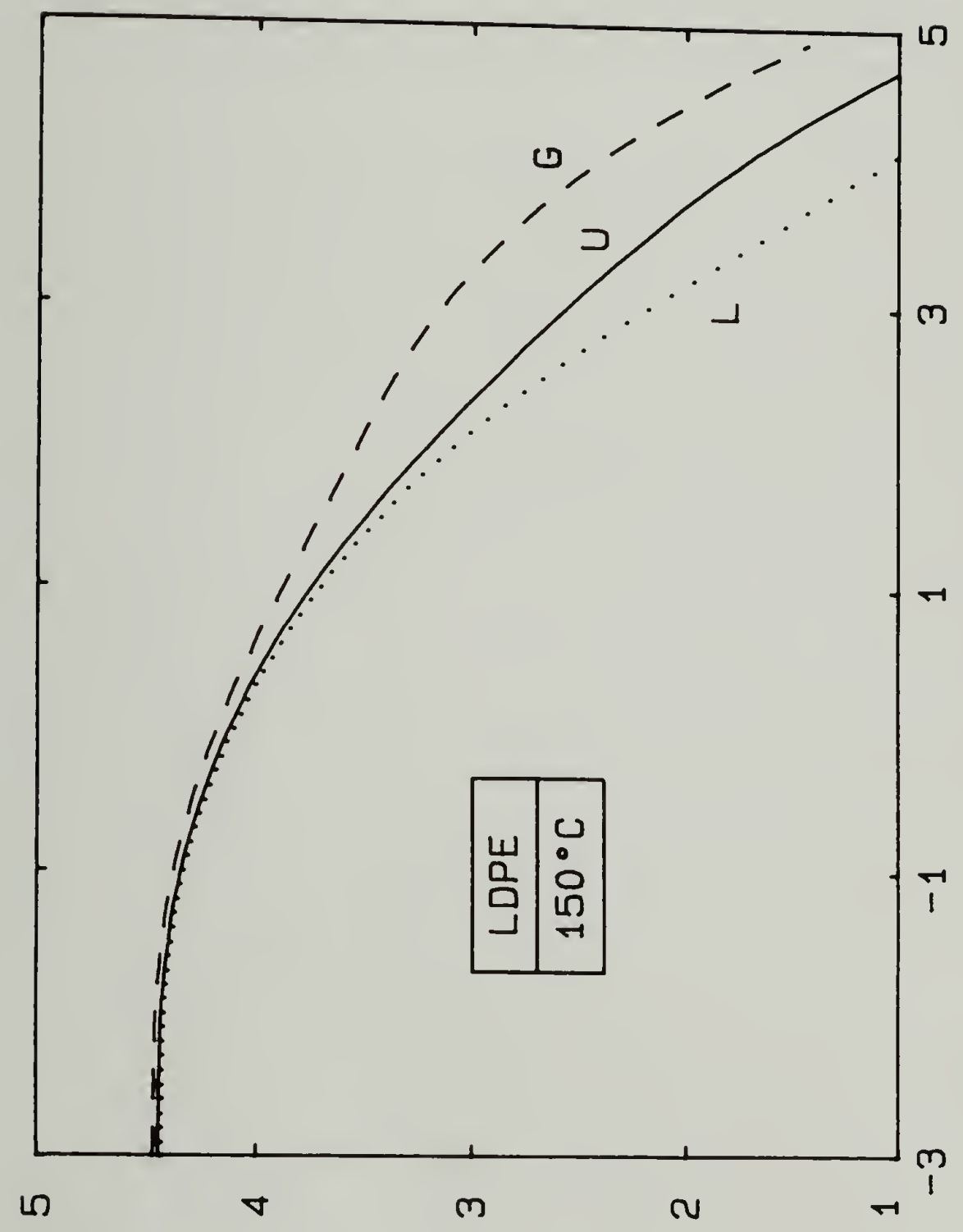

Figure 6.6. Simulated steady shear viscosity of LDPE after modification of the coefficients of the short relaxation times
G - Greater, U - Unmodified, L - Less
For description of G, U and L see text.

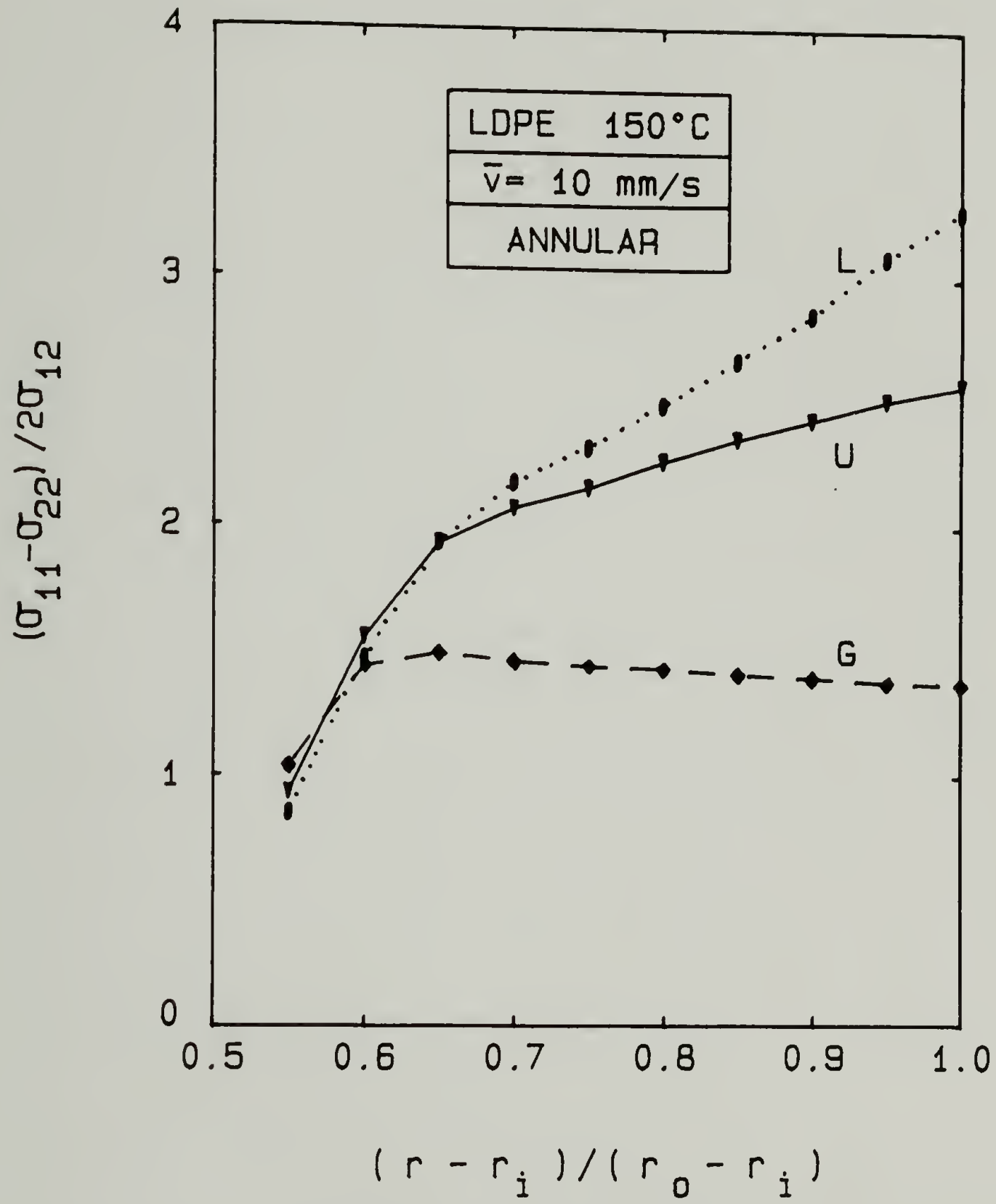

Figure 6.7. Stress ratio at the exit of annular die after modification of the coefficients of the short relaxation times
G - Greater
U - Unmodified
L - Less
For description of G, U and L see text.

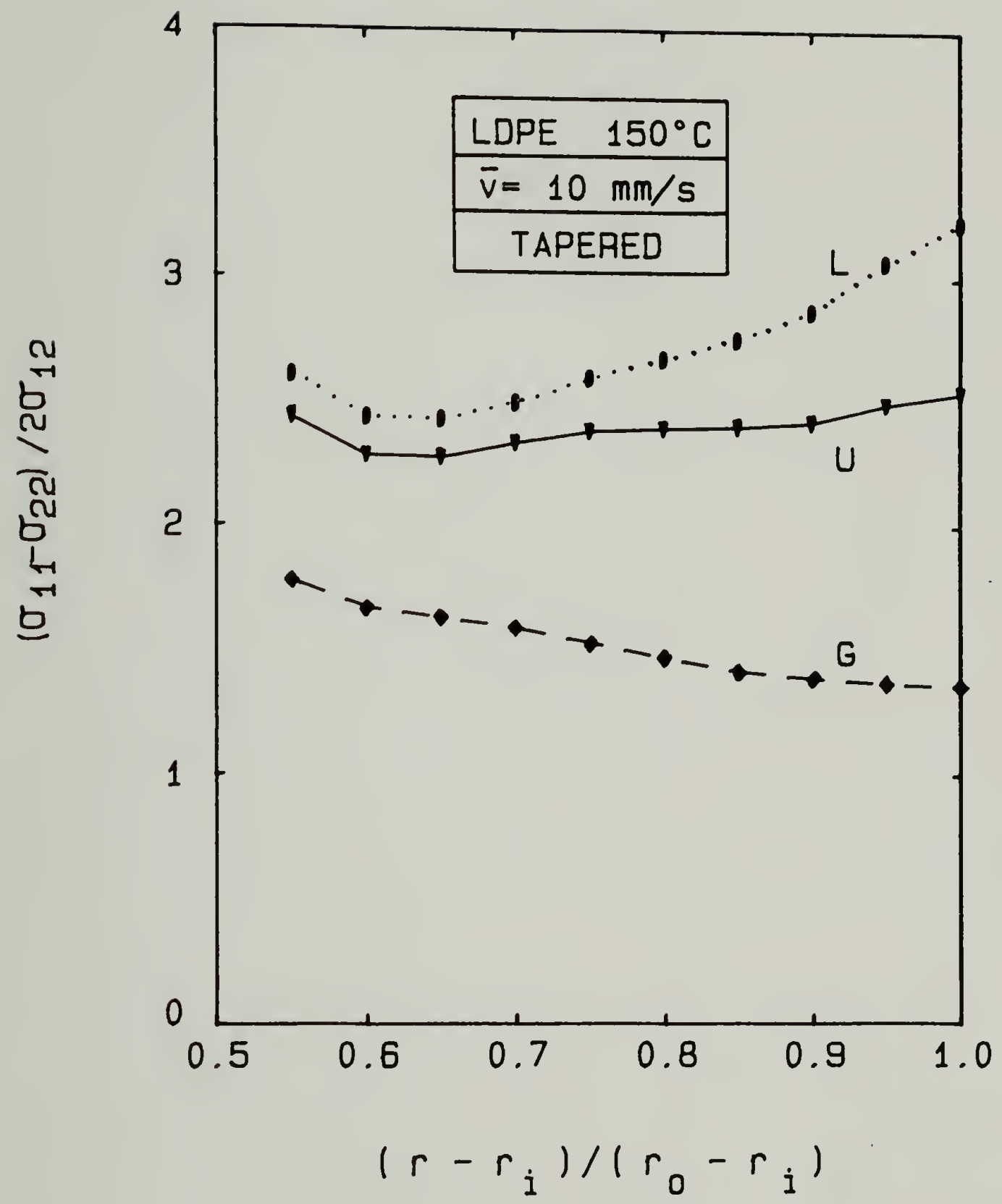

Figure 6.8. Stress ratio at the exit of tapered die after modification of the coefficients of the short relaxation times
G - Greater
U - Unmodified
L - Less
For description of G, U and L see text.

A conclusion drawn from the results of this chapter is that the modeling calculations for the stress state of a polymer at the exit of annular extrusion dies are very sensitive to small changes in the rheological properties of the polymer. The modeling calculations aid one in designing dies of differing geometry and provide predictions of the stress state of material elements in the flow when several polymers having even slightly different rheological properties are processed.

CHAPTER VII

CONCLUDING REMARKS AND SUGGESTIONS FOR FUTURE RESEARCH

7.1 Conclusions

Significant contributions to the fields of polymer melt rheology and process modeling have resulted from the research undertaken in this dissertation.

In the area of rheology, two novel rheological characterization techniques were developed: the shear step strain experiment in the parallel disk geometry and the equibiaxial extensional step strain experiment using a lubricated squeezing apparatus. The shear step strain experiment developed here allows one to obtain the large strain behavior of polymer melts in rheometers which up to this time were capable of measuring only small strain rheological behavior. The extensional strain function was directly determined from the equibiaxial extensional step strain experiment. Previously, the only data available for the extensional strain function of polymer melts was obtained by indirect means (Wagner, 1978). These step strain experiments were found to be sensitive to molecular structure such as long chain branching. Its application to that area of polymer characterization is discussed below. The development of these techniques provides a basis from which novel data may be obtained for other classes of polymer materials including filled polymer melts and liquid crystalline polymers.

In the area of process modeling, a strain dependent memory integral constitutive equation, which takes into account the entire shear and extensional deformation history of a material element, was utilized to calculate the stress-state of a polymer at the exit of extrusion dies. The process model accurately predicted the pressure drop and extensional behavior in the dies. The modeling procedure developed here is a valuable tool for understanding the flow in existing dies and for designing dies for specific processing applications. A more detailed discussion of these two areas follows.

7.1.1 Rheology

The shear step strain experiment in the parallel disk rheometer allows one to obtain the large shear strain behavior of the polymeric fluids. A correction method for the non-homogeneous strain in the parallel disks was proposed and experimentally verified. The shear relaxation modulus was found to be separable into a time dependent function and a strain dependent function thus supporting the separability assumption (Wagner, 1979) discussed in the second chapter. Since the shear relaxation modulus was separable, a strain function for shear was obtained from the step shear data. A sigmoidal form of the shear strain function having two material parameters was found to describe the experimental data as well as the previously proposed form containing the sum of two exponential functions and three material parameters (Osaki, 1976). The sigmoidal form actually predicted the shear strain function better at low strains.

The lubricated squeezing technique was utilized to measure the extensional relaxation modulus after a step in equibiaxial extensional strain. The extensional relaxation modulus was shown to approach the linear viscoelastic relaxation modulus at the limit of small strains just as the shear relaxation modulus does. The extensional relaxation modulus was also found to be separable into functions of time and strain similar to the shear relaxation modulus. This supports the validity of the strain dependent memory integral constitutive equation for polymer melts (Wagner and Stephenson, 1979b).

These lubricated squeezing experiments provided the first method to directly determine the extensional strain function (Wagner, 1978). The measured extensional strain function suggests that, for equibiaxial extension, the parameter α, in the generalized strain invariant proposed by Wagner (1979) should be $\alpha=1$.

7.1.2 Process Modeling

Three different extrusion dies having a constant annular cross-section, converging and diverging sections were modeled. An improved tracking procedure (Winter, 1982) was used to determine the strain history of material elements along pathlines in the flow.

The process model gave good predictions of the pressure drop in each die. A quantitative description of the strain history of a material element along a pathline at the die exit was determined from the modeling procedure and gave insight into the flow features of the process. The comparison of the modeling calculations to the measured flow

birefringence indicates that the process model describes the extensional behavior in the converging and diverging sections well and, together with the strain history calculations, indicates that a material element is subjected to an uniaxial extensional type deformation in the converging section and a biaxial extensional type deformation in the diverging section of the dies. The discrepancies between the predictions of the model and the flow birefringence were attributed to the overprediction of the shear deformations which dominate the flow in the three dies investigated.

The modeling procedure was also found to be very sensitive to the slight change of the rheological properties of the polymer. The accurate characterization of the properties associated with the long relaxation times in the linear viscoelastic spectrum is very important in annular die flow.

7.2 Suggestions for Future Research

The ultimate goal in modeling polymer processes is to be able to predict processing parameters, stress levels, and molecular orientation for a particular process purely from the molecular parameters of the polymer. Some of these molecular parameters include the structure of the monomer unit, molecular weight distribution, degree of branching and length of branches. The solution to this ultimate problem involves a similar two step process used in this dissertation. First, the choice of a suitable constitutive equation which describes the rheological behavior of the polymer is required and then a mathematical process

model relating the rheological properties to the stresses and the resultant orientation of the polymer chains is needed. Future research in these areas is proposed here.

7.2.1 Rheology

The memory integral constitutive equation used in this dissertation was developed from a molecular theory in the sense that the entanglement network was considered to consist of long chain freely jointed polymer molecules which formed temporary entanglement junctions: but, it does not take into account such molecular features as monomer unit structure or differences in molecular weight. The material parameters that are required for the constitutive equation must be obtained from experiments and empirical relations.

Recently, more sophisticated constitutive equations for polymer melts, based on reptation of the polymer molecule, have been developed (Doi and Edwards, 1978a, 1978b, 1978c and 1979; Curtiss and Bird, 1981). The reptation theory is based on the back-and-forth motion of the polymer chain along the chain backbone which is confined to a tube having a characteristic length; there is no consideration of entanglement junctions. These reptation theories take into account the molecular weight dependence of various rheological properties. Before these constitutive equations are used in process modeling, experimental studies of their predictions must be undertaken. Both small and large strain experiments should be done in both shear and extension to completely test these reptation models. Recently good agreement has been found between the

Doi-Edwards theory and the shear behavior of polymer solutions (Vrentas and Graessley, 1982) and melts (Lin, 1984).

The application of these theories to extensional rheology is urgently needed. By means of the novel rheological techniques developed in this dissertation, especially the equibiaxial extensional step strain experiment using the lubricated squeezing technique, these molecular constitutive equations can be tested for polymer melts. Therefore, the elongational rheology of linear polymers, such as polystyrenes, having well characterized molecular weights and narrow molecular weight distributions would be one area of continued research. Also, initial experiments on the two polyethylenes suggest that the step strain experiment is a very sensitive experimental technique to study the number and length of side branches in a polymer. A series of polymers having well characterized branch lengths and degree of branching may be of interest to investigate with the step strain techniques.

Besides considering constitutive equations based on more sophisticated molecular theories, further research can also include the development of better empirical forms for the shear strain function in the memory integral constitutive equation. Recent work by Larson and Monroe (1984) suggests that the generalized strain function obtained from the Wagner model for shear and uniaxial extension can be described just as well with the use of an entropic constitutive equation such as the BKZ model. The Wagner model, which does not possess an entropic equation of state, can violate the second law of thermodynamics in highly elastic mixed deformations. Therefore, it would be of interest to see how their

form of generalized strain function describes the data obtained in this dissertation.

A final area that needs future consideration is the development of techniques to measure the equibiaxial extensional rheology of polymer melts at high strains. One such way would be to improve the lubrication at small plate separations in the lubricated squeezing apparatus.

7.2.2 Process Modeling

New methods to improve the modeling of polymer processes are always needed. An area needing improvement in the process model discussed in this dissertation is in the determination of the kinematics for more abrupt flows. Further refinement of the velocity field may be required. New solution procedures for both the finite-difference (Court et al., 1981) and finite-element (Viriyayuthakorn and Caswell, 1980) numerical simulation of complex flows using integral rheological constitutive equations are being developed. An iterative procedure to improve on the initial kinematics, using the stress field calculated from the modeling procedure described here, would be an area to develop in the future. Any improved accuracy in the results would have to be weighed in terms of computation time.

Further experimental studies of stress measurement in other processing flows and comparison to the modeling calculations would be another area of future research. The modeling of a high extension process would be an important area to consider. Now that some experimental techniques are available to rheologically measure higher extensional flows, the modeling of such flows can give information about the

processing behavior from a more fundamental understanding of the deformation. The suitability of the constitutive equation to such flows can also be determined. Higher extensional flows such as film blowing or blow molding should be considered.

Modelling of processes such as film blowing and blow molding would be a logical extension to the work accomplished in this dissertation since annular die flow is an essential part of these processes. In regards to the modeling, the handling of the velocity field rearrangement region near the die exit where the flow changes from a parabolic-like constrained flow to a plug-like free surface flow and the associated swelling phenomena are important areas of research to continue.

Finally, the incorporation of a constitutive equation based on molecular theory as discussed in the previous section to predict molecular orientation due to the deformation of a processing flow would be an ultimate goal. In order to make progress in this area, methods for experimentally determining the molecular orientation, not only in the rheologically simple flows, but also in processing flows are required.

Further research in these areas may someday lead to a complete description of the flow and shaping of polymers based on the fundamental understanding of the polymer molecule itself.

REFERENCES

Adams, E. B., J. C. Whitehead and D. C. Bogue, AIChE J., 11, 1026 (1965).

Bagley, E. B., J. Appl. Phys., 28, 624 (1957).

Baily, E. D., Trans. Soc. Rheol., 18, 635 (1974).

Bernstein, B., E. A. Kearsley and L. J. Zapas, Trans. Soc. Rheol., 7, 391 (1963).

Bernstein, B., E. A. Kearsley and L. J. Zapas, J. Res. Natl. Bur. Std., 68B, 103 (1964).

Bernstein, B. and D. S. Malkus, "Steady Flows of Memory Fluids with Finite Elements," Progress Report of NSF Grant MCS-81-02089, October (1981).

Bevington, P. R., "Data Reduction and Error Analysis for the Physical Sciences," McGraw-Hill, N.Y., p. 134 (1969).

Bird, R. B., R. C. Armstrong and O. Hassager, "Dynamics of Polymeric Liquids," Vol. 1, John Wiley & Sons, N.Y. (1977a).

Bird, R. B. and P. J. Carreau, Chem. Eng. Sci., 23, 427 (1968).

Bird, R. B., O. Hassager, R. C. Armstrong and C. F. Curtiss, "Dynamics of Polymeric Liquids," Vol. 2, John Wiley & Sons, N.Y. (1977b).

Bogue, D. C. and J. L. White, "Engineering Analysis of Non-Newtonian Fluids," NATO Agardograph, 144 (1970).

Brizitsky, V. I., G. V. Vinogradov, A. I. Isayev and Y. Y. Podolsky, J. Appl. Polym. Sci., 22, 751 (1978).

Carreau, P. J., Trans. Soc. Rheol., 16, 99 (1972).

Chang, H. and A. S. Lodge, Rheol. Acta, 11, 127 (1972).

Chatraei, S., C. W. Macosko and H. H. Winter, J. Rheol., 25, 433 (1981).

Chen, I-J. and D. C. Bogue, Trans. Soc. Rheol., 16, 59 (1972).

Chen, I-J., G. E. Hagler, L. E. Abbott, J. N. Dalton, D. C. Bogue and J. L. White, Trans. Soc. Rheol., 16, 473 (1972).

Choi, K. J., J. L. White and J. E. Spruiell, J. Appl. Polym. Sci., 25, 2777 (1980).

Choi, K. J., J. E. Spruiell and J. L. White, J. Polym. Sci., Polym. Phys. Ed., 20, 27 (1982).

Cogswell, F. N., Trans. Soc. Rheol., 16, 383 (1972).

Court, H., A. R. Davies and K. Walters, J. Non-Newtonian Fluid Mech., 8, 95 (1981).

Cox, W. P. and E. H. Merz, J. Polym. Sci., 28, 619 (1958).

Crochet, M. J. and M. Bezy, J. Non-Newtonian Fluid Mech., 5, 201 (1979).

Curtiss, C. F. and R. B. Bird, J. Chem. Phys., 74, 2016 (1981).

Dealy, J. M., J. Non-Newtonian Fluid Mech., 4, 9 (1978).

Dealy, J. M., "Rheometers for Molten Plastics," Van Nostrand Reinhold Co., N.Y., (1982).

Denson, C. D. and R. J. Gallo, Polym. Eng. Sci., 11, 174 (1971).

Denson, C. D. and D. C. Hylton, Polym. Eng. Sci., 20, 535 (1980).

DeVries, A. J., C. Bonnebat and J. Beautemps, J. Polym. Sci., Polym. Symp., 58, 109 (1977).

Dexter, F. D., J. C. Miller and W. Phillippoff, Trans. Soc. Rheol., 5, 193 (1961).

Dietz, W. and J. L. White, Rheol. Acta, 17, 676 (1978).

Dietz, W., J. L. White and E. S. Clark, Polym. Eng. Sci., 18, 273 (1978).

Doi, M. and S. F. Edwards, J. Chem. Soc., Faraday Trans. II, 74, 1789 (1978a); ibid., 74, 1802 (1978b); ibid., 74, 1818 (1978c); ibid., 75, 38 (1979).

Einaga, Y., K. Osaki, M. Kurata, S. Kimura, N. Yamada and M. Tamura, Polymer J., 5, 91 (1973).

Ferry, J. D., J. Amer. Chem. Soc., 72, 3746 (1950).

Ferry, J. D., "Viscoelastic Properties of Polymers," 3rd ed., J. Wiley & Sons, New York (1980).

Fischer, E., Rheol. Acta, 20, 44 (1981a).

Fischer, E., Kunststoffe, 71, 380 (1981b).

Fisher, R. J. and M. M. Denn, AIChE J., 22, 236 (1976).

Frank, A. J. P., "Elongational Testing of Polymer Melts Using Uniaxial Extensional Flow and Lubricated Squeezing Flow Techniques," Conf. Engineering Rheology, London (1983).

Fukuda, M., K. Osaki and M. Kurata, J. Polym. Sci., Polym. Phys. Ed., 13, 1563 (1975).

Goettler, L. A., R. I. Leib and A. J. Lambright, Rubber Chem. Technol., 52, 838 (1979).

Gortemaker, F. H., M. G. Hansen, B. deCindio, and H. Janeschitz-Kriegl, Rheol. Acta, 15, 242 (1976a).

Gortemaker, F. H., H. Janeschitz-Kriegl and K. te Nijenhuis, Rheol. Acta, 15, 487 (1976b).

Green, M. S. and A. V. Tobolsky, J. Chem. Phys., 14, 80 (1946).

Han, C. D., Rheol. Acta, 14, 173 (1975).

Han, C. D. and L. H. Drexler, J. Appl. Polym. Sci., 17, 2329 (1973a).

Han, C. D. and L. H. Drexler, J. Appl. Polym. Sci., 17, 2369 (1973b).

Holmes, D. R. and R. P. Palmer, J. Polym. Sci., 31, 345 (1958).

Huang, D. C. and J. L. White, Polym. Eng. Sci., 19, 609 (1979).

Huang, D. C. and J. L. White, Polym. Eng. Sci., 20, 182 (1980).

Isayev, A. I. and C. A. Hieber, Rheol. Acta, 19, 168 (1980).

Janeschitz-Kriegl, H., "Polymer Melt Rheology and Flow Birefringence," Springer-Verlag, Berlin (1983).

Jones, T. T., Pure & Appl. Chem., 45, 39 (1976).

Joye, D. D., G. W. Poehlein and C. D. Denson, Trans. Soc. Rheol., 16, 421 (1972).

Joye, D. D., G. W. Poehlein and C. D. Denson, Trans. Soc. Rheol., 17, 287 (1973).

Kaye, A., College of Aeronautics, Note No. 134, Cranfield, U.K. (1962).

Kaye, A., Brit. J. Appl. Phys., 17, 803 (1966).

Kimura, S., K. Osaki and M. Kurata, J. Polym. Sci., Polym. Phys. Ed., 19, 151 (1981).

Kuhn, W., Kolloidzschr., 68, 2 (1934).

Kuhn, W., Kolloidzschr., 76, 258 (1936).

Kuhn, W. and F. Grün, Kolloidzschr., 101, 248 (1942).

Larson, R. G. and K. Monroe, Rheol. Acta, 23, 10 (1984).

Laun, H. M., Rheol. Acta, 17, 1 (1978).

Laun, H. M. and H. Münstedt, Rheol. Acta, 15, 517 (1976).

Laun, H. M., M. H. Wagner and H. Janeschitz-Kriegl, Rheol. Acta, 18, 615 (1979).

Leonov, A. I., Rheol. Acta, 15, 85 (1976).

Lin, Y-H., J. Rheol., 28, 1 (1984).

Lodge, A. S., Trans. Faraday Soc., 52, 120 (1956).

Lodge, A. S., Kolloidzschr., 171, 46 (1960).

Lodge, A. S., "Elastic Liquids," Academic Press, London-New York (1964).

Lodge, A. S., Rheol. Acta, 7, 379 (1968).

Lodge, A. S. and J. Meissner, Rheol. Acta, 11, 351 (1972).

Maerker, J. M. and W. R. Schowalter, Rheol. Acta, 13, 627 (1974).

Malkus, D. S., J. Non-Newtonian Fluid Mech., 8, 223 (1981).

Marquardt, D. W., J. SIAM, 11, 2 (1963).

Matsui, M. and D. C. Bogue, Polym. Eng. Sci., 16, 735 (1976).

Matsui, M. and D. C. Bogue, Trans. Soc. Rheol., 21, 133 (1977).

Matsumoto, T. and D. C. Bogue, J. Polym. Sci., Polym. Phys. Ed., 15, 1663 (1977).

McKelvey, J. M., "Polymer Processing," John Wiley & Sons, N.Y. (1962).

Meissner, J., J. Appl. Polym. Sci., 16, 2877 (1972).

Meissner, J., T. Raible and S. E. Stephenson, J. Rheol., 25, 1 (1981).

Menezes, E. V. and W. W. Graessley, J. Polym. Sci., Polym. Phys. Ed., 20, 1817 (1982).

Middleman, S., "Fundamentals of Polymer Processing," McGraw-Hill, N.Y. (1977).

Oda, K., J. L. White and E. S. Clark, Polym. Eng. Sci., 18, 53 (1978).

Ong, C., D. Y. Yoon and R. S. Stein, J. Polym. Sci., Polym. Phys. Ed., 12, 1319 (1974).

Orbey, N., Ph.D. Dissertation, McGill University, Montreal, Canada (1983).

Osaki, K., Proc. VII Int. Congr. Rheology, Gothenburg, 104 (1976).

Osaki, K., N. Bessho, T. Kojimoto and M. Kurata, J. Rheol., 23, 457 (1979a).

Osaki, K., N. Bessho, T. Kojimoto and M. Kurata, J. Rheol., 23, 617 (1979b).

Osaki, K., N. Bessho, T. Kojimoto and M. Kurata, J. Rheol., 24, 125 (1980).

Osaki, K., S. Kimura and M. Kurata, J. Polym. Sci., Polym. Phys. Ed., 19, 517 (1981).

Papanastasiou, A. C., L. E. Scriven and C. W. Macosko, J. Rheol., 27, 387 (1983).

Petrie, C. J. S., Rheol. Acta, 12, 92 (1973).

Petrie, C. J. S., AIChE J., 21, 275 (1975).

Petrie, C. J. S., "Elongational Flows," Pitman, London (1979).

Rabinowitsch, B., Z. Physik-Chemie, A145, 1 (1929).

Racano, R., T. Mitslai, L. Buteau, G. Lei and W. Phillippoff, J. Rheol., 23, 39 (1979).

Raible, T., A. Demarmels and J. Meissner, Polymer Bulletin, 1, 397 (1979).

Rhi-Sausi, J. and J. M. Dealy, Polym. Eng. Sci., 21, 227 (1981).

Shurcliff, W. A., "Polarized Light," Harvard Univ. Press, Cambridge, Mass. (1962).

Soskey, P. R. and H. H. Winter, SPE Tech. Papers, Vol. XXVIII, 47 (1982).

Spearot, J. A. and A. B. Metzner, Trans. Soc. Rheol., 16, 495 (1972).

Stein, R. S., J. Polym. Sci., 31, 335 (1958).

Stein, R. S., Rubber Chem. Technol., 49, 458 (1976).

Stephenson, S. E. and J. Meissner, Proc. VIII Int. Congr. Rheology, Naples, 431 (1980).

Tadmor, Z., J. Appl. Polym. Sci., 18, 1753 (1974).

Tadmor, Z., and C. G. Gogos, "Principles of Polymer Processing," John Wiley & Sons, N.Y. (1979).

Talbott, W. H. and J. D. Goddard, Rheol. Acta, 18, 505 (1979).

Theocaris, P. S. and E. E. Gdoutos, "Matrix Theory of Photoelasticity," Springer Series in Optical Sciences, Vol. 11, Springer-Verlag, N.Y. (1979).

Throne, J. L., "Plastics Process Engineering," Marcel Dekker, N.Y. (1979).

Tovstiga, G., M.S. Thesis, University of Massachusetts, Amherst (1983).

Treloar, L. R. G., "The Physics of Rubber Elasticity," 3rd ed., Clarendon Press, Oxford (1975).

van Aken, J. A., F. H. Gortemaker, H. Janeschitz-Kriegl and H. M. Laun, Rheol. Acta, 19, 159 (1980).

van Aken, J. A. and H. Janeschitz-Kriegl, Rheol. Acta, 19, 744 (1980).

van Aken, J. A. and H. Janeschitz-Kriegl, Rheol. Acta, 20, 419 (1981).

Viriyayuthakorn, M. and B. Caswell, J. Non-Newtonian Fluid Mech., 7, 245 (1980).

Vrentas, C. M. and W. W. Graessley, J. Rheol., 26, 359 (1982).

Wagner, M. H., Rheol. Acta, 15, 136 (1976).

Wagner, M. H., J. Non-Newtonian Fluid Mech., 4, 39 (1978).

Wagner, M. H., Rheol. Acta, 18, 33 (1979).

Wagner, M. H. and H. M. Laun, Rheol. Acta, 17, 138 (1978).

Wagner, M. H. and J. Meissner, Makromol. Chem., 181, 1533 (1980).

Wagner, M. H., T. Raible and J. Meissner, Rheol. Acta, 18, 427 (1979).

Wagner, M. H. and S. E. Stephenson, Rheol. Acta, 18, 463 (1979a).

Wagner, M. H. and S. E. Stephenson, J. Rheol., 23, 489 (1979b).

Wales, J. L. S., "The Application of Flow Birefringence to Rheological Studies of Polymer Melts," Delft Univ. Press (1976).

Wales, J. L. S. and H. Janeschitz-Kriegl, J. Polym. Sci., Polym. Phys. Ed., 5, 781 (1967).

Wales, J. L. S., J. van Leeuwen and R. v. d. Vijgh, Polym. Eng. Sci., 12, 358 (1972).

White, J. L. and W. Dietz, Polym. Eng. Sci., 19, 1081 (1979).

Williams, M. L., R. F. Landel and J. D. Ferry, J. Amer. Chem. Soc., 77, 3701 (1955).

Winter, H. H., Adv. Heat Transfer, 13, 205 (1977).

Winter, H. H., J. Non-Newtonian Fluid Mech., 10, 157 (1982).

Winter, H. H. and E. Fischer, Polym. Eng. Sci., 21, 366 (1981).

Winter, H. H., C. W. Macosko and K. E. Bennett, Rheol. Acta, 18, 323 (1979).

Winter, H. H. and P. R. Soskey, Proc. 2nd World Cong. Chem. Eng., Vol. VI, 341 (1981).

Yamamoto, M., J. Phys. Soc. Jpn., 11, 413 (1956).

Yamamoto, M., J. Phys. Soc. Jpn., 12, 1148 (1957).

Yamamoto, M., J. Phys. Soc. Jpn., 13, 1200 (1958).

Yoo, H. J. and C. D. Han, J. Rheol., 25, 115 (1981).

Zapas, L. J. and J. C. Phillips, J. Res. Natl. Bur. Std., 75A, 103 (1971).

APPENDIX A

NOMENCLATURE

a	material parameter in shear strain function, see Eq. (3.36)
a_T	temperature shift factor
A	complex Jones matrix for annular flow
b	material parameter in shear strain function, see Eq. (3.36)
C	stress-optical coefficient
C_1, C_2	material constants in WLF equation, see Eq. (2.54)
$\underline{\underline{C}}$	Cauchy-Green strain tensor
$\underline{\underline{C}}^{-1}$	Finger strain tensor
D	diameter of capillary or disks
D_P	diameter of piston
e	end correction factor for capillary flow experiments
$\underline{e}_i$	material vectors
E_o	activation energy, see Eq. (2.55)
f	material parameter in shear strain function, see Eq. (3.34)
F	axial force on disk in extensional rheometer
$\underline{\underline{F}}$	deformation gradient tensor
g_i	discrete relaxation time coefficients
G_a	apparent relaxation modulus
G_e	extensional relaxation modulus
G_s	shear relaxation modulus
G'	storage modulus
G''	loss modulus
$\overset{\circ}{G}$	linear viscoelastic relaxation modulus
h_e	extensional strain function
h_s	shear strain function

H	separation between parallel disks in shear and extensional rheometers
$H(\lambda)$	linear viscoelastic relaxation spectrum
H^*	strain functional, see Eq. (2.51)
I	generalized strain invariant; intensity of light
I_1, I_2	first and second invariants of strain tensor respectively
k	Boltzman's constant
ℓ	length of a freely-jointed rigid link
L	length of capillary
L_p	optical path length
L_1	stretch in pathline direction
L_2	separation of neighboring stream surfaces
L_3	stretch in circumferential direction
m	memory function
$\bar{M}_n$	number average molecular weight
$\bar{M}_w$	weight average molecular weight
n	power-law exponent
$\underline{\underline{n}}$	refractive index tensor
n_1, n_2	material parameters in shear strain function, see Eq. (3.34)
n_{13}	average birefringence across annular gap
$\underline{\underline{N}}$	indicatrix tensor
N_i	creation rate per unit volume of network segments
N_o	number of segments per unit volume in a rubber network
p	isotropic pressure
$P(r)$	probability density

P_e	pressure at the entrance of a capillary
P_o	pressure at the die exit
P^*	pressure at the die entrance
Q	volume flow rate
r	distance between entanglement junctions; radius
r_i	inner radius of annulus
r_o	outer radius of annulus
R	radius of shear and extensional rheometer fixtures
$\underline{\underline{R}}$	rotation tensor
$S(r)$	entropy of individual network segments
S_{13}	normal stress difference $\sigma_{11}-\sigma_{33}$
S_{23}	normal stress difference $\sigma_{22}-\sigma_{33}$
S'_{13}	principal normal stress difference $\sigma'_{11}-\sigma'_{33}$
t	time
T	temperature
T_o	reference temperature
T_g	glass transition temperature of a polymer
v_p	velocity of piston
v_r	radial velocity in annular flow
v_z	axial velocity in annular flow
$\bar{v}$	average velocity across the annular die gap
z	axial distance along annular die

Greek

α	material parameter in generalized strain invariant, see Eq. (2.46)
β	volume expansion coefficient; angle between the flow direction and the incident polarization direction, see Figure 5.21.
γ	shear strain
$\dot{\gamma}$	shear rate
δ	phase angle between stress and strain in oscillatory experiments
δ_T	total retardation angle
ε_a	axisymmetric extensional strain
ε_b	equibiaxial extensional strain
$\dot{\varepsilon}_a$	axisymmetric extension rate
$\dot{\varepsilon}_b$	equibiaxial extension rate
η_b	equibiaxial extensional viscosity
η_s	shear viscosity
η_o	zero-shear-viscosity
η_∞	infinite-shear-viscosity
η^o	reference viscosity in power-law, see Eq. (5.2)
η^*	complex viscosity
θ	shear angle
Θ	angular displacement of shear rheometer
λ	time constant in Carreau model, see Eq. (5.3)
λ_i	discrete relaxation times
λ_o	wavelength of light in vacuum
μ	linear viscoelastic memory function
ρ	density

$\underline{\underline{\sigma}}$	stress tensor
$\underline{\underline{\sigma}}_A$	contribution to stress tensor upstream of die entrance
τ	total torque on the plate in a rotational shear rheometer
τ_w	shear stress at the wall of a capillary
ϕ	angle between local coordinate system and principal coordinate system, see Figure 5.2
Φ	cone angle of cone and plate geometry
χ	correction factor for step strain experiments in a parallel disk geometry
ψ	angle between the principal axis of the indicatrix ellipsoid and the 3-axis of Figure 5.4
Ψ	streamlines of annular flow, see Eq. (4.6)
ω	angular frequency
Ω	angle between streamline and symmetry axis of axisymmetric flow

APPENDIX B

COMPUTER PROGRAM CODE

```
      PROGRAM DIEB
C
C  *********   LATEST VERSION 4-18-84    *********
C
      REAL ID,MFR
      COMMON / VISDAT/ AI(10),TAU(10),EN(2),FJ(2),ITAU,IPAR,ALPHA
      COMMON /   P1  / IW,IR
      COMMON / INPUT / T(40),V(40),R(40),SR(40),TEMP(40),A(40)
      COMMON /   NP  / NP,PSI,NS,NDF
      COMMON / TSHFT / ER,TO
      COMMON / DENSIT/ VEC,DEN,TDEN
      DIMENSION X(40),ID(40),OD(40),VA(40,21)
      DIMENSION RR(21),T11(21),T22(21),T33(21),T12(21),T1P(21)
     1 ,T2P(21),T3P(21),CHI(21),AB(21),DELTA(21)
      DIMENSION AFILE(9),BFILE(9),CFILE(9)
      TYPE*,'ENTER INPUT FILE NAME'
      ACCEPT50,AFILE
   50 FORMAT(9A2)
      OPEN(UNIT=1,NAME=AFILE,TYPE='OLD')
      TYPE*,'ENTER OUTPUT FILE NAME'
      ACCEPT50,BFILE
      OPEN(UNIT=2,NAME=BFILE,TYPE='NEW')
      TYPE*,'ENTER PLOT FILE NAME'
      ACCEPT50,CFILE
C
      IR= 1
      IW= 2
      READ(IR,51)
   51 FORMAT(50H                                                  )
      READ(IR,*) ITAU
      READ(IR,*) (AI(I),I=1,ITAU)
      READ(IR,*) (TAU(I),I=1,ITAU)
      READ(IR,*) IPAR,(EN(I),I=1,IPAR),(FJ(J),J=1,IPAR)
      READ(IR,*) ALPHA,ER,TO
      READ(IR,*) VEC,DEN,TDEN
      READ(IR,*) NAXP
      READ(IR,*) NDF,NRE,NPAR,NBL,NS
      READ(IR,*) (X(I),I=1,NAXP)
      READ(IR,*) (OD(I),I=1,NAXP)
      READ(IR,*) (ID(I),I=NRE,NAXP)
      READ(IR,*) TEXP,MFR,C,ZLAM,RERR
      CLOSE(UNIT=1)
      NP= NAXP
      NDF1= NDF-1
      NRAP=61
      OPEN(UNIT=3,DISP='DELETE')
```

```
      CALL VELFLD (NRAP,NAXP,X,ID,OD,MFR,TEXP,NDF,DP)
      REWIND 3
      NRAP=21
      DO 202 N=NDF,NAXP
  202 READ(3,60) (VA(N,L),L=1,NRAP)
   60 FORMAT(1H ,E15.7)
      CLOSE(UNIT=3)
C
C*******
      VFR= MFR*277.7778/DENSIT(TEXP)
      VB=VFR/(.7854*(OD(NDF)**2-ID(NDF)**2))
      DO 250 N=NRE,NAXP
  250 TEMP(N)=TEXP
      DO 254 L=1,NRAP
      DO 253 N=NRE,NDF1
      VA(N,L)= (VA(NDF,L)-VB)*(FLOAT(N-NRE))/(FLOAT(NDF-NRE)) + VB
  253 CONTINUE
  254 CONTINUE
      NDFP1= NDF+1
      NREP1= NRE+1
      DO 260 I=NDFP1,NAXP
  260 X(I)= X(I) + X(NDF)
      DO 261 I=NREP1,NAXP
  261 X(I)= X(I) + X(NRE)
C*******
C
      OPEN(UNIT=3,NAME=CFILE,TYPE='NEW')
      RO= OD(NRE)*.5
      HO= (OD(NRE)-ID(NRE))*.5
      WRITE(IW,90) MFR,TEXP,DP/6.895E3,DP/1.E5,RO,HO,VB,
     '             X(NDF)-X(NRE),X(NAXP)-X(NDF)
     '              ,NAXP,NDF,NRE,NS
   90 FORMAT(1H1,10X,21HMODELLING OF DIE FLOW
     '/1HO,14HMASS FLOW RATE,19X,F5.2,8H   KG/HR
     '/1H ,15HDIE TEMPERATURE,17X,F5.1,5H    C
     '/1H ,13HPRESSURE DROP,18X,F6.1,7H    PSI,F10.1,7H    BAR
     '/1HO,25HRADIUS AT DIE EXIT     RO,F13.2,5H   MM
     '/1H ,25HGAP WIDTH AT DIE EXIT  HO,F13.2,5H   MM
     '/1H ,25HVELOCITY AT DIE EXIT   VO,F13.2,7H   MM/S
     '/1H ,30HLENGTH OF REARRANGEMENT REGION,F9.3,4H  MM
     '/1H ,25HLENGTH OF DIE FLOW REGION,F13.2,5H   MM
     '/1HO,25HTOTAL NUMBER OF INTERVALS,I13
     '/1H ,28HINTERVAL WHERE DIE FLOW ENDS,I10
     '/1H ,33HINTERVAL WHERE REARRANGEMENT ENDS,I5
     '/1H ,35HINTERVAL WHERE STRESS IS CALCULATED,I3)
```

```
      WRITE(IW,1)
    1 FORMAT(1HO,16HRHEOLOGICAL DATA)
      WRITE(IW,51)
      WRITE( 3,51)
      WRITE(3,8)MFR
      WRITE(IW,2) TO,ER
    2 FORMAT(1HO,4X,26HREFERENCE TEMPERATURE  TO=,F5.0,2H K,
     *8X,5HE/R =,F8.0)
      WRITE(IW,3)
    3 FORMAT(1HO,4X,12HCOEFFICIENTS,3X,14HTIME CONSTANTS,6X,
     *27HSTRAIN FUNCTIONAL CONSTANTS)
      WRITE(IW,4)
    4 FORMAT(11X,1HA,13X,3HTAU,11X,2HF1,4X,2HF2,4X,2HN1,4X,2HN2,
     *4X,5HALPHA)
      WRITE(IW,5) FJ(1),FJ(2),EN(1),EN(2),ALPHA
    5 FORMAT(8X,7H(N/M2S),10X,3H(S),8X,4F6.3,F8.4)
      WRITE(IW,6) (AI(I),TAU(I),I=1,ITAU)
    6 FORMAT(1H ,2E15.3)
      WRITE(IW,9) VEC,DEN,TDEN
    9 FORMAT(1HO,12HDENSITY DATA
     */1HO,28HVOLUME EXPANSION COEFFICIENT,E11.2,5H  1/C
     */1H ,17HREFERENCE DENSITY,F20.4,9H    G/CM3
     */1H ,21HREFERENCE TEMPERATURE,F15.1,6H     C)
C
      WRITE(IW,7)
    7 FORMAT(1HO,7X,1HX,9X,2HID,8X,2HOD
     */1H ,5X,4H(MM),7X,4H(MM),6X,4H(MM)/1H )
      WRITE(IW,8) (X(I),ID(I),OD(I),I,I=1,NAXP)
    8 FORMAT(2H  ,3F10.3,I5)
C
      NRAP1=NRAP-1
      NAXP1=NAXP-1
C
      OPEN(UNIT=4,DISP='DELETE')
      CALL STRMLN (NRAP,NAXP,X,ID,OD,TEMP,VA,MFR,NDF,NRE,NPAR,NBL,NS)
      REWIND 4
C
      DO 207 IT=2,NRAP1
      PSI= 0.05 + (IT-2)*.05
      READ(4,70) (T(I),V(I),R(I),SR(I),I=NS,NAXP)
   70 FORMAT(1H ,4E15.7)
C
      DO 206 I=NS,NAXP
  206 R(I)= (R(I)*(OD(I)-ID(I)) + ID(I)) * .5
      DO 205 I=NS,NAXP
      IF(I.EQ.NS) A(I)= ATAN(-(R(I+1)-R(I))/(X(I+1)-X(I)))
      IF(I.EQ.NAXP) A(I)= ATAN(-(R(I)-R(I-1))/(X(I)-X(I-1)))
```

```
      IF(I.GT.NS.AND.I.LT.NAXP)A(I)= ATAN(-(R(I+1)-R(I-1))/(X(I+1)
     *                                                      -X(I-1)))
      V(I)= V(I)/COS(A(I))
      A(I)= 57.3*A(I)
  205 CONTINUE
      CALL GRID
      CALL STRSSF (T1,T2,T3,SHRT,RERR)
      RR(IT)= R(NS)
      T11(IT)= T1
      T22(IT)= T2
      T33(IT)= T3
      T12(IT)= SHRT
  207 CONTINUE
      CLOSE(UNIT=4)
C
      RR(1)= ID(NS) * .5
      RR(NRAP)= OD(NS) * .5
      CALL WALLS(NRAP,RR,T11)
      CALL WALLS(NRAP,RR,T22)
      CALL WALLS(NRAP,RR,T33)
      CALL WALLS(NRAP,RR,T12)
C
      PI= 3.14159
C
C  CALCULATE PRINCIPAL STRESSES
C
      DO 208 I=1,NRAP
      X2T= 2.*T12(I)
      Y= T11(I)-T22(I)
      IF(Y.NE.0.) GO TO 220
      CHI(I)= PI/4.
      GO TO 221
  220 CHI(I)= .5 * ATAN2(X2T,Y)
  221 CS= COS(CHI(I))
      SN= SIN(CHI(I))
      CS2= CS*CS
      SN2= SN*SN
      T1P(I)= T11(I)*CS2 + T22(I)*SN2 + X2T*SN*CS
      T2P(I)= T11(I)*SN2 + T11(I)*CS2 - X2T*SN*CS
      T3P(I)= T33(I)
      ZN1= C*T1P(I)
      ZN2= C*T2P(I)
      ZN3= C*T3P(I)
```

```
      ZA= 1./SQRT( (1./ZN2**2.)*SN2 + (1./ZN1**2.)*CS2 )
      ZB= ZN3
      AB(I)= ABS( ZA-ZB )
  208 CONTINUE
      ZZ= PI*( RR(NRAP)-RR(1) )/( ZLAM*NRAP1)
      DELTA(NRAP)= 0.
      DO 209 I=1,NRAP1
      DELTA(I)= ( AB(I) + AB(I+1) ) * ZZ
      DELTA(NRAP)= DELTA(I)+DELTA(NRAP)
  209 CONTINUE
C
      WRITE(3,11)
   11 FORMAT('                T11        T22        T33        T12',
     1 '      N1/2T12       CHI')
      DO 210 I=1,NRAP
  210 WRITE(3,12) (I-1.)/(NRAP-1.),T11(I),T22(I),T33(I),T12(I),
     1 ABS((T11(I)-T22(I))/(2*T12(I))),CHI(I)*57.3
   12 FORMAT(7F10.2)
      WRITE(3,14)
   14 FORMAT('              T11-122    T22-T33    T11-T33')
      DO 212 I=1,NRAP
  212 WRITE(3,12) (I-1.)/(NRAP-1.),T11(I)-T22(I),T22(I)-T33(I),
     1 T11(I)-T33(I)
      WRITE(3,15) C,ZLAM
   15 FORMAT(2E15.4)
      WRITE(3,16)
   16 FORMAT('              T1P-T2P    T2P-T3P    T1P-T3P     A-B/C'
     1 ,'     DELTA')
      DO 213 I=1,NRAP
  213 WRITE(3,17) (I-1.)/(NRAP-1.),T1P(I)-T2P(I),T2P(I)-T3P(I),
     1 T1P(I)-T3P(I),AB(I)/C,DELTA(I)
   17 FORMAT(5F10.2,E10.3)
      CLOSE(UNIT=3)
      CLOSE(UNIT=2)
      STOP 'END OF DIEB PROGRAM'
      END


                SUBROUTINE VELFLD (NRAP,NAXP,X,ID,OD,MFR,TEXP,NDF,DP)
C
C  *********    LAST MODIFICATION 10-11-82    *********
```

```
      REAL KAPA,ID,MFR
      COMMON /   P1  / IW,IR
      DIMENSION X(60),ID(60),OD(60)
      DIMENSION R(61),RN(61),RS(61),VZ(61),RDRDR(61),GAMD(61),ETA(61),
     *AR(61),AU(61),B(61),CL(61),CM(61),CR(61),DVZ(61),ETAD(61),GAMM(61)
      RELAX= 1.
      DELTAV= .0001
      NRAP1=NRAP-1
      VFR= MFR*277.7778/DENSIT(TEXP)
C
      VZ(1)= 0.
      VZ(NRAP)= 0.
      DP= 0.
      DO 120 L=2,NRAP1
  120 VZ(L)= 1.
      DO 110 N=NDF,NAXP
      RO=OD(N)*.5
      RI=ID(N)*.5
      VB=VFR/(.7854*(OD(N)**2-ID(N)**2))
      GAMB=VB/(RO-RI)
      ETAB=VISC(GAMB,TEXP)
      KAPA=RI/RO
      XKAP=KAPA
      H=1.-KAPA
      DR=H/(FLOAT(NRAP1))
      R(1)=KAPA
      R(NRAP)=1.
      RN(1)=KAPA+DR/2.
      RS(NRAP)=1.-DR/2.
      DO 100 M=2,NRAP1
      R(M)=KAPA+DR*(FLOAT(M)-1.)
      RN(M)=R(M)+DR/2.
      RS(M)=R(M)-DR/2.
      RDRDR(M)=R(M)*DR**2
  100 CONTINUE
      VZM= 1.
      GAMD(1)=1.
      GAMD(NRAP1)=1.
      GAMD(NRAP)=1.
      IT=0
  101 IT=IT+1
      DIF1=(GAMD(1)-GAMDIW)*.1
      DIF2=(GAMD(NRAP1)-GAMDOW)*.1
      IF(ABS(DIF1).LT.ABS(DIF2)) DIF1=DIF2
      GAMDIW=GAMD(1)
      GAMDOW=GAMD(NRAP1)
```

```
      DO 102 M=1,NRAP1
      GAMM(M)=ABS((VZ(M+1)-VZ(M))*VB/(DR*RO))
      GAMD(M)= GAMM(M)*RO/VB
  102 ETAD(M)= VISC(GAMM(M),TEXP)/ETAB
      CALL VAX(ETAD,RN,RS,R,RDRDR,VZ,DVZ,NRAP,DIF1,DR,
     *DPDL,VZM,XKAP,CL,CM,CR,AU,AR,B,RELAX)
      IF(IT.GT.400) STOP 'ITERATIONS = 400'
      IF(ABS(DIF1).GT.DELTAV) GO TO 101
      WRITE(3,60) (VZ(MM)*VB,MM=1,NRAP,3)
   60 FORMAT(1H ,E15.7)
      IF(N.EQ.NAXP) GO TO 110
      DPDZ= (R(3)*ETAD(3)*GAMM(3) - R(1)*ETAD(1)*GAMM(1))*ETAB/
     1 (R(2)*RO*(R(3)-R(1)))
      DP= -DPDZ * (X(N+1)-X(N)) + DP
  110 CONTINUE
      RETURN
      END
```

```
                    FUNCTION VISC(GAM,TEMPC)
C
      COMMON / VISDAT/ AI(10),TAU(10),EN(2),FJ(2),ITAU,IPAR,ALPHA
      VISC=0.
      SF= TSHFT(TEMPC)
      DO 4 I=1,ITAU
      TAUS= TAU(I)*SF
      AIS= AI(I)/SF
      DO 4 J=1,IPAR
    4 VISC=VISC+AIS*TAUS**2*FJ(J)/ (1.+TAUS*EN(J)*ABS(GAM))**2
      RETURN
        END
```

```
      SUBROUTINE STRMLN(NRAP,NAXP,X,ID,OD,TEM,VA,MFR,NDF,NRE,NPAR
     *,NBL,NS)
C
C  *********    LAST MODIFICATION 3-25-82    *********
C
      REAL ID,MFR
      COMMON /   P1   / IW,IR
      DIMENSION X(60),ID(60),OD(60),TEM(60),TIME(60,21)
     *,RPS(60,21),SRA(60,21),VA(60,21)
      DIMENSION PSIE(21),PSII(21),RP(21),SRG(21),RPI(21)
     *,SRGI(21),VW(21),VI(21)
      NRAP1=NRAP-1
      VFR= MFR*277.7778/DENSIT(TEM(NS))
      RI=ID(NS)*.5
      RO=OD(NS)*.5
      VB=VFR/(.7854*(OD(NS)**2-ID(NS)**2))
      DR=(OD(NS)-ID(NS))/(2.*FLOAT(NRAP1))
      R=ID(NS)*0.5-DR
      PSIE(1)=0.
      DO 300 L=1,NRAP
      TIME(NS,L)=0.
      IF(L.EQ.1) SRA(NS,L)=(VA(NS,L+1)-VA(NS,L))/DR
      IF(L.EQ.NRAP) SRA(NS,L)=(VA(NS,L)-VA(NS,L-1))/DR
      IF(L.GT.1.AND.L.LT.NRAP) SRA(NS,L)=(VA(NS,L+1)-VA(NS,L-1))/(2.*DR)
      RPS(NS,L)=(FLOAT(L)-1.)*DR/(RO-RI)
      IF(L.EQ.NRAP) GO TO 300
      R=R+DR
      PSIE(L+1)=PSIE(L)+(VA(NS,L)*R+VA(NS,L+1)*(R+DR))*
     *DR/(RO**2-RI**2)/VB
300   CONTINUE
      NSP1= NS+1
      DO 308 N=NSP1,NAXP
      VFR= MFR*277.7778/DENSIT(TEM(N))
      RI=ID(N)*.5
      RO=OD(N)*.5
      VB=VFR/(.7854*(OD(N)**2-ID(N)**2))
      PSII(1)=0.
      IF(VA(N,1).LT.0.) GO TO 309
      DR=(OD(N)-ID(N))/(2.*FLOAT(NRAP1))
      RP(1)=ID(N)/2.
      SRG(1)=(VA(N,2)-VA(N,1))/DR
      VW(1)=VA(N,1)
      DO 301 L=2,NRAP
      RP(L)=RP(L-1)+DR
      VW(L)=VA(N,L)
      PSII(L)=PSII(L-1)+(VA(N,L-1)*RP(L-1)+VA(N,L)*RP(L))*
```

```
     *DR/(RO**2-RI**2)/VB
      IF(L.EQ.NRAP) SRG(L)=(VA(N,NRAP)-VA(N,NRAP1))/DR
      IF(L.NE.NRAP) SRG(L)=(VA(N,L+1)-VA(N,L-1))/(2.*DR)
  301 CONTINUE
C*******
      IF(N.LE.NBL) GO TO 320
      IF(N.GT.NBL.AND.N.LE.NPAR) GO TO 322
      IF(N.GT.NPAR.AND.N.LT.NRE) GO TO 320
      IF(N.GE.NRE.AND.N.LE.NDF) GO TO 333
C*******
      IF(OD(N).EQ.OD(N-1).AND.ID(N).EQ.ID(N-1)) GO TO 303
  333 CONTINUE
      CALL INTERP(NRAP,PSII,RP,NRAP,PSIE,RPI)
      CALL INTERP(NRAP,RP,SRG,NRAP,RPI,SRGI)
      CALL INTERP(NRAP,RP,VW,NRAP,RPI,VI)
      DO 302 L=1,NRAP
      RPS(N,L)=(RPI(L)-RP(1))/DR/NRAP1
      SRA(N,L)=SRGI(L)
      VA(N,L)=VI(L)
  302 CONTINUE
      GO TO 305
  303 DO 304 L=1,NRAP
      VA(N,L)=VA(N-1,L)
      RPS(N,L)=RPS(N-1,L)
      SRA(N,L)=SRA(N-1,L)
  304 CONTINUE
      GO TO 305
  320 CALL INTERP(NRAP,PSII,RP,NRAP,PSIE,RPI)
      DO 321 L=1,NRAP
      RPS(N,L)=(RPI(L)-RP(1))/DR/NRAP1
      SRA(N,L)=SRA(N-1,L)
  321 CONTINUE
      GO TO 305
  322 DO 323 L=1,NRAP
      RPS(N,L)= RPS(N-1,L)
      SRA(N,L)= SRA(N-1,L)
  323 CONTINUE
C*******
  305 CONTINUE
      DO  307 L=2,NRAP1
      IF(VA(N,L).EQ.VA(N-1,L)) GO TO 306
      TIME(N,L)=TIME(N-1,L)+(X(N-1)-X(N))/(VA(N-1,L)-VA(N,L))*
     *ALOG(VA(N-1,L)/ VA(N,L))
      GO TO 307
  306 TIME(N,L)=TIME(N-1,L)+(X(N-1)-X(N))/VA(N,L)
  307 CONTINUE
  308 CONTINUE
```

```
      WRITE(4,70)((-TIME(N,L),VA(N,L),RPS(N,L),SRA(N,L),N=NS,NAXP),
     *L=2,NRAP1)
   70 FORMAT(1H ,4E15.7)
C
  309 CONTINUE
C
      RETURN
      END
```

```
            SUBROUTINE GRID
      REAL L1,L2,L3
      COMMON / INPUT / T(60),V(60),R(60),SR(60),TEMP(60),A(60)
      COMMON /   NP  / NP,PSI,NS,NDF
      COMMON / GRIDF / L1(60),L2(60),L3(60),P(60),Q(60),GAMMA(60)
      COMMON / GRIDT / U(60)
      COMMON /   P1  / IW,IR
      DIMENSION XX(60)
      DNS= DENSIT(TEMP(NS))
C
      NSP1= NS+1
      DO 101 I=NS,NP
      L1(I)= V(NS)/V(I)
      L3(I)= R(NS)/R(I)
      L2(I)= DENSIT(TEMP(I))/(DNS*L1(I)*L3(I))
      P(I)= -L2(I)/L1(I)
      Q(I)= (L1(I)*SR(I))/ L2(I)
  101 CONTINUE
C
      GAMMA(NS)= 0.
      XX(NS)= 0.
      U(NS)= 0.
C
      DO 102 I=NSP1,NP
      DT= T(I)-T(I-1)
      DT2= (T(I)**2-T(I-1)**2)*.5
      GAMMA(I)= GAMMA(I-1)+P(I)*(Q(I)*T(I) - Q(I-1)*T(I-1) -
     *                    ((Q(I)-Q(I-1))*DT2/DT))
      XX(I)= XX(I-1) + DT*(V(I)+V(I-1))*.5
      AT= 1./TSHFT(TEMP(I))
      AT1= 1./TSHFT(TEMP(I-1))
      U(I)= U(I-1) - ( AT*T(I) - AT1*T(I-1) - ((AT-AT1)*DT2/DT))
  102 CONTINUE
```

```
      WRITE(IW,12) PSI
   12 FORMAT(1HO,30X,18HSTREAMLINE (PSI) =,F7.4)
      WRITE(IW,13)
   13 FORMAT(1H ,6X,1HT,8X,1HV,7X,1HA,7X,1HR,7X,2HSR,5X,4HTEMP,6X,2HL1,
     *7X,2HL2,7X,2HL3,7X,1HP,8X,1HQ,7X,5HGAMMA,5X,1HU,8X,2HXX)
      WRITE(IW,14)
   14 FORMAT(1H ,5X,3H(S),4X,6H(MM/S),4X,3H(D),4X,4H(MM),4X,5H(1/S),4X,
     *3H(C),60X,3H(S),6X,4H(MM))
      WRITE(IW,15) (T(I),V(I),A(I),R(I),SR(I),TEMP(I),L1(I),L2(I),
     *   L3(I),P(I),Q(I),GAMMA(I),U(I),XX(I),I,I=NS,NP)
   15 FORMAT(1H ,2F9.3,F7.1,2F9.3,F8.2,8F9.3,I6)
C
      RETURN
      END



        SUBROUTINE STRSSF (T11T,T22T,T33T,T12T,RERR)
C
C  *********    LATEST REVISION 2-8-83    *********
C
      REAL L1S,L2S,L3S
      COMMON / INPUT / T(60),V(60),R(60),SR(60),TEMP(60),A(60)
      COMMON /   NP  / NP,PSI,NS,NDF
      COMMON /   P1  / IW,IR
      COMMON /   SF  / RSTFMI
      EXTERNAL T11,T22,T33,T12
      DIMENSION STR(4)
      AERR= 0.
      NP1= NP-1
      WRITE(IW,23)
   23 FORMAT(1HO,7X,2HN1,9X,2HN2,9X,2HN3,9X,3HT12,4X,7HN1/2T12,9X,
     *1HH,10X,3HI11,4H I22,4H I33,4H I12)
      RSTFMI= 1.
      T11A= 0.
      T22A= 0.
      T33A= 0.
      T12A= 0.
      DO 201 L=1,4
  201 STR(L)= 0.
C
      DO 202 I=NS,NP1
      AA= T(I)
      BB= T(I+1)
```

```
      CALL FINGER(AA,L1S,L2S,L3S,GAMMAS)
      CALL STRAIN(L1S,L2S,L3S,GAMMAS,RSTFAA)
      IF(RSTFAA.LT.RSTFMI)RSTFMI=RSTFAA
      CT11= ROMB(T11,AA,BB,AERR,RERR,ER11,I11)
      IF(ABS(CT11).LT..01.AND.I.GT.NDF) GO TO 204
      STR(1)= CT11+STR(1)
      STR(2)= ROMB(T22,AA,BB,AERR,RERR,ER22,I22) + STR(2)
      STR(3)= ROMB(T33,AA,BB,AERR,RERR,ER33,I33) + STR(3)
      STR(4)= ROMB(T12,AA,BB,AERR,RERR,ER12,I12) + STR(4)
C
      IF(STR(4).EQ.0.) GO TO 222
      RECSHR= (STR(1) - STR(2))/(2.*STR(4))
      GO TO 223
  222 RECSHR=0.0
  223 CONTINUE
      WRITE(IW,25) (STR(1)-STR(2),STR(2)-STR(3),STR(1)-STR(3),STR(4),
     * RECSHR,RSTFMI,I+1,I11,I22,I33,I12)
   25 FORMAT(1H ,4F11.1,2E12.4,5I4)
      IF(I.NE.NP1) GO TO 202
      CALL FINGER(BB,L1S,L2S,L3S,GAMMAS)
      CALL STRAIN(L1S,L2S,L3S,GAMMAS,RSTFBB)
      CALL UATS(BB,US,ATS)
      CALL IMEMF(US,RIMF)
      RRR= RIMF*RSTFBB
      T11A= RRR * (1.+GAMMAS**2)*L1S**2
      T22A= RRR * L2S**2
      T33A= RRR * L3S**2
      T12A= RRR * (-GAMMAS*L1S*L2S)
      WRITE(IW,26) T11A-T22A,T22A-T33A,T11A-T33A,T12A,RSTFBB
   26 FORMAT(1H ,4F11.1,12X,E12.4,3X,19HADDITIONAL STRESSES)
C
  204 CONTINUE
      T11T= STR(1) + T11A
      T22T= STR(2) + T22A
      T33T= STR(3) + T33A
      T12T= STR(4) + T12A
      WRITE(IW,27)
   27 FORMAT(1H ,45H_____________________________________________)
      WRITE(IW,28) T11T-T22T,T22T-T33T,T11T-T33T,T12T
   28 FORMAT(1H ,4F11.1,9X,14HTOTAL STRESSES)
      GO TO 203
C
  202 CONTINUE
  203 CONTINUE
C
      RETURN
      END
```

```
      FUNCTION T11(S)
REAL L1S,L2S,L3S
CALL FINGER(S,L1S,L2S,L3S,GAMMAS)
CALL STRAIN(L1S,L2S,L3S,GAMMAS,RSTF)
CALL UATS(S,US,ATS)
CALL LVEMEM(US,ATS,RMF)
T11= RMF*RSTF*(1.+GAMMAS**2)*(L1S**2)
RETURN
END
```

```
      FUNCTION T22(S)
REAL L1S,L2S,L3S
CALL FINGER(S,L1S,L2S,L3S,GAMMAS)
CALL STRAIN(L1S,L2S,L3S,GAMMAS,RSTF)
CALL UATS(S,US,ATS)
CALL LVEMEM(US,ATS,RMF)
T22= RMF*RSTF*L2S**2
RETURN
END
```

```
      FUNCTION T33(S)
REAL L1S,L2S,L3S
CALL FINGER(S,L1S,L2S,L3S,GAMMAS)
CALL STRAIN(L1S,L2S,L3S,GAMMAS,RSTF)
CALL UATS(S,US,ATS)
CALL LVEMEM(US,ATS,RMF)
T33= RMF*RSTF*L3S**2
RETURN
END
```

```
      FUNCTION T12(S)
REAL L1S,L2S,L3S
CALL FINGER(S,L1S,L2S,L3S,GAMMAS)
CALL STRAIN(L1S,L2S,L3S,GAMMAS,RSTF)
CALL UNTS(S,US,ATS)
CALL LVEMEM(US,ATS,RMF)
T12= RMF*RSTF*(-GAMMAS*L1S*L2S)
RETURN
END
```

```
      SUBROUTINE FINGER(S,L1S,L2S,L3S,GAMMAS)
REAL L1,L2,L3,L1S,L2S,L3S
COMMON / INPUT / T(60),V(60),R(60),SR(60),TEMP(60),A(60)
COMMON / GRIDF / L1(60),L2(60),L3(60),P(60),Q(60),GAMMA(60)
COMMON /   NF  / NF,FSI,NS,NDF
C
      DNS= DENSIT(TEMP(NS))
      DO 301 I=NS,NF
301   IF(T(I).GT.S) GO TO 302
302   CONTINUE
      IF(S.EQ.T(NF)) I=NF
      FT= (S-T(I-1))/(T(I)-T(I-1))
      L1S= L1(I-1) + FT*(L1(I)-L1(I-1))
      L3S= L3(I-1) + FT*(L3(I)-L3(I-1))
      TEMPS= TEMP(I-1) + FT*(TEMP(I)-TEMP(I-1))
      L2S= DENSIT(TEMPS)/(DNS*L1S*L3S)
      SRS= SR(I-1) + FT*(SR(I)-SR(I-1))
      PS = -L2S/L1S
      QS = (L1S*SRS)/L2S
      GAMMAS= GAMMA(I-1) + PS*(QS*S - Q(I-1)*T(I-1) -
     "      ((Q(I)-Q(I-1))*(S**2-T(I-1)**2)*.5/(T(I)-T(I-1))))
      RETURN
      END
```

```
      SUBROUTINE STRAIN(L1S,L2S,L3S,GAMMAS,RSTF)
REAL L1S,L2S,L3S
COMMON / VISDAT/ AI(10),TAU(10),EN(2),FJ(2),ITAU,IPAR,ALPHA
COMMON /   SF  / RSTFMI
RSTF= 0.
FI= (1.+GAMMAS**2)*(L1S**2) + L2S**2 + L3S**2
SI= 1./L1S**2 + (1.+GAMMAS**2)/L2S**2 + 1./L3S**2
ROOT= SQRT(ABS((1.-ALPHA)*SI+ALPHA*FI-3.))
DO 602 J=1,IPAR
E= EN(J)*ROOT
IF(E.GT.65.) GO TO 601
QQ= FJ(J)*EXP(-E)
GO TO 602
601 QQ= 0.
602 RSTF= RSTF + QQ
IF(RSTF.GT.RSTFMI) RSTF=RSTFMI
RETURN
END
```

```
      SUBROUTINE LVEMEM(US,ATS,RMF)
COMMON / VISDAT/ AI(10),TAU(10),EN(2),FJ(2),ITAU,IPAR,ALPHA
RMF= 0.
DO 502 I=1,ITAU
E= US/TAU(I)
IF(E.LT.-65.) GO TO 501
QQ= EXP(E)
GO TO 502
501 QQ= 0.
502 RMF= RMF + AI(I)*ATS*QQ
RETURN
END
```

```
            SUBROUTINE UATS(S,US,ATS)
      COMMON / INPUT / T(60),V(60),R(60),SR(60),TEMP(60),A(60)
      COMMON / GRIDT / U(60)
      COMMON /   NP  / NP,PSI,NS,NDF
C
      DO 401 I=NS,NP
  401 IF(T(I).GT.S) GO TO 402
  402 CONTINUE
      FT= (S-T(I-1))/(T(I)-T(I-1))
      TEMPS= TEMP(I-1) + FT*(TEMP(I)-TEMP(I-1))
      ATS= 1./TSHFT(TEMPS)
      AT = 1./TSHFT(TEMP(I))
      AT1= 1./TSHFT(TEMP(I-1))
      US= U(I-1) - ( ATS*S - AT1*T(I-1) - ((AT-AT1)*(S**2-T(I-1)**2)
     .                                        *.5/(T(I)-T(I-1))))
      RETURN
      END
```

```
            SUBROUTINE IMEMF(US,RIMF)
      COMMON / VISDAT/ AI(10),TAU(10),EN(2),FJ(2),ITAU,IPAR,ALPHA
      RIMF= 0.
      DO 702 I=1,ITAU
      E= US/TAU(I)
      IF(E.LT.-65.) GO TO 701
      QQ= EXP(E)
      GO TO 702
  701 QQ= 0.
  702 RIMF= RIMF + AI(I)*TAU(I)*QQ
      RETURN
      END
```

```
                FUNCTION TSHFT(TEMPC)
C
C  THIS FUNCTION CALCULATES THE SHIFT FACTOR FOR THE RELAXATION TIME
C  SPECTRUM USING AN ARRHENIUS TYPE EQUATION TO FIT THE DATA.
C
C  ER       ACTIVATION ENERGY DIVIDED BY THE GAS CONSTANT    (K)
C  TO       REFERENCE TEMPERATURE OF RELAXATION TIMES    (K)
C  TEMPC    TEMPERATURE TO WHICH THE TIMES ARE TO BE
C           SHIFTED    (C)
C                                                              (INPUT)
      COMMON / TSHFT / ER,TO
      TEMPK= TEMPC+273.16
      TSHFT= EXP(ER*(1./TEMPK-1./TO))
      RETURN
      END
```

```
                FUNCTION DENSIT(T)
C
C  THIS FUNCTION CALCULATES THE MELT DENSITY AS A FUNCTION OF
C  TEMPERATURE     UNITS OF (G/CM3)
C
C  VEC      VOLUME EXPANSION COEFFICIENT    (1/C)
C  DEN      REFERENCE DENSITY      (G/CM3)
C  TDEN     REFERENCE TEMPERATURE      (C)
C  T        TEMPERATURE AT WHICH DENSITY IS TO BE CALCULATED  (C)
C
      COMMON / DENSIT/ VEC,DEN,TDEN
      DENSIT = DEN * (1. + VEC * (TDEN - T) )
      RETURN
      END
```